

**Extensional and  
Surface-Tension-Driven Fluid Flows in  
Microstructured Optical Fibre  
Fabrication**

Hayden Tronnolone

*Thesis submitted for the degree of*

*Doctor of Philosophy*

*in*

*Applied Mathematics*

*at*

*The University of Adelaide*

*(Faculty of Engineering, Computer and Mathematical Sciences)*

Department of Applied Mathematics



February 1, 2016



For my mother, Sharon



And I looked at that painting *Sunflowers*. And for a  
bogan from Hamilton like myself I could actually see  
beauty in that frustration.

Phil Walsh



# Contents

<b>Contents</b>	<b>vii</b>
<b>Abstract</b>	<b>xv</b>
<b>Signed Statement</b>	<b>xvii</b>
<b>Acknowledgements</b>	<b>xix</b>
<b>List of Variables</b>	<b>xxiii</b>
<b>List of Figures</b>	<b>xxvii</b>
<b>List of Tables</b>	<b>xxxv</b>
<b>1 Introduction</b>	<b>1</b>
1.1 Microstructured Optical Fibres . . . . .	1
1.2 Microstructured Optical Fibre Fabrication . . . . .	5
1.3 Previous Work . . . . .	10
1.4 Thesis Content . . . . .	13
<b>2 Glass and Its Properties</b>	<b>17</b>
2.1 Introduction . . . . .	17

2.2	Glass Properties . . . . .	19
2.2.1	Viscosity . . . . .	19
2.2.2	Material Constitutive Equation . . . . .	22
2.2.3	Density . . . . .	24
2.2.4	Surface Tension . . . . .	25
2.2.5	Heat Transfer . . . . .	28
2.3	Summary of Assumptions . . . . .	31
<b>3</b>	<b>Slenderness Model</b>	<b>33</b>
3.1	Introduction . . . . .	33
3.2	Trouton Models . . . . .	34
3.3	Slenderness Model . . . . .	39
3.3.1	Governing Equations and Slenderness Approximation . .	39
3.3.2	Scaled Equations and Series Expansions . . . . .	43
3.3.3	Temperature and Viscosity in the Slender Limit . . . . .	47
3.3.4	Axial Flow Equations . . . . .	49
3.3.5	Leading-Order Kinematic Condition and Conservation of Mass . . . . .	60
3.3.6	Transverse Equations . . . . .	61
3.3.7	Zero-Surface-Tension Transverse Solution . . . . .	62
3.3.8	Transverse System and Reduced Time . . . . .	63
3.4	Summary . . . . .	66
<b>4</b>	<b>Stokes Flows and Complex Variables</b>	<b>69</b>
4.1	Introduction . . . . .	69
4.2	Stokes Equations . . . . .	74
4.2.1	Basic Theory . . . . .	74

4.2.2	The Biharmonic Equation . . . . .	75
4.2.3	Complex Variables . . . . .	76
4.2.4	Complex Analytic Functions . . . . .	79
4.2.5	The Airy Stress Function . . . . .	82
4.2.6	The Goursat Functions and Physical Quantities . . . . .	87
4.2.7	Dynamic Boundary Condition . . . . .	89
4.2.8	Kinematic Boundary Condition . . . . .	95
4.2.9	Uniqueness of the Goursat Representation . . . . .	96
4.2.10	Geometric Quantities . . . . .	98
4.3	Exact Solutions . . . . .	99
4.3.1	An Annulus . . . . .	99
4.3.2	Hopper's Exact Solutions . . . . .	104
4.4	Summary . . . . .	104
<b>5</b>	<b>Numerical Solution of Stokes Flows</b>	<b>107</b>
5.1	Introduction . . . . .	107
5.2	Spectral Collocation Method . . . . .	111
5.2.1	Overview of Method . . . . .	111
5.2.2	Conformal Map . . . . .	112
5.2.3	Goursat Functions . . . . .	114
5.2.4	Mapped Dynamic Boundary Condition . . . . .	115
5.2.5	Mapped Kinematic Boundary Condition . . . . .	117
5.2.6	Algorithm . . . . .	118
5.2.7	Convergence . . . . .	119
5.2.8	Calculating Geometric Quantities . . . . .	120
5.2.9	Comparison with Exact Solution for an Annulus . . . . .	122
5.2.10	3-Hole Preforms . . . . .	123

5.2.11	6- and 7-Hole Preforms . . . . .	131
5.3	Alternative Spectral Method . . . . .	133
5.3.1	Overview of Method . . . . .	133
5.3.2	Conformal Maps . . . . .	136
5.3.3	Goursat Functions . . . . .	136
5.3.4	Boundary Conditions . . . . .	138
5.3.5	Inverting the Conformal Maps . . . . .	139
5.3.6	Calculating Geometric Quantities . . . . .	142
5.3.7	Convergence and Comparison with Known Solutions . . . . .	144
5.3.8	Application to Elliptical Boundaries . . . . .	146
5.3.9	3-Hole Preforms with an Elliptical Central Hole . . . . .	148
5.4	Method of Fundamental Solutions . . . . .	149
5.4.1	Motivation . . . . .	149
5.4.2	Overview of Method . . . . .	152
5.4.3	Mathematical Formulation . . . . .	152
5.4.4	Convergence . . . . .	156
5.4.5	Comparison with Exact Solution . . . . .	157
5.4.6	Van de Vorst Example and Comparison of Methods . . . . .	158
5.5	Elliptical Pore Models . . . . .	161
5.5.1	Overview of Method . . . . .	161
5.5.2	$n$ -Ring Preforms . . . . .	162
5.6	Summary . . . . .	170
<b>6</b>	<b>Stretching Fluid Cylinders</b>	<b>175</b>
6.1	Introduction . . . . .	175
6.2	Governing Equations . . . . .	176
6.2.1	Overview . . . . .	176

6.2.2	Scales . . . . .	176
6.2.3	Axial Problem and Lagrangian Co-ordinate . . . . .	178
6.2.4	Coupling the Axial and Transverse Problems . . . . .	181
6.2.5	Solution for Small Inertia . . . . .	182
6.2.6	Solutions for Weak and Zero Surface Tension . . . . .	185
6.3	Cylinders with No Internal Structure . . . . .	187
6.3.1	Overview . . . . .	187
6.3.2	Solution for a Solid Rod . . . . .	188
6.3.3	Influence of Surface Tension and Geometry . . . . .	193
6.4	Cylinders with Internal Structure . . . . .	201
6.4.1	Overview . . . . .	201
6.4.2	Stretching Tube . . . . .	203
6.4.3	3-Hole Experiment . . . . .	208
6.5	Including Inertia . . . . .	212
6.6	Summary . . . . .	215
<b>7</b>	<b>Modelling Extrusion</b>	<b>219</b>
7.1	Introduction . . . . .	219
7.2	Die Effects . . . . .	220
7.3	Extrusion Model . . . . .	223
7.3.1	Parameters and Governing Equations . . . . .	224
7.3.2	Lagrangian Co-ordinate and Reduced Time . . . . .	227
7.3.3	Solutions for Zero and Weak Surface Tension . . . . .	231
7.4	Geometries with No Internal Holes . . . . .	233
7.4.1	Solution for a Solid Rod . . . . .	233
7.4.2	Influence of Surface Tension and Geometry . . . . .	234
7.5	Controlling Deformation and Exact Solution for an Annulus . . . . .	235

7.5.1	Overview	235
7.5.2	Measuring Deformation	237
7.5.3	Solution for an Annulus	237
7.5.4	Controlling Deformation	238
7.6	MOF Preform Examples	240
7.6.1	Overview	240
7.6.2	3-Hole Preform	244
7.6.3	7-Hole Preform	244
7.6.4	7-Ring Preform	249
7.6.5	Cooling After Extrusion	249
7.7	Pinch-Off	255
7.7.1	Overview	255
7.7.2	Exact Solution for Zero Surface Tension	257
7.7.3	Exact Solution for a Solid Rod	258
7.7.4	Solution for General Geometries	258
7.8	Summary	259
<b>8</b>	<b>Preform Stacking and Cusp-Like Deformations</b>	<b>263</b>
8.1	Introduction	263
8.2	Coalescing Tubes	266
8.2.1	Map for Two Tubes	266
8.2.2	Map for More Than Two Tubes	275
8.3	Deformed 3-Hole Preforms	289
8.3.1	Geometry at the Die Exit	289
8.3.2	Computing Initial Maps	291
8.3.3	Extrusion Example	295
8.4	Fluid Flow Inside the Die	300

8.4.1	Motivation . . . . .	300
8.4.2	Model . . . . .	304
8.4.3	Examples . . . . .	305
8.5	Summary . . . . .	312
<b>9</b>	<b>Conclusions</b>	<b>315</b>
<b>A</b>	<b>Transport Theorems</b>	<b>321</b>
<b>B</b>	<b>Numerical Methods for Solving Polynomial Equations</b>	<b>323</b>
B.1	Overview . . . . .	323
B.2	Companion Matrix . . . . .	324
B.3	Newton's Method . . . . .	324
B.4	Argument Principle . . . . .	325
B.5	Other Methods . . . . .	326
<b>C</b>	<b>Experimental Set-Up and Measurements</b>	<b>327</b>
C.1	General method . . . . .	327
C.2	Tube . . . . .	329
C.3	3-Hole Cylinder . . . . .	333
	<b>Bibliography</b>	<b>335</b>
	<b>Index</b>	<b>359</b>



# Abstract

Microstructured optical fibres (MOFs) are a design of optical fibre comprising a series of longitudinal air channels within a thread of material that form a waveguide for light. The flexibility of this design allows optical fibres to be created with adaptable and previously unrealised optical properties. A MOF is typically constructed by first creating a macroscopic version of the design, known as a preform, with a centimetre-scale diameter that is later drawn into a fibre with a micrometer-scale diameter.

There are several methods for constructing a preform. In the extrusion method molten material is forced through a die containing an array of blocking elements that match the required pattern of channels. Preforms may also be constructed by stacking tubes and fusing them together with heat. In both processes the fluid flow that arises can deform the air channels, rendering the fibre useless. At present there is only a limited understanding of the relative importance of the various physical parameters in determining the final preform geometry, which means that the development of new MOF technology requires time-consuming and costly experimentation.

This thesis develops mathematical models of the fluid flows that occur during the extrusion and stacking methods of MOF preform fabrication. These models are used to determine which physical mechanisms are important during

the manufacturing process so as to inform the fabrication of MOF preforms.

A model is constructed of a fixed slender fluid cylinder with internal structure stretching under gravity and with surface-tension-driven deformation. The molten material is modelled as a Newtonian fluid with a temperature-dependent viscosity, which is assumed known. The variables are expanded as series in powers of a slenderness parameter so that, after dropping higher-order terms, the resulting equations partially decouple into a one-dimensional model for the axial flow and a two-dimensional model for the transverse flow. Under a suitable transformation of variables the transverse equations are precisely the Stokes equations with unit surface tension. After reviewing the use of complex variables to represent the transverse problem, three numerical solution methods are considered: two based upon spectral methods and one using the method of fundamental solutions (MFS). These methods are compared for their efficiency and accuracy.

Several example solutions for stretching cylinders are presented and the role of surface tension is investigated using approximate solutions derived for zero and small surface tension. The model is validated against experimental data and found to be in good agreement. The stretching model is extended to the case of an extruded fluid cylinder, neglecting extrudate-swell effects, where again the fluid flow decouples in axial and transverse models. The results are compared with experimental observations and the model used to analyse the formation of distortions during preform extrusion and how these may be controlled. Two problems related to preform fabrication are considered that feature cross sections with non-circular initial outer boundaries. A technique is developed for deriving initial conformal maps describing such domains, which are used in the stretching and extrusion models to analyse the proposed problems.

# Signed Statement

I certify that this work contains no material which has been accepted for the award of any other degree or diploma in my name in any university or other tertiary institution and, to the best of my knowledge and belief, contains no material previously published or written by another person, except where due reference has been made in the text. In addition, I certify that no part of this work will, in the future, be used in a submission in my name for any other degree or diploma in any university or other tertiary institution without the prior approval of the University of Adelaide and, where applicable, any partner institution responsible for the joint award of this degree.

I give consent to this copy of my thesis, when deposited in the University Library, being made available for loan and photocopying, subject to the provisions of the Copyright Act 1968. I also give permission for the digital version of my thesis to be made available on the web, via the University's digital research repository, the Library Search and also through web search engines, unless permission has been granted by the University to restrict access for a period of time.

SIGNED: ..... DATE: .....



# Acknowledgements

## Personal Acknowledgements

Throughout my PhD I have received support from many people, without which I could not have completed this thesis. I am grateful to everyone who has assisted me over the last few years.

I am thankful to have received financial support for this research from both the Australian Federal Government, via an Australian Postgraduate Award, and the A. F. Pillow Applied Mathematics Trust, without which I could not have undertaken this work. I would also like to thank the School of Mathematical Sciences and the University of Adelaide for supporting my research by providing me a space to work and equipment to do so. I am especially thankful to the administrative staff within the School who have helped me arrange travel to numerous conferences and supported this work in many other ways.

I have been fortunate to receive significant support from the academic staff within the School and would like to thank, in particular: Finnur Lárusson and Nick Buchdahl for advice on complex analysis; Trent Mattner for helpful discussions on numerical methods; and Ed Green for many Friday nights at the Staff Club.

This project was motivated by research being performed at the Institute

for Photonics and Advanced Sensing (IPAS) at the University of Adelaide and I have greatly appreciated the assistance and insight provided by the members of IPAS. I am especially grateful to Heike Ebendorff-Heidipriem, who has assisted this project with great enthusiasm from the start and has provided invaluable advice and support. I am indebted to both Alastair Dowler, for his experimental expertise; and Herbert Tze Cheung Foo, who has worked untold hours running experiments, collecting the data used in this thesis and who was receptive to every outlandish experiment I proposed.

I am very grateful for the conversations I've had with the other members of the fibre modelling group, namely Peter Buchak, for many discussions on and assistance with numerical methods; and Mike Chen, for advice on using experimental data and discussions on code.

My time as a postgraduate has been greatly improved for having shared it with other students in the postgraduate office. I am particularly thankful to: David Price, for lengthy football discussions and running the office football tipping; Sophie Calabretto, for sharing practical jokes, TV shows and lecturer merchandise; Kale Davies, for maths discussions and keeping pubcrawls interesting; and Mingmei Teo, for taking photographs used in this thesis, sharing the highs and lows of trade weeks, and remaining in the adjacent desk while baring the full force of my complaints (and illegally-placed bookshelf). I would like to extend special thanks to Michael Albanese, with whom I wasted more time than anybody else and have no regrets for doing so. From giving a joint seminar, to building a Cantor set from empty drink cans, my PhD wouldn't have been half as interesting without these diversions.

My family and friends have been forced to accept me being unavailable for large periods of time over the last few years and I am grateful for all of

their tolerance and support. I am particularly grateful to my mother, Sharon, without whose support I would never have attended university, let alone have completed this thesis. I would also like to thank my girlfriend, Ali, who has provided invaluable support and has tolerated my undulating mood over the course of this project.

I started my candidature under the supervision of Matt Finn, who taught me about complex variables, producing good writing and creating good code, and whose lessons I am still influenced by. I have also received expert advice on complex variables and Stokes flows under the supervision of Darren Crowdy, first as an external supervisor and later as a secondary supervisor, to whom I am very grateful.

Finally, I want to offer profound thanks to Yvonne Stokes, who recommended this project and has been my primary supervisor throughout. She has been supportive, encouraging, patient as deadlines were missed, invaluable in providing advice and tireless in proofreading my work. I have been extremely fortunate to have her support and I hope that this thesis, in some small way, reflects her efforts.

## Image Credits

Figure 1.1.3e was originally published by Manning (2011) as part of a PhD thesis and is reproduced with permission from the author.

Figure 1.1.3f was created by IPAS and is reproduced courtesy of Heike Ebendorff-Heidepriem on behalf of IPAS.

Figure 1.1.3g was originally published by Ebendorff-Heidepriem and Monro (2007) and is reproduced with permission from The Optical Society and the authors.

Figure 1.1.3h is reproduced with permission from AIP Publishing LLC under license number 3732340375332.

Figure 5.4.21 contains a reproduction of a solution computed by van de Vorst (1993) and is reproduced with non-exclusive permission from Cambridge University Press.

The photographs from Figures 1.2.4, 1.2.6, 7.2.2b and 8.3.13 photographs were taken with the assistance of Mingmei Teo.

The photographs from Figure 6.4.15 were taken by Herbert Tze Cheung Foo from IPAS.

# List of Variables

Bi	$\frac{h\mathcal{L}}{k}$	Biot number
Ca	$\frac{\mu_0\mathcal{U}}{\gamma}$	Capillary number
De	$\frac{\mathcal{T}_c}{\mathcal{T}}$	Deborah number
Fr	$\frac{\mathcal{U}}{\sqrt{g\mathcal{L}}}$	Froude number
Pe	$\frac{\alpha}{\mathcal{L}\mathcal{U}}$	Péclet number
Re	$\frac{\rho\mathcal{U}\mathcal{L}}{\mu_0}$	Reynolds number
$g^*$	$\frac{\rho g\mathcal{L}^2}{\mu_0\mathcal{U}}$	Dimensionless gravity
$\gamma^*$	$\frac{1}{\epsilon\text{Ca}}$	Dimensionless surface tension

$\mathcal{A}$	Airy stress function	$r$	radial co-ordinate
$c$	axial tension	$R$	radius
$c_p$	specific heat	$s$	arc length
$C_n$	boundary $n$	$S$	cross-sectional area
$d$	hole spacing/diameter	$\mathcal{S}$	area scale
$e$	rate of strain	$t$	time
$E$	strain	$t_a$	cooling time
$f$	Goursat function	$t_c$	critical time
$F$	composed Goursat function	$t_e$	effective cooling time
$g$	gravitational acceleration/ Goursat function	$t_f$	final time
		$T$	temperature
$G$	composed Goursat function	$T_a$	atmospheric temperature
$h$	heat transfer coefficient	$\mathcal{T}$	temperature scale
$H$	integrating factor	$u$	$x$ velocity
$i$	imaginary unit	$\mathbf{u}$	velocity vector
$\mathbf{i}$	$x$ unit vector	$\mathcal{U}$	velocity scale
$\mathbf{j}$	$y$ unit vector	$v$	$y$ velocity
$k$	thermal conductivity	$V$	volume
$\bar{k}$	Eötvös constant	$V_m$	molar volume
$\mathbf{k}$	$z$ unit vector	$w$	$z$ velocity
$L$	cylinder length	$\mathcal{W}$	bianalytic function
$\mathcal{L}$	axial length scale	$x$	Cartesian co-ordinate
$m$	viscosity harmonic mean	$\mathbf{x}$	Cartesian co-ordinate vector
$p$	pressure	$y$	Cartesian co-ordinate
$\mathcal{P}$	analytic function	$z$	Cartesian co-ordinate/ complex number
$Q$	flux		
$\mathcal{Q}$	flux scale		

$\alpha$	thermal diffusivity
$\beta$	coefficient of thermal expansion
$\gamma$	surface tension
$\Gamma$	boundary length
$\epsilon$	slenderness ratio
$\zeta$	complex variable
$\eta$	Lagrangian co-ordinate
$\theta$	angle
$\kappa$	curvature
$\Lambda$	hole spacing
$\mu$	viscosity
$\xi$	Lagrangian co-ordinate
$\rho$	density
$\sigma$	stress tensor
$\sigma_E$	tensile stress
$\tau$	reduced time
$\phi$	annular aspect ratio
$\chi$	square root of cross-sectional area
$\psi$	stream function
$\omega$	vorticity
$\Omega$	domain



# List of Figures

1.1.1	The four layers of a conventional optical fibre. . . . .	2
1.1.2	Sketch of a slice through a microstructured optical fibre. . .	3
1.1.3	Four MOF designs and typical experimental results. . . . .	4
1.2.4	A MOF preform. . . . .	5
1.2.5	Sketch of an extrusion tower. . . . .	7
1.2.6	Underside of a die with three pins used for MOF preform extrusion. . . . .	8
1.2.7	Sketch of a drawing tower used to pull a preform into a fibre.	9
2.2.1	Sketch of the surface tension force on the boundary of a fluid region. . . . .	26
2.2.2	Thermal diffusivity $\alpha$ plotted against temperature in degrees Celsius for F2 glass. . . . .	30
3.2.1	Sketch of a solid axisymmetric cylinder stretching under gravity. . . . .	35
3.3.2	Sketch of a cylinder with internal structure representative of the geometries considered throughout this thesis. . . . .	40
3.3.3	Typical multiply connected domain with two inner boundaries.	52

5.2.1	Sketch of a conformal map from a circle domain. . . . .	113
5.2.2	Geometry used to illustrate the accuracy of the spectral method. . . . .	120
5.2.3	Errors in the dynamic and kinematic boundary conditions for the first spectral method at reduced time $\tau = 0$ . . . . .	121
5.2.4	Inner and outer radii of an annular region of fluid with initial inner radius 0.5 and unit outer radius computed up to reduced time $\tau = 0.73$ by the first spectral method, along with the exact values. . . . .	124
5.2.5	Desired shape of the 3-hole preform. . . . .	126
5.2.6	Evolution of the 3-hole preform geometry at reduced times $\tau = 0.02, 0.04, 0.06$ and $0.08$ as computed by the first spectral method. . . . .	127
5.2.7	Shape of the domain computed by the first spectral method at $\tau = 0.06$ for $d = 0.3$ and $d = 0.4$ . . . . .	128
5.2.8	Geometry of the 3-hole preform from Table 5.2.1 at reduced time $\tau = -0.03$ found by running the first spectral method backwards in reduced time. . . . .	130
5.2.9	6- and 7-hole preform geometries. . . . .	132
5.2.10	Evolution of the 6-hole preform geometry at reduced times $\tau = 0.02, 0.04, 0.06$ and $0.08$ computed by the first spectral method. . . . .	134
5.2.11	Evolution of the 7-hole preform geometry at reduced times $\tau = 0.02, 0.04, 0.06,$ and $0.08$ computed by the first spectral method. . . . .	135

5.3.12	Example of the conformal maps used in the alternative spectral method. . . . .	137
5.3.13	Mean computation times of the algorithms for finding the zeros of a polynomial. . . . .	143
5.3.14	Inner and outer radii of an annular region of fluid with initial inner radius 0.5 and unit outer radius as computed by the alternative spectral method up to reduced time $\tau = 0.73$ , along with the exact values. . . . .	145
5.3.15	Solution for the 3-hole preform described in Table 5.2.1 at reduced time $\tau = 0.06$ as computed by both spectral methods.	146
5.3.16	3-hole geometry starting with an elliptical central hole with aspect ratio 2.0254 computed by the alternative spectral method up to reduced time $\tau = 0.06$ . . . . .	150
5.4.17	Initial condition for a two-dimensional Stokes flow problem solved by van de Vorst (1993). . . . .	151
5.4.18	Sketch of the singularity locations using the method of fundamental solutions for a triply connected region. . . . .	154
5.4.19	Error in the MFS dynamic boundary condition at reduced time $\tau = 0$ plotted against the number of stresslets around each boundary. . . . .	157
5.4.20	Evolution of the inner and outer radii of an annulus with initial inner radius 0.5 and unit outer radius. as computed by the method of fundamental solutions, along with the exact values. . . . .	159

5.4.21	Comparison between the solutions at $\tau = 0.25$ for the geometry shown in Figure 5.4.17 as found by van de Vorst (1993), the spectral method and the method of fundamental solutions.	160
5.5.22	Schematic showing parameters for an $n$ -ring preform. . . . .	163
5.5.23	Evolution of the 4-ring preform geometry with $\Lambda = 3$ mm, $d/\Lambda = 0.3$ and $R = 15$ mm at reduced times $\tau = 0.005, 0.01, 0.015$ and $0.02$ computed using the elliptical pore model. . .	165
5.5.24	Evolution of the 4-ring preform geometry at reduced time $\tau = 0.02$ computed using the elliptical pore model for $R = 15$ mm for $\Lambda/d = 9/25, 9/20, 3/5$ and $3/4$ . . . . .	166
5.5.25	7-ring preform with $\Lambda = 2$ mm, $d/\Lambda = 0.5$ and $R = 15$ mm. .	167
5.5.26	Evolution of the 7-ring preform geometry with $\Lambda = 2$ mm, $d/\Lambda = 0.5$ and $R = 15$ mm, scaled to have unit area, at reduced times $\tau = 0.005, 0.01, 0.015$ and $0.02$ computed by the elliptical pore model. . . . .	168
5.5.27	Evolution of 7-ring preform geometries for $R = 15$ mm at reduced time $\tau = 0.02$ computed by the elliptical pore model for $d/\Lambda = 2/3$ and $10/17$ . . . . .	169
6.2.1	Sketch of the Eulerian and Lagrangian axial co-ordinates for a stretching fluid cylinder. . . . .	179
6.3.2	Area of a solid axisymmetric rod with $S_0(\xi) = 1$ and $\gamma^* = 0.1$ shown at times $t = 0, 0.5, 1, 1.5, 2$ and $2.5$ . . . . .	191
6.3.3	Fixed point $\xi_f$ for a solid axisymmetric rod as a function of $\gamma^*$ for the case $c \equiv 0$ . . . . .	192
6.3.4	Epicycloid used as an initial cross section geometry. . . . .	194

6.3.5	Areas corresponding to the ZST–WST solution, and the full problem for each of the rod and epicycloid. . . . .	196
6.3.6	Cross section at $\xi = 0.5$ and $t = 2$ for the stretching circular cylinder. . . . .	197
6.3.7	Cross section at $\xi = 0.5$ for the stretching cylinder with initial cross sections in the shape of an epicycloid. . . . .	198
6.3.8	Comparison between the solutions to the transverse (scaled) problem for an epicycloid with $\gamma^* = 10^{-1}$ . . . . .	200
6.4.9	Schematic showing the set-up for the annular tube experiment.	202
6.4.10	Area plotted against Lagrangian position for a tube. . . . .	205
6.4.11	Aspect ratios of the annuli from the transverse problem at $t = 1$ for initial values $\phi_0 = 0.2, 0.3, \dots, 0.9$ . . . . .	206
6.4.12	Comparison of the dimensionless inner and outer radii from the transverse flow model for the stretching annular tube. . . . .	209
6.4.13	Comparison of the aspect ratio for the stretching annular tube problem. . . . .	210
6.4.14	Initial configuration for the three-channel cylinder. . . . .	211
6.4.15	Comparison between the experiments and model for the 3-hole cylinder. . . . .	213
7.2.1	Schematic of a typical extrusion die design. . . . .	220
7.2.2	Sketch of a die and extruded preform, and a photo of the end of an extruded preform. . . . .	222
7.2.3	Cross section through a circular die showing extrudate swell.	223
7.3.4	Illustration of the Eulerian and Lagrangian co-ordinates for an extruded fluid cylinder. . . . .	228

7.4.5	Areas corresponding to the ZST–WST solution and the full problem for an extruded rod and epicycloid. . . . .	236
7.5.6	Deformation errors plotted against the dimensionless surface tension for annuli with initial aspect ratios $\phi = 0.3, 0.5$ and $0.7$ . . . . .	239
7.6.7	Extruded 3-hole preform with cross sections at three values of $\eta$ . . . . .	245
7.6.8	Area and reduced time plotted against position for the extruded 3-hole preform. . . . .	246
7.6.9	Extruded 7-hole preform with cross sections at three values of $\eta$ . . . . .	247
7.6.10	Area and reduced time plotted against position $\eta$ for the extruded 7-hole preform. . . . .	248
7.6.11	Extruded 7-ring preform with cross sections at three values of $\eta$ . . . . .	250
7.6.12	Area and reduced time plotted against position $\eta$ for the extruded 7-ring preform. . . . .	251
7.6.13	Value of $M(\eta, t)$ for five values of $\eta$ between 0 and $t_f$ . . . . .	254
7.6.14	Area and reduced time for the cooling 3-hole preform at times $t = t_f, t_e$ and $t_a$ . . . . .	256
7.7.15	Points at which pinch-off occurs plotted against dimensionless surface tension for a rod and an epicycloid. . . . .	260
8.2.1	Conformal map from a circle domain to a pair of coalescing tubes. . . . .	267

8.2.2	Truncation error plotted against the number of non-zero terms for a conformal map describing two coalescing tubes with $r = 0.2$ . . . . .	272
8.2.3	Inner boundary error plotted against the radius for a conformal map describing two coalescing tubes with 100 non-zero terms. . . . .	273
8.2.4	Comparison of the exact geometry and the computed map for two tubes with inner radii 0.2 and 0.8. . . . .	274
8.2.5	Coalescence of two stretching tubes each having unit outer radius and inner radius 0.2 with cross sections at three values of $\xi$ . . . . .	276
8.2.6	Area and reduced time plotted against Lagrangian position $\xi$ for the coalescence of two tubes with unit outer radius and inner radius 0.2. . . . .	277
8.2.7	Illustration of a conformal map from a circle domain to three coalescing tubes. . . . .	279
8.2.8	Truncation error plotted against the number of non-zero terms in a conformal map describing three coalescing tubes with inner radii 0.2 and $a = 1.4$ . . . . .	283
8.2.9	Inner boundary error plotted against the radius for a conformal map describing three coalescing tubes with 35 non-zero terms. . . . .	284
8.2.10	Comparison of the exact geometry and the computed map for three tubes with 35 non-zero terms and $a = 1.4$ for inner radii 0.2 and 0.8. . . . .	285

8.2.11	Areas of the medial hole and the lateral holes from the transverse problem corresponding to three coalescing tubes with inner radius 0.2, unit outer radius and $a = 1.4$ . . . . .	286
8.2.12	Areas of the medial and lateral holes along the length of three coalescing tubes. . . . .	288
8.3.13	Section from an extruded 3-hole preform that was at the die exit when the material solidified. . . . .	290
8.3.14	Illustration of a conformal map from a circle domain to the deformed 3-hole preform domain. . . . .	292
8.3.15	Errors for the deformed 3-hole preform maps. . . . .	296
8.3.16	Comparison between the exact geometry and the computed map for the deformed 3-hole preform. . . . .	297
8.3.17	Geometry of the deformed 3-hole preform with cross sections shown at three values of $\eta$ . . . . .	301
8.3.18	Area and reduced time for the deformed 3-hole preform. . .	302
8.3.19	Comparison between the geometry at the end of the 3-hole preform and the deformed 3-hole preform. . . . .	303
8.4.20	Welding chamber axial flow for the 3-hole die. . . . .	307
8.4.21	Welding chamber axial flow for the 7-hole die. . . . .	308
8.4.22	Welding chamber axial flow for the 7-ring die. . . . .	309
8.4.23	Axial velocity for the 3-hole, 7-hole and 7-ring dies along the non-negative portions of the $x$ - and $y$ -axes. . . . .	311
C.1	Schematic of the drop after stretching under gravity. . . . .	332
C.2	Initial shape of the cylinder used in the stretching tube experiment. . . . .	332

# List of Tables

2.2.1 Glass reference viscosities. . . . .	20
2.2.2 Temperatures in °C corresponding to reference viscosities for some common optical glasses. . . . .	20
2.2.3 VFTH equation coefficients for F2 glass. . . . .	21
2.2.4 Typical densities and coefficients of thermal expansion for some common optical glasses. . . . .	25
2.2.5 Surface tension coefficients for some common optical glasses. . .	28
3.3.1 Important physical parameters and scales used in the models for the gravitational stretching and extrusion of a fluid cylinder. . .	43
5.2.1 Dimensions of the 3-hole preform. . . . .	125
5.2.2 Dimensions of the 6- and 7-hole preforms. . . . .	132
6.2.1 Typical parameters values for the gravitational stretching and extrusion of a fluid cylinder. . . . .	177
7.3.1 Typical parameter values for extrusion. . . . .	224
7.6.2 Parameter values used for the extrusion examples. . . . .	242
7.6.3 Area scales, axial length scales and dimensionless parameters used for the extrusion examples. . . . .	243

8.2.1 Area scale, axial length scale and dimensionless parameters for two coalescing tubes. . . . .	275
8.2.2 Area scale, axial length scale and dimensionless parameters for three coalescing tubes. . . . .	287
8.3.3 Parameter values for the deformed 3-hole preform map. . . . .	294
8.3.4 Area scale, axial length scale and dimensionless parameters for the deformed-preform extrusion example. . . . .	299
C.1 Physical parameters for the stretching tube experiment. . . . .	330
C.2 Data recorded from the stretching tube experiment. . . . .	331
C.3 Data recorded from the three-channel stretching experiment. . . . .	334

# Chapter 1

## Introduction

### 1.1 Microstructured Optical Fibres

An optical fibre is a thin thread of material through which light may be guided, allowing the transmission of light from one end of the fibre to the other. Conventional optical fibres are comprised of two materials: an inner material through which light travels, called the core, and an outer material called the cladding. The core and cladding are contained within two protective layers called the buffer and jacket (see Figure 1.1.1) that do not influence the optical properties. The core is constructed from a transparent material, typically silica glass or a polymer, and is only a few microns in diameter. In order to confine light within the fibre, the outer material is chosen to have a lower refractive index than the material in the core. This difference in refractive index between the two materials creates a waveguide that transmits light through the core with only small losses in energy (DeCusatis and DeCusatis, 2006; Thevenaz, 2011). In order to create such a fibre it is necessary to find materials for the core and cladding that have suitably different refractive indices but similar

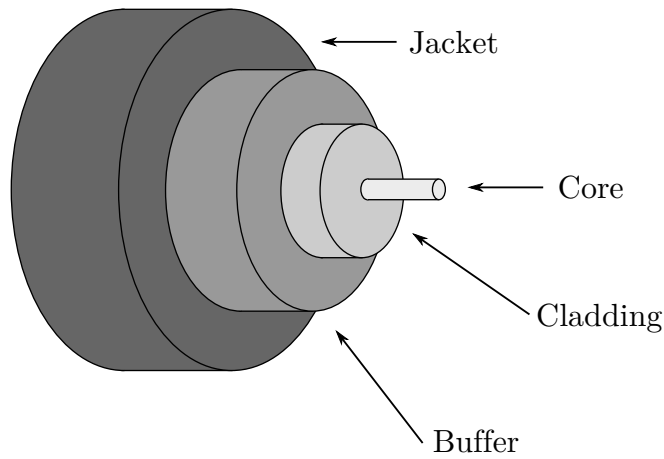


Figure 1.1.1: A schematic showing the four layers of a conventional optical fibre: the core, cladding, buffer and jacket.

enough material properties to be able to form a satisfactory fibre. Furthermore, this design necessitates the use of a homogenous core. These restrictions limit the optical properties of conventional optical fibre technology.

A *microstructured optical fibre* (or MOF, sometimes referred to as a holey fibre or photonic crystal fibre) consists of a glass or polymer thread containing an arrangement of cylindrical cavities that run along the length of the fibre, as illustrated by the example in Figure 1.1.2. The air channels reduce the average refractive index of the material in the outer region so that light travelling through the core is contained by total internal reflection in a manner similar to conventional optical fibres. MOFs, however, have the advantage that the air channels may be arranged in, effectively, an unlimited number of patterns, demonstrated by the variety of configurations shown in Figure 1.1.3. This flexibility allows optical fibres to be created with adaptable (and previously unrealisable) optical properties. For example, an optical fibre that carries only a single ray of light is said to be a single-mode fibre. It is possible to construct

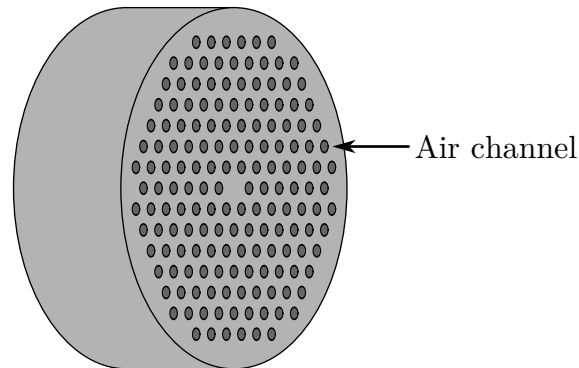


Figure 1.1.2: A sketch of a slice through a microstructured optical fibre. The air channels run along the length of the fibre modifying the refractive index.

MOFs that are single-mode at all wavelengths, which is not possible using conventional methods (Monro and Ebendorff-Heidepriem, 2006). MOFs also allow a high degree of control over other optical properties such as nonlinearity, dispersion and polarisation (Monro and Ebendorff-Heidepriem, 2006; Ebendorff-Heidepriem and Monro, 2009).

Due to this flexibility, MOFs have applications in a wide range of areas, including surgical lasers (Urich, Maier, Yu, Knight, Hand and Shephard, 2013); chemical and biological sensing (Warren-Smith, Ebendorff-Heidepriem, Foo, Moore, Davis and Monro, 2009; Monro, Warren-Smith, Schartner, François, Heng, Ebendorff-Heidepriem and V, 2010); electro-optical devices (Zhang, Manning, Ebendorff-Heidepriem and Monro, 2013); and high-speed data transmission (van Eijkelenborg, Large, Argyros, Zagari, Manos, Issa, Bassett, Fleming, McPhedran, de Sterke and Nicorovici, 2001). While in theory it is possible to construct MOFs with almost any specified geometry, this technology is limited by the practicalities of the fabrication process.

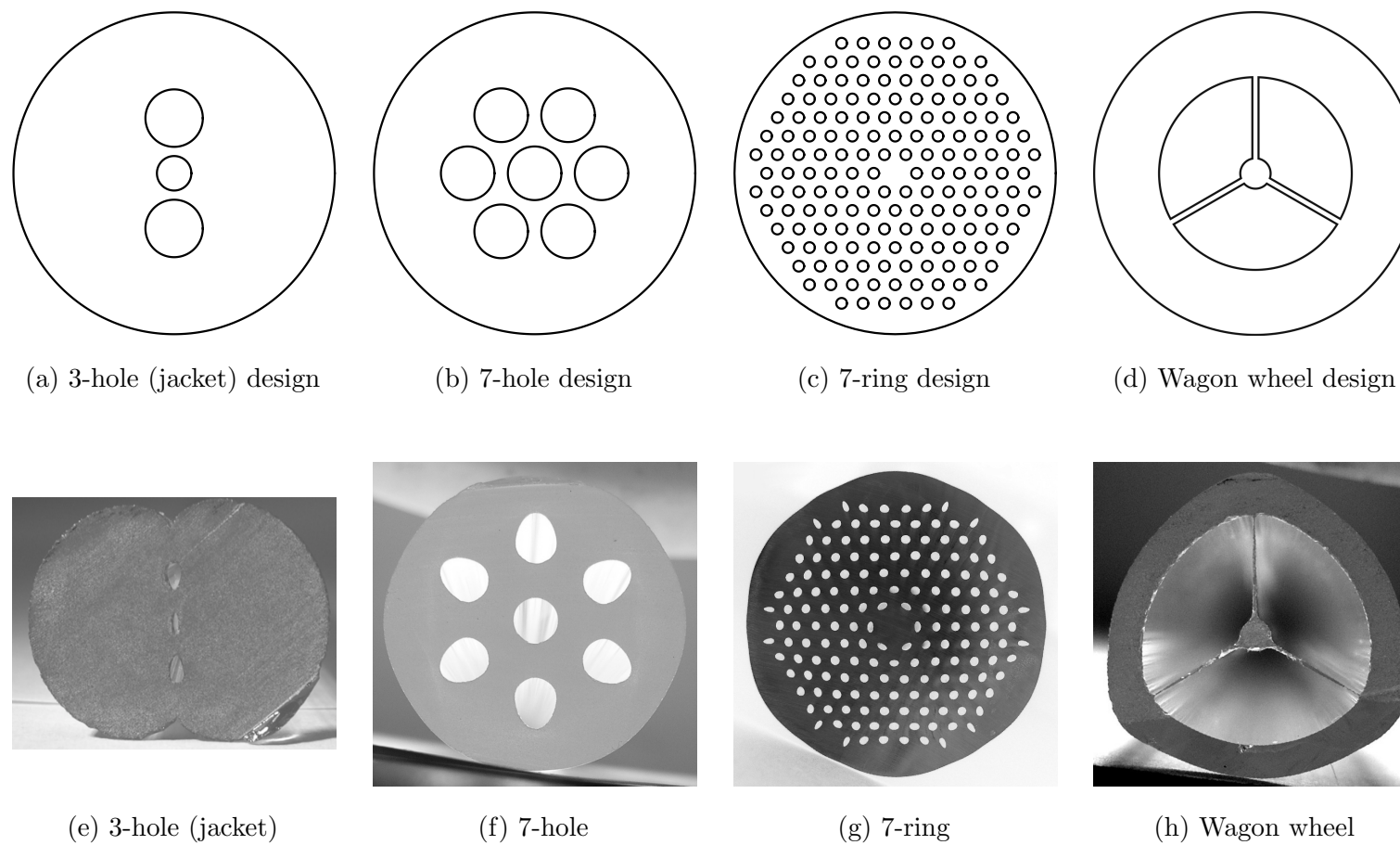


Figure 1.1.3: Four MOF preform designs (top row) and typical experimental results (bottom row). Experimental images from (e) Manning (2011), (f) Ebendorff-Heidepriem (2011) (g) Ebendorff-Heidepriem and Monro (2007) and (h) Ebendorff-Heidepriem *et al.* (2008).



Figure 1.2.4: A MOF preform.

## 1.2 Microstructured Optical Fibre Fabrication

MOFs are typically constructed in two stages: (1) the fabrication of a *preform* and (2) the pulling of the preform into a long fibre. Both stages present a number of significant challenges.

A preform, such as shown in Figure 1.2.4, is a macroscopic version of the final fibre typically around 30 cm in length with a radius around 6 mm and air channels with millimetre-scale radii. There are various methods available to construct the preform. Early preforms were fabricated by *drilling* (Knight, Birks, Russell and Atkin, 1996), which involves drilling the required pattern of air channels into a solid cylinder of material. This method is able to produce a precise design but requires a significant amount of time for designs with large numbers of air channels. While suitable for polymers (Barton, van Eijkelenborg, Henry, Large and Zagari, 2004), drilling glass preforms produces rough surfaces that require further polishing and that can limit the performance of the resulting fibre. Drilling can also lead to cracking of the material, while the drill-bit length restricts the length of preform that can be created. Drilling is further limited to geometries with circular holes (Ebendorff-Heidepriem and Monroe, 2007).

Preforms have also been constructed by *casting*. In this method molten

material is forced into a mould containing a number of blocking rods in the required pattern. Once the material cools the rods are removed by dissolving them in acid (Guiyao, Zhiyun, Shuguang and Lantian, 2006), or by lubricating them so they may be pulled out directly (Zhang, Li, Wang, Ren, Zhao, Miao, C. J. Large and Van Eijkelenborg, 2006). Again, this has been limited to air channels with circular cross sections.

Another method for manufacturing preforms is *capillary stacking*, in which a collection of capillary tubes is arranged to give the required geometry and then fused together using heat (van Eijkelenborg *et al.*, 2001; Knight, 2003; Russell, 2003). While this technique has been used frequently (Monro and Ebendorff-Heidepriem, 2006), it can be labour intensive, especially for complicated designs, and is not suited to automation. The fluid flow arising during the fusing process can also lead to unwanted deformations.

The *extrusion* method of preform fabrication allows considerable design flexibility. In this method a solid cylinder of glass or polymer (called a *billet*) is placed in an extrusion tower, as shown in Figure 1.2.5, and heated so that the material becomes molten. Next, a ram presses down on the billet forcing the material through a die, an example of which is shown in Figure 1.2.6. The die contains a number of blocking elements around which the material flows, giving rise to air channels within the preform (Ebendorff-Heidepriem and Monro, 2007). A preform formed using this technique is sometimes referred to as an *extrudate*. The extrusion method is highly flexible and is capable of producing a wider range of geometries than the methods discussed above. In particular, extrusion can be used to produce air channels with non-circular cross sections and it is no more laborious to extrude a preform with many air channels than it is a preform with one air channel. Extrusion is also suited to automation;

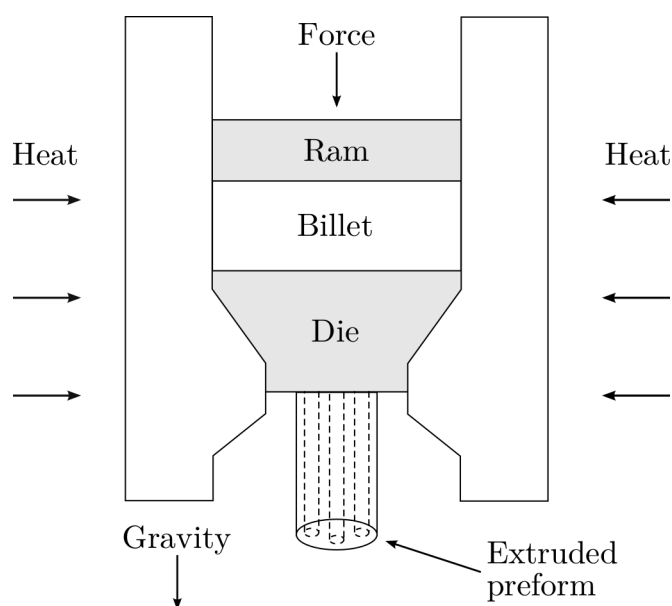


Figure 1.2.5: A sketch of an extrusion tower adapted from the diagram given by Ebendorff-Heidepriem and Monro (2007).

however, like capillary stacking, extrusion is complicated by the fluid flow that arises during the process that can lead to unwanted distortions in the preform.

Once the preform is manufactured, the second stage in the fibre fabrication process is the drawing or ‘spinning’ of the preform to produce a fibre. In this step, the preform is fixed at one end to a clamp and placed inside a drawing tower, illustrated in Figure 1.2.7. The preform is first heated inside a susceptor until the free end stretches and forms a drop, which is fixed to a rotating spool. The preform is fed into the heated region slower than it is drawn by the spool, which extends the preform to a kilometre or more in length, reducing the diameter to a few millimetres and the air channels to micron scales. This process differs from the extrusion stage as the material is stretched rather than forced through a die by a ram. While some fibres are drawn directly from a

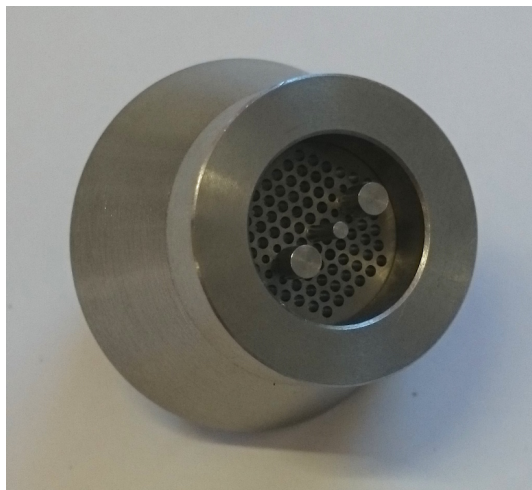


Figure 1.2.6: The underside of a die with three pins used for MOF preform extrusion.

preform this may not be possible in cases where the final spacing between the interior boundaries is of the order of microns. Instead, the preform is first stretched into a *cane* of diameter 1–2 mm, which is then inserted into the central channel of a larger object known as a *jacket* (Monro and Ebendorff-Heidepriem, 2006). The jacket is typically a tube or other simple design such as the design shown in Figure 1.1.3a and may be made of a different material to the cane. The combined cane and jacket are then drawn into a fibre. The process of forming a cane is referred to as *canning* and is similar to fibre drawing, while jackets are typically fabricated using the same techniques as used for preforms so, for the purposes of this thesis, will be considered a type of preform.

In order to achieve the desired optical properties MOFs must be constructed with a precise configuration of air channels. Even small defects within the air channels can reduce the effectiveness of a fibre or render it useless. While it is possible to specify an initial pattern of air channels, the fluid flows that

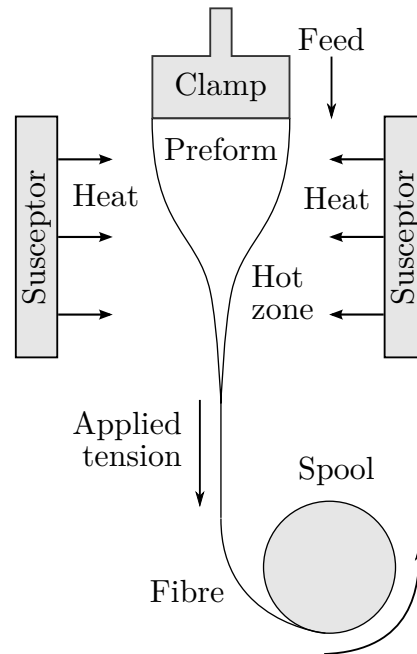


Figure 1.2.7: A sketch of a drawing tower used to pull a preform into a fibre.

arise during the fabrication of a preform, caning and drawing can give rise to unwanted distortions in the preform, such as changes in the size, shape or location of air channels, or the closure of air channels altogether. Such defects are evident in the experimental results shown in Figure 1.1.3. Even small defects in the air channels can reduce the effectiveness of a fibre or render it useless. Because of this MOF design is accompanied by a costly and time-consuming trial-and-error experimental process. Additionally, the extruded preform can bend in the axial direction as it exits the die, which may renders the preform useless (Belwalkar, Xiao, Misiolek and Toulouse, 2010). An analysis of this problem has been given by Stokes (2010).

There are several physical process that may influence the fluid flow and hence the observed distortions. Surface tension acts at air–glass interfaces to smooth boundary segments of high curvature. This is not necessarily desirable

and can cause air channels to shrink and close, which in turn distorts other channels. An extensional component of the flow arises due to the pulling action of the drawing tower and, particularly in preform extrusion, the effect of gravity, which reduces the cross-sectional area and hence increases the effect of surface tension. Even a minor variation in temperature arising during extrusion or drawing can lead to a substantial change in the viscosity of the materials used, particularly for glasses, dramatically altering the fluid flow. Extrudate swell (often referred to as die swell), which is the swelling of a fluid as it exits a die, may deform the geometry during extrusion. Internal–external pressure differences are also sometimes induced during MOF fabrication to alter the size of the air channels. In addition, there may be other as-yet-unknown phenomena that have a significant impact on the final geometry. Little is known of the relative influence these mechanisms have on the fluid flow.

### 1.3 Previous Work

There exists a significant body of work focusing on the drawing of fluid fibres. Much of this theory stems from the work of Trouton (1906), who developed a model for the steady stretching of a viscous fibre under gravity. Matovich and Pearson (1969) later extended this model to include surface-tension effects, while Schultz and Davis (1982) provided a systematic derivation of this model, making use of a small aspect ratio, and computed higher-order corrections that justified the use of a one-dimensional model. Yarin, Gospodinov and Roussinov (1994) found numerical solutions for the drawing of thin-walled cylinders with surface tension and gravity, while Fitt, Furusawa, Monro, Please and Richardson (2002) investigated the steady-state drawing of capillary tubes

---

through several limiting cases. A review of comparisons between experimental data and slenderness models for fibre drawing has been given by Denn (1980), which showed that one-dimensional models provide a good approximation. Xue, Tanner, Barton, Lwin, Large and Poladian (2005*a,b*) and Xue, Large, Barton, Tanner, Poladian and Lwin (2006) have used finite element simulations to study several fibre drawing problems, both steady state and time-dependent. Yarin (1995) has studied the formation of preforms using layers of materials driven by surface tension without gravity, making use of Fourier expansions to solve the resulting equations. This work assumed that the boundaries of each layer can be represented by small perturbations to circles and made use of a transformed time to link the transverse flow to a uniform axial stretching. It is noted that the equations may also be applied to single-layer preforms. A similar approach to those described above has been used to construct an area-averaged extrusion model (Lin and Jou, 1995). Eggers and Dupont (1994) have studied drop formation in an axisymmetric cylinder using a one-dimensional model derived by expanding variables in series using the radial co-ordinate, which is assumed small.

Each of the studies discussed above employed an Eulerian description of the fluid flow; however, many studies of extensional flow, including the present work, make use of a Lagrangian co-ordinate system (Wilson, 1988; Kaye, 1991). Lagrangian descriptions have been used to study the gravitational stretching of axisymmetric slender drops neglecting surface tension and inertia (Wilson, 1988; Stokes, 2000), with inertia (Stokes and Tuck, 2004) and with surface tension (Wilson, 1988; Stokes, Bradshaw-Hajek and Tuck, 2011). Similar equations also arise in the study of thin sheets of fluid (Wilmott, 1989; Stokes, 1999). A slenderness model with a Lagrangian co-ordinate has been used to study a

fibre stretched at both ends (Dewynne, Ockendon and Wilmott, 1989, 1992), while a detailed derivation of the leading-order model for drawing, including the effects of both inertia and gravity, has been given by Dewynne, Howell and Willmot (1994). This derivation included an appendix on the effect of surface tension but assumed that this did not enter into the leading-order analysis.

Cummings and Howell (1999) made the critical observation that, by transforming to a reduced time variable  $\tau$  and making use of a Lagrangian co-ordinate system, these methods could be used to model solid fibres with an arbitrary but simply connected cross section. The surface tension coefficient was assumed to be suitably large so that surface tension appeared in the leading-order analysis. Their work showed that the *geometry* (that is, the *shape*) of each cross section evolves like a two-dimensional Stokes flow with unit surface tension, while the *area* of each section evolves according to a one-dimensional equation as before, with an additional term that depends upon surface tension and the boundary length from the two-dimensional problem. This work did not give a complete derivation of this coupling process. A similar method has been used to model the drawing of a thin-walled tube (a viscida) by Griffiths and Howell (2007, 2008, 2009). Chakravarthy and Chiu (2009) applied the slenderness model of Cummings and Howell (1999) to the drawing of fibres with multiply connected cross-sectional geometries, and investigated the relative effects of surface tension, axial inertia and gravity. While they showed that the cross section evolves like a two-dimensional Stokes flow, they did not make use of the reduced time  $\tau$  nor a Lagrangian co-ordinate. A detailed description of the coupling between the axial and transverse flows was given by Stokes, Buchak, Crowdy and Ebendorff-Heidepriem (2014), who investigated the drawing of a preform into a fibre neglecting gravitational effects. An important feature

of this work was the use of the reduced-time variable of the two-dimensional transverse problem for the one-dimensional axial flow problem, which led to a solution for fibres with arbitrary cross-sectional geometry in terms of the function

$$H(\tau) = \exp\left(-\frac{1}{12} \int_0^\tau \tilde{\Gamma}(\tau') d\tau'\right),$$

where  $\tilde{\Gamma}$  is the total scaled boundary length from the transverse model. A similar function will feature in the present work also.

Finite element simulations have been used to study the effect of slip boundary conditions within the die during preform extrusion in the absence of gravity, surface tension and temperature variations (Trabelssi, Ebendorff-Heidepriem, Richardson, Monro and Joseph, 2014, 2015). In these studies the level of slip has been determined by fitting the model to experimental data. Ebendorff-Heidepriem and Monro (2012) have developed a simplified model of the fluid flow inside the die during extrusion that relates the ram speed, temperature and ram pressure. This model depends upon a parameter known as the die constant that may be determined theoretically or by experiment. Relative to fibre drawing, however, preform extrusion has received significantly less theoretical study.

## 1.4 Thesis Content

This thesis is motivated by the need for detailed theoretical insight into the extrusion of MOF preforms. Specifically, the aim of this work is to provide an understanding of the link between the mechanics of preform extrusion and the observed deformations. To this end, we will develop a model of the stretching under gravity of a viscous fluid cylinder with internal structure and surface

tension. This model may be applied to cross-sectional geometries of arbitrary connectivity, and will make use of reduced time  $\tau$  to decouple the transverse flow. This model differs significantly from existing models of fibre drawing due to the inclusion of gravity, which greatly complicates the solution process, and may also be applied to fibre drawing problems in which gravity is important. The model developed will be used to analyse stretching fluid cylinders, along with the extrusion and stacking methods of MOF preform fabrication. As part of this study we will determine the relative importance of surface tension and gravity. This thesis is structured as follows.

As the modelling presented here typically concerns problems involving molten glass, Chapter 2 contains a discussion of the properties of glass and some basic assumptions regarding this material on which the work of subsequent chapters depends.

Chapter 3 discusses the model for a thin, fluid cylinder stretching under gravity with surface tension acting on the boundaries. This model makes use of a slenderness approximation that is discussed in detail. It will be shown that the governing equations divide into a two-dimensional transverse system, comprising the Stokes equations with unit surface tension, and a one-dimensional axial equation that admits an exact solution dependent upon the solution to the transverse problem. That this solution technique applies to a problem in which both surface tension and gravity are important is a novel result.

Owing to the decoupling of the transverse flow, in Chapter 4 we review the use of complex variables to represent two-dimensional Stokes flows. This theory shows that the transverse problem, with two spatial dimensions, can be reduced to the problem of finding complex-analytic functions that satisfy the stress boundary condition, which has only one spatial dimension. Through this

---

review we also establish conventions for the complex-variable representation that will be used throughout this thesis.

In Chapter 5 we discuss numerical methods for solving the transverse flow problem. After reviewing the relevant literature we make use of the complex-variable theory from Chapter 4 to develop three suitable numerical methods. Two of these are spectral methods that describe the boundaries using conformal maps; the first developed in parallel with other authors and the second extending previous techniques from the literature. The third method, based upon a novel formulation of the method of fundamental solutions, uses a set of discrete points and is used primarily to validate the spectral methods. We also provide a brief review of elliptical pore models. The accuracy and efficiency of the methods are discussed, with a focus on selecting the appropriate method for a given geometry.

Chapter 6 uses the slenderness model and transverse solutions to analyse the evolution of a slender cylinder of very viscous fluid with an arbitrary cross section. Several representative geometries are considered and solutions are compared with the weak- and zero-surface-tension limits. The importance of surface tension is analysed using the model solutions and comparisons with experimental data.

Building upon the stretching model, in Chapter 7 we construct a model of the extrusion of a fluid cylinder with internal structure that is stretching under gravity with surface tension acting on the boundaries. We discuss how the deformations can be controlled by adjusting the system parameters with a particular focus on MOF preform extrusion. Some solutions for typical MOF preform geometries are presented and compared with experimental observations.

Chapter 8 describes a new technique for deriving conformal maps that

describe two-dimensional geometries with non-circular boundaries, which are used as initial conditions in one of the spectral numerical methods. These are used to model the fabrication of preforms using coalescing tubes. Maps are also developed to test a hypothesis that explains some of the large deformations seen during MOF extrusion. An alternative hypothesis is tested by developing a basic model of the fluid flow within the die.

Finally, Chapter 9 discusses the conclusions drawn from this study. Some areas for future research are also identified.

Parts of this research have been submitted for publication (Tronmolone, Stokes, Foo and Ebendorff-Heidepriem, 2016).

# Chapter 2

## Glass and Its Properties

### 2.1 Introduction

This thesis is primarily concerned with structures composed of glass. As such, in this chapter we describe how glass is defined and discuss material properties that are relevant to the present study. This discussion will include justification for the glass modelling assumptions throughout this thesis.

A glass is an example of a broader category of materials known as *amorphous solids*, meaning ‘solids without form’. These materials are so named as they do not possess the ordered atomic structure found in crystalline solids such as ice and metals. As such, these materials are also referred to as *non-crystalline solids*. Examples of amorphous solids include gels and some polymers.

Glass is a particular type of amorphous solid characterised by undergoing a *glass transition* (Shelby, 2005), which occurs when a liquid is cooled quickly relative to the time over which crystallisation takes place. During this process, known as *supercooling* or *undercooling*, the material experiences a corresponding rapid increase in viscosity and hence cannot develop a crystalline structure so

instead retains the structure of a liquid. Eventually the viscosity becomes so large that the material is effectively fixed and forms an amorphous solid. The process of cooling a material to form a glass is known as *vitrification*, while glasses are sometimes referred to as *undercooled liquids* (Morey, 1938), since they have the same structure as the liquid phase.

In practice the transition from a liquid to a glass state occurs over a range of temperatures; however, it is often described as occurring at a single point called the *glass transition temperature*, denoted  $T_g$ . In cases where the material also possesses a crystalline solid state with melting temperature  $T_m$  these two temperatures satisfy  $T_g < T_m$ . The absence of a standard phase transition in the fabrication of a glass leads to difficulties in describing the state of the material. To avoid confusion, in this thesis we will refer to the solid-like state at temperatures below  $T_g$  as ‘glass’ and the state above  $T_g$  as molten glass.

A characteristic feature of preform fabrication by extrusion or capillary stacking (and also of fibre drawing) is the change in temperature of the materials used. The material must be heated from room temperature until it becomes soft enough to work, after which it then cools back to room temperature. For preform extrusion the glass is typically heated to around 525–650 °C (Ebendorff-Heidepriem and Monro, 2007) in order to achieve the desired viscosity, although, as discussed below, this can vary greatly depending upon the glass composition.

Almost every material property of importance exhibits some dependence upon temperature, making it vital to determine when such variations are important. In the following section we briefly discuss the physical properties relevant to preform fabrication with a particular focus on temperature dependence.

## 2.2 Glass Properties

### 2.2.1 Viscosity

The *viscosity*, denoted  $\mu$ , arises due to internal friction between fluid particles and provides a measure of a fluid's resistance to deformation: the higher the viscosity, the greater the resistance. In SI units viscosity is measured in  $\text{N} \cdot \text{s} \cdot \text{m}^{-2}$ , which is usually written as Pascal seconds,  $\text{Pa} \cdot \text{s}$ . The cgs system measures viscosity in Poise P, with the relationship that  $10 \text{ P} = 1 \text{ Pa} \cdot \text{s}$ . Many texts on glass report viscosities in Poise.

Although not precisely defined, the term *very viscous fluid* is often used to refer to fluids with large viscosities. One such example of a very viscous fluid is golden syrup. This is evident in the difficulty to stir or pour golden syrup, which, at room temperature, has viscosity  $10^2 \text{ Pa} \cdot \text{s}$ , compared with water at the same temperature with viscosity  $10^{-4} \text{ Pa} \cdot \text{s}$ . Several reference viscosities for glass are listed in Table 2.2.1. During MOF preform extrusion the glass has a viscosity in the range  $10^{6.5}$ – $10^{8.5} \text{ Pa} \cdot \text{s}$ , which is around the softening point, so may be considered a very viscous fluid. (This is also true of polymers.) During fibre drawing the viscosity is in the range  $10^5$ – $10^6 \text{ Pa} \cdot \text{s}$ . Temperatures corresponding to reference viscosities as given by Holloway (1973) for some common optical glasses are given in Table 2.2.2.

The viscosity of molten glass is strongly dependent on the temperature  $T$ . A change in temperature as small as  $20^\circ\text{C}$  can alter the viscosity by several orders of magnitude, radically affecting the behaviour of the molten glass. To complicate matters further, the relationship between the two quantities is not known exactly; rather, it is typically approximated by empirical relationships.

One frequently-used approximation (Shelby, 2005) is the Vogel–Fulcher–

Table 2.2.1: Glass reference viscosities as given by Holloway (1973) and Shelby (2005).

Name	$\mu$ (Pa · s)	Description
Strain point	$10^{13.5}$	Stresses reduce within hours
Annealing point	$10^{12}$ – $10^{12.4}$	Stresses reduce within minutes
Glass transformation $T_g$	$\sim 10^{11.3}$	Transition from solid to liquid
Softening point	$10^{6.6}$	Deforms under own weight
Working point	$10^3$	Set by definition
Melting temperature	1–10	Production temperature

Table 2.2.2: Temperatures in °C corresponding to reference viscosities for some common optical glasses as given by Holloway (1973). No working point data is given for silica as it cannot be reduced below  $10^7$  Pa · s.

Reference	Silica	Soda–lime–silica	Borosilicate	Lead silicate
Strain	1000	470	520	390
Annealing	1100	510	565	430
Softening	1600	700	820	620
Working	–	1000	1220	970

Table 2.2.3: VFTH equation coefficients reported by Richardson (2012) for F2 glass over two temperature ranges.

Coefficient	Unit	Low temperatures	High Temperatures
$A$	log(Pa · s)	−14.498	2.314
$B$	°C	17 806.6	4065.2
$T_0$	°C	−251	137

Tammann–Hesse (VFTH) equation, sometimes referred to as the the Vogel–Fulcher–Tammann (VFT) equation or simply the Fulcher equation. In this thesis the abbreviation VFTH will be used. This approximation was developed independently by Vogel (1921), Fulcher (1925) and Tammann and Hesse (1926). This states that

$$\log_{10} \mu = -A + \frac{B}{T - T_0}, \quad (2.2.1)$$

where  $A$ ,  $B$  and  $T_0$  are constants that are determined by fitting (2.2.1) to observed values. For example, knowledge of three of the temperatures from Table 2.2.2 would determine the three coefficients needed. The VFTH equation uses the base 10 logarithm since the viscosity can vary by several orders of magnitude as the temperature changes. While a single VFTH equation can provide a good approximation to the viscosity over a large range of temperatures, for improved accuracy it is possible to subdivide the temperature range and fit a separate VFTH equation to each of these. VFTH equations have been used in other studies of molten glass, such as Xue *et al.* (2006) and Stokes *et al.* (2014). The fitting of VFTH equations has been discussed in detail by Mano and Pereira (2004). VFTH equation coefficients found by Richardson (2012) for lead flint (F2) glass for two temperature ranges are given in Table 2.2.3.

Another possible relationship is the *Arrhenius equation*

$$\log_{10} \mu = A + \frac{B}{T},$$

which includes only two parameters and has been used by Ebendorff-Heidepriem and Monro (2012) to study preform extrusion, and by Lee and Jaluria (1997) to study fibre drawing conditions. A further common approximation is an exponential law having the general form

$$\log \mu = A - B \left( \frac{T - T_0}{C} \right).$$

Typically one of these parameters is fixed while the remaining parameters are set using experimental data. Relationships of this form have been used with  $C = 1$  both over the whole temperature range (Huang, Miura and Wylie, 2008), defined piecewise (Huang, Miura, Ireland and Puil, 2003), and with  $B = 1$  (Huang, Wylie, Miura and Howell, 2007).

When required throughout this thesis, we use a VFTH relationship to relate temperature and viscosity using the coefficients from Table 2.2.3 corresponding to the required temperature range. This approximation is preferred as it provides accurate results over a large temperature range.

### 2.2.2 Material Constitutive Equation

Depending upon the time scale of interest, glass may behave as a solid or as a fluid. This behaviour is described by a constitutive equation relating the stress and strain within the material. Thus, as part of the modelling process we must consider the appropriate constitutive equation for the problems under consideration in this thesis.

A fluid in which the stress is directly proportional to the rate of strain is said to be *Newtonian*. The constant of proportionality in this relationship is

precisely the viscosity; that is, for shear stress  $\sigma$  and rate of strain  $e$ , both of which are tensors, we have

$$\sigma = \mu e. \quad (2.2.2)$$

Newtonian fluids immediately relax when a stress is applied, no matter how small the stress. Molten glass has been assumed Newtonian in much of the recent work on fibre drawing (Cummings and Howell, 1999; Xue *et al.*, 2005a; Griffiths and Howell, 2007; Voyce, Fitt and Monro, 2008; Stokes *et al.*, 2014).

A solid material that returns to its original shape after deformation is known as an *elastic material*. Elastic equations for which the stress and strain have a linear relationship are described by Hooke's Law,

$$\sigma = GE, \quad (2.2.3)$$

where  $G$  is the shear modulus and  $E$  is the strain tensor. For a glass we have  $G \approx 2 \times 10^{10}$  Pa.

Fluids that do not exhibit a linear relationship between stress and strain are broadly classified as *non-Newtonian*. One example is a material that exhibits characteristics of both a Newtonian fluid and an elastic solid, known as a *viscoelastic material*. For such materials the rate of strain depends upon both the stress and the rate the stress is applied. Materials exhibiting this behaviour may be modelled as a *Maxwellian* fluid, for which

$$\frac{1}{G}\sigma_t + \frac{\sigma}{\mu} = e, \quad (2.2.4)$$

where the left-hand side reflects the dependence upon both  $\sigma$  and its time derivative. For small values of  $\sigma_t$  this relationship is similar to that for a Newtonian fluid (2.2.2), while for large values of  $\sigma_t$  this relationship is like that for an elastic material (2.2.3). Glass has been modelled as a Maxwellian fluid by Gupta, Schultz, Arruda and Lu (1996) and Stokes (2000).

Under a suitable scaling, such as will be defined later in (3.3.7), the relationship (2.2.4) may be written as

$$\text{De} \hat{\sigma}_{\dot{t}} + \hat{\sigma} = \hat{e},$$

where De is the Deborah number, defined

$$\text{De} = \frac{t_r}{t_c},$$

$t_r = \mu/G$  is the stress relaxation time and  $t_c = \mathcal{L}/\mathcal{U}$  is a characteristic time of observation for velocity  $\mathcal{U}$  and length  $\mathcal{L}$ . Small values of De correspond to Newtonian behaviour, while larger values reflect the greater importance of elastic effects. For the problems under consideration in this thesis, the viscosity is at most  $10^8$ , so that  $t_r$  is  $O(10^{-2})$ , while we will later see that the characteristic time  $t_c$  is  $O(10^4)$ . These values suggest that De is  $O(10^{-6})$ . As this is small, throughout this thesis we will assume that molten glass is a Newtonian fluid and ignore elastic effects.

### 2.2.3 Density

The density, denoted  $\rho$ , typically decreases as temperature increases. The change in volume with temperature is described by the (volumetric) coefficient of thermal expansion  $\beta$ , which has units  $^{\circ}\text{C}^{-1}$ . The densities and coefficients of thermal expansion for some common optical glasses are given in Table 2.2.4.

Suppose that the temperature of a glass with initial density  $\rho_0$ , mass  $M$  and volume  $V$  increases by  $\Delta T$ , so that the density decreases to  $\rho_1$ . We thus have that

$$\rho_1 = \frac{M}{(1 + \beta\Delta T)V} = \frac{\rho_0}{1 + \beta\Delta T},$$

Table 2.2.4: Typical densities and coefficients of thermal expansion for some common optical glasses as given by [1] Wang *et al.* (1994), [2] Schott (2013) and [3] Munasinghe *et al.* (2013). No data for the coefficient of thermal expansion for lead–germanate glass could be found.

Glass	$\rho$ ( $10^3 \text{ kg} \cdot \text{m}^{-3}$ )	$\beta$ ( $10^{-6} \text{ }^\circ\text{C}^{-1}$ )	Source (see caption)
Silica	2.2	5	[1]
Lead flint (F2)	3.6	7.8	[2]
Lead–germanate	6.16	–	[3]
Tellurite	5.5	120–170	[1]

or

$$\frac{\rho_0}{\rho_1} = 1 + \beta\Delta T.$$

That is, the relative change in the density is  $\beta\Delta T$ , which is a dimensionless quantity. Since  $\beta$  is  $O(10^{-4})$  and the temperature change  $\Delta T$  for the problems considered in this thesis is at most  $O(10^2)$ , the relative (dimensionless) change in density  $\beta\Delta T$  is approximately  $O(10^{-2})$ . Thus, we shall assume that the density is constant.

### 2.2.4 Surface Tension

The role of *surface tension* in the deformation of geometry is of particular interest in this work. This fluid property quantifies the resistance of the surface to applied forces acting against its contractive tendency. All particles within the fluid experience an attractive force arising from the surrounding particles (de Gennes, Brochard-Wyart and Quéré, 2013), so that a particle that is not on the surface is attracted equally in all directions and hence experiences zero

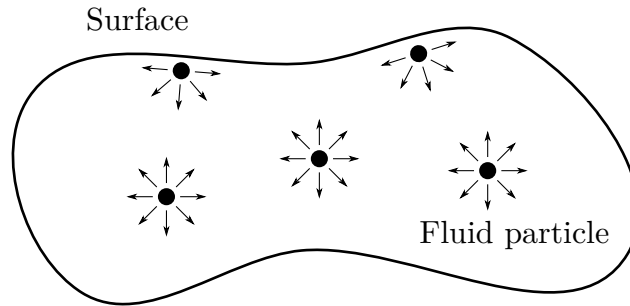


Figure 2.2.1: A sketch of the surface tension force on the boundary of a fluid region. Each particle in the fluid experiences an attractive force from the surrounding particles. A particle that is not on the surface is attracted equally in all directions, while on the surface there is a net force directed into the fluid region.

net force, as sketched in Figure 2.2.1. While a particle on the surface may experience some small cohesive force from the surrounding atmosphere the attractive forces from within the fluid are much greater and result in a net force directed into the fluid region. This tension causes the surface to resist external forces and return to its equilibrium state in which surface tension forces are balanced by internal pressure.

The result of surface tension is to cause a free surface to change shape so as to minimise the surface area, subject to competing forces. This is equivalent to minimising the curvature or minimising the total surface energy. For example, surface tension will cause a fluid region in two dimensions to become circular, while in three dimensions a drop will become spherical. In general, surface tension ‘smooths out’ the fluid boundary.

The normal force acting upon a boundary due to surface tension is proportional to the curvature of the boundary, which means that a larger curvature results in a stronger surface tension force. The constant of proportionality is

known as the surface tension coefficient and is typically denoted  $\gamma$ . In the SI system this is measured in units of  $\text{N} \cdot \text{m}^{-1}$  or, equivalently,  $\text{J} \cdot \text{m}^{-2}$ ; the former is preferred when considering the force on a surface and the latter when the surface energy is of primary concern. Just as for viscosity, it is also common for the surface tension coefficient to be measured in the cgs system using  $\text{dyn} \cdot \text{cm}^{-1}$  or, again equivalently,  $\text{erg} \cdot \text{cm}^{-2}$ , with the simple relationship that

$$1 \text{ dyn} \cdot \text{cm}^{-1} = 10^{-3} \text{ N} \cdot \text{m}^{-1}.$$

The surface tension coefficients of some glasses as measured by Boyd, Ebendorff-Heidepriem, Monro and Munch (2012) are given in Table 2.2.5. From this table we note that the value varies depending upon the composition of the glass.

The surface tension also varies with the temperature of the material. The surface tension decreases with increasing temperature and is zero at temperature  $T_c$ , known as the *critical temperature*. The precise relationship between surface tension and temperature is not known but may be approximated by empirical formulae. One such relationship is the Eötvös rule, which states that

$$\gamma V_m^{\frac{2}{3}} = k(T_c - T), \quad (2.2.5)$$

where  $k = 2.1 \times 10^{-7} \text{ J} \cdot \text{K}^{-1} \cdot \text{mol}^{-2/3}$  is the Eötvös constant,  $V_m$  is the volume occupied by one mole of mass and  $T_c$  is the critical temperature. Rearranging (2.2.5) shows that

$$\gamma = k V_m^{-\frac{2}{3}} (T_c - T),$$

which is just a linear equation relating  $\gamma$  and  $T$ . Experimental studies of lead silicate glasses (El-Hadp, Khalida, El-Kheshen and Moustaffa, 1995), borate glasses (Berkemeier, Voss, Árpád W. Imre and Mehrer, 2005) and phosphate glasses (Chanshetti, Shelke, Jadhav, Shankarwar, Chondhekar, Shankarwar, Sudarsan

Table 2.2.5: Surface tension coefficients for some common optical glasses as given by Boyd *et al.* (2012).

Glass	$\gamma$ (N · m <sup>-1</sup> )	Temperature (°C)
Silica	0.300	2400–2600
Lead flint (F2)	0.230 ± 0.004	1100
Lead–Germanate	0.240 ± 0.010	700
Bismuth	0.230 ± 0.007	1100
Tellurite	0.163 ± 0.009	700

and Jogad, 2011) have found molar volumes between  $2.5 \times 10^{-5} \text{ m}^3 \cdot \text{mol}^{-1}$  and  $6 \times 10^{-5} \text{ m}^3 \cdot \text{mol}^{-1}$ . Using these values of  $V_m$  and scaling by a typical surface tension from Table 2.2.5, the coefficient multiplying  $T$  is at most  $O(10^{-3})$ . As  $T$  is  $O(10^2)$ , this shows that the surface tension coefficient varies little with temperature. This agrees with the result of Lee and Jaluria (1997, Appendix B), who state that the surface tension of silica glass is constant below the softening point. The experimental results of Babcock (1940), Shartsis and Smock (1947), and Parikh (1958) also suggest that the surface tension varies little with temperature. We thus assume that the surface tension of glass is constant.

### 2.2.5 Heat Transfer

The heat flow within glass is influenced by three parameters: the density  $\rho$ , which has already been assumed constant; the specific heat  $c_p$ ; and the thermal conductivity  $k$ . These terms appear together (see (3.3.5c)) in the thermal

diffusivity

$$\alpha = \frac{k}{c_p \rho},$$

which has units  $\text{m}^2 \cdot \text{s}^{-1}$ . Strictly, both  $c_p$  and  $k$ , and hence also  $\alpha$ , vary with temperature. Through experimental analysis Lee and Jaluria (1997, Appendix B) found that the thermal conductivity  $k$  may be fit by a cubic polynomial in  $T$  for temperatures between 310.78 K and 1921.89 K, and lies in the range  $1.3855\text{--}1.9339 \text{ W} \cdot \text{m}^{-1} \cdot \text{K}^{-1}$ . The specific heat  $c_p$  varies like a quartic polynomial in  $T$  for temperatures between 310.78 K and 1921.89 K. Outside of the respective intervals the parameters are constant and equal to the value at the nearest endpoint. Figure 2.2.2 shows the thermal diffusivity  $\alpha$  plotted against temperature in degrees Celsius for F2 glass with  $\rho = 3600$  at temperatures between  $20^\circ\text{C}$  and  $800^\circ\text{C}$ . We note that the value of  $\alpha$  is in the range  $4.2767 \times 10^{-7}\text{--}5.6678 \times 10^{-7} \text{ m}^2 \cdot \text{s}^{-1}$  so varies by only  $1.3911 \times 10^{-7} \text{ m}^2 \cdot \text{s}^{-1}$ . Scaling by the minimum value of  $\alpha$  shows that the dimensionless maximum change is 0.32528. The standard deviation of  $\alpha$  over this interval is  $3.9109 \times 10^{-8} \text{ m}^2 \cdot \text{s}^{-1}$ , or  $9.1448 \times 10^{-2}$  when scaled by the minimum value of alpha. Since these dimensionless variations are small compared to unity we assume that the thermal diffusivity does not vary significantly with temperature. The same assumption has been made in previous work on the stretching of glass electrodes (Huang *et al.*, 2003) and the drawing of capillary tubes (Griffiths and Howell, 2008).

There are two important mechanisms by which heat may enter or leave the glass during heating (Modest, 2013). Under Newton's law of cooling, the heat exchange at an interface between air and glass due to convection is proportional to the difference in temperature between the two materials. The constant of proportionality is the heat transfer coefficient  $h$ , which is typically taken to be in the range  $150\text{--}300 \text{ W} \cdot \text{m}^{-2} \cdot \text{K}^{-1}$  (Paek and Runk, 1978; Lee and Jaluria,

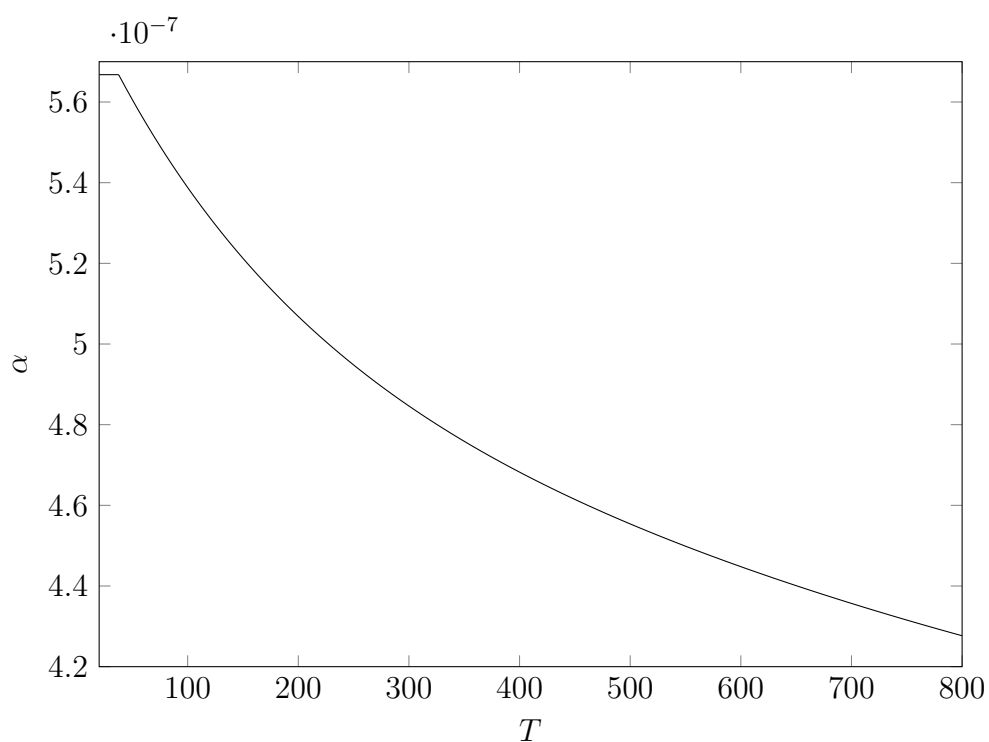


Figure 2.2.2: The thermal diffusivity  $\alpha$  plotted against temperature in degrees Celsius using the results of Lee and Jaluria (1997) for F2 glass with  $\rho = 3600$ . For temperatures between 20 °C and 800 °C the value of  $\alpha$  varies by  $1.3911 \times 10^{-7} \text{ m}^2 \cdot \text{s}^{-1}$  with standard deviation  $3.9109 \times 10^{-8} \text{ m}^2 \cdot \text{s}^{-1}$ .

1997; Huang *et al.*, 2008), and is assumed to be independent of temperature. Heat may also be transferred by radiation, in which the heat flux is typically taken to be proportional to the difference in the temperature of the glass and the atmosphere each raised to the fourth power. The constant of proportionality depends upon the Stefan–Boltzman constant  $5.670\,367 \times 10^{-8} \text{ W} \cdot \text{m}^{-2} \cdot \text{K}^{-4}$  and the (dimensionless) emissivity, which is typically taken to be  $O(10^{-1})$  (Wylie and Huang, 2007; Taroni, Breward, Cummings and Griffiths, 2013) and assumed to be independent of temperature.

## 2.3 Summary of Assumptions

In this chapter we have described the glass state. Several constitutive laws relating the stress and strain have been considered so as to select an appropriate relationship for the fluid flows considered in this thesis. As thermal variations are an essential element of MOF fabrication, we have considered how the important material parameters change with temperature. This analysis has produced five key assumptions:

- (1) molten glass is a Newtonian fluid;
- (2) the viscosity varies with temperature, which is best described by a VFTH equation;
- (3) the density is independent of temperature and hence constant;
- (4) the surface tension coefficient is independent of temperature and hence constant; and
- (5) the thermal diffusivity, heat transfer coefficient and emissivity are independent of temperature and hence constant.

These assumptions will be applied for the remainder of this thesis.

# Chapter 3

## Slenderness Model

### 3.1 Introduction

This thesis considers problems involving stretching fluid cylinders deforming due to gravity and surface tension. These problems may be broadly divided into two categories based upon the boundary condition applied at the top of the cylinder: (1) the stretching of a fluid cylinder fixed at one end; and (2) the extrusion of a fluid cylinder from a die. In the first, the velocity at the top of the cylinder is zero, while the second has a non-zero velocity boundary condition there. Both problems may be described by similar models that differ only in the axial Lagrangian co-ordinate best suited to each boundary condition. Due to this similarity, in this chapter we derive a general model applicable to both problems for the stretching under gravity of a cylindrical fluid region with internal structure, surface tension and inertia. This model will be used to study stretching fluid cylinders (case 1) in Chapter 6 and extrusion (case 2) in Chapter 7.

We first discuss models applicable to an axisymmetric solid cylinder, for

which a force balance may be written down directly. These are often referred to as Trouton models after the pioneering experimental and theoretical work of Trouton (1906). Motivated by these examples we then derive formally the central model that will be used throughout this thesis, making use of the assumptions developed in Chapter 2. Previous models of stretching cylinders have either applied only to domains with no internal holes (Cummings and Howell, 1999), have not completely decoupled the transverse flow (Chakravarthy and Chiu, 2009) or have neglected gravity due to other dominant applied forces (Griffiths and Howell, 2008; Stokes *et al.*, 2014; Chen, Stokes, Buchak, Crowdy and Ebendorff-Heidepriem, 2015). We here show that these models generalise to the stretching under gravity of a slender fluid region of arbitrary cross section in which, through the use of a Lagrangian co-ordinate system and reduced time, the transverse flow decouples from the axial flow and evolves in reduced time as a two-dimensional Stokes flow with unit surface tension. Because of the moving boundary at the free end of the cylinder the problem is unsteady and the area evolution equation depends upon the initial position of each cross section. While some elements of this derivation have been described previously by Cummings and Howell (1999) we here consider each step in detail so as to verify that the model applies to arbitrary cross-sectional geometries.

## 3.2 Trouton Models

To motivate the general model we first consider a model for the stretching under gravity of a solid axisymmetric fluid cylinder, which is based upon the work of Trouton (1906). For this reason, models of this type are referred to as Trouton models. The fluid flow is an example of an *extensional flow*.

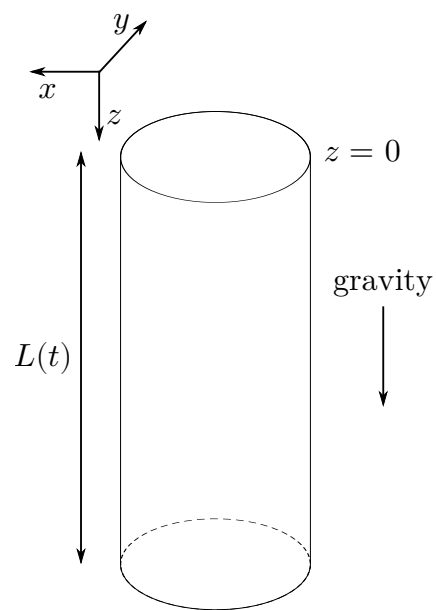


Figure 3.2.1: A sketch of a solid axisymmetric cylinder stretching under gravity. The  $z$ -axis is aligned with the cylinder, while the  $x$ - and  $y$ -axes lie in the transverse plane. The cylinder is fixed at  $z = 0$  and the length of the cylinder at time  $t$  is denoted  $L(t)$ .

Consider a solid axisymmetric cylinder of Newtonian fluid stretching under gravity with no surface tension and neglecting inertia. We introduce a Cartesian co-ordinate system in which the  $z$ -axis is aligned with the cylinder, while the  $x$ - and  $y$ -axes lie in the transverse plane, as shown in Figure 3.2.1. One end of the cylinder is fixed at  $z = 0$ . The corresponding velocity vector is denoted  $(u, v, w)$ , the fluid density  $\rho$  and gravitational acceleration  $g$ . The length of the cylinder at time  $t$  is denoted  $L(t)$ . Using extensional flow theory, the associated rate-of-strain tensor has the form

$$e = \begin{pmatrix} e_1 & 0 & 0 \\ 0 & e_2 & 0 \\ 0 & 0 & e_3 \end{pmatrix}$$

such that  $e_1 + e_2 + e_3 = 0$  (Irgens, 2008). The stretching of a fluid in one direction only, in this case the axial ( $z$ ) direction, is referred to as *uniaxial extensional flow*. This is described by the rates of strain

$$e_1 = e_2 = -\frac{e}{2}, \quad e_3 = e = \frac{\partial w}{\partial z}.$$

For a Newtonian fluid, the stress tensor is

$$\sigma = -pI + 2\mu e,$$

where  $p$  is the pressure. The pressure terms can be eliminated by introducing the net tensile stress

$$\sigma_E = \sigma_{33} - \sigma_{11} = \sigma_{33} - \sigma_{22} = 2\mu e - 2\mu \left(-\frac{e}{2}\right) = 3\mu e. \quad (3.2.1)$$

The quantity  $\mu_E = 3\mu$  in (3.2.1) is referred to as the *Trouton viscosity* or *tensile viscosity*, introduced by Trouton (1906), while the ratio  $\mu_E/\mu$  is known as the *Trouton ratio*. Repeating the above derivation for a uniaxial flow in two

dimensions produces a Trouton ratio of 4. This appears in models of stretching glass sheets (Stokes, 2000), which feature similar equations to the present work. Different ratios are produced by biaxial flows, which are outside the scope of this thesis.

Substituting for the rate of strain in (3.2.1) we find that

$$\sigma_E = 3\mu \frac{\partial w}{\partial z}.$$

Denoting the cross-sectional area at axial position  $z$  and time  $t$  by  $S(z, t)$  and the length of the cylinder by  $L(t)$ , a force balance yields

$$3\mu S \frac{\partial w}{\partial z} = \int_z^L \rho g S dz,$$

which, differentiating with respect to  $z$ , produces the governing equation

$$-\frac{\partial}{\partial z} \left( 3\mu S \frac{\partial w}{\partial z} \right) = \rho g S. \quad (3.2.2)$$

Applying conservation of mass to a fixed volume of fluid lying between  $z = Z(t)$  and  $z = L(t)$ , and using Leibniz's rule, shows that

$$\frac{\partial}{\partial t} \int_{Z(t)}^{L(t)} \rho S dz = \int_{Z(t)}^{L(t)} \frac{\partial}{\partial t} (\rho S) dz + \rho S(L(t), t) L'(t) - \rho S(Z(t), t) z'(t) = 0.$$

Differentiating with respect to  $z$  and recognising that  $Z'(t) = w(z, t)$  yields

$$\frac{\partial S}{\partial t} + \frac{\partial(wS)}{\partial z} = 0,$$

which is equivalent to

$$-S \frac{\partial w}{\partial z} = \frac{\partial S}{\partial t} + w \frac{\partial S}{\partial z} = \frac{DS}{Dt},$$

where  $D/Dt$  is the material derivative. This is used to eliminate  $Sw_z$  from the momentum equation (3.2.2), giving

$$\frac{\partial}{\partial z} \left( 3\mu \frac{DS}{Dt} \right) = g\rho S. \quad (3.2.3)$$

When other effects are included a modified Trouton model may again be derived by considering a force balance, such as done by Wilson (1988) for surface tension and Sauter and Buggisch (2005) for both surface tension and inertia. We denote the radius of the cylinder by  $R(z, t)$ , so that, provided the cylinder is sufficiently slender, the curvature may be approximated by  $\kappa = 1/R$ , and introduce the surface tension coefficient  $\gamma$ , so that the contribution from surface tension is  $\gamma\kappa$ . The modified net tensile stress is then (Petrie, 1995)

$$\sigma_E = 3\mu e - \gamma\kappa = 3\mu e - \frac{\gamma}{R}.$$

In addition to gravity, there is also a compressive axial force due to surface tension given by  $2\pi R\gamma$ . Balancing force and the rate of change in momentum in a fixed volume of fluid between  $z = Z(t)$  and  $z = L(t)$  yields

$$\frac{\partial}{\partial t} \int_{Z(t)}^{L(t)} \rho S w \, dz = \int_{Z(t)}^{L(t)} \rho g S \, dz - S(z, t) \sigma_E(z, t) - 2\pi R\gamma.$$

We again apply Leibniz's rule and differentiate with respect to  $z$ . Making use of conservation of mass and recognising that  $S = \pi R^2$ , this equation reduces to

$$\rho S \frac{Dw}{Dt} - \frac{\partial}{\partial z} \left( 3\mu S \frac{\partial w}{\partial z} \right) = \gamma \pi \frac{\partial R}{\partial z} + \rho g S.$$

Comparing this with (3.2.3) and denoting the boundary length of cross section  $z$  by  $\Gamma(z) = 2\pi R$ , we note that the additional term due to surface tension that appears on the right-hand side is in the form

$$\frac{\gamma}{2} \Gamma_z.$$

Using this result and again using conservation of mass yields the governing equation

$$\rho S \frac{Dw}{Dt} + \frac{\partial}{\partial z} \left( 3\mu \frac{DS}{Dt} \right) = \frac{\gamma}{2} \frac{\partial \Gamma}{\partial z} + \rho g S. \quad (3.2.4)$$

While it was possible to derive these equations using extensional flow theory and force balances for a solid axisymmetric cylinder it is not clear how this process can be replicated for other geometries, particularly those with higher connectivity. In order to derive a version of (3.2.4) for general geometries we instead consider a formal asymptotic expansion, which is discussed in the next section. We will later compare the form of the resulting equation with that of (3.2.4).

### 3.3 Slenderness Model

#### 3.3.1 Governing Equations and Slenderness Approximation

Consider a glass cylinder with internal structure, as shown in Figure 3.3.2, with an outer boundary and  $N \geq 0$  interior boundaries. We introduce a Cartesian co-ordinate system in which the  $z$ -axis is directed vertically downwards along the cylinder axis, while the  $x$ - and  $y$ -axes lie in the transverse plane. The corresponding velocity vector is denoted  $(u, v, w)$  and the pressure  $p$ . The length of the cylinder at time  $t$  is denoted  $L(t)$ , while the cross section at position  $z$  and time  $t$  is  $S(z, t)$ . The total perimeter of each cross section is  $\Gamma(z, t)$ . The axial velocity at the top of the cylinder  $w(0, t)$  is assumed known and may be zero (corresponding to the stretching problem) or non-zero (corresponding to the extrusion problem). The initial area profile  $S_0(z) = S(z, 0)$  and initial length  $L_0 = L(0)$  are also assumed known. Both the initial cross-sectional area and shape may vary with position  $z$ ; that is, they are not necessarily uniform. The temperature of the material is  $T(x, y, z, t)$  with known initial temperature

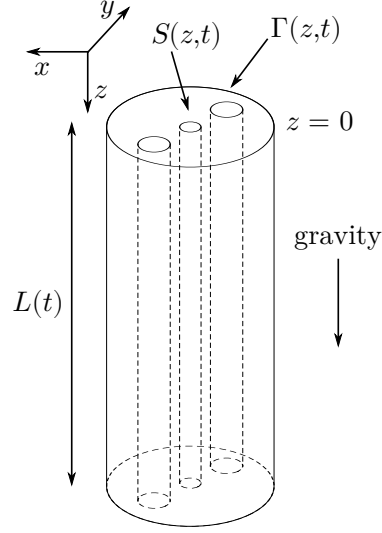


Figure 3.3.2: A sketch of a cylinder with internal structure representative of the geometries considered throughout this thesis. A Cartesian co-ordinate system is employed in which the  $z$ -axis is directed along the axis of the cylinder, while the  $x$ - and  $y$ -axes are oriented in the transverse direction. The length and cross-sectional area are denoted  $L(t)$  and  $S(z, t)$ , respectively. The total boundary length of each cross section is denoted  $\Gamma(z, t)$ . The cylinder is aligned such that gravity acts in the direction of increasing  $z$ .

$$T_0(x, y, z) = T(x, y, z, 0).$$

Under assumptions (1) to (4) made in Chapter 2, we model the molten glass as an incompressible Newtonian fluid with varying viscosity and under the influence of gravity. As such, the fluid flow may be described by the Navier–Stokes and continuity equations (Batchelor, 1967), which represent conservation of momentum and mass, respectively. Since the viscosity depends upon the temperature, we also require an equation representing conservation of energy. Thus, the governing equations, representing conservation of momentum,

mass and energy, are, respectively,

$$\rho \left( \frac{\partial \mathbf{u}}{\partial t} + \mathbf{u} \cdot \nabla \mathbf{u} \right) = -\nabla p + \nabla^2(\mu \mathbf{u}) + \rho g \mathbf{k}, \quad (3.3.5a)$$

$$\nabla \cdot \mathbf{u} = 0, \quad (3.3.5b)$$

$$\frac{\partial T}{\partial t} + \mathbf{u} \cdot \nabla T = \alpha \nabla^2 T, \quad (3.3.5c)$$

where  $\rho$  is the fluid density,  $\mu = \mu(T(x, y, z, t)) = \mu(x, y, z, t)$  is the viscosity,  $g$  is the gravitational acceleration,  $\mathbf{k}$  is the unit vector pointing in the positive  $z$  direction and  $\alpha$  is the thermal diffusivity.

Each boundary of the fluid region may be described as the solution to

$$G^{(n)}(x, y, z, t) = 0, \quad n = 0, 1, \dots, N,$$

for some function  $G^{(n)}$ . As this notation is cumbersome and the same conditions are imposed on each boundary, from this point onwards we drop the superscripts on these functions and instead refer to all the boundaries as the solution to  $G(x, y, z, t) = 0$ , with the understanding that a different function is used on each boundary. The unit normal to the boundaries is

$$\mathbf{n} = \frac{\nabla G}{|\nabla G|}.$$

We must apply three conditions along the boundary  $G = 0$ . The dynamic boundary condition represents a force balance and states that the stress is balance by surface tension and the atmospheric pressure  $p_a(t)$ , while the kinematic boundary condition states that the boundary moves with the fluid. We also need a condition describing the heat flux across the boundary; however, there is no consensus on the exact form this condition should take. Some studies have included radiative heat transfer in the boundary condition (Huang *et al.*, 2003, 2007), while radiative terms may also be included in both the

energy equation and boundary condition through the use of the Rosseland approximation (Paek and Runk, 1978; Huang *et al.*, 2008). Lee and Jaluria (1997, p. 856, eqn (A3b)) presented an approximate expression for the apparent additional conductivity due to radiation under such an approximation, which is  $O(T^3)$ . Through a scaling argument, Wylie and Huang (2007) showed that radiation is not important in the drawing of fibres with small cross-sectional areas, while Taroni *et al.* (2013) modelled fibre drawing with both convective and radiative heat transfer at the boundary. Radiation between internal boundaries is often ignored in complex geometries (Lyytikäinen, Zagari, Barton and Canning, 2004); however, numerical simulations by Xue, Poladian, Barton and Large (2007) showed that including radiation caused preforms to reach thermal equilibrium faster, and that by including radiation between internal boundaries thermal equilibrium was attained even faster. The inclusion of radiative heat transfer between internal boundaries is difficult as the heat flux depends upon the geometry of the boundaries. We here apply a simple Newton cooling condition, which states that the rate of change in temperature at the boundaries is the product of the heat transfer coefficient with the difference in the material and atmospheric temperatures. (It will be argued later that the precise form of the heat flux does not alter the leading-order equations.) Thus, the dynamic, kinematic and energy boundary conditions applied on  $G = 0$  are, respectively,

$$-p\mathbf{n} + 2\mu[\nabla\mathbf{u} + (\nabla\mathbf{u})^T]\mathbf{n} = (-\gamma\kappa - p_a(t))\mathbf{n}, \quad (3.3.6a)$$

$$\frac{\partial G}{\partial t} + \mathbf{u} \cdot \nabla G = 0, \quad (3.3.6b)$$

$$-k\nabla T \cdot \mathbf{n} = h(T - T_a). \quad (3.3.6c)$$

Here,  $\gamma$  is the coefficient of surface tension,  $\kappa$  the curvature,  $h$  the heat transfer

Table 3.3.1: Important physical parameters and scales used in the models for the gravitational stretching and extrusion of a fluid cylinder.

Parameter	Symbol	Units
Surface tension	$\gamma$	$\text{N} \cdot \text{m}^{-1}$
Viscosity	$\mu_0$	$\text{Pa} \cdot \text{s}$
Density	$\rho$	$\text{kg} \cdot \text{m}^{-3}$
Thermal diffusivity	$\alpha$	$\text{m}^2 \cdot \text{s}^{-1}$
Heat transfer coefficient	$h$	$\text{W} \cdot \text{m}^{-2} \cdot \text{K}^{-1}$
Thermal conductivity	$k$	$\text{W} \cdot \text{m}^{-1} \cdot \text{K}^{-1}$
Cross-sectional area	$\mathcal{S}$	$\text{m}^2$
Axial length	$\mathcal{L}$	$\text{m}$
Velocity	$\mathcal{U}$	$\text{m} \cdot \text{s}^{-1}$
Temperature	$\mathcal{T}$	$^\circ\text{C}$

coefficient and  $T_a$  the atmospheric temperature. We assume that the atmospheric pressure is constant and that there is no pressurisation of the internal channels so without loss of generality set  $p_a = 0$ .

### 3.3.2 Scaled Equations and Series Expansions

Table 3.3.1 lists the parameters important in the stretching and extrusion problems. The area  $\mathcal{S}$  represents a typical cross-sectional area (often  $S_0$  is constant and so we take  $\mathcal{S} = S_0$ ). From these values we define the slenderness ratio

$$\epsilon = \frac{\sqrt{\mathcal{S}}}{\mathcal{L}},$$

which represents the ratio of a typical cross-sectional length to a typical axial length. Thus,  $\epsilon$  provides a measure of the slenderness of the geometry: smaller values of  $\epsilon$  correspond to more-slender geometries, while  $\epsilon = 1$  indicates equal axial and cross-sectional length scales. We assume that  $\epsilon \ll 1$ , which will be verified later for both the stretching and extrusion problems. Using the parameters from Table 3.3.1 and  $\epsilon$  we introduce the following scaled quantities, denoted by carets:

$$(x, y, z) = \mathcal{L}(\epsilon\hat{x}, \epsilon\hat{y}, \hat{z}), \quad (3.3.7a)$$

$$(u, v, w) = \mathcal{U}(\epsilon\hat{u}, \epsilon\hat{v}, \hat{w}), \quad (3.3.7b)$$

$$S = \mathcal{S}\hat{S}, \quad (3.3.7c)$$

$$\Gamma = \epsilon\mathcal{L}\hat{\Gamma}, \quad (3.3.7d)$$

$$t = \frac{\mathcal{L}}{\mathcal{U}}\hat{t}, \quad (3.3.7e)$$

$$T = \mathcal{T}\hat{T}, \quad (3.3.7f)$$

$$p = \frac{\mu_0\mathcal{U}}{\mathcal{L}}\hat{p}, \quad (3.3.7g)$$

$$\kappa = \frac{1}{\epsilon\mathcal{L}}\hat{\kappa}. \quad (3.3.7h)$$

Since the viscosity is sensitive to temperature we write

$$\mu(x, y, z, t) = \mu_0\mu^*(\hat{x}, \hat{y}, \hat{z}, \hat{t}),$$

where  $\mu_0$  is a typical viscosity and  $\mu^*$  is the scaled quantity. As discussed in Chapter 2, the surface tension  $\gamma$  and density  $\rho$  are both assumed to be independent of temperature and are taken to be constant along the length of the cylinder. The scaled surface normal vector is

$$\hat{\mathbf{n}} = (\hat{n}_1, \hat{n}_2, \epsilon\hat{n}_3),$$

which, to leading-order in  $\epsilon$ , is orthogonal to the  $z$ -axis. With these scales, the Navier–Stokes equations (3.3.5a) become

$$\begin{aligned} \epsilon^2 \text{Re} & \left( \frac{\partial \hat{u}}{\partial \hat{t}} + \hat{u} \frac{\partial \hat{u}}{\partial \hat{x}} + \hat{v} \frac{\partial \hat{u}}{\partial \hat{y}} + \hat{w} \frac{\partial \hat{u}}{\partial \hat{z}} \right) \\ & = - \frac{\partial \hat{p}}{\partial \hat{x}} + \frac{\partial}{\partial \hat{x}} \left( 2\mu^* \frac{\partial \hat{u}}{\partial \hat{x}} \right) + \frac{\partial}{\partial \hat{y}} \left[ \mu^* \left( \frac{\partial \hat{u}}{\partial \hat{y}} + \frac{\partial \hat{v}}{\partial \hat{x}} \right) \right] + \frac{\partial}{\partial \hat{z}} \left[ \mu^* \left( \epsilon^2 \frac{\partial \hat{u}}{\partial \hat{z}} + \frac{\partial \hat{w}}{\partial \hat{x}} \right) \right] \end{aligned} \quad (3.3.8a)$$

$$\begin{aligned} \epsilon^2 \text{Re} & \left( \frac{\partial \hat{v}}{\partial \hat{t}} + \hat{u} \frac{\partial \hat{v}}{\partial \hat{x}} + \hat{v} \frac{\partial \hat{v}}{\partial \hat{y}} + \hat{w} \frac{\partial \hat{v}}{\partial \hat{z}} \right) \\ & = - \frac{\partial \hat{p}}{\partial \hat{y}} + \frac{\partial}{\partial \hat{x}} \left[ \mu^* \left( \frac{\partial \hat{u}}{\partial \hat{y}} + \frac{\partial \hat{v}}{\partial \hat{x}} \right) \right] + \frac{\partial}{\partial \hat{y}} \left( 2\mu^* \frac{\partial \hat{v}}{\partial \hat{y}} \right) + \frac{\partial}{\partial \hat{z}} \left[ \mu^* \left( \epsilon^2 \frac{\partial \hat{v}}{\partial \hat{z}} + \frac{\partial \hat{w}}{\partial \hat{y}} \right) \right], \end{aligned} \quad (3.3.8b)$$

$$\begin{aligned} \epsilon^2 \text{Re} & \left( \frac{\partial \hat{w}}{\partial \hat{t}} + \hat{u} \frac{\partial \hat{w}}{\partial \hat{x}} + \hat{v} \frac{\partial \hat{w}}{\partial \hat{y}} + \hat{w} \frac{\partial \hat{w}}{\partial \hat{z}} \right) \\ & = - \epsilon^2 \frac{\partial \hat{p}}{\partial \hat{z}} + \frac{\partial}{\partial \hat{x}} \left[ \mu^* \left( \epsilon^2 \frac{\partial \hat{u}}{\partial \hat{z}} + \frac{\partial \hat{w}}{\partial \hat{x}} \right) \right] + \frac{\partial}{\partial \hat{y}} \left[ \mu^* \left( \frac{\partial \hat{v}}{\partial \hat{z}} + \frac{\partial \hat{w}}{\partial \hat{y}} \right) \right] \\ & \quad + \epsilon^2 \frac{\partial}{\partial \hat{z}} \left( 2\mu^* \frac{\partial \hat{w}}{\partial \hat{z}} \right) + \epsilon^2 g^*. \end{aligned} \quad (3.3.8c)$$

These scaled equations contain two important dimensionless parameters. The first is the Reynolds number

$$\text{Re} = \frac{\rho \mathcal{U} \mathcal{L}}{\mu_0},$$

which represents the ratio of inertial and viscous forces. The second is the scaled gravity

$$g^* = \frac{\rho g \mathcal{L}^2}{\mu_0 \mathcal{U}} = \frac{\text{Re}}{\text{Fr}^2},$$

where Fr is the Froude number  $\mathcal{U}/\sqrt{g\mathcal{L}}$ . The parameter  $g^*$  represents the ratio of gravitational and viscous forces.

The scaled continuity equation retains the same form as (3.3.5b), specifically

$$\frac{\partial \hat{u}}{\partial \hat{x}} + \frac{\partial \hat{v}}{\partial \hat{y}} + \frac{\partial \hat{w}}{\partial \hat{z}} = 0.$$

Scaling the energy equation (3.3.5c) yields

$$\epsilon^2 \text{Pe} \left( \frac{\partial \hat{T}}{\partial \hat{t}} + \hat{u} \frac{\partial \hat{T}}{\partial \hat{x}} + \hat{v} \frac{\partial \hat{T}}{\partial \hat{y}} + \hat{w} \frac{\partial \hat{T}}{\partial \hat{z}} \right) = \frac{\partial^2 \hat{T}}{\partial \hat{x}^2} + \frac{\partial^2 \hat{T}}{\partial \hat{y}^2} + \epsilon^2 \frac{\partial^2 \hat{T}}{\partial \hat{z}^2}, \quad (3.3.9)$$

where

$$\text{Pe} = \frac{\mathcal{L}\mathcal{U}}{\alpha}$$

is the Péclet number and represents the relative rate of advective and diffusive heat transport.

Scaling the stress conditions (3.3.6a) on  $G = 0$  yields

$$-\hat{p}\hat{n}_1 + \mu^* \left[ 2 \frac{\partial \hat{u}}{\partial \hat{x}} \hat{n}_1 + \left( \frac{\partial \hat{u}}{\partial \hat{y}} + \frac{\partial \hat{v}}{\partial \hat{x}} \right) \hat{n}_2 + \left( \epsilon^2 \frac{\partial \hat{u}}{\partial \hat{z}} + \frac{\partial \hat{w}}{\partial \hat{x}} \right) \hat{n}_3 \right] = -\gamma^* \hat{\kappa} \hat{n}_1, \quad (3.3.10a)$$

$$-\hat{p}\hat{n}_2 + \mu^* \left[ \left( \frac{\partial \hat{u}}{\partial \hat{y}} + \frac{\partial \hat{v}}{\partial \hat{x}} \right) \hat{n}_1 + 2 \frac{\partial \hat{v}}{\partial \hat{y}} \hat{n}_2 + \left( \epsilon^2 \frac{\partial \hat{v}}{\partial \hat{z}} + \frac{\partial \hat{w}}{\partial \hat{y}} \right) \hat{n}_3 \right] = -\gamma^* \hat{\kappa} \hat{n}_2, \quad (3.3.10b)$$

$$-\epsilon^2 \hat{p}\hat{n}_3 + \mu^* \left[ \left( \epsilon^2 \frac{\partial \hat{u}}{\partial \hat{z}} + \frac{\partial \hat{w}}{\partial \hat{x}} \right) \hat{n}_1 + \left( \epsilon^2 \frac{\partial \hat{v}}{\partial \hat{z}} + \frac{\partial \hat{w}}{\partial \hat{y}} \right) \hat{n}_2 + 2 \epsilon^2 \frac{\partial \hat{w}}{\partial \hat{z}} \hat{n}_3 \right] = -\epsilon^2 \gamma^* \hat{\kappa} \hat{n}_3, \quad (3.3.10c)$$

where we have introduced the dimensionless surface tension

$$\gamma^* = \frac{\gamma}{\epsilon \mu_0 \mathcal{U}} = \frac{1}{\epsilon \text{Ca}}$$

and capillary number  $\text{Ca} = \mu_0 \mathcal{U} / \gamma$ . The parameter  $\gamma^*$  represents the ratio of viscous to surface-tension forces using the velocity scale  $\epsilon \mathcal{U}$ . The scaled kinematic boundary condition (3.3.6b) is

$$\frac{\partial G}{\partial \hat{t}} + \hat{u} \frac{\partial G}{\partial \hat{x}} + \hat{v} \frac{\partial G}{\partial \hat{y}} + \hat{w} \frac{\partial G}{\partial \hat{z}} = 0,$$

while the scaled energy boundary condition (3.3.6c) is

$$\frac{\partial \hat{T}}{\partial \hat{x}} \hat{n}_1 + \frac{\partial \hat{T}}{\partial \hat{y}} \hat{n}_2 + \epsilon^2 \frac{\partial \hat{T}}{\partial \hat{z}} \hat{n}_3 = -\epsilon \text{Bi} \left( \hat{T} - \hat{T}_a \right), \quad (3.3.11)$$

where

$$\text{Bi} = \frac{h\mathcal{L}}{k}$$

is the Biot number, which represents the ratio of internal to surface heat transfer.

Since  $\epsilon$  is small, we expand each of the dependent variables as series in powers of  $\epsilon^2$  except for temperature  $\hat{T}$ , which is expanded in powers of  $\epsilon$ :

$$\hat{u} = \hat{u}_0 + \epsilon^2 \hat{u}_1 + \epsilon^4 \hat{u}_2 + \dots \quad (3.3.12a)$$

$$\hat{v} = \hat{v}_0 + \epsilon^2 \hat{v}_1 + \epsilon^4 \hat{v}_2 + \dots \quad (3.3.12b)$$

$$\hat{w} = \hat{w}_0 + \epsilon^2 \hat{w}_1 + \epsilon^4 \hat{w}_2 + \dots \quad (3.3.12c)$$

$$\hat{p} = \hat{p}_0 + \epsilon^2 \hat{p}_1 + \epsilon^4 \hat{p}_2 + \dots \quad (3.3.12d)$$

$$\hat{\kappa} = \hat{\kappa}_0 + \epsilon^2 \hat{\kappa}_1 + \epsilon^4 \hat{\kappa}_2 + \dots \quad (3.3.12e)$$

$$\hat{T} = \hat{T}_0 + \epsilon \hat{T}_1 + \epsilon^2 \hat{T}_2 + \dots \quad (3.3.12f)$$

These are substituted into the scaled governing equations, from which we obtain equations at different orders of  $\epsilon$ .

### 3.3.3 Temperature and Viscosity in the Slender Limit

To derive leading-order equations for the temperature under the slenderness approximation we must first make some assumptions regarding the size of the parameters from the scaled energy equations. These will be justified later using typical parameter values from the problems under consideration. We assume that the Péclet number  $\text{Pe}$  is  $O(1)$ , so that the the term  $\epsilon^2 \text{Pe}$  from the left-hand side of the energy equation (3.3.9) is  $O(\epsilon^2)$ . We also assume that the Biot number  $\text{Bi}$  from the energy boundary condition (3.3.11) is  $O(1)$ . Note that the term  $\epsilon \text{Bi} = h\sqrt{\mathcal{S}}/k$  represents a Biot number defined using the transverse

length scale. The estimates of both Pe and Bi agree with the values given by Huang *et al.* (2007). After substituting the series (3.3.12) and making use of these assumptions, the leading-order terms from the energy equation (3.3.9) and boundary condition (3.3.11) are

$$\frac{\partial^2 \hat{T}_0}{\partial \hat{x}^2} + \frac{\partial^2 \hat{T}_0}{\partial \hat{y}^2} = 0, \quad (3.3.13a)$$

$$\frac{\partial \hat{T}_0}{\partial \hat{x}} \hat{n}_1 + \frac{\partial \hat{T}_0}{\partial \hat{y}} \hat{n}_2 = 0 \quad \text{on } G = 0. \quad (3.3.13b)$$

Thus, to leading order the temperature satisfies Laplace's equation subject to a homogeneous Neumann boundary condition. This implies that  $\hat{T}_0$  is a function of  $z$  and  $t$  only, and is thus uniform within any cross section at a given time. Since the viscosity depends solely on the temperature,  $\mu^*$  is also independent of  $x$  and  $y$ , so that  $\mu^* = \mu^*(z, t)$ .

The right-hand side of the Newton cooling condition (3.3.6c) is  $h(T - T_a)$ . A radiative condition would instead have the form  $h_r(T^4 - T_a^4)$ , where  $h_r$  is a parameter that depends upon the emissivity and the Stefan–Boltzman constant; however, even with the inclusion of this term, to leading order the energy boundary condition would still reduce to a homogeneous Neumann condition provided that  $h_r$  was sufficiently small (Huang *et al.*, 2003, 2007; Griffiths and Howell, 2008). Thus, the viscosity would still be independent of the transverse co-ordinates.

While the choice of energy condition does not affect the leading-order problem, this condition will enter into the higher-order equations, from which a one-dimensional model for the heat flow in the axial direction  $z$  may be derived (Yarin, Rusinov, Gospodinov and Radev, 1989; Huang *et al.*, 2007; Griffiths and Howell, 2008; Taroni *et al.*, 2013). Since the exact form of the heat flux is unknown, for the purposes of this study we assume that the temperature, and

hence also the viscosity, are known functions of  $z$  and  $t$  and instead focus on the solution of the momentum equations. Knowledge of the temperature profile is required in order to find the geometry along the entire length of the cylinder, making determining the temperature profile an important albeit challenging problem that must be considered as part of future work. This is in contrast to fibre drawing, in which only the geometry at the end of the hot zone is of interest and for which it has been shown that the solution may be found without knowledge of temperature and viscosity provided that the fibre tension is known (Stokes *et al.*, 2014).

### 3.3.4 Axial Flow Equations

As we expect gravitational effects are important we assume that  $g^*$  is  $O(1)$ , while for surface-tension effects to appear in the leading-order equations we also require  $\gamma^*$  to be  $O(1)$ . For generality we will, for now, assume that  $\text{Re}$  is  $O(1)$  but will later consider solutions with  $\text{Re} = 0$ . So as to simplify the notation, from this point onwards we drop hats on dimensionless variables, while asterisks are retained on dimensionless parameters so as to avoid later confusion. As per Cummings and Howell (1999), the axial and transverse flow components of the momentum equations and stress conditions decouple and it will be useful to consider the resulting equations separately. The leading-order continuity equation is

$$\frac{\partial u_0}{\partial x} + \frac{\partial v_0}{\partial y} + \frac{\partial w_0}{\partial z} = 0. \quad (3.3.14)$$

Similarly, the leading-order kinematic condition is

$$\frac{\partial G}{\partial t} + u_0 \frac{\partial G}{\partial x} + v_0 \frac{\partial G}{\partial y} + w_0 \frac{\partial G}{\partial z} = 0. \quad (3.3.15)$$

Using that  $\mu^* = \mu^*(z, t)$ , the leading-order momentum equation and dynamic boundary condition are

$$\frac{\partial^2 w_0}{\partial x^2} + \frac{\partial^2 w_0}{\partial y^2} = 0, \quad (3.3.16a)$$

$$\frac{\partial w_0}{\partial x} \frac{\partial G}{\partial x} + \frac{\partial w_0}{\partial y} \frac{\partial G}{\partial y} = 0 \quad \text{on } G = 0. \quad (3.3.16b)$$

Again, since this is Laplace's equation with homogeneous Neumann boundary conditions in the  $xy$ -plane, the leading-order axial velocity component  $w_0$  is independent of the transverse co-ordinates; that is,  $w_0 = w_0(z, t)$ . This means that, to leading order, every cross section moves with a uniform axial velocity.

The  $O(\epsilon^2)$  momentum equation and stress boundary condition in the  $z$ -direction are

$$\begin{aligned} & \text{Re} \left( \frac{\partial w_0}{\partial t} + w_0 \frac{\partial w_0}{\partial z} \right) + \frac{\partial p_0}{\partial z} \\ &= \mu^* \left[ \frac{\partial}{\partial x} \left( \frac{\partial w_1}{\partial x} + \frac{\partial u_0}{\partial z} \right) + \frac{\partial}{\partial y} \left( \frac{\partial w_1}{\partial y} + \frac{\partial v_0}{\partial z} \right) \right] + \frac{\partial}{\partial z} \left( 2\mu^* \frac{\partial w_0}{\partial z} \right) + g^*, \end{aligned} \quad (3.3.17a)$$

$$\begin{aligned} & -\gamma^* \kappa_0 \frac{\partial G}{\partial z} \\ &= \mu^* \left[ \left( \frac{\partial w_1}{\partial x} + \frac{\partial u_0}{\partial z} \right) \frac{\partial G}{\partial x} + \left( \frac{\partial w_1}{\partial y} + \frac{\partial v_0}{\partial z} \right) \frac{\partial G}{\partial y} + 2 \frac{\partial w_0}{\partial z} \frac{\partial G}{\partial z} \right] - p_0 \frac{\partial G}{\partial z}. \end{aligned} \quad (3.3.17b)$$

Introducing the transverse operator

$$\nabla_{\perp} = \left( \frac{\partial}{\partial x}, \frac{\partial}{\partial y} \right)$$

we can write the system (3.3.17) in the form

$$\begin{aligned} \mu^* \nabla_{\perp}^2 w_1 &= \operatorname{Re} \left( \frac{\partial w_0}{\partial t} + w_0 \frac{\partial w_0}{\partial z} \right) - \mu^* \frac{\partial}{\partial z} \left( \frac{\partial u_0}{\partial x} + \frac{\partial v_0}{\partial y} \right) \\ &\quad + \frac{\partial}{\partial z} \left( p_0 - 2\mu^* \frac{\partial w_0}{\partial z} \right) - g^*, \end{aligned} \quad (3.3.18)$$

$$\mu^* \nabla_{\perp} w_1 \cdot \nabla_{\perp} G = \left( p_0 - 2\mu^* \frac{\partial w_0}{\partial z} - \gamma^* \kappa_0 \right) \frac{\partial G}{\partial z} - \mu^* \left( \frac{\partial u_0}{\partial z} \frac{\partial G}{\partial x} + \frac{\partial v_0}{\partial z} \frac{\partial G}{\partial y} \right). \quad (3.3.19)$$

This is Poisson's equation with an inhomogeneous Neumann boundary condition.

Writing this in the form

$$\mu^* \nabla_{\perp}^2 w_1 = f, \quad (3.3.20a)$$

$$\mu^* \nabla_{\perp} w_1 \cdot \nabla_{\perp} G \frac{1}{|\nabla_{\perp} G|} = \mu^* \frac{\partial w_1}{\partial \hat{\mathbf{n}}} = b, \quad (3.3.20b)$$

so that the boundary condition involves the unit normal, and applying the divergence theorem, we find that this problem must satisfy the compatibility condition

$$\iint_{\Omega} f \, dx \, dy = \oint_{\partial\Omega} b \, ds, \quad (3.3.21)$$

where the term on the left-hand side is an integral over the cross section  $\Omega$  at some fixed  $z$  such that  $0 \leq z \leq L(t)$ , while the integral on the right-hand side is taken around the corresponding boundary  $\partial\Omega$ . This is a single equation that represents the momentum balance and stress condition for the axial problem. The latter of these requires a careful interpretation and is of critical importance. Typically, MOF preforms have multiply connected cross sections so that  $\partial\Omega$  comprises an outer boundary  $C_0$  and  $N \geq 0$  inner boundaries  $C_n$ ,  $n = 1, 2, \dots, N$ , as shown in the example in Figure 3.3.3. Each boundary is equipped with the standard orientation, which is taken to be counter-clockwise on the outer boundary and clockwise on inner boundaries. Any integral over

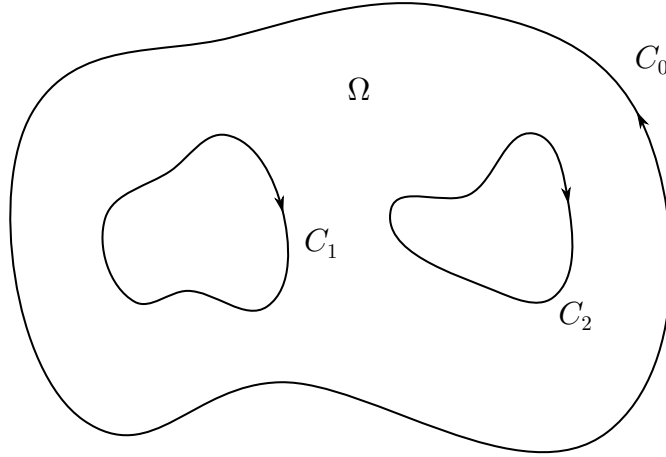


Figure 3.3.3: A multiply connected domain  $\Omega$  with two inner boundaries. The total boundary  $\partial\Omega$  consists of the outer boundary  $C_0$  and the inner boundaries  $C_1$  and  $C_2$ . The arrows indicate the standard orientation of each boundary. Integrals around the total boundary  $\partial\Omega$  are to be taken around each of the curves  $C_0$ ,  $C_1$  and  $C_2$  with respect to the indicated orientations.

$\partial\Omega$  may thus be expressed as

$$\oint_{\partial\Omega} \cdot ds = \oint_{C_0+C_1+\dots+C_N} \cdot ds = \sum_{n=0}^N \oint_{C_n} \cdot ds. \quad (3.3.22)$$

Unless otherwise required, the more-compact notation on the left-hand side will be used throughout this thesis. Importantly, the divergence theorem and the transport theorems given in Appendix A may be applied to multiply connected domains.

The functions  $f$  and  $b$  that appear in the compatibility condition (3.3.21) both depend upon the leading-order transverse velocities  $u_0$  and  $v_0$ . For now we assume that these are known. Written out in full, the compatibility condition

(3.3.21) is

$$\begin{aligned} & \iint_{\Omega} \left[ \operatorname{Re} \left( \frac{\partial w_0}{\partial t} + w_0 \frac{\partial w_0}{\partial z} \right) - \mu^* \frac{\partial}{\partial z} \left( \frac{\partial u_0}{\partial x} + \frac{\partial v_0}{\partial y} \right) \right. \\ & \quad \left. + \frac{\partial}{\partial z} \left( p_0 - 2\mu^* \frac{\partial w_0}{\partial z} \right) - g^* \right] dx dy = \\ & \oint_{\partial\Omega} \frac{1}{|\nabla_{\perp} G|} \left[ \left( p_0 - 2\mu^* \frac{\partial w_0}{\partial z} - \gamma^* \kappa_0 \right) \frac{\partial G}{\partial z} - \mu^* \left( \frac{\partial u_0}{\partial z} \frac{\partial G}{\partial x} + \frac{\partial v_0}{\partial z} \frac{\partial G}{\partial y} \right) \right] ds. \end{aligned} \quad (3.3.23)$$

By interchanging the order of differentiation, the second term inside the integral on the left-hand side may be written as a divergence using the transverse operator  $\nabla_{\perp}$ . Applying the divergence theorem it may be shown that the leading-order transverse velocity vector  $(u_0, v_0)$  satisfies

$$\begin{aligned} \iint_{\Omega} \mu^* \frac{\partial}{\partial z} \left( \frac{\partial u_0}{\partial x} + \frac{\partial v_0}{\partial y} \right) dx dy &= \iint_{\Omega} \mu^* \nabla_{\perp} \cdot \left( \frac{\partial u_0}{\partial z}, \frac{\partial v_0}{\partial z} \right) dx dy \\ &= \oint_{\partial\Omega} \frac{\mu^*}{|\nabla_{\perp} G|} \left( \frac{\partial u_0}{\partial z} \frac{\partial G}{\partial x} + \frac{\partial v_0}{\partial z} \frac{\partial G}{\partial y} \right) ds. \end{aligned}$$

Upon substitution into (3.3.23) we obtain

$$\begin{aligned} & \iint_{\Omega} \left[ \operatorname{Re} \left( \frac{\partial w_0}{\partial t} + w_0 \frac{\partial w_0}{\partial z} \right) + \frac{\partial}{\partial z} \left( p_0 - 2\mu^* \frac{\partial w_0}{\partial z} \right) - g^* \right] dx dy = \\ & \quad \oint_{\partial\Omega} \frac{1}{|\nabla_{\perp} G|} \left( p_0 - 2\mu^* \frac{\partial w_0}{\partial z} - \gamma^* \kappa_0 \right) \frac{\partial G}{\partial z} ds. \end{aligned} \quad (3.3.24)$$

Inspecting (3.3.24), we note that the term

$$\phi = p_0 - 2\mu^* \partial w_0 / \partial z$$

occurs on both the left- and right-hand sides. It is possible to combine these terms by making use of transport theorem (A.2) given in Appendix A. Applying this theorem and cancelling terms yields

$$\begin{aligned} & \iint_{\Omega} \left[ \operatorname{Re} \left( \frac{\partial w_0}{\partial t} + w_0 \frac{\partial w_0}{\partial z} \right) - g^* \right] dx dy + \frac{\partial}{\partial z} \iint_{\Omega} \left( p_0 - 2\mu^* \frac{\partial w_0}{\partial z} \right) dx dy = \\ & \quad - \oint_{\partial\Omega} \frac{\gamma^* \kappa_0}{|\nabla_{\perp} G|} \frac{\partial G}{\partial z} ds. \end{aligned} \quad (3.3.25)$$

We can make further simplifications by introducing an Airy stress function  $\mathcal{A}$ , which is named after the work of Airy (1863) into problems involving plane elasticity and by definition satisfies

$$-2 \frac{\partial^2 \mathcal{A}}{\partial y^2} = -p_0 + 2\mu^* \frac{\partial u_0}{\partial x}, \quad (3.3.26a)$$

$$-2 \frac{\partial^2 \mathcal{A}}{\partial x^2} = -p_0 + 2\mu^* \frac{\partial v_0}{\partial y}, \quad (3.3.26b)$$

$$2 \frac{\partial^2 \mathcal{A}}{\partial x \partial y} = \mu \left( \frac{\partial u}{\partial y} + \frac{\partial v}{\partial x} \right). \quad (3.3.26c)$$

Using (3.3.26a), (3.3.26b) and the continuity equation (3.3.14) we find that

$$\nabla_{\perp}^2 \mathcal{A} = p_0 - \mu^* \left( \frac{\partial u_0}{\partial x} + \frac{\partial v_0}{\partial y} \right) = p_0 + \mu^* \frac{\partial w_0}{\partial z},$$

which may be solved for  $p_0$ , yielding

$$p_0 = \nabla_{\perp}^2 \mathcal{A} - \mu^* \frac{\partial w_0}{\partial z}.$$

This allows elimination of  $p_0$  from (3.3.25), which, after some rearrangement, yields

$$\begin{aligned} \iint_{\Omega} \left[ \operatorname{Re} \left( \frac{\partial w_0}{\partial t} + w_0 \frac{\partial w_0}{\partial z} \right) - g^* \right] dx dy - \frac{\partial}{\partial z} \iint_{\Omega} \left( 3\mu^* \frac{\partial w_0}{\partial z} \right) dx dy = \\ - \oint_{\partial\Omega} \frac{\gamma^* \kappa_0}{|\nabla_{\perp} G|} \frac{\partial G}{\partial z} ds - \frac{\partial}{\partial z} \iint_{\Omega} (\nabla_{\perp}^2 \mathcal{A}) dx dy. \end{aligned} \quad (3.3.27)$$

The right-hand side of (3.3.27) involves the integrals

$$\begin{aligned} I_1 &= \oint_{\partial\Omega} \frac{\gamma^* \kappa_0}{|\nabla_{\perp} G|} \frac{\partial G}{\partial z} ds \text{ and} \\ I_2 &= \iint_{\Omega} (\nabla_{\perp}^2 \mathcal{A}) dx dy, \end{aligned}$$

which may both be simplified significantly. We first consider the evaluation of  $I_1$ , which is taken around the boundary and is the more difficult of the two integrals.

We can make progress by considering each boundary  $C_n$ ,  $n = 0, 1, 2, \dots, N$ , separately, computing

$$I_1^n = \oint_{C_n} \frac{\gamma^* \kappa_0}{|\nabla_{\perp} G|} \frac{\partial G}{\partial z} ds$$

and summing the results. For each boundary  $C_n$  we introduce a parameterisation  $\mathbf{x}_n = (x(s, z), y(s, z), z)$ , where  $s$  denotes the arc length and the parameterisation follows the standard orientation (see Figure 3.3.3). By definition,  $G = 0$  on  $C_n$ , so that differentiation with respect to  $z$  yields

$$\frac{\partial G}{\partial x} \frac{\partial x}{\partial z} + \frac{\partial G}{\partial y} \frac{\partial y}{\partial z} + \frac{\partial G}{\partial z} = 0,$$

which may be rearranged to show that

$$\frac{\partial G}{\partial z} = -\frac{\partial G}{\partial x} \frac{\partial x}{\partial z} - \frac{\partial G}{\partial y} \frac{\partial y}{\partial z} = -\nabla_{\perp} G \cdot (x_z, y_z),$$

where subscripts denote differentiation. By the definition of  $G$ , the term  $-\nabla_{\perp} G$  is an inwards-pointing surface normal while, using the parameterisation  $\mathbf{x}_n$ , the inwards-pointing *unit* surface normal is  $(-y_s, x_s)$ . Thus, by normalising  $-\nabla_{\perp} G$  we can write

$$-\frac{\nabla_{\perp} G}{|\nabla_{\perp} G|} \cdot (x_z, y_z) = (-y_s, x_s) \cdot (x_z, y_z).$$

Thus, we find that

$$I_1^n = \gamma^* \oint_{C_n} \kappa_0 (-y_s, x_s) \cdot (x_z, y_z) ds.$$

The first Frenet–Serret formula (Kreyszig, 2005) is

$$(x_{ss}, y_{ss}) = \kappa_0 (-y_s, x_s),$$

which may be substituted to give

$$I_1^n = \gamma^* \oint_{C_n} (x_{ss}, y_{ss}) \cdot (x_z, y_z) ds. \quad (3.3.28)$$

Because  $(x_s, y_s)$  is a unit vector it follows that  $x_s^2 + y_s^2 = 1$ . Differentiating this identity with respect to  $z$  shows that  $x_s x_{sz} + y_s y_{sz} = 0$ . Making use of this identity we find that

$$\begin{aligned} \frac{\partial}{\partial s} (x_s x_z + y_s y_z) &= x_{ss} x_z + x_s x_{sz} + y_{ss} y_z + y_s y_{sz} \\ &= x_{ss} x_z + y_{ss} y_z, \\ &= (x_{ss}, y_{ss}) \cdot (x_z, y_z), \end{aligned}$$

which is precisely the integrand from (3.3.28). Introducing

$$\Gamma_n(z, t) = \oint_{C_n(z, t)} ds$$

which represents the length of boundary  $C_n$  at axial position  $z$  and time  $t$ , we may write

$$I_1^n = \gamma^* \oint_{C_n} (x_{ss}, y_{ss}) \cdot (x_z, y_z) ds = \oint_{C_n} \frac{\partial}{\partial s} (x_s x_z + y_s y_z) ds = [x_s x_z + y_s y_z]_{s=0}^{s=\Gamma_n}$$

Both  $x$  and  $y$  are necessarily periodic in  $s$  with period  $\Gamma_n$  and hence so too are  $x_s$  and  $y_s$  and hence we may write

$$x(\Gamma_n(z), z) - x(0, z) = 0.$$

Differentiating this expression with respect to  $z$ , being careful to account for the change due to the first argument  $s = \Gamma_n(z)$ , shows that

$$x_s(\Gamma_n(z), z) \frac{\partial \Gamma_n}{\partial z} + x_z(\Gamma_n(z), z) - x_z(0, z) = 0.$$

After applying the same steps to  $y(s, z)$  we find that

$$\begin{aligned} x_z(\Gamma_n(z), z) - x_z(0, z) &= -x_s(\Gamma_n, z) \frac{\partial \Gamma_n}{\partial z}, \\ y_z(\Gamma_n(z), z) - y_z(0, z) &= -y_s(\Gamma_n, z) \frac{\partial \Gamma_n}{\partial z}. \end{aligned}$$

Thus, owing to the periodicity of  $x_s$  and  $y_s$ , and after again using that  $(x_s, y_s)$  is a unit vector, we find that

$$\begin{aligned} [x_s x_z + y_s y_z]_{s=0}^{s=\Gamma_n} &= x_s(0, z) [x_z(\Gamma_n(z), z) - x_z(0, z)] \\ &\quad + y_s(0, z) [y_z(\Gamma_n(z), z) - y_z(0, z)] \\ &= - (x_s^2(0, z) + y_s^2(0, z)) \frac{\partial \Gamma_n}{\partial z} \\ &= - \frac{\partial \Gamma_n}{\partial z}. \end{aligned}$$

That is, we have shown that

$$I_1^n = \oint_{C_n} \frac{\gamma^* \kappa_0}{|\nabla_{\perp} G|} \frac{\partial G}{\partial z} ds = -\gamma^* \frac{\partial \Gamma_n}{\partial z}.$$

Summing the contributions from each boundary yields

$$I_1 = \oint_{\partial \Omega} \frac{\gamma^* \kappa_0}{|\nabla_{\perp} G|} \frac{\partial G}{\partial z} ds = -\gamma^* \frac{\partial \Gamma}{\partial z}.$$

We now consider the evaluation of  $I_2$ . Using the definition of the Airy stress function (3.3.26) and the leading-order terms from the transverse dynamic boundary conditions (3.3.10a) and (3.3.10b), it may be shown that

$$\frac{\partial \mathcal{A}}{\partial \mathbf{n}} = \frac{\gamma^*}{2} + \mathbf{a} \cdot \mathbf{n}, \quad (3.3.29)$$

where  $\mathbf{a}$  is a constant vector. (This result will be established in Subsection 4.2.7 for the case  $\gamma^* = 1$ , although the same derivation applies for  $\gamma^* \neq 1$ .) Applying the divergence theorem to convert  $I_2$  to an integral around the boundary and then using the above form of the dynamic boundary condition we find that

$$I_2 = \iint_{\Omega} (\nabla_{\perp}^2 \mathcal{A}) dx dy = \oint_{\partial \Omega} \frac{\partial \mathcal{A}}{\partial \mathbf{n}} ds = \oint_{\partial \Omega} \left( \frac{\gamma^*}{2} + \mathbf{a} \cdot \mathbf{n} \right) ds.$$

Applying the divergence theorem shows that

$$\oint_{\partial \Omega} \mathbf{a} \cdot \mathbf{n} ds = \iint_{\Omega} \nabla \cdot \mathbf{a} dx dy = 0. \quad (3.3.30)$$

In addition,  $\gamma^*/2$  is constant and so may be taken outside the integral, so that

$$I_2 = \frac{\gamma^*}{2} \oint_{\partial\Omega} ds = \frac{\gamma^*}{2} \Gamma.$$

Finally, we note that all of the terms within the integrals on the left-hand side of (3.3.27) are independent of both  $x$  and  $y$  so may be taken outside of the integrals. Noting that

$$S(z, t) = \iint_{\Omega(z, t)} dx dy, \quad (3.3.31)$$

and substituting  $I_1$  and  $I_2$  into (3.3.27), we arrive at the axial momentum equation

$$\text{Re}S \left( \frac{\partial w_0}{\partial t} + w_0 \frac{\partial w_0}{\partial z} \right) - \frac{\partial}{\partial z} \left( 3\mu^* S \frac{\partial w_0}{\partial z} \right) = Sg^* + \frac{\gamma^*}{2} \frac{\partial \Gamma}{\partial z}. \quad (3.3.32)$$

Many variations of this equation have been derived in previous work. As discussed in Section 3.2, a version of this equation was first presented by Trouton (1906, p. 432, eqn (2)) for solid, axisymmetric geometries neglecting surface tension. Note that (3.3.32), ignoring the inertial terms, has a form similar to (3.2.4) and again includes the (now dimensionless) Trouton viscosity  $3\mu^*$ . A version of (3.3.32) with inertia, gravity and surface tension was derived by Matovich and Pearson (1969, p. 514, eqn (20)) for an axisymmetric cylinder drawn by an applied force. Denn (1980, p. 373, eqn (7)) presented a similar equation using area-averaged quantities, in which the area was replaced by the explicit expression  $\pi R^2$ . A Lagrangian version has been derived by Wilson (1988, p. 564, eqn (15)) for an axisymmetric extruded fluid with surface tension and gravity, which is discussed further in Chapter 7. A systematic derivation was used by Dewynne *et al.* (1989, p. 985, eqn (2.6)) for axisymmetric cylinders in the absence of inertia, gravity and surface tension. This analysis was later extended to show that a similar equation applied for arbitrary connected

domains without inertia, gravity and surface tension (Dewynne *et al.*, 1992, p. 330, eqn (4.4)), and with inertia and gravity but still neglecting surface tension Dewynne *et al.* (1994, p. 546, eqn (16)). Related equations have been found for two-dimensional sheets under gravity Stokes (1999, p. 2753, eqn (2.10)). A version for geometries with no internal boundaries, but which include inertia, surface tension and gravity was derived by Cummings and Howell (1999, p. 368, eqn (3.12)). An equation similar to (3.3.32) was found by Chakravarthy and Chiu (2009, p. 162, eqn (2.20)), but this did not make use of (3.3.30) to eliminate the constants and instead argued that these integrals were only zero for geometries with cyclic symmetry. Griffiths and Howell (2008, p. 185, eqn (3.7)) presented a version of this equation for a thin-walled hollow tube with inertia and surface tension but neglecting gravity, while Stokes *et al.* (2014, p. 181, eqn (2.5)) extended this to multiply connected cylinders of arbitrary shape. Thus, (3.3.32) differs from previous work in that it includes inertia, gravity and surface tension, applies to multiply connected geometries and does not include unnecessary constants.

As an aside, a similar model has been proposed by Fitt *et al.* (2002) that applies to the drawing of capillary tubes. This model was used by Kostecki, Ebendorff-Heidepriem, Warren-Smith and Monro (2014) to model the drawing of cylinders with three internal holes. To make use of the model the authors considered the three internal holes to be one hole with the same cross-sectional area. As the model required the total boundary length this also had to be approximated. By comparing with experimental observations it was found that the best approximation to the boundary length was given by summing the perimeters of the three internal holes and the outer boundary, rather than using the perimeter of the single larger hole used in the approximation and the

outer boundary. This agrees with the derivation here that includes the total boundary length  $\Gamma$ .

### 3.3.5 Leading-Order Kinematic Condition and Conservation of Mass

Since the axial momentum equation (3.3.32) has now been written in terms of the cross-sectional area  $S$  we now seek to do the same with the kinematic condition (3.3.15). After dividing through by  $|\nabla_{\perp} G|$  and rearranging, this condition is integrated around  $\partial\Omega$ , yielding

$$\oint_{\partial\Omega} \frac{1}{|\nabla_{\perp} G|} \left( \frac{\partial G}{\partial t} + w_0 \frac{\partial G}{\partial z} \right) ds = - \oint_{\partial\Omega} \frac{1}{|\nabla_{\perp} G|} \left( u_0 \frac{\partial G}{\partial x} + v_0 \frac{\partial G}{\partial y} \right) ds.$$

The boundary integral on the right-hand side can be converted to an area integral, resulting in

$$\oint_{\partial\Omega} \frac{1}{|\nabla_{\perp} G|} \left( \frac{\partial G}{\partial t} + w_0 \frac{\partial G}{\partial z} \right) ds = - \iint_{\Omega} \nabla_{\perp} \cdot (u_0, v_0) dx dy.$$

Using the leading-order continuity condition (3.3.14), the transverse velocities from the integrand on the right-hand side can be eliminated, yielding

$$\oint_{\partial\Omega} \frac{1}{|\nabla_{\perp} G|} \left( \frac{\partial G}{\partial t} + w_0 \frac{\partial G}{\partial z} \right) ds = \iint_{\Omega} \frac{\partial w_0}{\partial z} dx dy.$$

The order of differentiation and integration on the right-hand side can be interchanged using transport theorem (A.2). Cancelling terms then leaves

$$\oint_{\partial\Omega} \frac{G_t}{|\nabla_{\perp} G|} ds = \frac{\partial}{\partial z} \iint_{\Omega} w_0 dx dy.$$

Finally, applying transport theorem (A.1) shows that

$$\frac{\partial}{\partial t} \iint_{\Omega} dx dy = - \oint_{\partial\Omega} \frac{G_t}{|\nabla_{\perp} G|} ds,$$

and hence

$$\frac{\partial}{\partial t} \iint_{\Omega} dx dy + \frac{\partial}{\partial z} \iint_{\Omega} w_0 dx dy = 0.$$

As  $w_0$  is independent of  $x$  and  $y$  we have, using the expression for  $S$  (3.3.31),

$$\frac{\partial S}{\partial t} + \frac{\partial}{\partial z}(w_0 S) = 0, \quad (3.3.33)$$

which represents conservation of mass. Together, (3.3.32) and (3.3.33) form the system of equations to be solved in the axial direction, which involve both the area  $S$  and leading-order axial velocity  $w_0$ . At this point it is useful to consider the transverse equations, which are discussed in the following subsections.

### 3.3.6 Transverse Equations

Substituting the expansions (3.3.12) into the remaining momentum equations (3.3.8a) and (3.3.8b) and keeping only leading-order terms in  $\epsilon$  yields

$$\begin{aligned} \frac{\partial p_0}{\partial x} &= \frac{\partial}{\partial x} \left( 2\mu^* \frac{\partial u_0}{\partial x} \right) + \frac{\partial}{\partial y} \left[ \mu^* \left( \frac{\partial u_0}{\partial y} + \frac{\partial v_0}{\partial x} \right) \right] + \frac{\partial}{\partial z} \left( \mu^* \frac{\partial w_0}{\partial x} \right), \\ \frac{\partial p_0}{\partial y} &= \frac{\partial}{\partial x} \left[ \mu^* \left( \frac{\partial u_0}{\partial y} + \frac{\partial v_0}{\partial x} \right) \right] + \frac{\partial}{\partial y} \left( 2\mu^* \frac{\partial v_0}{\partial y} \right) + \frac{\partial}{\partial z} \left( \mu^* \frac{\partial w_0}{\partial y} \right). \end{aligned}$$

Here, we have assumed that  $\epsilon^2 \text{Re} \ll 1$ . Since both  $\mu$  and  $w_0$  are functions of  $z$  and  $t$  only, the  $x$  and  $y$  derivatives of these are both zero. Assuming we can interchange the order of differentiation and making use of the leading-order continuity equation (3.3.14), these reduce to the two-dimensional Stokes equations

$$\frac{\partial p_0}{\partial x} = \mu^* \left( \frac{\partial^2 u_0}{\partial x^2} + \frac{\partial^2 u_0}{\partial y^2} \right), \quad (3.3.34a)$$

$$\frac{\partial p_0}{\partial y} = \mu^* \left( \frac{\partial^2 v_0}{\partial x^2} + \frac{\partial^2 v_0}{\partial y^2} \right). \quad (3.3.34b)$$

Substituting the series expansions into the stress conditions (3.3.10a) and (3.3.10b) and recalling that  $w_0 = w_0(z)$ , so that any derivatives of  $w_0$  with respect to  $x$  and  $y$  are zero, we obtain the leading-order stress conditions

$$-p_0 n_1 + \mu^* \left[ 2 \frac{\partial u_0}{\partial x} n_1 + \left( \frac{\partial u_0}{\partial y} + \frac{\partial v_0}{\partial x} \right) n_2 \right] = -\gamma^* \kappa n_1, \quad (3.3.35a)$$

$$-p_0 n_2 + \mu^* \left[ \left( \frac{\partial u_0}{\partial y} + \frac{\partial v_0}{\partial x} \right) n_1 + 2 \frac{\partial v_0}{\partial y} n_2 \right] = -\gamma^* \kappa n_2. \quad (3.3.35b)$$

### 3.3.7 Zero-Surface-Tension Transverse Solution

Dewynne *et al.* (1992) showed that in the limit of zero-surface-tension (ZST) the transverse solution is given by

$$\begin{aligned} p_{\text{ZST}} &= -\frac{\partial w_0}{\partial z}, \\ u_{\text{ZST}} &= -\frac{x}{2\mu^*} \frac{\partial w_0}{\partial z}, \\ v_{\text{ZST}} &= -\frac{y}{2\mu^*} \frac{\partial w_0}{\partial z}, \end{aligned}$$

from which they recognised that an axial velocity gradient results in a change of scale of the cross section but does not change the shape, and further showed that in a rescaled Lagrangian reference frame the cross-sectional geometry does not change in time. Introducing the Lagrangian co-ordinate system  $(\tilde{x}, \tilde{y}, \tilde{z}, \tilde{t})$  defined by

$$\begin{aligned} \tilde{x} &= x(\tilde{x}, \tilde{y}, \tilde{z}, 0), \\ \tilde{y} &= y(\tilde{x}, \tilde{y}, \tilde{z}, 0), \\ \tilde{z} &= z(\tilde{x}, \tilde{y}, \tilde{z}, 0), \\ \tilde{t} &= t, \end{aligned}$$

so that each fluid particle is labelled by its initial position, the appropriate scalings of the transverse co-ordinates are

$$\begin{aligned}x(\tilde{x}, \tilde{y}, \tilde{z}, \tilde{t}) &= \sqrt{S(\tilde{z}, \tilde{t})}\tilde{x}, \\y(\tilde{x}, \tilde{y}, \tilde{z}, \tilde{t}) &= \sqrt{S(\tilde{z}, \tilde{t})}\tilde{y},\end{aligned}$$

Then, in these scaled co-ordinates, the boundary of the cross section is given by

$$\tilde{G}(\tilde{x}, \tilde{y}, \tilde{z}) = G(x, y, z, 0),$$

which is independent of time. This means that, for the cross section with Lagrangian label  $\tilde{z}$ , the kinematic condition becomes

$$u_{\text{ZST}} \frac{\partial \tilde{G}}{\partial \tilde{x}} + v_{\text{ZST}} \frac{\partial \tilde{G}}{\partial \tilde{y}} = 0. \quad (3.3.36)$$

This result is useful in the analysis of the surface-tension-driven problem.

### 3.3.8 Transverse System and Reduced Time

Having considered the zero-surface-tension solution we now make use of this to analyse the problem with non-zero surface tension. Just as for the ZST problem we introduce the scaled transverse co-ordinates

$$(x, y) = \sqrt{S(\tilde{z}, \tilde{t})}(\tilde{x}, \tilde{y}).$$

With the inclusion of surface tension the transverse geometry may change in scale due to axial motion *and* deform due to surface tension acting on the boundaries. Thus,  $\tilde{x}$  and  $\tilde{y}$  are no longer Lagrangian co-ordinates for a fluid particle in cross section  $\tilde{z}$ ; however, the initial axial co-ordinate  $\tilde{z} = z(\tilde{x}, \tilde{y}, \tilde{z}, 0)$  is still a Lagrangian co-ordinate that labels each cross section.

Following Cummings and Howell (1999), we write the pressure and transverse velocity components as

$$p_0 = p_{\text{ZST}} + \frac{\gamma^*}{\sqrt{S}} \tilde{p}, \quad (3.3.37a)$$

$$u_0 = u_{\text{ZST}} + \frac{\gamma^*}{\mu^*} \tilde{u}, \quad (3.3.37b)$$

$$v_0 = v_{\text{ZST}} + \frac{\gamma^*}{\mu^*} \tilde{v}; \quad (3.3.37c)$$

that is, as the sum of the zero-surface-tension solution discussed above and a component due to surface tension. Introducing  $\tilde{G}(\tilde{x}, \tilde{y}, \tilde{z}, \tilde{t}) = G(x, y, z, t)$  and using (3.3.36) to eliminate the ZST solution, the kinematic boundary condition reduces to

$$\frac{\mu\sqrt{S}}{\gamma^*} \frac{\partial \tilde{G}}{\partial \tilde{t}} + \tilde{u} \frac{\partial \tilde{G}}{\partial \tilde{x}} + \tilde{v} \frac{\partial \tilde{G}}{\partial \tilde{y}} = 0 \quad \text{on } \tilde{G} = 0. \quad (3.3.38)$$

As was found by Cummings and Howell (1999), on introducing the reduced time  $\tau$  defined by

$$\frac{\partial \tau}{\partial t} = \frac{\gamma^*}{\mu^* \sqrt{S}}, \quad (3.3.39)$$

(3.3.38) simplifies to the standard kinematic condition

$$\frac{\partial \tilde{G}}{\partial \tau} + \tilde{u} \frac{\partial \tilde{G}}{\partial \tilde{x}} + \tilde{v} \frac{\partial \tilde{G}}{\partial \tilde{y}} = 0 \quad \text{on } \tilde{G} = 0. \quad (3.3.40)$$

Integrating (3.3.39) and requiring that  $\tau = 0$  when  $t = 0$  yields the relationship

$$\tau = \int_0^{\tilde{t}} \frac{\gamma^*}{\mu^* \sqrt{S}} d\tilde{t}. \quad (3.3.41)$$

Upon substituting (3.3.37) into the leading-order continuity equation (3.3.14), transverse momentum equations (3.3.34), dynamic boundary conditions (3.3.35) and kinematic boundary condition (3.3.40), we find, after some simplification, that the surface-tension-driven transverse flow is governed by the following

system of equations:

$$\frac{\partial \tilde{u}}{\partial \tilde{x}} + \frac{\partial \tilde{v}}{\partial \tilde{y}} = 0, \quad (3.3.42a)$$

$$\frac{\partial^2 \tilde{u}}{\partial \tilde{x}^2} + \frac{\partial^2 \tilde{u}}{\partial \tilde{y}^2} = \frac{\partial \tilde{p}}{\partial \tilde{x}}, \quad (3.3.42b)$$

$$\frac{\partial^2 \tilde{v}}{\partial \tilde{x}^2} + \frac{\partial^2 \tilde{v}}{\partial \tilde{y}^2} = \frac{\partial \tilde{p}}{\partial \tilde{y}}, \quad (3.3.42c)$$

$$-pn_1 + 2\frac{\partial \tilde{u}}{\partial \tilde{x}}n_1 + \left(\frac{\partial \tilde{u}}{\partial \tilde{y}} + \frac{\partial \tilde{v}}{\partial \tilde{x}}\right)n_3 = -\tilde{\kappa}n_1 \quad \text{on } \tilde{G} = 0, \quad (3.3.42d)$$

$$-pn_2 + \left(\frac{\partial \tilde{u}}{\partial \tilde{y}} + \frac{\partial \tilde{v}}{\partial \tilde{x}}\right)n_1 + 2\frac{\partial \tilde{v}}{\partial \tilde{y}}n_2 = -\tilde{\kappa}n_2 \quad \text{on } \tilde{G} = 0, \quad (3.3.42e)$$

$$\frac{\partial \tilde{G}}{\partial \tau} + \tilde{u}\frac{\partial \tilde{G}}{\partial \tilde{x}} + \tilde{v}\frac{\partial \tilde{G}}{\partial \tilde{y}} = 0 \quad \text{on } \tilde{G} = 0. \quad (3.3.42f)$$

The system (3.3.42) is a surface-tension-driven free-boundary Stokes flow problem with unit area and unit surface tension. Importantly, this transverse problem is independent of the axial flow and, consequently, we can solve the transverse flow problem for any given geometry without knowledge of the axial flow. This solution alone governs the *shape* of the cross sections, which is also true in models of fibre drawing (Stokes *et al.*, 2014). This result is in contrast to the model of Chakravarthy and Chiu (2009), who did not transform to reduced time and instead used an unmodified kinematic condition, equivalent to (3.3.40), which does depend on the axial problem.

The reduced time variable provides a useful measure of the deformation: the larger the value of  $\tau$  in a particular cross section, the greater the deformation. This suggests that deformations may be mitigated by adjusting the problem parameters to keep  $\tau$  as small as possible. From the definition (3.3.41), it is clear that this may be achieved by minimising the time  $t$  and dimensionless surface tension coefficient  $\gamma^*$  while maximising the viscosity  $\mu$ .

### 3.4 Summary

At this point it is worth briefly summarising the key results derived thus far. The leading-order axial flow equations form a homogeneous Neumann problem (3.3.16), from which it follows that the leading-order axial velocity is independent of the transverse co-ordinates  $x$  and  $y$ . This means that, at this order, the axial velocity is uniform within each cross section. Under the slenderness approximation the temperature and hence also viscosity are also constant within each cross section. For the purposes of this thesis we have assumed that both of these quantities are known and have focused on the fluid flow problem. The  $O(\epsilon^2)$  axial flow reduces to Poisson's equation with a Neumann boundary condition (3.3.20), which may be combined into a single compatibility condition (3.3.21). Integrating this equation over each cross section yields a one-dimensional differential equation (3.3.32) for the area  $S$ , which depends upon the unknown boundary length  $\Gamma$ . This is coupled with (3.3.33), which arises from integrating the leading-order terms from the kinematic boundary condition over each cross section and represents conservation of mass.

In the absence of surface tension, each cross section changes in scale only according to the zero-surface tension solution. Subtracting this solution, converting to a Lagrangian co-ordinate system and introducing the reduced time  $\tau$ , which depends upon the viscosity  $\mu^*$ , dimensionless surface tension coefficient  $\gamma^*$  and cross-sectional area  $S$ , the resulting equations are precisely a two-dimensional Stokes flow moving boundary problem. That is, the *shape* of each cross section evolves as a purely two-dimensional problem, while the *area* is governed by the axial flow.

Importantly, we have shown that the coupled axial and transverse models described by Cummings and Howell (1999) extend to cross sections of arbitrary

shape and connectivity, and to problems including gravity, surface tension and inertia. This is a novel result that has not been published previously to this work.

In deriving these equations it has been assumed that  $\epsilon \ll 1$ , and that  $\text{Re}$ ,  $\text{Pe}$ ,  $\text{Bi}$ ,  $g^*$  and  $\gamma^*$  are all  $O(1)$ . These assumptions will be verified later using typical parameter values from the problems under consideration.

The model described in this section applies to both zero and non-zero values of the leading-order axial velocity at the top of the cylinder  $w_0(0, t)$ . The case  $w_0(0, t) = 0$ , which describes a cylinder stretching under gravity, will be considered in Chapter 6 and the case  $w_0(0, t) \neq 0$ , which describes the extrusion of fluid from a die, in Chapter 7. The different boundary conditions are implemented by using appropriate definitions for the axial Lagrangian co-ordinate  $\tilde{z}$ , which will be introduced in the relevant chapters, and rewriting the axial momentum equation (3.3.32) using these co-ordinates. As solutions to the axial equation for a particular geometry depend upon solving the associated transverse problem we discuss the theory for two-dimensional Stokes flows in Chapter 4 and appropriate numerical methods for solving such problems in Chapter 5.



# Chapter 4

## Stokes Flows in Two Dimensions and Complex Variables

### 4.1 Introduction

In Chapter 3 it was shown that, under the slenderness approximation, the stretching of a fluid cylinder under gravity with surface tension is described by a two-dimensional transverse system (3.3.42) that governs the shape of each cross section and the one-dimensional system (3.3.32) and (3.3.33) governing the axial flow, which depends upon the transverse solution. Transformed to reduced time  $\tau$ , the governing equations within the transverse system were the Stokes equations with unit surface tension acting on the boundaries. The ability to determine the evolution of a given cylinder geometry rests upon solving this transverse system. As such, in this chapter we review the theory of two-dimensional Stokes flows with free boundaries driven by surface tension, with a particular focus on finite domains with an outer boundary and an arbitrary finite number of interior boundaries, such as those seen in MOFs.

Much of the theory presented here for two-dimensional Stokes flows has its origin in the study of plane elasticity. It has been shown (Kolosov, 1909) that the stresses and displacements describing a two-dimensional elastic material can be described by a biharmonic function known as the Airy stress function, so named for its introduction by Airy (1863). In addition, by using complex variables and the Goursat representation for biharmonic functions, introduced by Goursat (1898), the stress function may be described by two complex analytic functions, now referred to as Goursat functions. This formulation was popularised by the influential treatises on elasticity by Muskhelishvili (1975) and Sokolnikov (1956). Owing to this the equations relating the stresses and Goursat functions are referred to as the Kolosov–Muskhelishvili equations, and the Goursat functions as Kolosov–Muskhelishvili functions (Hopper, 1993; Linkov, 2002). The theory of biharmonic functions is closely connected to that of bianalytic functions as summarised by Balk and Zuev (1970).

In both elasticity and very viscous fluid flows the stresses and strains are related by linear constitutive equations, known as Hooke’s law in the case of elasticity with a similar law for fluids proposed by Newton. Interpreting the displacement of an elastic material as a velocity and setting Poisson’s ratio to 0.5, which corresponds to an incompressible material, the equations governing elastic materials are precisely those that govern an incompressible Newtonian Stokes flow. Owing to this relationship, the theory discussed above for planar elasticity problems may also be applied to planar Stokes flow problems. Some of the earliest examples of this include the analysis of the steady axisymmetric flow of a viscous jet under gravity using an asymptotic expansion (Clarke, 1968), and of steady flows with prescribed free and fixed boundaries (Garabedian, 1966). Both of these studies, however, neglected surface tension.

This formulation was extended by Richardson (1968) to study the evolution of an inviscid fluid bubble in an infinite region of viscous fluid under shear and pure strain including, importantly, surface tension effects. Later, Richardson (1973) applied this method to parabolic flows. These two studies are notable for their use of the Kolosov–Muskhelishvili equations to write the dynamic boundary condition in terms of the Goursat functions. This approach was also adopted by Buckmaster and Flaherty (1973), who gave an approximate solution for a two-dimensional drop with a non-zero viscosity in a corner flow. The studies of Richardson (1968, 1973) and Buckmaster and Flaherty (1973) are notable for using a conformal map  $z(\zeta)$  to describe the shape of the drop and rewriting the boundary conditions in terms of the mapping variable  $\zeta$ .

In the first of a series of influential articles, Hopper (1990) considered an arbitrary finite simply connected fluid region bounded by a smooth closed curve. The region was described by a conformal map  $\Omega(\zeta, t)$  from the unit circle  $|\zeta| = 1$ . Using the complex variable formulation Hopper derived an equation for the time evolution of the map  $\Omega$ . This work rested on the conjecture that certain forms of the map  $\Omega$  would remain in the same form for all time. This included polynomial maps

$$P_N(\zeta, t) = \sum_{n=1}^N a_n(t)\zeta^n,$$

partial fraction maps

$$F_N(\zeta, t) = \zeta \sum_{n=1}^N \frac{a_N(t)}{1 - b_n(t)\zeta^n},$$

and rational maps

$$R_N(\zeta, t) = \frac{\zeta P_{M-1}}{Q_N},$$

where  $Q_N$  is a polynomial map. The validity of this conjecture rests upon being able to solve the evolution equation for the map coefficients. This method

was applied to the coalescence of two equal cylinders (Hopper, 1984, 1990), epitrochoids, nephroids, a half-plane bounded by a trochoid, (Hopper, 1990), the flow in the infinite region external to a hypotrochoid (Hopper, 1991), the coalescence of a cylinder with a half-plane (Hopper, 1992), and the flow exterior to a parabola (Hopper, 1993). The techniques used by Hopper were extended by Richardson (1992) to include two unequal touching cylinders and limaçons. Howison and Richardson (1995) have also used these methods to develop solutions for the suction of fluid from an epitrochoid for various values of the surface tension.

Complex variable formulations and conformal maps have also been used to study the evolution of a single bubble in an infinite region of Stokes flow for polynomial flows (Antanovskii, 1994), linear shear flows and expanding or contracting bubbles (Tanveer and Vasconcelos, 1995). Crowdy (2003*a*) extended these results to the case of a compressible bubble, while Crowdy, Tanveer and Vasconcelos (2005) used similar methods to study a pair of interacting bubbles. Crowdy (2004) has also developed an *elliptical pore model* for modelling multiple bubbles (pores) in Stokes flow. This was motivated by the study of sintering, which is the process by which a collection of particles is heated and fused together. The elliptical pore model again uses conformal mapping techniques and relies on the assumption that the pores are in a straining flow. The original elliptical pore model has been extended to include a circular outer boundary (Buchak, Crowdy, Stokes and Ebendorff-Heidepriem, 2015).

Exact solutions using conformal maps have been found for annular viscous blobs driven by surface tension (Crowdy and Tanveer, 1998), which were later used for doubly connected unimodal and bimodal packings of disks (Crowdy, 2003*b*).

There are several important connections between two-dimensional Stokes flow problems and Hele-Shaw flows. Conformal mapping techniques have been used extensively in the study of Hele-Shaw problems with evolving boundaries due to fluid injection in the absence of surface tension to study cusp development (Howison, 1986*a*), fingering (Howison, 1986*b*) and blobs in thin channels (Richardson, 1982). Richardson (1997*b*) considered domains generated by injecting fluid into a Hele-Shaw cell at  $N$  points and showed that if such a domain evolved as a surface-tension-driven Stokes flow then the configuration at all future times could be constructed by shifting the injection points. This method was used to describe the evolution of multiple touching disks forming simply connected domains but could be applied to other geometries, such as cardioid-like domains with cusps (Richardson, 1997*a*), and was later extended to touching disks forming doubly connected regions (Richardson, 2000).

Richardson (1972) showed that Hele-Shaw flows arising from fluid injection could be described by an infinite set of conserved moments, sometimes referred to as ‘Richardson’s moments’, while similar conserved quantities were subsequently defined for two-dimensional Stokes flow (Cummings, Howison and King, 1997; Crowdy, 1999). It has also been shown that general classes of free boundary problems, including Stokes and Hele-Shaw flows, can be analysed by considering a Cauchy transformation of the domain and reduced to computing the evolution of a finite set of parameters (Crowdy, 2002*b*). Crowdy (2002*a*) made use of the above work to show that the evolution of multiply connected fluid domains can be found by tracking the boundary with an algebraic curve described by a finite set of time-dependent parameters, rather than a conformal map. The method was demonstrated by finding the solution to the evolution of a quintuply connected domain formed by five touching cylinders described by

just five parameters.

Howison and Richardson (1995) used complex-variable methods to study cusp development in viscous blobs from which fluid is removed at a single point. Using the results of Richardson (1992), this study showed that surface tension prevented the formation of cusps, and hence avoided physically-unrealistic solutions; however, solutions could be found that were graphically indistinguishable from true cusps. Jeong and Moffatt (1992) observed similar cusp-like shapes develop due to rotating cylinders in Stokes flow.

In the remainder of this chapter we summarise the theory of two-dimensional Stokes flows driven by surface tension, the biharmonic equation and the use of complex variables, which provide an efficient method for solving the transverse problem (3.3.42). While some exact solutions will be presented, the results presented here will later be used in Chapter 5 to construct numerical methods for solving the transverse flow problem for general geometries. From this point onwards we drop the tildes on variables from the transverse problem.

## 4.2 Stokes Equations

### 4.2.1 Basic Theory

As previously noted, (3.3.42b) and (3.3.42c) from the transverse problem are the Stokes equations. These two equations may be combined and the pressure terms eliminated by subtracting the  $x$ -derivative of (3.3.42c) from the  $y$ -derivative of (3.3.42b), which, assuming the order of differentiation may be interchanged, yields

$$\frac{\partial^3 u}{\partial x^2 \partial y} + \frac{\partial^3 u}{\partial y^3} - \frac{\partial^3 v}{\partial x^3} - \frac{\partial^3 v}{\partial x \partial y^2} = 0. \quad (4.2.1)$$

Since the fluid is incompressible, we introduce a stream function  $\psi$  defined by

$$u = \frac{\partial\psi}{\partial y}, \quad v = -\frac{\partial\psi}{\partial x}. \quad (4.2.2)$$

It is simple to verify that this definition ensures the continuity equation (3.3.42a) is satisfied. Substituting (4.2.2) into (4.2.1) yields the single governing equation

$$\frac{\partial^4\psi}{\partial x^4} + 2\frac{\partial^4\psi}{\partial x^2\partial y^2} + \frac{\partial^4\psi}{\partial y^4} = 0, \quad (4.2.3)$$

known as the *biharmonic equation*. This equation has a rich theory that is vital to the work presented in this thesis, which is described in the following subsections.

### 4.2.2 The Biharmonic Equation

Composing the transverse *Laplace operator* with itself yields

$$\begin{aligned} (\nabla \cdot \nabla)^2 &= \nabla^2 \nabla^2 = \nabla^4 = \left( \frac{\partial^2}{\partial x^2} + \frac{\partial^2}{\partial y^2} \right) \left( \frac{\partial^2}{\partial x^2} + \frac{\partial^2}{\partial y^2} \right) \\ &= \frac{\partial^4}{\partial x^4} + 2\frac{\partial^4}{\partial x^2\partial y^2} + \frac{\partial^4}{\partial y^4}, \end{aligned}$$

where we have assumed that we may interchange the order of differentiation. The operator  $\nabla^4$  is known as the *biharmonic operator*. Importantly, the biharmonic operator gives precisely the combination of terms found in (4.2.3). Thus, the stream function satisfies the biharmonic equation

$$\nabla^4\psi = 0. \quad (4.2.4)$$

This may be simplified by using complex variables.

### 4.2.3 Complex Variables

Within this chapter and Chapter 5 we make use of the complex variables

$$z = x + iy,$$

$$\bar{z} = x - iy,$$

where  $i = \sqrt{-1}$  is the imaginary unit and  $\bar{z}$  is the complex conjugate of  $z$ .

Using these definitions and the chain rule we find that

$$\frac{\partial}{\partial x} = \frac{\partial z}{\partial x} \frac{\partial}{\partial z} + \frac{\partial \bar{z}}{\partial x} \frac{\partial}{\partial \bar{z}} = \frac{\partial}{\partial z} + \frac{\partial}{\partial \bar{z}} \quad (4.2.5)$$

and

$$\frac{\partial}{\partial y} = \frac{\partial z}{\partial y} \frac{\partial}{\partial z} + \frac{\partial \bar{z}}{\partial y} \frac{\partial}{\partial \bar{z}} = i \frac{\partial}{\partial z} - i \frac{\partial}{\partial \bar{z}}, \quad (4.2.6)$$

which are known as *Wirtinger derivatives* after their use and popularisation by Wirtinger (1927). Importantly, by using the Wirtinger derivatives the two-dimensional Laplacian may now be written as

$$\begin{aligned} \nabla^2 &= \frac{\partial^2}{\partial x^2} + \frac{\partial^2}{\partial y^2} \\ &= \left( \frac{\partial}{\partial z} + \frac{\partial}{\partial \bar{z}} \right)^2 + i^2 \left( \frac{\partial}{\partial z} - \frac{\partial}{\partial \bar{z}} \right)^2 \\ &= \frac{\partial^2}{\partial z^2} + 2 \frac{\partial^2}{\partial z \partial \bar{z}} + \frac{\partial^2}{\partial \bar{z}^2} - \left( \frac{\partial^2}{\partial z^2} - 2 \frac{\partial^2}{\partial z \partial \bar{z}} + \frac{\partial^2}{\partial \bar{z}^2} \right) \\ &= 4 \frac{\partial^2}{\partial z \partial \bar{z}}. \end{aligned}$$

The biharmonic operator thus has compact form

$$\nabla^4 = (\nabla^2)^2 = \left( 4 \frac{\partial^2}{\partial z \partial \bar{z}} \right)^2 = 16 \frac{\partial^4}{\partial z^2 \partial \bar{z}^2},$$

and hence the biharmonic equation reduces to

$$\frac{\partial^4 \psi}{\partial z^2 \partial \bar{z}^2} = 0.$$

Strictly speaking, by changing variables we should introduce a new function  $\Psi(z, \bar{z})$  defined by

$$\Psi(z(x, y), \bar{z}(x, y)) = \psi(x, y);$$

however, this adds unnecessary complication and can obscure some of the results presented. Thus, while strictly an abuse of notation, we will use  $\psi$  to represent both of these functions.

Writing the governing equation in the form (4.2.3) has the advantage that we may now solve this equation by direct integration with respect to  $z$  and  $\bar{z}$ , yielding

$$\psi = \bar{z}A(z) + zB(\bar{z}) + C(z) + D(\bar{z}), \quad (4.2.7)$$

where  $A, B, C$  and  $D$  are arbitrary functions. Since  $\psi$  represents physical quantities we require it to be real-valued and hence  $\psi = \bar{\psi}$ . The conjugate of (4.2.7) is

$$\bar{\psi} = z\bar{A}(\bar{z}) + \bar{z}\bar{B}(z) + \bar{C}(\bar{z}) + \bar{D}(z), \quad (4.2.8)$$

where we have defined  $\overline{f(z)} = \bar{f}(\bar{z})$ . Equating (4.2.7) and (4.2.8) gives

$$\bar{z}A(z) + zB(\bar{z}) + C(z) + D(\bar{z}) = z\bar{A}(\bar{z}) + \bar{z}\bar{B}(z) + \bar{C}(\bar{z}) + \bar{D}(z).$$

For this to be true for all  $z$  and  $\bar{z}$  we must have that  $A = \bar{B}$  and  $C = \bar{D}$ . Using these relationships we may write (4.2.7) as

$$\begin{aligned} \psi &= \bar{z}A(z) + z\bar{A}(\bar{z}) + C(z) + \bar{C}(\bar{z}) \\ &= \bar{z}A(z) + C(z) + \overline{\bar{z}A(z) + C(z)}. \end{aligned}$$

That is,  $\psi$  is the sum of some function  $\bar{z}A(z) + C(z)$  and its complex conjugate. By defining the functions

$$\frac{f(z)}{2i} = A(z), \quad \frac{g(z)}{2i} = C(z),$$

$\psi$  may be written in the form

$$\psi = \frac{1}{2i} \left[ \bar{z}f(z) + g(z) - \overline{(\bar{z}f(z) + g(z))} \right] = \Im(\bar{z}f(z) + g(z)). \quad (4.2.9)$$

This form is called the *Goursat representation* of  $\psi$ , with the functions  $f$  and  $g$  known as *Goursat functions*, in recognition of the pioneering work carried out by Goursat (1898) in developing a similar solution. They are occasionally referred to as Kolosov–Muskhelishvili functions due to their use by Kolosov (1909) and Muskhelishvili (1975). By instead setting  $A(z) = f(z)/2$  and  $C(z) = g(z)/2$  we could show that  $\psi$  is the *real* part of the function  $\bar{z}f + g$ . While this form has been used (Carrier, Krook and Pearson, 1966) it is more common to see  $\psi$  written as the imaginary part, such as may be observed in the literature reviewed at the start of this chapter. The two forms are, however, equivalent, and switching from one to the other corresponds to multiplying a complex function by  $i$ .

In general, we will be concerned with problems that depend on reduced time  $\tau$ . In this case the functions  $f$  and  $g$  will strictly also depend on  $\tau$ , so we could write

$$\psi = \Im(\bar{z}f(z, \tau) + g(z, \tau)).$$

Similarly, both the velocity and pressure depend on  $\tau$ ; however, as the Stokes equations and hence also the biharmonic equation are instantaneous, the solution at some reduced time  $\tau$  does not depend on the solution at previous reduced times. Due to this,  $\tau$  plays no role in the above formulation and thus, to avoid cumbersome notation, we suppress this dependence.

### 4.2.4 Complex Analytic Functions

The vorticity  $\boldsymbol{\omega}$  is defined

$$\boldsymbol{\omega} = \nabla \times \mathbf{u},$$

so that in two dimensions the vorticity is easily verified to be

$$\boldsymbol{\omega} = \left( 0, 0, \frac{\partial v}{\partial x} - \frac{\partial u}{\partial y} \right).$$

Thus, the vorticity has only one non-zero component, and this is orthogonal to the  $x$ - and  $y$ -axes. We thus define

$$\omega = \frac{\partial v}{\partial x} - \frac{\partial u}{\partial y}, \quad (4.2.10)$$

and, by substituting for the velocity using the definition of the stream function (4.2.2) we observe that

$$-\omega = \frac{\partial^2 u}{\partial x^2} + \frac{\partial^2 v}{\partial y^2} = \nabla^2 \psi.$$

From (4.2.3) we know that  $\psi$  satisfies the biharmonic equation, which yields

$$-\nabla^2 \omega = \nabla^4 \psi = 0,$$

That is,  $\omega$  satisfies Laplace's equation so is a *harmonic function*. Taking the divergence of the Stokes equations and using the continuity equation  $\nabla \cdot \mathbf{u} = 0$ , we find that

$$\nabla \cdot \nabla p = \nabla^2 p = \nabla \cdot \nabla^2 \mathbf{u} = \nabla^2 (\nabla \cdot \mathbf{u}) = 0,$$

so that the pressure  $p$  is also a harmonic function. Here, we have assumed that we can swap the order of the differential operators used.

For a complex analytic function  $f = f_r + if_i$  the *Cauchy–Riemann equations* state that the real part  $f_r$  and imaginary part  $f_i$  must satisfy

$$\frac{\partial f_r}{\partial x} = \frac{\partial f_i}{\partial y}, \quad \frac{\partial f_r}{\partial y} = -\frac{\partial f_i}{\partial x}. \quad (4.2.11)$$

Two functions that satisfy these equations are harmonic and, furthermore, are said to be *harmonic conjugates*. Following the method used by Langlois (1964) we now show that the pressure  $p$  and vorticity  $\omega$  are harmonic conjugates. Differentiating (4.2.10) with respect to  $x$  gives

$$\frac{\partial \omega}{\partial x} = \frac{\partial^2 v}{\partial x^2} - \frac{\partial^2 u}{\partial x \partial y},$$

while the continuity equation yields

$$-\frac{\partial u}{\partial x} = \frac{\partial v}{\partial y}.$$

Combining these we find that

$$\frac{\partial \omega}{\partial x} = \frac{\partial^2 v}{\partial x^2} + \frac{\partial^2 v}{\partial y^2} = \nabla^2 v. \quad (4.2.12)$$

By instead differentiating (4.2.10) by  $y$  it may be shown that

$$\frac{\partial \omega}{\partial y} = -\frac{\partial^2 u}{\partial x^2} - \frac{\partial^2 u}{\partial y^2} = -\nabla^2 u. \quad (4.2.13)$$

Finally, the Stokes equations (3.3.42b) and (3.3.42c) state that

$$\nabla^2 u = \frac{\partial p}{\partial x}, \quad \nabla^2 v = \frac{\partial p}{\partial y}.$$

Substituting these relationships into (4.2.12) and (4.2.13) to eliminate the velocity terms yields

$$\frac{\partial p}{\partial x} = \frac{\partial(-\omega)}{\partial y}, \quad \frac{\partial p}{\partial y} = -\frac{\partial(-\omega)}{\partial x}. \quad (4.2.14)$$

That is,  $p$  and  $-\omega$  satisfy the Cauchy–Riemann equations so are the real and imaginary parts, respectively, of the complex analytic function

$$\mathcal{P} = p - i\omega.$$

Multiplying the preceding equation by  $i$  shows that *positive*  $\omega$  and  $p$  are the real and imaginary parts, respectively, of the complex analytic function  $i\mathcal{P}$ , which is the form used by Langlois (1964).

We can also derive the above relationship using vector calculus identities. Since  $\omega = \mathbf{k} \cdot \boldsymbol{\omega}$ , where  $\mathbf{k} = (0, 0, 1)$ , we can write  $\nabla\omega = \nabla(\mathbf{k} \cdot \boldsymbol{\omega})$ . For vector fields  $\mathbf{A}$  and  $\mathbf{B}$  it is known that

$$\nabla(\mathbf{A} \cdot \mathbf{B}) = (\mathbf{A} \cdot \nabla)\mathbf{B} + (\mathbf{B} \cdot \nabla)\mathbf{A} + \mathbf{A} \times (\nabla \times \mathbf{B}) + \mathbf{B} \times (\nabla \times \mathbf{A}).$$

Applying this identity yields

$$\nabla\omega = (\mathbf{k} \cdot \nabla)\boldsymbol{\omega} + (\boldsymbol{\omega} \cdot \nabla)\mathbf{k} + \mathbf{k} \times (\nabla \times \boldsymbol{\omega}) + \boldsymbol{\omega} \times (\nabla \times \mathbf{k}).$$

Since  $\mathbf{k}$  is constant the second term  $(\boldsymbol{\omega} \cdot \nabla)\mathbf{k}$  and fourth term  $\boldsymbol{\omega} \times (\nabla \times \mathbf{k})$  are zero. Since  $\mathbf{k} \cdot \nabla = \partial/\partial z$  and  $\boldsymbol{\omega}$  is a function of  $x$  and  $y$  only the first term is also zero. Finally,  $\boldsymbol{\omega} = \nabla \times \mathbf{u}$ , so after substituting we can rewrite the remaining term as

$$\nabla\omega = \mathbf{k} \times (\nabla \times (\nabla \times \mathbf{u})) = \mathbf{k} \times (\nabla(\nabla \cdot \mathbf{u}) - \nabla^2\mathbf{u}),$$

Using the continuity equation  $\nabla \cdot \mathbf{u} = 0$  and eliminating the remaining velocity terms using the Stokes equations  $\nabla^2\mathbf{u} = \nabla p$  leaves

$$\nabla\omega = \mathbf{k} \times -\nabla p.$$

This equation represents a vector form of the Cauchy–Riemann equations (4.2.11) in  $p$  and  $-\omega$ .

### 4.2.5 The Airy Stress Function

Combining the Wirtinger derivatives (4.2.5) and (4.2.6) we find that

$$\begin{aligned}\frac{\partial}{\partial z} &= \frac{1}{2} \left( \frac{\partial}{\partial x} - i \frac{\partial}{\partial y} \right), \\ \frac{\partial}{\partial \bar{z}} &= \frac{1}{2} \left( \frac{\partial}{\partial x} + i \frac{\partial}{\partial y} \right).\end{aligned}$$

It is easily verified that, using these derivatives, the Cauchy–Riemann equations (4.2.11) may be written in the complex form

$$\frac{\partial f}{\partial \bar{z}} = 0. \quad (4.2.15)$$

The standard Cauchy–Riemann equations may be recovered by taking the real and imaginary parts of this equation. Any analytic function is a solution to this equation and a similar result holds for higher-order derivatives as follows. A *bianalytic function* is defined (Balk and Zuev, 1970) to be the general solution to

$$\frac{\partial^2 F}{\partial \bar{z}^2} = 0. \quad (4.2.16)$$

By integrating twice with respect to  $\bar{z}$  we find that a bianalytic function can be written in the form  $F = \bar{z}f(z) + g(z)$ , where  $f(z)$  and  $g(z)$  are arbitrary analytic functions. Writing (4.2.16) in terms of the real co-ordinates  $x$  and  $y$  yields

$$\frac{\partial^2 F}{\partial \bar{z}^2} = \left( \frac{\partial^2}{\partial x^2} + 2i \frac{\partial^2}{\partial x \partial y} - \frac{\partial^2}{\partial y^2} \right) F = 0. \quad (4.2.17)$$

Since we may write  $F = A + iB$ , where  $A$  and  $B$  are real-valued functions, the real and imaginary parts of (4.2.17) yields the system of equations

$$\frac{\partial^2 A}{\partial x^2} - \frac{\partial^2 A}{\partial y^2} = 2 \frac{\partial B}{\partial x \partial y}, \quad (4.2.18a)$$

$$\frac{\partial^2 B}{\partial x^2} - \frac{\partial^2 B}{\partial y^2} = -2 \frac{\partial A}{\partial x \partial y}. \quad (4.2.18b)$$

Just as the real and imaginary parts of (4.2.15) formed the Cauchy–Riemann equations for *harmonic* functions, the real and imaginary parts of (4.2.16) represent generalised Cauchy–Riemann equations for *biharmonic* functions (Balk and Zuev, 1970; Cummings, Howison and King, 1999). While the real and imaginary parts of an analytic function are harmonic conjugates, the real and imaginary parts of a bianalytic function are known as *biharmonic conjugates*.

In the same way as the continuity equation  $\nabla \cdot \mathbf{u} = 0$  can be satisfied by introducing a stream function, the momentum equation  $\nabla \cdot \sigma = 0$  can be satisfied with a suitably defined potential. This may be demonstrated using the method given by Muskhelishvili (1975). The components of this equation are

$$\frac{\partial \sigma_{11}}{\partial x} + \frac{\partial \sigma_{12}}{\partial y} = 0, \quad (4.2.19)$$

$$\frac{\partial \sigma_{21}}{\partial x} + \frac{\partial \sigma_{22}}{\partial y} = 0. \quad (4.2.20)$$

The first of these is satisfied by introducing a function  $A$  such that

$$\sigma_{11} = -\frac{\partial A}{\partial y}, \quad \sigma_{12} = \frac{\partial A}{\partial x}.$$

Similarly, the second momentum equation is satisfied by introducing a function  $B$  such that

$$\sigma_{22} = -\frac{\partial B}{\partial x}, \quad \sigma_{21} = \frac{\partial B}{\partial y}.$$

By definition we know that  $\sigma_{12} = \sigma_{21}$ , which implies that

$$\frac{\partial A}{\partial x} - \frac{\partial B}{\partial y} = 0.$$

This condition may be satisfied by introducing another function  $\hat{A}$  such that

$$A = \frac{\partial \hat{A}}{\partial y}, \quad B = \frac{\partial \hat{A}}{\partial x}.$$

It is easily verified that the function  $\hat{\mathcal{A}}$  satisfies the momentum equations. This function is precisely an *Airy stress function*. Here, however, we instead extract a factor of 2 and define the Airy stress function  $\mathcal{A}$  such that

$$-2\frac{\partial^2 \mathcal{A}}{\partial y^2} = \sigma_{11}, \quad (4.2.21a)$$

$$-2\frac{\partial^2 \mathcal{A}}{\partial x^2} = \sigma_{22}, \quad (4.2.21b)$$

$$2\frac{\partial^2 \mathcal{A}}{\partial x \partial y} = \sigma_{12} = \sigma_{21}. \quad (4.2.21c)$$

This matches the definition given in (3.3.26) for the leading-order velocities. Subtracting (4.2.21b) from (4.2.21a) and dividing by 2 we find that

$$\begin{aligned} \frac{\partial^2 \mathcal{A}}{\partial x^2} - \frac{\partial^2 \mathcal{A}}{\partial y^2} &= \frac{1}{2}(\sigma_{11} - \sigma_{22}) \\ &= \frac{1}{2} \left( -p + 2\frac{\partial u}{\partial x} + p - 2\frac{\partial v}{\partial y} \right) \\ &= \frac{\partial^2 \psi}{\partial x \partial y} + \frac{\partial^2 \psi}{\partial y \partial x} \\ &= 2\frac{\partial^2 \psi}{\partial x \partial y}. \end{aligned}$$

In addition, multiplying (4.2.21c) by  $-1$  yields

$$\begin{aligned} -2\frac{\partial^2 \mathcal{A}}{\partial x \partial y} &= -\frac{\partial u}{\partial y} - \frac{\partial v}{\partial x} \\ &= \frac{\partial^2 \psi}{\partial x^2} - \frac{\partial^2 \psi}{\partial y^2}, \end{aligned}$$

By choosing this definition, the Airy stress function  $\mathcal{A}$  and the stream function  $\psi$  are solutions to the biharmonic Cauchy–Riemann equations (4.2.18) and hence are the real and imaginary parts of a bianalytic function. Thus, using the general form for a bianalytic function derived above we conclude that we can write

$$\mathcal{W} = \mathcal{A} + i\psi = \bar{z}f(z) + g(z), \quad (4.2.22)$$

where  $f$  and  $g$  are arbitrary analytic functions. This agrees precisely with the form for  $\psi$  given in (4.2.9). Finally, we note that using the continuity equation we can write

$$\begin{aligned}\nabla^2 \mathcal{A} &= \frac{1}{2} (-\sigma_{22} - \sigma_{11}) \\ &= \frac{1}{2} \left( p - 2 \frac{\partial v}{\partial y} + p - 2 \frac{\partial u}{\partial x} \right) \\ &= p.\end{aligned}$$

Thus, we see that

$$\begin{aligned}\nabla^2 \mathcal{W} &= \nabla^2 \mathcal{A} + i \nabla^2 \psi \\ &= p - i\omega \\ &= \mathcal{P}.\end{aligned}$$

Some care must be taken when using these results and, in particular, when comparing results from different authors. As was noted in Subsection 4.2.4, we could multiply  $\mathcal{P}$  and  $\mathcal{W}$  by powers of  $i$  to obtain an equivalent representation. Due to this freedom some studies present results derived with the real and imaginary parts of both  $\mathcal{W}$  and  $\mathcal{P}$  interchanged or with the opposite sign.

In addition, it may be observed that the definition in (4.2.21) includes a factor of 2 multiplying the stress function terms so that  $\mathcal{A}$  and  $\psi$  are biharmonic conjugates. Muskhelishvili (1975) instead defined the alternative stress function  $\hat{\mathcal{A}} = -2\mathcal{A}$ , which is used in the work of many authors writing on Stokes flows (Clarke, 1968; Richardson, 1968; King, 1989; Karageorghis and Phillips, 1989; Owens and Phillips, 1994; Cummings and Howell, 1999). Indeed, it has been suggested by Hopper (1990, p. 353) that this form gained popularity as it had been present in textbooks on elasticity such as those by Muskhelishvili (1975) and Sokolnikov (1956). In addition to removing the factor of 2, this

choice moves the negative signs from (4.2.21a) and (4.2.21b) to the mixed derivative in (4.2.21c). If this form is used then we must modify the definition of the bianalytic function accordingly. For instance, it may be deduced that Richardson (1968, pp. 476–477) uses the function

$$\widehat{\mathcal{W}} = \psi + i\hat{\mathcal{A}}/2 = \psi - i\mathcal{A} = -i\mathcal{W}.$$

Other authors use the stress function  $2\mathcal{A}$  and define the stream function  $\tilde{\psi} = -\psi$  (Coleman, 1981); however, this form for the stream function is not generally used within fluid mechanics. It would also be possible to define the stream function  $\hat{\psi} = \psi/2$ , which is a biharmonic conjugate of  $\hat{\mathcal{A}}$ .

The definition given in (4.2.21) matches the dimensional form used by Cummings *et al.* (1999), although the authors ultimately employ the bianalytic function  $-\mathcal{W}$ . The definition (4.2.21) given above is also used by Tanveer and Vasconcelos (1995), which, using the present notation and written in dimensionless form, gives  $\nabla^2\mathcal{A} = p$ , whereas the alternative definition would yield  $\nabla^2\hat{\mathcal{A}} = 2p$ . This formulation has also been used extensively by Crowdy (Crowdy and Tanveer, 1998; Crowdy, 1999, 2002*a*, 2003*a*, 2004; Crowdy *et al.*, 2005; Crowdy and Or, 2010).

Any of these choices lead to equivalent representations, provided they are used consistently. In this thesis we use the form given in (4.2.21) as it best matches the theory of bianalytic functions and the conventions established in fluid mechanics.

At this point it is worth summarising the key results established thus far:

- by introducing a stream function  $\psi$  the Stokes equations may be reduced to the biharmonic equation  $\nabla^4\psi = 0$ ;
- the stream function is the biharmonic conjugate of the Airy stress function

$\mathcal{A}$ . The function  $\mathcal{W} = \mathcal{A} + i\psi$  is a bianalytic function;

- using the Goursat representation we can write  $\mathcal{W} = \bar{z}f(z) + g(z)$  where  $f(z)$  and  $g(z)$  are analytic functions;
- the pressure  $p$  and the vorticity component  $-\omega$  are harmonic conjugates, so  $\mathcal{P} = p - i\omega$  is an analytic function; and
- the functions  $\mathcal{P}$  and  $\mathcal{W}$  are related by  $\nabla^2\mathcal{W} = \mathcal{P}$ .

#### 4.2.6 The Goursat Functions and Physical Quantities

In the previous subsections it was shown that solutions to the Stokes equations may be represented using the Goursat functions  $f(z)$  and  $g(z)$ . These functions are chosen so that they satisfy the prescribed boundary conditions, which, in general, will be written in terms of physical quantities such as the velocity, pressure and stress. Thus, in order to rewrite these conditions in terms of the Goursat functions we here derive relationships between the Goursat functions and the physical quantities of interest connected to Stokes flows.

It is convenient to write the two velocity components as the complex velocity  $u + iv$ . We then note that this may be expressed as

$$u + iv = \frac{\partial\psi}{\partial y} - i\frac{\partial\psi}{\partial x},$$

which implies that

$$(u + iv) = -i \left( \frac{\partial\psi}{\partial x} + i\frac{\partial\psi}{\partial y} \right) = -2i\frac{\partial\psi}{\partial\bar{z}}.$$

The operator  $2\partial/\partial\bar{z}$  is a complex representation of the two-dimensional gradient, which can be seen directly by substituting the derivatives from (4.2.5) and

(4.2.6). Using the Goursat representation we can write

$$\begin{aligned}\psi &= \Im(\bar{z}f(z) + g(z)) \\ &= \frac{1}{2i}(\bar{z}f(z) + g(z) - z\overline{f'(z)} - \overline{g'(z)}),\end{aligned}$$

Using this expression we find that

$$2\frac{\partial\psi}{\partial\bar{z}} = -i(f(z) - z\overline{f'(z)} - \overline{g'(z)}),$$

and hence the complex velocity is given by

$$u + iv = -f(z) + z\overline{f'(z)} + \overline{g'(z)}.$$

We can also find expressions for the pressure and vorticity. Taking the Laplacian of  $\mathcal{W}$  and again using the Goursat representation yields

$$\begin{aligned}\nabla^2\mathcal{W} &= \nabla^2\mathcal{A} + i\nabla^2\psi \\ &= p - i\omega \\ &= 4\frac{\partial^2}{\partial z\partial\bar{z}}(\bar{z}f(z) + g(z)) \\ &= 4f'(z).\end{aligned}$$

The real and imaginary parts of this expression are then, respectively,

$$\begin{aligned}p &= 4\Re(f'(z)), \\ \omega &= -4\Im(f'(z)).\end{aligned}$$

Finally, we derive expressions for the rates of strain  $e_{ij}$ . For an incompressible fluid flow we have that

$$e_{11} = \frac{\partial u}{\partial x} = -\frac{\partial v}{\partial y} = -e_{22}.$$

In addition,  $e_{12} = e_{21}$  by definition. Thus, we need only determine  $e_{11}$  and  $e_{12}$  to know all the rates of strain. We determine the complex quantity  $e_{11} + ie_{12}$ , which is given by

$$\begin{aligned}
e_{11} + ie_{12} &= \frac{\partial u}{\partial x} + \frac{i}{2} \left( \frac{\partial u}{\partial y} + \frac{\partial v}{\partial x} \right) \\
&= \frac{\partial^2 \psi}{\partial x \partial y} + \frac{i}{2} \left( \frac{\partial^2 \psi}{\partial y^2} - \frac{\partial^2 \psi}{\partial x^2} \right) \\
&= -\frac{i}{2} \left( \frac{\partial^2 \psi}{\partial x^2} + 2i \frac{\partial^2 \psi}{\partial x \partial y} - \frac{\partial^2 \psi}{\partial y^2} \right) \\
&= -\frac{4i}{2} \frac{\partial^2 \psi}{\partial \bar{z}^2} \\
&= \frac{-2i}{2i} \frac{\partial^2}{\partial \bar{z}^2} [\bar{z}f(z) + g(z) - z\bar{f}(\bar{z}) - \bar{g}(\bar{z})] \\
&= z\overline{f''(z)} + \overline{g''(z)}.
\end{aligned}$$

We have thus established that

$$u + iv = -f(z) + z\overline{f'(z)} + \overline{g'(z)}, \quad (4.2.23a)$$

$$p - i\omega = 4f'(z), \quad (4.2.23b)$$

$$e_{11} + ie_{12} = z\overline{f''(z)} + \overline{g''(z)}. \quad (4.2.23c)$$

### 4.2.7 Dynamic Boundary Condition

We here reformulate the dynamic boundary condition (3.3.42d) and (3.3.42e) using the complex representation described above. In terms of the rates of strain, these expressions become

$$-pn_1 + 2e_{11}n_1 + 2e_{12}n_2 = -\kappa n_1, \quad (4.2.24a)$$

$$-pn_2 + 2e_{21}n_1 + 2e_{22}n_2 = -\kappa n_2. \quad (4.2.24b)$$

It is possible to combine these two real equations into a single complex equation. Multiplying (4.2.24b) by  $i$  and adding this to (4.2.24a) yields

$$-p(n_1 + in_2) + 2(e_{11}n_1 + e_{12}n_2 + ie_{21}n_1 + ie_{22}n_2) = -\kappa(n_1 + in_2).$$

As established in the previous subsection,  $e_{11} = -e_{22}$  and  $e_{12} = e_{21}$ , and hence we find that

$$\begin{aligned} e_{11}n_1 + e_{12}n_2 + ie_{21}n_1 + ie_{22}n_2 &= e_{11}n_1 + e_{12}n_2 + ie_{12}n_1 - ie_{11}n_2 \\ &= (e_{11} + ie_{12})(n_1 - in_2) \\ &= (e_{11} + ie_{12})\bar{n}, \end{aligned}$$

where we have defined the complex normal  $n = n_1 + in_2$ . Thus, the dynamic boundary condition can be written in the complex form

$$-pn + 2(e_{11} + ie_{12})\bar{n} = -\kappa n.$$

Using (4.2.23c) and the real part of (4.2.23c) from the previous subsection we can write this condition in terms of the Goursat functions, which yields

$$-\left(f'(z) + \overline{f'(z)}\right)n + \left(z\overline{f''(z)} + \overline{g''(z)}\right)\bar{n} = -\frac{\kappa n}{2}. \quad (4.2.25)$$

As noted by Tanveer and Vasconcelos (1995, p. 329), this can be simplified further by introducing the function

$$J(z, \bar{z}) = f(z) + z\overline{f'(z)} + \overline{g'(z)}.$$

The partial derivatives of this function are

$$\begin{aligned} \frac{\partial J}{\partial z} &= f'(z) + \overline{f'(z)}, \\ \frac{\partial J}{\partial \bar{z}} &= z\overline{f''(z)} + \overline{g''(z)}, \end{aligned}$$

which are precisely the combinations of Goursat functions that arise in (4.2.25). Given a boundary  $C_n$  we define  $z(s) = x(s) + iy(s)$  to be the parameterisation of the boundary with respect to arc length  $s$  with the standard orientation (Tanveer and Vasconcelos use a clockwise orientation, which gives the opposite direction). Then, we can write

$$n = -i \frac{dz}{ds} = -ie^{i\theta(s)}$$

where  $\theta(s)$  is the angle between the tangent at the point  $z(s)$  and the positive real axis and, by definition,  $\theta(s)$  is related to the curvature  $\kappa$  by

$$\kappa = \frac{d\theta}{ds}.$$

Substituting these quantities into (4.2.25) we find that the boundary condition reduces to

$$\frac{\partial J}{\partial z} \frac{dz}{ds} + \frac{\partial J}{\partial \bar{z}} \frac{d\bar{z}}{ds} = \frac{1}{2} \frac{d\theta}{ds} \frac{dz}{ds}.$$

Finally, we note that

$$\frac{d^2 z}{ds^2} = \frac{d}{ds} \frac{dz}{ds} = \frac{d}{d\theta} \frac{dz}{ds} \frac{d\theta}{ds} = ie^{i\theta} \frac{d\theta}{ds} = i \frac{dz}{ds} \frac{d\theta}{ds}. \quad (4.2.26)$$

Using this result the boundary condition may be written as

$$\frac{\partial J}{\partial z} \frac{dz}{ds} + \frac{\partial J}{\partial \bar{z}} \frac{d\bar{z}}{ds} = -\frac{i}{2} \frac{d^2 z}{ds^2}.$$

The left-hand side of this equation is just the total derivative of  $J$  with respect to arc length  $s$ . Thus, by integrating this equation over the boundary we arrive at the dynamic boundary condition

$$f(z) + z \overline{f'(z)} + \overline{g'(z)} = -\frac{i}{2} z_s + A_n, \quad (4.2.27)$$

where  $z_s$  is the derivative of  $z$  with respect to  $s$ . As Stokes flows are instantaneous, the  $A_n$  may be considered constants of integration associated with

boundary  $C_n$ ; however, as both  $f$  and  $g$  are strictly functions of reduced time so too are the  $A_n$ .

This condition has also been derived by Krakowski and Charnes (1953), Richardson (1968) and Hopper (1990) using the results given by Muskhelishvili (1975, pp. 114–115). Accounting for the factor of 2 in the definition of the Airy stress function, the Kolosov–Muskhelishvili traction equation states that

$$f(z) + z\overline{f'(z)} + \overline{g'(z)} = \frac{i}{2} \int (T_x(s) + T_y(s)) ds + A_n,$$

where  $(T_x(s), T_y(s))$  is the traction at a point  $z(s)$  on the boundary and  $A_n$  is an arbitrary constant of integration. In the current problem, the traction due to surface tension is given in complex form by  $-i\kappa z_s = -i\kappa e^{i\theta(s)}$ . Recalling that  $\kappa = \theta_s$  and using (4.2.26), the traction equation integral is given by

$$\int -i\kappa e^{i\theta(s)} ds = - \int z_{ss} ds = -z_s.$$

Substituting this into the traction equation we recover the complex dynamic boundary condition (4.2.27).

Importantly, (4.2.27) expresses the dynamic boundary condition using only the complex representation of the unit tangent vector  $z_s$  and the Goursat functions. This reduces the problem of determining appropriate stresses and velocities to simply choosing two analytic functions  $f$  and  $g$  that satisfy this expression.

The dynamic boundary condition can also be expressed in terms of the Airy stress function as follows. The outward-pointing complex unit normal is  $n = -i(x'(s) + iy'(s)) = y'(s) - ix'(s)$ , which corresponds to the real vector  $(y'(s), -x'(s))$ . We can then write the first component of the dynamic boundary condition (4.2.24a) as

$$-\kappa y' = \sigma_{11}y' - \sigma_{12}x' = -2\frac{\partial^2 \mathcal{A}}{\partial y^2} \frac{\partial y}{\partial s} - 2\frac{\partial^2 \mathcal{A}}{\partial x \partial y} \frac{\partial x}{\partial s} = -2\frac{\partial \mathcal{A}_y}{\partial s}.$$

Similarly, the second component (4.2.24b) is

$$\kappa x' = \sigma_{21}y' - \sigma_{22}x' = 2\frac{\partial^2 \mathcal{A}}{\partial x \partial y} \frac{\partial y}{\partial s} + 2\frac{\partial^2 \mathcal{A}}{\partial x^2} \frac{\partial x}{\partial s} = 2\frac{\partial \mathcal{A}_x}{\partial s}.$$

These two expressions yield

$$\frac{\partial \mathcal{A}_x}{\partial s} = \frac{1}{2}\kappa x', \quad (4.2.28a)$$

$$\frac{\partial \mathcal{A}_y}{\partial s} = \frac{1}{2}\kappa y'. \quad (4.2.28b)$$

From (4.2.26), we have that  $z_{ss} = iz_s\theta_s$ . Since  $\theta_s = \kappa$ , we can write

$$x'' + iy'' = i\kappa(x' + iy') = \kappa(-y' + ix');$$

that is,

$$x'' = -\kappa y',$$

$$y'' = \kappa x'.$$

This is equivalent to the first Frenet–Serret formula (Kreyszig, 2005), which states that  $\mathbf{t}' = -\kappa\mathbf{n}$  for an *outward*-pointing normal (typically this is presented for an *inwards*-pointing normal). With these relationships we can write (4.2.28) as

$$\begin{aligned} \frac{\partial \mathcal{A}_x}{\partial s} &= \frac{y''}{2}, \\ \frac{\partial \mathcal{A}_y}{\partial s} &= -\frac{x''}{2}, \end{aligned}$$

which may be integrated with respect to arc length to give

$$\begin{aligned} \mathcal{A}_x &= \frac{y'}{2} + a_{n,1}, \\ \mathcal{A}_y &= -\frac{x'}{2} + a_{n,2}, \end{aligned}$$

where  $a_{n,1}$  and  $a_{n,2}$  are constants of integration corresponding to the  $n$ th boundary. Recalling that  $\mathbf{n} = (y', -x')$  is the unit normal, this expression may be written in the vector form

$$\nabla\mathcal{A} = \frac{1}{2}\mathbf{n} + \mathbf{a}_n, \quad (4.2.29)$$

where  $\mathbf{a}_n = (a_{n,1}, a_{n,2})$ . Finally, taking the dot product with  $\mathbf{n}$  yields

$$\frac{\partial\mathcal{A}}{\partial\mathbf{n}} = \frac{1}{2} + \mathbf{a}_n \cdot \mathbf{n}. \quad (4.2.30)$$

For a connected domain, which only has one boundary, we can use the freedom in the definition of  $\mathcal{A}$  to set  $\mathbf{a}_n = \mathbf{0}$ ; however, for multiply connected regions we can do this on at most one boundary. Note that this is precisely (3.3.29) with  $\gamma^* = 1$ . This expression can also be derived in a more direct manner by making use of the Goursat representation  $\mathcal{A} + i\psi = \bar{z}f + g$ . Taking the real part of this equation and differentiating with respect to  $\bar{z}$  shows that

$$2\frac{\partial\mathcal{A}}{\partial\bar{z}} = f + z\bar{f}' + \bar{g}'.$$

Substituting this for the left-hand side of (4.2.27) yields

$$\nabla\mathcal{A} = -\frac{i}{2}z_s + A_n.$$

Since  $-iz_s = n$  is the complex normal vector, and using  $\nabla\mathcal{A} = 2\mathcal{A}_{\bar{z}}$ , this condition reduces to

$$2\frac{\partial\mathcal{A}}{\partial\bar{z}} = \frac{1}{2}n + A_n,$$

which is simply the complex version of the vector expression found in (4.2.29).

Equating terms, we find that the constant vectors  $\mathbf{a}_n = (a_{n,1}, a_{n,2})$  are related to the complex constants  $A_n$  from (4.2.27) by

$$A_n = a_{n,1} + ia_{n,2}.$$

### 4.2.8 Kinematic Boundary Condition

The kinematic boundary condition states that the normal velocity of the boundary is equal to the normal velocity of the fluid along the boundary. If we denote the velocity of a point on the boundary by  $\mathbf{V}$ , this condition may be written as

$$\mathbf{V} \cdot \mathbf{n} = \mathbf{u} \cdot \mathbf{n}. \quad (4.2.31)$$

As was done for the dynamic boundary condition, we can rewrite the kinematic boundary condition in terms of the Goursat functions. In order to do so, we first need an expression for the dot product for complex representations of vectors. If  $\mathbf{a} = (a_1, a_2)$  and  $\mathbf{b} = (b_1, b_2)$  and we introduce the corresponding complex numbers  $a = a_1 + ia_2$  and  $b = b_1 + ib_2$ , then we observe that

$$a\bar{b} = (a_1 + ia_2)(b_1 - ib_2) = a_1b_1 - ia_1b_2 + ia_2b_1 + a_2b_2.$$

Thus, it is clear that

$$\mathbf{a} \cdot \mathbf{b} = \Re(a\bar{b}).$$

With this formulation, we can write (4.2.31) in the complex form

$$\Re\left(\frac{dz}{d\tau}i\bar{z}_s\right) = \Re([u + iv]i\bar{z}_s),$$

where  $dz/dt$  is the velocity of the boundary. Using (4.2.23a) we can substitute for the fluid velocity, which gives

$$\Re\left(\frac{dz}{d\tau}i\bar{z}_s\right) = \Re\left(\left[-f(z) + z\overline{f'(z)} + \overline{g'(z)}\right]i\bar{z}_s\right).$$

Finally, using the dynamic boundary condition (4.2.27) we find that along the  $n$ th boundary we have

$$u + iv = -f(z) + z\overline{f'(z)} + \overline{g'(z)} = -2f(z) - \frac{i}{2}z_s + A_n.$$

Substituting this into the condition above yields

$$\Re \left( \frac{dz}{d\tau} i\bar{z}_s \right) = \Re \left( \left[ -2f(z) - \frac{i}{2}z_s + A_n \right] i\bar{z}_s \right). \quad (4.2.32)$$

Using the definition of the stream function Eq. (4.2.2) we find that

$$(u, v) \cdot (n_1, n_2) = \left( \frac{\partial\psi}{\partial y}, -\frac{\partial\psi}{\partial x} \right) \cdot \left( \frac{\partial y}{\partial s}, -\frac{\partial x}{\partial s} \right) = \frac{\partial\psi}{\partial y} \frac{\partial y}{\partial s} + \frac{\partial\psi}{\partial x} \frac{\partial x}{\partial s} = \frac{\partial\psi}{\partial s}.$$

Thus, the kinematic boundary condition may also be expressed as

$$\frac{\partial\psi}{\partial s} = V_n,$$

where  $V_n = \mathbf{V} \cdot \mathbf{n}$ .

### 4.2.9 Uniqueness of the Goursat Representation

We must give some consideration to the uniqueness of the Goursat representation for the free-boundary Stokes flow problem. There are two sources of ambiguity in the representation of the solution: the Goursat representation and zero-surface-tension eigensolutions.

First, following Langlois (1964), suppose that we replace the Goursat functions  $f$  and  $g$  by the new functions  $f + az + b$  and  $g + \bar{b}z + c$ , respectively, where  $a$  is a real constant and both  $b$  and  $c$  are complex. Substituting these into the expression for the stream function (4.2.9) yields the transformed stream function

$$\hat{\psi} = \psi + \Im(c).$$

That is, these transformations result only in the addition of the constant  $\Im(c)$  to the stream function, which leaves the streamlines and velocity unchanged. Thus, in general, the Goursat representation for Stokes flows is only unique

up to the given transformations. We note, however, that this transformation results in the modified pressure  $p + a$ .

For the transverse problem under consideration here the Goursat functions are set by the dynamic boundary condition (4.2.27). In this problem any solution that satisfies the dynamic boundary condition is unique only up to the addition of a zero-surface-tension eigensolution; that is, a solution to the governing equations in the absence of surface tension (see, for example, Cummings and Howell (1999)). Such a solution corresponds to a translation and rotation of the entire domain, represented by the Goursat functions  $f(z) = T + iRz$  and  $g(z) = -\bar{T}z$ , for some complex constant  $T$  and real constant  $R$ . Direct substitution shows that these satisfy the dynamic boundary condition but give rise to the complex velocity  $-2T - 2iRz$ ; thus,  $T$  corresponds to a translation and  $R$  a rotation. This means that the solution is unique to within an arbitrary translation and rotation.

Suppose that  $f$  and  $g$  are Goursat functions that satisfy the dynamic boundary condition on boundary  $C_n$ . Combining both transformations discussed above, we introduce the transformed Goursat functions

$$\begin{aligned}\tilde{f}(z) &= f + az + b + T + iRz, \\ \tilde{g}(z) &= g + \bar{b}z + c - \bar{T}z.\end{aligned}$$

We also introduce the transformed constants  $\tilde{A}_n = A_n + \hat{A}_n$ . Substituting these into the dynamic boundary condition yields

$$2az + 2b = \hat{A}_n.$$

Equating coefficients we find that  $\hat{A}_n = 2b$  and  $a = 0$ . The latter equation shows that the constant  $a$  is set to zero by the dynamic boundary condition.

Combining the remaining transformations and introducing  $K_1 = b + T$  and  $K_2 = \overline{b - T}$ , we find that if  $f$ ,  $g$  and  $A_n$  satisfy the dynamic boundary condition then so do the transformed quantities

$$\tilde{f}(z) = f(z) + iRz + K_1, \quad (4.2.33a)$$

$$\tilde{g}(z) = g(z) + K_2z + c, \quad (4.2.33b)$$

$$\tilde{A}_n = A_n + 2b. \quad (4.2.33c)$$

We note that  $2b = K_1 + \overline{K_2}$ , which is set by the choice of  $K_1$  and  $K_2$ . Thus, there are seven degrees of freedom arising from  $R$  and the real and imaginary parts of  $K_1$ ,  $K_2$  and  $c$ . In practice, however, the physical quantities of interest (4.2.23) involve only derivatives of  $g$  and so  $c$  does not enter the problem, leaving five degrees of freedom. Each of these must be set as part of the solution method and will be addressed further in Section 5.2.

#### 4.2.10 Geometric Quantities

Throughout this thesis it will be useful to have expressions for the boundary length and area of a given domain  $\Omega$  with boundary  $C = C_0 + C_1 + \dots + C_N$ , which is given by

$$\Gamma = \int_C ds. \quad (4.2.34)$$

To calculate the area  $S$  we make use of the complex form of Green's theorem, which states that a function  $f$  that is continuously differentiable on  $\Omega$  satisfies

$$\oint_C f dz = i \int_{\Omega} \left( \frac{\partial f}{\partial x} + i \frac{\partial f}{\partial y} \right) dA.$$

If we take  $f = \bar{z}$  the right-hand side is  $2iS$ , so that

$$S = \frac{1}{2i} \int_C \bar{z} dz. \quad (4.2.35)$$

## 4.3 Exact Solutions

In this section we present three exact solutions to the transverse problem that will be used in later chapters. A solution for an annulus is derived similar to the method employed by Stokes *et al.* (2014). The remaining solutions are those found by Hopper (1990) for an epicycloid and two touching disks.

### 4.3.1 An Annulus

In the case of an annular fluid region it is possible to derive an exact solution to the two-dimensional Stokes flow problem. An *implicit* solution to this problem for a region with inner radius 0.5 and unit outer radius has been given by van de Vorst (1993), while an *explicit* solution for unit area has been found by Stokes *et al.* (2014). So as to compare with the solution of van de Vorst (1993) we here generalise the explicit solution of Stokes *et al.* (2014) to non-unit area. Solutions to the transverse problem, which requires unit area, are easily recovered by setting the area in the general solution to one. The full derivation is provided for completeness.

Because of the rotational symmetry of this geometry it is convenient to use polar co-ordinates  $(r, \theta)$  where  $r$  and  $\theta$  are the radial and azimuthal co-ordinates, respectively. We denote the outer radius  $R(\tau)$  and the ratio of the inner radius to the outer radius  $\phi(\tau)$ , so that the inner radius is  $\phi(\tau)R(\tau)$ . The area of the domain is thus  $\pi R^2(1 - \phi^2) = A$ , from which we find that

$$R(\tau) = \sqrt{\frac{A}{\pi(1 - \phi^2)}}. \quad (4.3.36)$$

In axisymmetric polar co-ordinates, the Stokes equations are

$$\frac{1}{r} \frac{\partial}{\partial r} (rv) = 0, \quad (4.3.37)$$

$$\frac{\partial p}{\partial r} + \frac{1}{r} \frac{\partial}{\partial r} \left( r \frac{\partial v}{\partial r} \right) - \frac{v}{r^2} = 0, \quad (4.3.38)$$

where  $v(r)$  is the radial velocity and  $p(r)$  is the pressure. The dynamic and kinematic boundary condition are, respectively,

$$-p + 2 \frac{\partial v}{\partial r} = -\kappa, \quad (4.3.39)$$

$$\frac{\partial G}{\partial \tau} + v = 0, \quad (4.3.40)$$

which apply on the boundary  $G = 0$ ; for an annulus the boundary comprises the curves  $r = R(\tau)$  and  $r = \phi(\tau)R(\tau)$ . Integrating (4.3.37) yields

$$v(\tau) = \frac{C_1}{r},$$

where  $C_1$  is a constant of integration. Substituting this into (4.3.38) and integrating yields

$$p = C_2,$$

where  $C_2$  is a constant of integration. On  $r = R$  the curvature is  $\kappa = 1/R$ , while on  $r = \phi R$  we have  $\kappa = -1/(\phi R)$ . Substituting for  $v, p$  and  $\kappa$  in the dynamic boundary condition (4.3.39) yields

$$\begin{aligned} \frac{2}{R^2} C_1 + C_2 &= \frac{1}{R}, \\ \frac{2}{\phi^2 R^2} C_1 + C_2 &= -\frac{1}{\phi R}, \end{aligned}$$

which is a linear system of equations for  $C_1$  and  $C_2$ . Solving, we find that

$$\begin{aligned} C_1 &= -\frac{\phi R}{2(1-\phi)}, \\ C_2 &= \frac{1}{R(1-\phi)}. \end{aligned}$$

Substituting these solutions into the kinematic condition (4.3.40), summing and integrating shows that

$$R(1 - \phi) = \frac{\tau}{2} + \alpha_0 = \alpha(\tau),$$

where  $\alpha_0$  is a constant of integration and we have introduced the function  $\alpha(\tau)$  that represents the difference in the radii at reduced time  $\tau$  such that  $\alpha(0) = \alpha_0$ . Using (4.3.36) to substitute for  $R$  we find that

$$R(1 - \phi) = \sqrt{\frac{A(1 - \phi)}{\pi(1 + \phi)}},$$

from which we deduce that

$$\phi(\tau) = \frac{A - \pi\alpha^2}{A + \pi\alpha^2}. \quad (4.3.41)$$

The evolution of any annular region can be computed as follows. The initial geometry can be described by some combination of the initial values of the outer radius  $R(0)$ , the ratio  $\phi(0)$ , the radius  $R_i(0) = \phi(0)R(0)$  and the area  $A$ . These are related by

$$\begin{aligned} \frac{R_i}{R} &= \phi, \\ \pi R^2(1 - \phi^2) &= A. \end{aligned}$$

Since the four parameters are related by two equations, knowledge of any two values determines the remaining two. Since the transverse problem (3.3.42) is scaled to have unit area we will typically set  $A = 1$  and specify  $\phi(0)$ . For a given domain we then calculate

$$\alpha_0 = \sqrt{\frac{A(1 - \phi_0)}{\pi(1 + \phi_0)}}.$$

From this we can determine  $\alpha(\tau)$  at any  $\tau$  and hence also, using (4.3.41),  $\phi(\tau)$ . We can then compute  $R(\tau)$  using

$$R(\tau) = \frac{\alpha(\tau)}{1 - \phi(\tau)} = \frac{\tau/2 + \alpha_0}{1 - \phi(\tau)},$$

and hence also the inner radius. Regardless of the geometry both radii will decrease until the inner hole closes at some reduced time  $\tau_f$ . This is equivalent to  $\phi = 0$ , which, from (4.3.41), can be shown to occur when

$$\alpha = \sqrt{\frac{A}{\pi}}.$$

Setting  $\alpha(\tau_f) = \sqrt{A/\pi}$  and solving for  $\tau_f$  shows that the inner hole closes at reduced time

$$\tau_f = 2 \left( \sqrt{\frac{A}{\pi}} - \alpha_0 \right).$$

Beyond  $\tau_f$  the model is no longer valid. Physically, once the inner hole closes the outer radius will cease moving and remain fixed at  $R(\tau_f)$ . For an annulus with  $\phi(0) = 0.5$  and  $R(0) = 1$ , the inner hole closes at  $\tau_f = \sqrt{3} - 1 \approx 0.73205$ , which agrees precisely with the value given by van de Vorst (1993, p. 676).

For completeness, we also show how to express this solution using the Goursat function representation derived in the previous section. It is simple to show that the vorticity  $\omega$  is zero so that  $4f'(z) = p - i\omega = C_2$ . We thus find that

$$f(z) = \frac{C_2 z}{4},$$

where we have set an arbitrary constant of integration to zero. Letting  $\mathbf{e}_r$  be the radial unit vector, the velocity may be written

$$\frac{C_1}{r} \mathbf{e}_r = \frac{C_1}{r} (\cos(\theta)\mathbf{i} + \sin(\theta)\mathbf{j}),$$

where  $\mathbf{i}$  and  $\mathbf{j}$  are the standard Cartesian co-ordinate vectors. Since  $r = \sqrt{x^2 + y^2} = |z|$ ,  $\cos(\theta) + i \sin(\theta) = z/|z|$ , and  $|z| = \sqrt{z\bar{z}}$ , we can write this as the complex velocity

$$u + iv = \frac{C_1}{|z|} \frac{z}{|z|} = \frac{C_1}{\bar{z}}.$$

Finally, using the expression for the complex velocity from (4.2.23a), we find that

$$u + iv = \frac{C_1}{\bar{z}} = -f(z) + z\overline{f'(z)} + \overline{g'(z)},$$

which, upon simplification, yields

$$g'(z) = \frac{C_1}{z}.$$

Integrating and setting an arbitrary constant of integration to zero shows that

$$g(z) = C_1 \log(z).$$

We also note that in axisymmetric polar co-ordinates the stream function is given by

$$\frac{\partial \psi}{\partial \theta} = rv,$$

which, upon setting the constant of integration to zero, implies that

$$\psi = C_1 \theta.$$

Using that both  $C_1$  and  $C_2$  are real, this agrees precisely with the Goursat representation for the stream function given by

$$\begin{aligned} \psi &= \Im(\bar{z}f + g) \\ &= \frac{1}{2i} \left( \frac{C_2 z \bar{z}}{4} + C_1 \log(z) - \frac{C_2 z \bar{z}}{4} - C_1 \overline{\log(z)} \right) \\ &= \frac{C_1}{2i} \left( \log(z) - \overline{\log(z)} \right) \\ &= C_1 \arg z \\ &= C_1 \theta. \end{aligned}$$

### 4.3.2 Hopper's Exact Solutions

Hopper (1990) found that the evolution of an epicycloid and two touching disks may be described by a time-dependent parameter  $\lambda$  and a map  $z(\zeta)$  from the unit disk in the  $\zeta$ -plane. The evolution of  $\lambda$  is described by an ODE, which is readily solved by a suitable numerical method. While Hopper (1990) presented the solutions to have area  $\pi$ , we rescale them to have unit area and write them using reduced time so as to match the transverse problem. Both solutions are expressed in terms of the complete elliptic integral of the first kind,

$$K(k) = \int_0^\pi \frac{1}{\sqrt{1 - k^2 \sin^2 \phi}} d\phi.$$

Using this function, an epicycloid with  $N$  cusps is described by the differential equation and map

$$\begin{aligned} \frac{d\lambda}{d\tau} &= -\frac{\lambda}{\pi} \left( \frac{1 + \frac{\lambda^{2N}}{N+1}}{1 - \frac{\lambda^{2N}}{N+1}} \right) \left( 1 + \frac{\lambda^{2N}}{N+1} \right)^{\frac{1}{2}} K(\lambda^N), \\ z(\zeta) &= \frac{1}{\sqrt{\pi}} \left( 1 + \frac{\lambda^{2N}}{N+1} \right)^{-\frac{1}{2}} \left( \zeta - \frac{\lambda^N}{N+1} \zeta^{N+1} \right). \end{aligned}$$

Similarly, two touching disks are described by the differential equation and map

$$\begin{aligned} \frac{d\lambda}{d\tau} &= -\frac{\lambda}{\pi} (1 + \lambda^4)^{\frac{1}{2}} K(\lambda^2), \\ z(\zeta) &= \frac{1 - \lambda^4}{\sqrt{\pi} (1 + \lambda^4)^{\frac{1}{2}}} \frac{\zeta}{1 + (\lambda\zeta)^2}. \end{aligned}$$

## 4.4 Summary

In this chapter we have reviewed the use of complex variables to represent solutions to the transverse problem (3.3.42), which is a two-dimensional Stokes

---

flow driven by unit surface tension. This approach describes all of the physical quantities of interest using two complex-differentiable functions, known as Goursat functions, that depend only on the instantaneous boundary conditions. Such a representation exists regardless of the connectivity of the domain. Crucially, this formulation reduces the transverse problem from a system of PDEs to the simpler problem of determining analytic functions that satisfy the boundary conditions, decreasing the number of spatial dimensions from two down to one. This efficiency is evident in the exact solutions presented in this chapter, which will be used throughout this thesis. Together, the Goursat representation and reduction in spatial dimensions also form the basis for efficient numerical methods for solving the transverse problem on general geometries, which are discussed in Chapter 5.



# Chapter 5

## Numerical Solution of Stokes Flows in Two Dimensions

### 5.1 Introduction

It was shown in Chapter 3 that, after transforming to reduced time, the transverse problem for a slender stretching fluid cylinder is precisely the two-dimensional Stokes equations with unit surface tension (3.3.42). Motivated by this, Chapter 4 reviewed the use of complex variables to represent the solutions of such problems, where it was shown that this formulation reduces the transverse problem from a system of coupled PDEs down to the problem of finding complex analytic functions that satisfy the boundary conditions. In doing this we replace a two-dimensional problem over the whole domain to a one-dimensional problem on the boundaries.

While exact solutions exist on particular geometries, in general the solution must be found using a numerical method. Thus, the aim of this chapter is to use the complex-variable formulation of the transverse problem to develop

efficient numerical solution methods. These methods must apply to multiply connected domains with a variety of boundary shapes.

There exists a significant body of literature regarding the solution of two-dimensional Stokes flows. Some studies have investigated solving the biharmonic equation on rectangular grids using finite difference schemes (Greenspan and Schultz, 1972; Ehrlich and Gupta, 1975). Typically these decompose the biharmonic equation  $\nabla^4\psi$  into the coupled system  $\nabla^2\mathbf{u} = -\omega$  and  $\nabla^2\omega = 0$  for the velocity  $\mathbf{u}$  and vorticity  $\omega$ . This formulation has also been used in finite element studies, such as that by Glowinski and Pironneau (1979), which formulated the problem for solution on multiply connected domains. Studies involving finite elements have also used a vorticity-velocity-pressure formulation (Deang and Gunzburger, 1998).

Both the finite difference and finite element methods are, however, limited by the need to discretise the entire domain. In the moving-boundary Stokes flow problem under consideration here the flow is controlled by the boundary motion only and the fluid properties are uniform across the domain. As such, it is more efficient to consider numerical schemes that avoid such a discretisation.

Due to this dependence on the boundary motion, Stokes flow problems are amenable to boundary element methods (sometimes called boundary integral methods). These methods seek to write the Goursat functions as Cauchy-type integrals involving an unknown density function. This function is found using the Sherman–Lauricella integral equations. Greenbaum, Greengard and Mayo (1992) have used this method to solve a general biharmonic problem on a fixed, simply connected domain. Similar methods have been used for bounded, unbounded and wall problems in fixed multiply connected domains (Greengard, Kropinski and Mayo, 1996) and fixed doubly periodic domains (Greengard

and Kropinski, 2004). Moving boundaries have been studied, such as the motion of multiple solid particles in Stokes flow (Kropinski, 1999), bubbles with free boundaries (Kropinski, 2001), and both compressible and incompressible bubbles in finite and infinite domains (Kropinski, 2002). Kropinski and Lushi (2011) have also considered the effect of surfactants on incompressible bubbles. A Sherman-Lauricella formulation has also been used previously to study optical fibre problems (Chakravarthy and Chiu, 2009).

Biros, Ying and Zorin (2004) employed a boundary integral method, embedding the domain in a regular grid and applying appropriate boundary conditions. Different integral formulations have been used to study a compressible and an incompressible bubble (Pozrikidis, 2001). Boundary element methods were used by van de Vorst (1993) to study the sintering of doubly connected regions and various multiply connected arrays of cylinders. A summary of boundary integral methods can be found in the book by Pozrikidis (1992).

Spectral methods provide another suitable numerical scheme; Boyd (2000) has provided a general overview of such methods. Orszag (1980) described the use of spectral methods for problems on complex geometries, such as by splitting the domain, and by way of example solved the heat equation on an irregular annular region. Spectral methods have also been demonstrated for solving Poisson's equation on the unit disk and mapped to more-complicated domains (Heinrichs, 2004). A least-squares collocation point spectral method was used by Hellou and Coutanceau (1992) to study a rotating cylinder within a rectangular channel. Price, Mullin and Kobine (2003) used a variation of this method to study two-roll-mill flows in a circular domain, formulating the problem in terms of complex variables. In this work, the Goursat functions are written as infinite series in powers of the complex co-ordinate  $z$  and logarithms. This approach

has been extended to study batch stirrers with a single translating, rotating paddle (Finn and Cox, 2001), multiple moving paddles (Finn, Cox and Byrne, 2003*b*) and braided pipe mixers with slowly varying geometries (Finn, Cox and Byrne, 2003*a*). Cox and Finn (2007) showed how these methods could be extended to stirring rods with other geometries using conformal maps.

The method of fundamental solutions (MFS) has also been employed to solve Stokes flow problems. Typically, MFS solutions for Stokes flow problems have used Stokeslet singularities arranged in a single layer (Young, Jane, Fan, Murugesan and Tsai, 2006; Aboelkassem and Staples, 2013) or double layers (Boselli, Obrist and Kleiser, 2012), while periodic Stokeslets have also been used for problems with translational symmetry (Ogata, Amano, Sugihara and Okano, 2003; Ogata and Amano, 2010). The MFS has also been used for problems on multiply connected domains Reutskiy (2006). A review of techniques has been given by Fairweather and Karageorghis (1998). The MFS may also be used for Stokes flows formulated using the biharmonic equation (Karageorghis and Fairweather, 1987, 1989; Poulikkas, Karageorghis, Georgiou and Ascough, 1998). The MFS has been used to construct conformal maps Amano (1994), although we do not make use of the method in this manner here.

In a similar spirit to the MFS, Crowdy (2004) developed a simple elliptical pore model (EPM) of a collection of elliptical pores in a very viscous fluid in which the effect of each pore on all the others is approximated by a point sink. Each boundary is described by a conformal map that evolves according to a system of ODEs. The original EPM has been extended to include a strictly circular outer boundary, such as is observed in many MOF geometries, and has been used to study the drawing of MOFs (Buchak *et al.*, 2015). This extended model represents the pores using both a sink and a stresslet singularity, which

again yields a system of ODEs that describe the map parameters. While the EPM provides an efficient method for solving the transverse problem it is currently restricted to geometries with elliptical inner boundaries and a circular outer boundary.

We here consider four numerical methods for finding the evolution of arbitrary bounded multiply connected domains, such as those found in MOF preform cross sections, based upon the complex-variable formulation described in Chapter 4. Two of these are spectral methods in which conformal maps are used to describe the solution as complex power series and the boundary conditions are applied using a collocation method. While some authors refer to collocation-based spectral methods as pseudospectral methods (Boyd, 2000), within this thesis a numerical method that uses global basis functions will be referred to as a spectral method. The third numerical method considered is based upon the MFS, which represents the solution as a collection of discrete points rather than with conformal maps. These three methods are validated against known solutions and against one another. We conclude with a brief description of an elliptical pore model.

## 5.2 Spectral Collocation Method

### 5.2.1 Overview of Method

We first describe a spectral collocation method in which the initial geometry in the  $z$ -plane is described by a single conformal map from a suitable region in the  $\zeta$ -plane. This map is specified by a set of coefficients that evolve in reduced time. The Goursat functions are approximated by a linear combination of global basis functions, which are power series in terms in  $\zeta$ . The coefficients in this

linear combination are chosen by evaluating the dynamic boundary condition at a number of collocation points and solving the resulting linear equations. With the Goursat functions known the parameters in the conformal maps are updated using the kinematic boundary condition, again using a collocation approach and solving linear equations. This may be considered a generalisation of the approach used by Hopper (1990), who also represented the solution by computing the evolution of the parameters in a conformal map.

The method presented here was developed in parallel with that described by Buchak *et al.* (2015), which used the same form for the Goursat functions and conformal map but computed the unknown coefficients by equating powers of variables.

### 5.2.2 Conformal Map

It is convenient to describe the domain as a conformal map  $z(\zeta, \tau)$  from some suitable region in the  $\zeta$ -plane. The domain in the  $\zeta$ -plane is taken to be the unit disk with some number of smaller disks removed from the interior, which is referred to as a circle domain. As a conformal map preserves connectivity, the domain in the  $\zeta$ -plane must have the same connectivity as the geometry under consideration in the  $z$ -plane. We can describe each interior boundary in the  $\zeta$  plane by specifying the centre  $\delta_n(\tau)$  and radius  $\rho_n(\tau)$ , which both depend upon reduced time, the evolution of which must be determined as part of the solution. A typical map is sketched in Figure 5.2.1. In theory, we should always be able to find a suitable set of parameters for any MOF geometry. Fornberg (1980) developed methods for finding maps from the unit disk to bounded connected domains, which Kropf (2009) extended to the case of a multiply connected circle domain. These techniques, sometimes referred to as Fornberg methods,

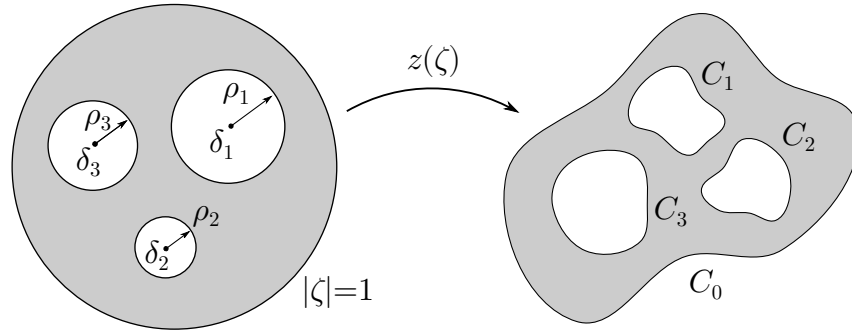


Figure 5.2.1: A sketch of a conformal map from a circle domain in the  $\zeta$ -plane to a region in the  $z$ -plane. The unit circle  $|\zeta|=1$  is mapped to the outer boundary  $C_0$ , while each inner boundary  $|\zeta - \delta_n| = \rho_n$  is mapped to  $C_n$ .

are based upon Newton's method and, as such, require a suitable initial guess in order to converge. Thus, in practice it may not be possible to find such a set of parameters. These methods are discussed further in Chapter 8.

As per Buchak *et al.* (2015), for  $N$  interior boundaries the domain is described by the series

$$z(\zeta, \tau) = \sum_{k=0}^{\infty} Z_{0,k}(\tau) \zeta^k + \sum_{n=1}^N \sum_{k=1}^{\infty} Z_{n,k}(\tau) \left( \frac{\rho_n(\tau)}{\zeta - \delta_n(\tau)} \right)^k. \quad (5.2.1)$$

In practice the infinite series are truncated after a finite number of terms  $K$ .

To evaluate the boundary conditions (4.2.27) and (4.2.31) we must be able to calculate  $z_s$ . To do this, we first observe that if a boundary is parameterised by some parameter  $\theta$  then we can write

$$z_s = \frac{z_\theta}{|z_\theta|}.$$

Thus, we need only calculate the derivative  $z_\theta$ . To relate this to the map (5.2.1) we use the chain rule to express this as

$$\frac{\partial z}{\partial \theta} = \frac{\partial z}{\partial \zeta} \frac{\partial \zeta}{\partial \theta}.$$

Differentiating (5.2.1) gives

$$\frac{\partial z}{\partial \zeta} = \sum_{k=0}^{\infty} Z_{0,k}(\tau) k \zeta^{k-1} + \sum_{n=1}^N \sum_{k=1}^{\infty} -Z_{n,k}(\tau) \frac{k}{\rho_n(\tau)} \left( \frac{\rho_n(\tau)}{\zeta - \delta_n(\tau)} \right)^{k+1}. \quad (5.2.2)$$

To find  $\zeta_\theta$  we must parameterise each boundary in the  $\zeta$ -plane, in each case using the standard orientation. On the outer boundary we write  $\zeta = e^{i\theta}$  where  $\theta \in [0, 2\pi)$ , so that  $\zeta_\theta = i\zeta$ . Finally,

$$\left| \frac{dz}{d\theta} \right| = |i\zeta z_\zeta| = |z_\zeta|,$$

which means that

$$z_s = \frac{i\zeta z'(\zeta)}{|z'(\zeta)|}.$$

Each inner boundary can be parameterised by  $\delta_j + \rho_j e^{-i\theta}$  where  $\theta \in [0, 2\pi)$ , so that

$$\zeta_\theta = -i(\zeta - \delta_j)$$

and hence

$$z_s = -\frac{i(\zeta - \delta_j) z'(\zeta)}{\rho_j |z'(\zeta)|}.$$

### 5.2.3 Goursat Functions

It is convenient to define the composed functions  $F(\zeta) = f(z(\zeta))$  and  $G(\zeta) = g'(z(\zeta))$ . We use  $g'$  rather than  $g$  as only the derivative appears in the boundary conditions. Just as for the conformal map, we write  $F$  and  $G$  as series in the  $\zeta$ -plane, so that

$$F(\zeta, \tau) = \sum_{j=0}^{\infty} F_{0,j}(\tau) \zeta^j + \sum_{n=1}^N \sum_{j=1}^{\infty} F_{n,j}(\tau) \left( \frac{\rho_n(\tau)}{\zeta - \delta_n(\tau)} \right)^j, \quad (5.2.3a)$$

$$G(\zeta, \tau) = \sum_{j=0}^{\infty} G_{0,j}(\tau) \zeta^j + \sum_{n=1}^N \sum_{j=1}^{\infty} G_{n,j}(\tau) \left( \frac{\rho_n(\tau)}{\zeta - \delta_n(\tau)} \right)^j. \quad (5.2.3b)$$

In practice the infinite series are truncated after a finite number of terms  $J$ .

### 5.2.4 Mapped Dynamic Boundary Condition

Substituting the composed Goursat functions into the dynamic boundary condition (4.2.27) yields the mapped condition

$$F(\zeta) + \frac{z(\zeta)}{z'(\zeta)} \overline{F'(\zeta)} + \overline{G(\zeta)} = -\frac{i}{2} z_s + A_n. \quad (5.2.4)$$

Importantly, for a given domain described by  $z(\zeta)$ , this condition is linear in the unknown coefficients  $F_{n,k}$  and  $G_{n,k}$ . Thus, we can evaluate (5.2.4) at a number of collocation points around the boundaries in the  $\zeta$ -plane to give a linear system to be solved for these coefficients. For optimal convergence these points are spaced evenly around the circular boundaries in the  $\zeta$ -plane (Boyd, 2000; Trefethen, 2000). Through experimentation, Cox and Finn (2007) found that using five times as many points as there are unknowns gives optimal results and we use this approach here.

In the previous section it was shown that the dynamic boundary condition does not uniquely determine the Goursat functions and, as such, additional degrees of freedom need to be set as part of the solution process. Substituting the mapped Goursat functions  $F(\zeta)$  and  $G(\zeta)$  into (4.2.33) shows that the dynamic boundary condition is still satisfied by the transformed quantities

$$\begin{aligned} \tilde{F}(\zeta) &= F(\zeta) + iRz(\zeta) + K_1, \\ \tilde{G}(\zeta) &= G(\zeta) + K_2, \\ \tilde{A}_n &= A_n + K_1 + \overline{K_2}. \end{aligned}$$

Note that since we are solving for  $G(\zeta) = g'(z)$ , rather than  $g(z)$ , the constant  $c$  no longer appears in the transformation. From this it is clear that there are five degrees of freedom to be set: the real and imaginary parts of  $K_1$  and  $K_2$ , and the real constant  $R$ . To set  $K_1$  and  $K_2$  we take  $F_{0,0} = G_{0,0} = 0$ .

Since  $z$  appears in the dynamic boundary condition multiplying  $F'$  we set  $R$  by setting the imaginary part of the linear coefficient of  $F$  to zero; that is, we set  $\Im(F_{0,1}) = 0$ . With these choices we ensure that the Goursat functions are uniquely determined and do not include any rotations or translations arising from zero-surface-tension eigensolutions.

Writing out (5.2.4) in full, the equations for the unknown coefficients  $F_{n,j}$ ,  $G_{n,j}$  and  $A_n$  are

$$\begin{aligned} & \sum_{j=1}^{\infty} F_{0,j} \zeta^j + \sum_{n=1}^N \sum_{j=1}^{\infty} F_{n,j} \left( \frac{\rho_n}{\zeta - \delta_n} \right)^j \\ & + \frac{z(\zeta)}{z'(\zeta)} \left[ \sum_{j=1}^{\infty} \overline{F_{0,j}} j \zeta^{j-1} + \sum_{n=1}^N \sum_{j=1}^{\infty} \overline{F_{n,j}} \left( -\frac{j}{\zeta - \delta_n} \right) \left( \frac{\rho_n}{\zeta - \delta_n} \right)^j \right] \\ & + \sum_{j=1}^{\infty} \overline{G_{0,j}} \zeta^j + \sum_{n=1}^N \sum_{j=1}^{\infty} \overline{G_{n,j}} \left( \frac{\rho_n}{\zeta - \delta_n} \right)^j - A_n = -\frac{i}{2} z_s, \end{aligned}$$

which apply on  $C_n$ ,  $n = 0, \dots, N$ . Evaluating this expression at the collocation points results in a linear system of complex equations involving unknown constants and their complex conjugates. This may be written in the form

$$P\mathbf{x} + Q\bar{\mathbf{x}} = \mathbf{b},$$

where  $\mathbf{x}$  is a vector containing the unknown coefficients,  $P$  and  $Q$  are complex matrices and  $\mathbf{b}$  is a complex vector; here,  $P$ ,  $Q$  and  $\mathbf{b}$  are known. To solve this system we solve for the real and imaginary parts of the unknowns  $\mathbf{x}$  separately. This approach yields the system of equations

$$\begin{bmatrix} \Re(P) + \Re(Q) & -\Im(P) + \Im(Q) \\ \Im(P) + \Im(Q) & \Re(P) - \Re(Q) \end{bmatrix} \begin{bmatrix} \Re(\mathbf{x}) \\ \Im(\mathbf{x}) \end{bmatrix} = \begin{bmatrix} \Re(\mathbf{b}) \\ \Im(\mathbf{b}) \end{bmatrix}. \quad (5.2.5)$$

Once solved, we use the kinematic condition to compute the evolution of the boundaries.

### 5.2.5 Mapped Kinematic Boundary Condition

Substituting (5.2.3a) into (4.2.32) yields the mapped kinematic boundary condition

$$\Re\left(\frac{dz}{d\tau}i\bar{z}_s\right) = \Re\left(\left[-2F(\zeta) - \frac{i}{2}z_s + A\right]i\bar{z}_s\right). \quad (5.2.6)$$

The right-hand side is completely determined by the Goursat functions, the constants  $A_n$  and the current map  $z(\zeta, \tau)$ , while the left-hand side includes the reduced-time derivative of  $z(\zeta, \tau)$ . This derivative requires particular care due to the reduced-time dependence of  $\zeta$  through the parameters  $\delta_n$  and  $\rho_n$ , and is given by

$$\frac{dz}{d\tau} = \frac{\partial z}{\partial \tau} + \frac{\partial z}{\partial \zeta} \frac{\partial \zeta}{\partial \tau},$$

where  $\partial/\partial\tau$  is computed holding  $\zeta$  fixed. On any boundary the partial derivative of  $z$  with respect to  $\tau$  is

$$\frac{\partial z}{\partial \tau} = \sum_{k=0}^{\infty} \dot{Z}_{0,k} \zeta^k + \sum_{n=1}^N \sum_{k=1}^{\infty} Z_{n,k} \left(\frac{\rho_n}{\zeta - \delta_n}\right)^k \left(\frac{\dot{Z}_{n,k}}{Z_{n,k}} + \frac{k\dot{\rho}_n}{\rho_n} + \frac{k\dot{\delta}_n}{\zeta - \delta_n}\right), \quad (5.2.7)$$

where dots denote differentiation with respect to  $\tau$ . In the  $\zeta$ -plane the outer boundary is fixed to be the unit circle  $|\zeta| = 1$  so  $\partial\zeta/\partial\tau = 0$ . Each inner boundary is of the form  $\zeta = \delta_n + \rho_n e^{i\theta}$  so can move in the  $\zeta$ -plane and hence  $\partial\zeta/\partial\tau$  can be non-zero. We compute  $z_\zeta$  using (5.2.2), while we find that

$$\begin{aligned} \frac{\partial \zeta}{\partial \tau} &= \dot{\delta}_n + \dot{\rho}_n e^{i\theta}, \\ &= \dot{\delta}_n + \dot{\rho}_n \frac{\zeta - \delta_n}{\rho_n}, \end{aligned}$$

with the second expression preferred as it does not involve  $\theta$  explicitly.

As was done for the dynamic boundary condition, we evaluate the kinematic boundary condition (5.2.6) at a number of collocation points spaced evenly around each boundary in the  $\zeta$ -plane, again taking five times as many points

as there are unknowns. This results in an over-determined system of linear equations for the unknowns, which we solve using least squares.

While the right-hand side of the kinematic condition (5.2.6) is real, the left-hand side is the real part of a linear combination of both complex unknowns (the  $\dot{Z}_{n,k}$  and  $\dot{\delta}_n$  terms) and real unknowns (the  $\dot{\rho}_n$ ). Letting  $\mathbf{c}$  and  $\mathbf{r}$  denote the complex and real unknowns, respectively, the equations in the linear system can be written in the form

$$\Re(A\mathbf{c} + B\mathbf{r}) = \mathbf{b},$$

where  $A$  and  $B$  are complex matrices and  $\mathbf{b}$  is a real vector. It is convenient to split the complex unknowns into real and imaginary components by writing this condition as

$$\Re(A)\Re(\mathbf{c}) - \Im(A)\Im(\mathbf{c}) + \Re(B)\mathbf{r} = \mathbf{b}. \quad (5.2.8)$$

Once the reduced-time derivatives of the parameters are known we integrate these forward in reduced time to find the evolution of the geometry, as described in the following subsection.

### 5.2.6 Algorithm

The general algorithm for this method is as follows:

- (1) Start with some initial geometry described by the map  $z(\zeta)$  on a circle domain.
- (2) Solve the linear system (5.2.5) to find the series coefficients for the Goursat functions  $F$  and  $G$ .

- (3) Use the Goursat functions to construct and solve the linear system (5.2.8) for the reduced-time derivatives of the map parameters  $\dot{Z}_{n,k}$ ,  $\dot{\delta}_n$  and  $\dot{\rho}_n$ .
- (4) Integrate the map parameters forward in reduced time to find the evolution of the geometry.
- (5) Repeat steps 2 through 4 until the desired reduced time is reached.

Unless stated otherwise, all solutions computed using this method are truncated by setting  $K = 30$  in the maps (5.2.3) and  $J = 30$  in the composed Goursat functions (5.2.3).

### 5.2.7 Convergence

The series (5.2.1) and (5.2.3) are effectively Fourier expansions around the boundary of the map and Goursat functions, respectively. Since these functions are smooth on the boundaries we expect these series to converge geometrically, if not faster, as the number of terms increases. It is assumed that this error is of the same magnitude as the error in the solution (Boyd, 2000).

To illustrate the convergence of this method we consider the geometry shown in Figure 5.2.2 and compute the Goursat functions and the reduced-time derivatives of the map parameters at reduced time  $\tau = 0$ . As described above, each of the boundary conditions is applied by solving a linear system that may be written in the general form  $A\mathbf{x} = \mathbf{b}$ . In each case we define the error to be  $\|A\mathbf{x} - \mathbf{b}\|/\|\mathbf{b}\|$  using the Euclidean norm. The errors in the dynamic and kinematic boundary conditions are denoted  $e_d(J)$  and  $e_k(K)$ , respectively, and are each functions of the number of terms taken in the respective series. Each error is evaluated over a range of values of the associated parameter, with the other parameter set to 30, and the results plotted in Figure 5.2.3. We note

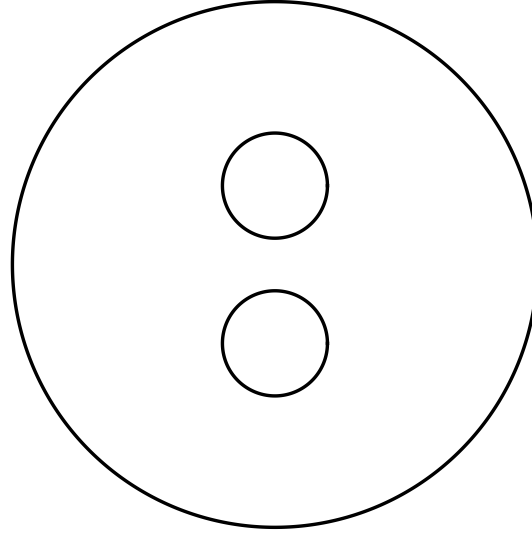


Figure 5.2.2: The geometry used to illustrate the accuracy of the spectral method.

that the errors for both boundary conditions decrease at an approximately geometric rate as the number of terms in the series increases until reaching machine precision at around 30 terms. This behaviour is consistent with the convergence assumption stated above. Thus, this method is highly efficient and produces accurate results with only a small number of terms in each series.

### 5.2.8 Calculating Geometric Quantities

To make use of the solutions computed using this method in our modelling of gravity-driven extensional flows in later chapters we must be able to calculate the total boundary length  $\Gamma$ , which is needed in the axial problem. On each inner boundary  $C_n$  we can write  $z = z(\zeta)$  where  $\zeta = \rho_n e^{i\theta} + \delta_n$  for  $\theta \in [0, 2\pi]$ . With this representation, we find that  $z_\theta = i(\zeta - \delta_n)z_\zeta$  so that  $|z_\theta| = |\rho_n z_\zeta|$ .

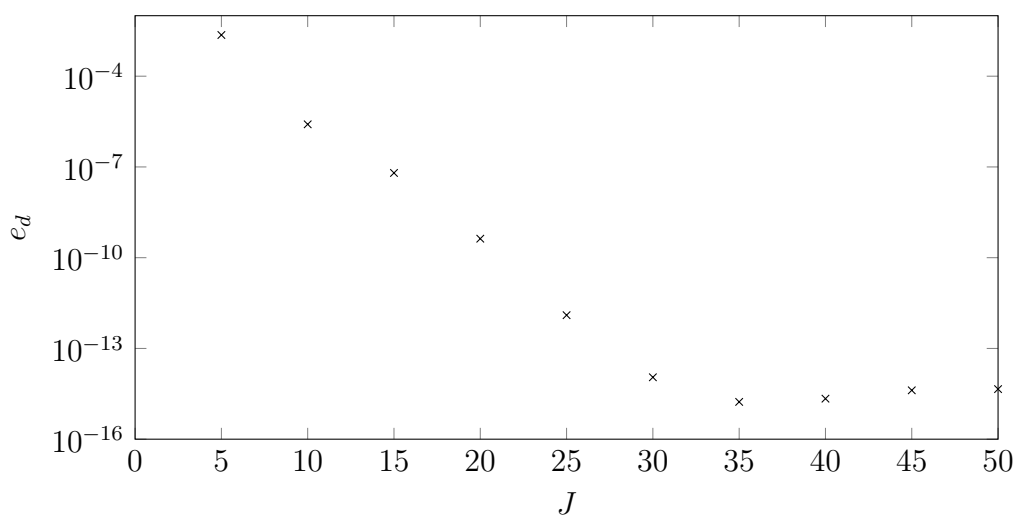
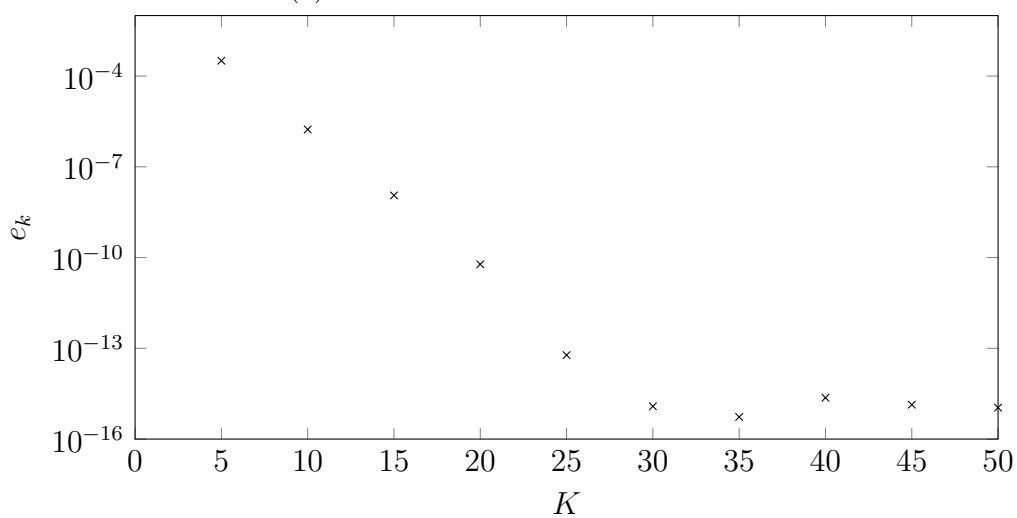
(a) Goursat functions with  $K = 30$ (b) Map parameter reduced-time derivatives with  $J = 30$ 

Figure 5.2.3: The errors in the dynamic and kinematic boundary conditions for the first spectral method at reduced time  $\tau = 0$ . The errors are denoted  $e_j$  and  $e_k$ , respectively. Both errors decrease at an approximately geometric rate as the number of terms increases, eventually reaching machine precision.

Using (4.2.34), the length of  $C_n$  is

$$\Gamma_n = \int_{C_n} ds = \int |z_\theta| d\theta = \int_0^{2\pi} |\rho_n z_\zeta(\theta)| d\theta.$$

On the outer boundary we write  $\zeta = e^{i\theta}$  so that  $|z_\theta| = |z_\zeta|$ . The total boundary length is thus

$$\Gamma = \int_0^{2\pi} |z_\zeta| d\theta + \sum_{n=1}^N \int_0^{2\pi} |\rho_n z_\zeta| d\theta.$$

Substituting these parameterisations into (4.2.35) shows that the area is

$$S = \int_0^{2\pi} \overline{z(\zeta(\theta))} z_\zeta(\theta) i \zeta(\theta) d\theta - \sum_{n=1}^N \int_0^{2\pi} \overline{z(\zeta(\theta))} z_\zeta(\theta) i (\zeta(\theta) - \delta_n) d\theta.$$

### 5.2.9 Comparison with Exact Solution for an Annulus

In order to provide some validation of the method described above we first compare it against the exact solution for an annulus developed in Subsection 4.3.1. In this case, the regions in both the  $\zeta$ - and  $z$ -planes are annuli. Since it is only possible to conformally map one annulus onto another if the radii are in the same ratio (Henrici, 1974), we deduce that the map must be of the form  $z(\zeta) = a\zeta$  for some  $a \in \mathbb{C}$ . Furthermore, by substituting this into the exact solution we also see that the composed Goursat functions must be in the form

$$F(\zeta) = b\zeta, \quad G(\zeta) = \frac{c}{\zeta},$$

where  $b$  and  $c$  are functions of reduced time. Thus, it is clear that the series for the map (5.2.1) and Goursat functions (5.2.3) contain the exact solution. We hence expect the numerical method to be able to capture this solution accurately.

For the comparison we use an annulus with unit outer radius and inner radius 0.5 as this matches the example given by van de Vorst (1993). Using the exact

solution we find that the inner hole closes at reduced time  $\tau_f = \sqrt{3} - 1 \approx 0.73205$ , which matches the time predicted by van de Vorst (1993). We thus compute the solution up to reduced time  $\tau = 0.73$  as beyond  $\tau_f$  both the exact and numerical solutions are no longer applicable. The coefficients from the numerical solution are integrated using the fourth-order Runge–Kutta method with a reduced-time step of  $10^{-2}$ . The exact and numerical solutions are shown in Figure 5.2.4. As expected, the two solutions agree very well and are indistinguishable to graphical accuracy. Furthermore, the form of the computed series is identical to the exact solution to within machine precision. Since the exact solution was contained in the series used in the numerical approximation it is not surprising that the two show such good agreement; however, this example provides some evidence the method is working correctly.

### 5.2.10 3-Hole Preforms

#### Example

As was noted in Chapter 3, the *shape* of each cross section in an extending fluid region is determined, up to the scale, by the Stokes flow described above. Thus, using the numerical method described in this section we are in a position to provide a preliminary analysis of the shape of MOF preforms. We here consider a preform geometry with three air channels shown in Figure 5.2.5, which we refer to as the 3-hole preform. This design is used as a jacket during the caning of electro-optical MOF preforms (Manning, 2011; Zhang *et al.*, 2013). The physical dimensions for the preform design considered here are given in Table 5.2.1. A cross section from an extruded 3-hole preform is shown in Figure 1.1.3e that is representative of the behaviour seen in similar preforms

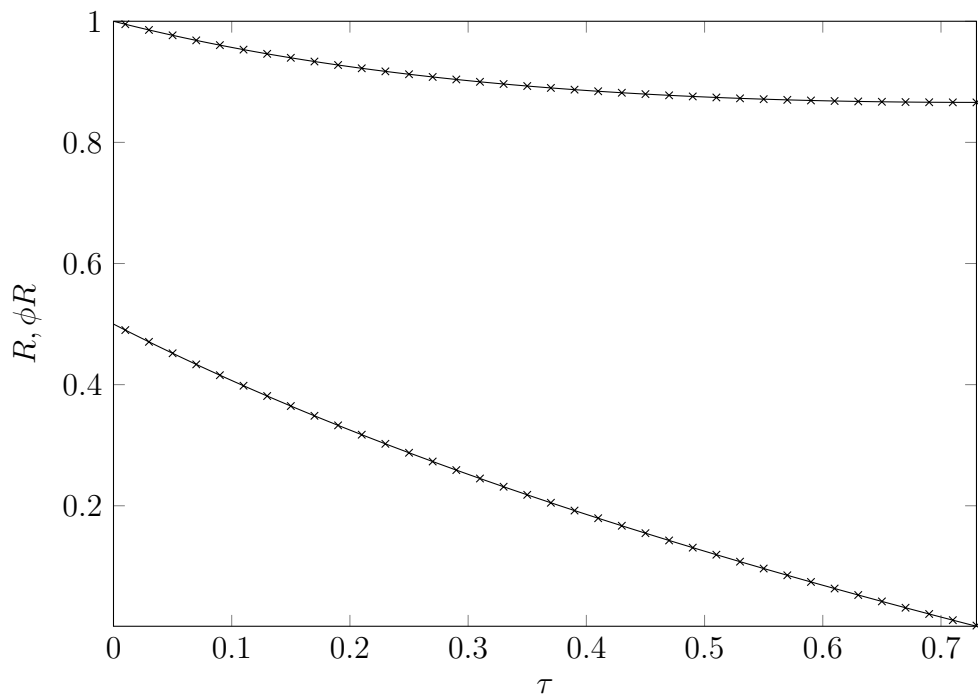


Figure 5.2.4: The inner radius  $\phi R$  and outer radius  $R$  of an annular region of fluid with initial inner radius 0.5 and unit outer radius computed up to reduced time  $\tau = 0.73$ . Shown are the exact solution (solid lines) and selected values from the spectral method (crosses). The numerical solution was integrated using a Runge–Kutta fourth-order method with a reduced-time step of  $10^{-2}$ . The two solutions are identical to graphical accuracy.

Table 5.2.1: Dimensions of the 3-hole preform.

Length	Value (mm)
Outer boundary radius	7
Outer hole radius	1.25
Central hole radius	0.75
Hole spacing	2.4

with different dimensions. We observe that all three inner boundaries and the outer boundary have deformed and no longer match the die geometry. The central inner hole has become elongated, while the outer holes have higher curvature at the points nearest the central hole than at the points near the outer boundary, while the outer boundary has formed cusp-like regions at the top and bottom of the preform near the inner holes. Thus, a particular focus of this section is to determine whether these characteristic deformations are replicated by the surface-tension-driven model and may thus be attributed to this effect.

In line with the analysis from Chapter 3, the physical lengths are scaled such that the entire domain has unit area. Using the values in Table 5.2.1 it is straightforward to determine that the area is  $725\pi/16 \text{ mm}^2$ , which corresponds to the length scale  $\sqrt{725\pi/16} \text{ mm}$ .

The shape of the preform at reduced times  $\tau = 0.02, 0.04, 0.06$  and  $0.08$  is shown in Figure 5.2.6. From these we observe that the three inner boundaries show similar behaviour as that seen in the experimental image from Figure 1.1.3e: the inner hole elongates along the vertical axis, while the two outer holes show higher curvature on the ends near the inner hole than on the ends near the

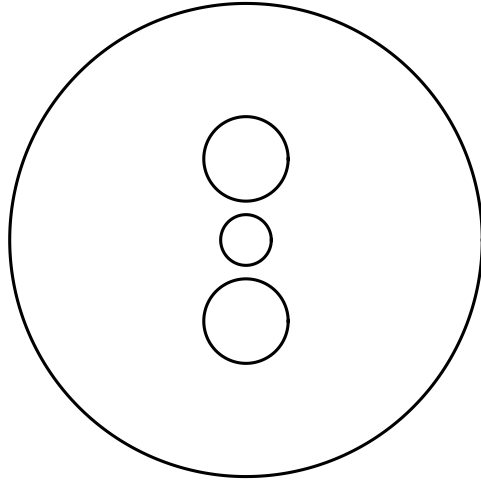


Figure 5.2.5: The desired shape of the 3-hole preform. This geometry is used as the initial condition in the spectral method.

outer boundary. In contrast, the outer boundary shows significantly different behaviour to that seen in experiments. Initially the outer boundary contracts in a horizontal direction but later becomes more circular with reduced time. In experiments the outer boundary displays cusp-like regions at the top and bottom of the preform, which are not captured by the model.

### Varying Outer Hole Location

We here briefly investigate how the outer hole spacing affects the evolution. In the above example the centres of the outer holes were a (dimensionless) distance of approximately  $d = 0.2012$  from the centre of the domain. We here consider two alternative positions:  $d = 0.3$  and  $d = 0.4$ . The shapes of these two examples at reduced time  $\tau = 0.06$  are shown in Figure 5.2.7. In the case  $d = 0.3$ , shown in Figure 5.2.7a, we note that both the outer holes and the inner hole show less elongation. The outer boundary has moved inwards

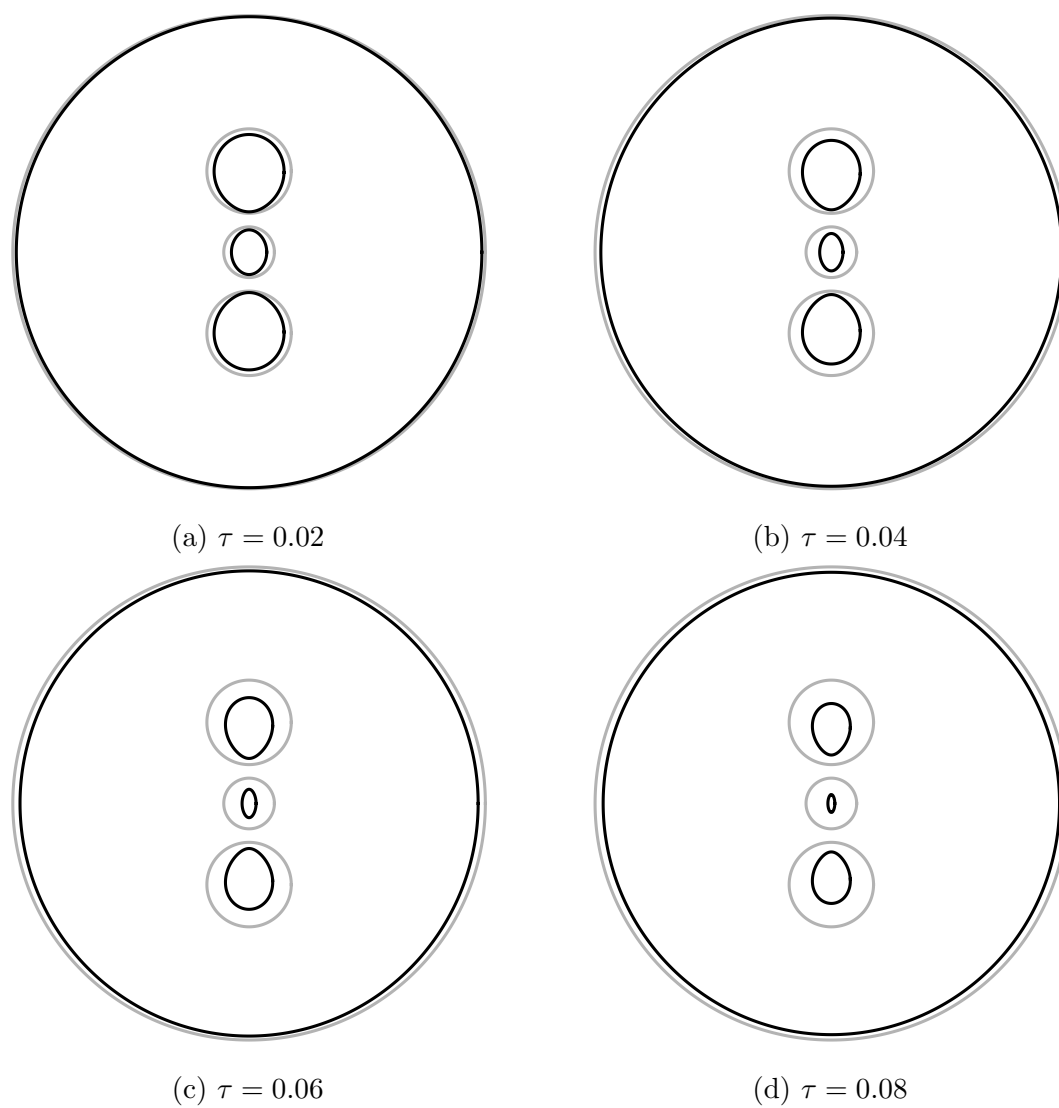


Figure 5.2.6: The evolution of the 3-hole preform geometry at reduced times  $\tau = 0.02, 0.04, 0.06$  and  $0.08$ . The black lines represent the geometry at the indicated reduced time while the grey lines show the initial condition. The holes show behaviour like that seen in experiments but the outer boundary remains approximately circular.

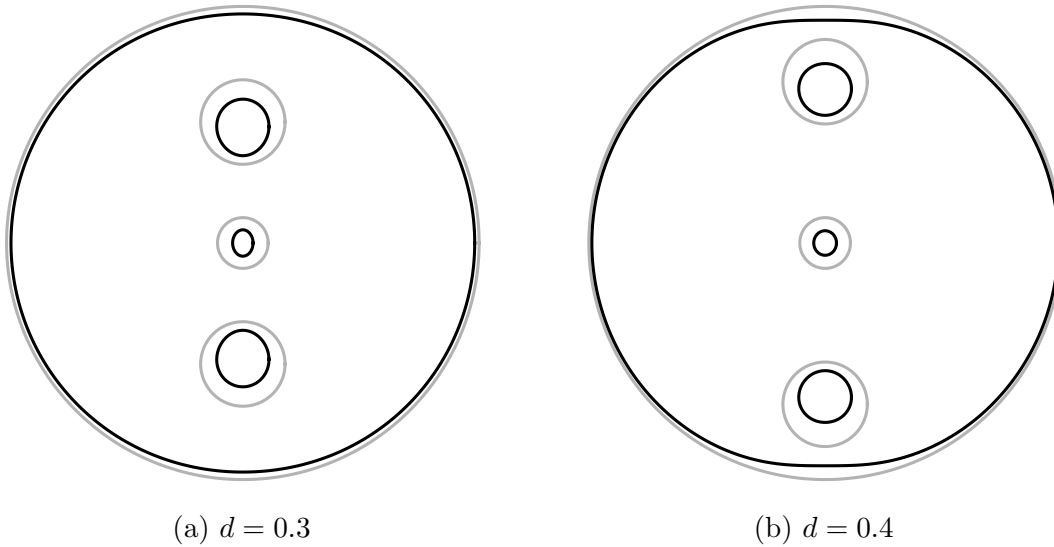


Figure 5.2.7: The shape of the domain at  $\tau = 0.06$  for (a)  $d = 0.3$  and (b)  $d = 0.4$ . As  $d$  increases the holes show less influence over each other and the central hole remains more circular; however, there is more distortion of the outer boundary.

in the vertical direction more than horizontally, which is in contrast to the behaviour of the original geometry. This boundary is, however, still relatively circular. Figure 5.2.7b shows the  $d = 0.4$  case. Here, we observe that the inner hole appears almost perfectly circular, while the two outer holes show some compression in the vertical direction, rather than horizontally as before. The outer boundary shows a significant change in behaviour, showing noticeable flattening at the top and bottom. While there is a small indication of a dip inwards at the centre of these flat regions we still do not see any cusp-like behaviour similar to that observed in the experiments. This discrepancy and the potential cause will be revisited in Chapter 8, following the discussion of an extrusion model in Chapter 7.

### Inverse Problem

It is possible to run the spectral code backwards in reduced time, starting from the desired pattern of circles, to determine possible initial conditions that would give rise to the desired geometry after deforming due to surface tension. One such example is shown in Figure 5.2.8 for the 3-hole geometry from Table 5.2.1, in which the desired geometry is evolved backwards in reduced time to  $\tau = -0.03$ . Thus, a fluid region with this cross section would be expected to deform to the desired 3-hole geometry in reduced time  $\tau = 0.03$ ; indeed, using the spectral method to evolve the geometry from Figure 5.2.8 *forwards* for 0.03 units of reduced time recovers the initial 3-hole geometry. The time over which the spectral code can be run backwards is limited: as the solution is computed backwards in reduced time the inner holes increase in size until eventually they will, to numerical precision, intersect. This can be seen in the example in Figure 5.2.8, which cannot be run backwards much further than  $\tau = -0.03$ . Circular die pins are typically, however, easier to fabricate, and some more-complicated geometries, such as the one from Figure 5.2.8, may be impossible to produce. Improvements in die fabrication, such as the use of three-dimensional printing, may allow the fabrication of more-general dies. Finally, as discussed by Buchak *et al.* (2015), the inverse problem is ill-posed and may require some form of regularisation.

### Conclusions

These examples have important implications for MOF preform extrusion. It is clear that the closer the outer holes are to the outer boundary the larger the deformation of the outer boundary along the vertical axis of symmetry. As  $d$  increases from 0.2 to 0.4 the largest deformation of the outer boundary

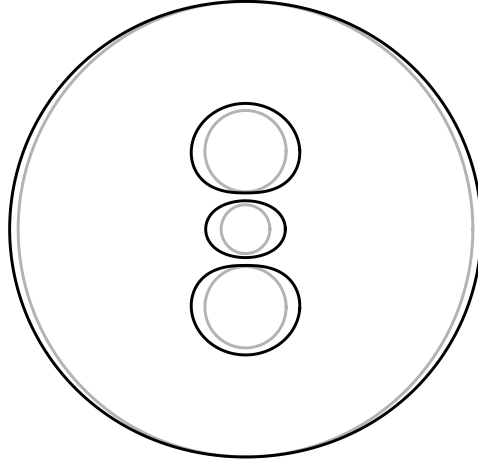


Figure 5.2.8: The geometry of the 3-hole preform from Table 5.2.1 at reduced time  $\tau = -0.03$  found by running the first spectral method backwards in reduced time. Evolving this geometry forwards in reduced time will recover the pattern of circles.

moves from the sides of the domain to the top. Despite this, even in the most extreme case  $d = 0.4$ , we do not see the cusp-like regions that are observed in the experiments. Thus, this behaviour cannot be explained by surface tension alone (nor, indeed, by both surface tension and gravity, as in this model the latter only acts to scale the domain but cannot influence the shape).

These examples do show, however, that the characteristic pattern of the inner holes that is seen in experiments *can* arise due to surface tension effects, as the model results shown in Figure 5.2.6 give very good qualitative agreement with experiments. This behaviour occurs when the inner holes are close together: as  $d$  increases the holes have less influence over each other. Thus, we conclude that the deformation of the inner holes is caused by the interaction of the three inner holes due to their closure under surface tension. It was observed by Manning (2011, p. 201) that it is most important for the central hole to remain

circular as it will later house a cane with a circular cross section, while it is less important that the outer holes remain circular. These results show that increasing  $d$  results in a more-circular inner hole, and thus this provides one method for controlling its distortion. This is balanced by increased distortion of the outer boundary as  $d$  increases, requiring a choice by an experimentalist as to the acceptable level of distortion in each. It must also be noted, however, that this choice would also require a better understanding of the cusp-like regions observed in the outer boundary. Further results on this behaviour will be presented in Chapter 8.

It has been shown that, given some desired geometry, it is possible to run the spectral code backwards in reduced time to compute possible initial geometries that will deform to the desired one given the required amount of deformation time. Whilst there are some complications, such as fabricating the matching die, our model provides a tool for predicting the initial geometry needed for a desired outcome.

### 5.2.11 6- and 7-Hole Preforms

As a final example of the spectral code we consider 6- and 7-hole preforms, shown in Figure 5.2.9. Both designs feature a ring of six circular inner boundaries, with the 7-hole design having an additional central circular hole. The aim of this investigation is to consider the influence of the additional central hole in the 7-hole preform compared with the 6-hole preform. The dimensions of these two designs considered here are given in Table 5.2.2.

Solutions at reduced times  $\tau = 0.02, 0.04, 0.06$  and  $0.08$  are shown for the 6- and 7-hole geometries in Figure 5.2.10 and Figure 5.2.11, respectively. For both geometries the holes forming the ring become smaller. In the 6-hole case, the

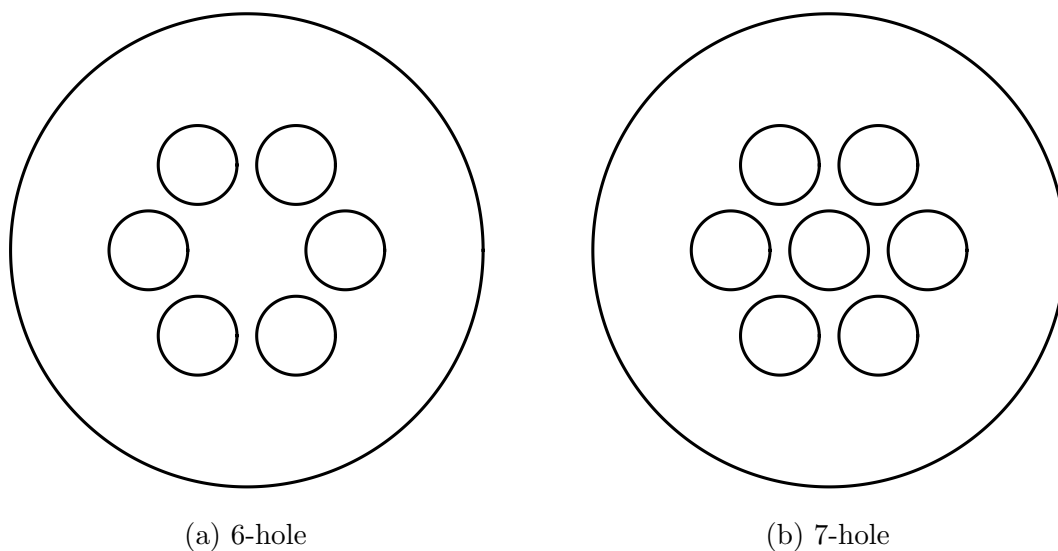


Figure 5.2.9: The 6- and 7-hole preform geometries.

Table 5.2.2: Dimensions of the 6- and 7-hole preforms.

Length	Value (mm)
Outer boundary radius	6
Inner hole radius	1
Ring radius	2.5

inner edges of the holes becomes flat, while the outer edges stay curved. When a central hole is included, the holes in the ring are pulled towards the centre as the central hole closes, which prevents the holes in the ring from developing the flat edge. Instead, these outer holes are approximately elliptical. These holes also shift towards the centre of the domain. The central hole remains circular but reduces in size.

We also note that the 7-hole geometries from Figure 5.2.11 show good qualitative agreement to the typical experimental result shown in Figure 1.1.3f. We thus conclude that surface tension is likely to be responsible for the deformations observed in extruded 7-hole preforms.

## 5.3 Alternative Spectral Method

### 5.3.1 Overview of Method

It was discussed earlier that use of the first spectral method requires a conformal map describing the initial geometry that may be difficult to compute. We here present another spectral method, referred to here as the alternative spectral method, which is based upon that used by Cox and Finn (2007) to study mixing with elliptical paddles. Rather than describe the geometry by a single map between multiply connected regions, each boundary is described by its own map from the unit circle. As shown in Figure 5.3.12, the interior of the unit circle is mapped to the interior of the outer boundary, while the exterior of the unit circle is mapped to the exterior of each inner boundary. This reduces the problem of determining the initial map to finding individual maps for each boundary. This simplification comes at the cost of additional computation at each iteration of the method.

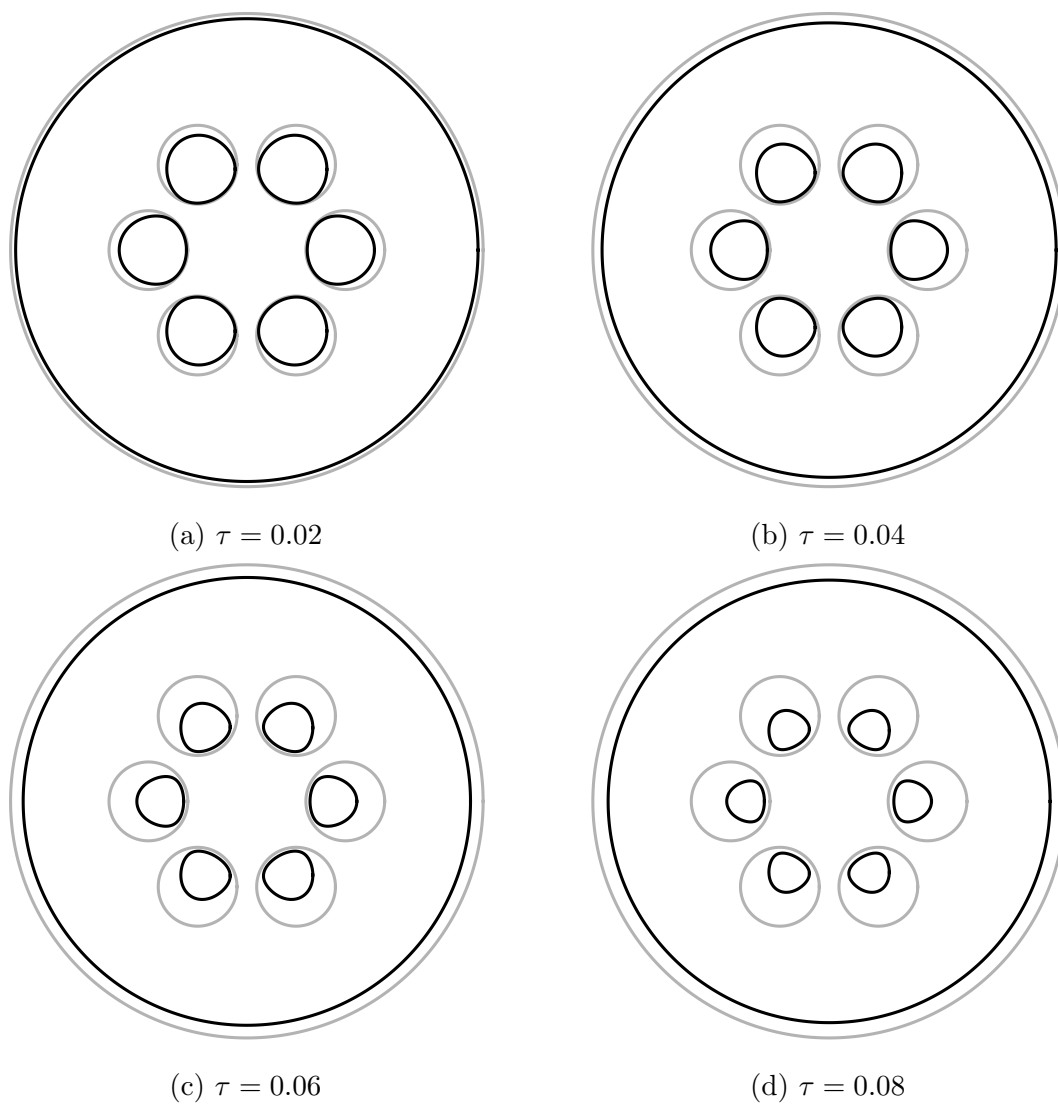


Figure 5.2.10: The evolution of the 6-hole preform geometry at reduced times  $\tau = 0.02, 0.04, 0.06$  and  $0.08$ . The dark lines represent the geometry at the indicated reduced time while the light lines show the initial condition. The holes show behaviour like that seen in experiments.

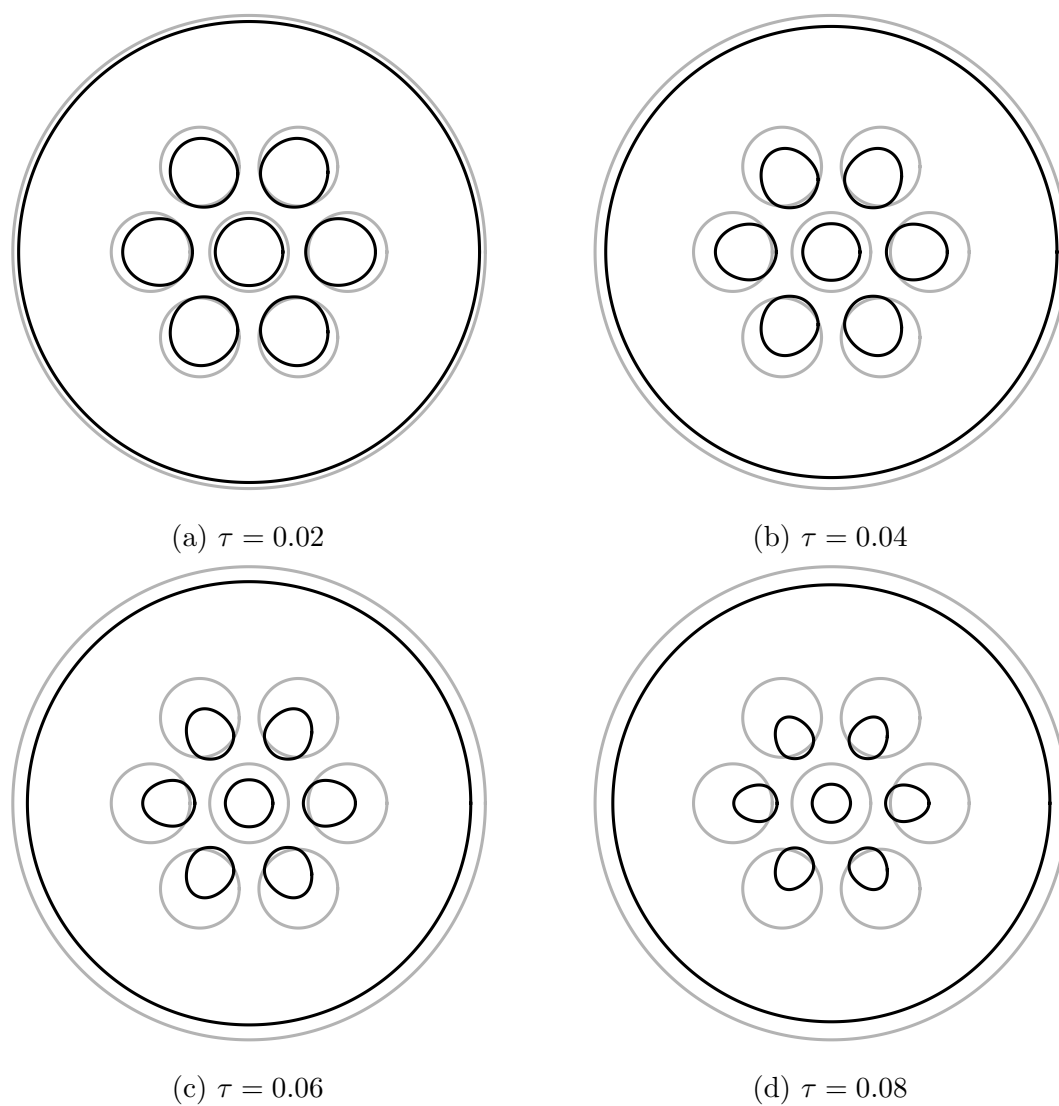


Figure 5.2.11: The evolution of the 7-hole preform geometry at reduced times  $\tau = 0.02, 0.04, 0.06,$  and  $0.08$ . The dark lines represent the geometry at the indicated reduced time while the light lines show the initial condition.

### 5.3.2 Conformal Maps

It is important to select the correct form for the conformal maps. Without careful selection of the forms the maps can cease to be conformal. Following DeLillo and Pfaltzgraff (1998), for each inner boundary  $C_n, n = 1, 2, \dots, N$ , we take

$$z = z_n(\zeta) = Z_{n,1}\zeta + \sum_{k=0}^{\infty} Z_{n,-k}\zeta^{-k}, \quad (5.3.9)$$

such that points  $\zeta$  on the unit circle map to points on boundary  $C_n$ , while on the outer boundary  $C_0$  we take

$$z = z_0(\zeta) = \sum_{k=0}^{\infty} Z_{0,k}\zeta^k, \quad (5.3.10)$$

such that points  $\zeta$  on the unit circle map to points on the boundary  $C_0$ . We will later need to refer to the inverses of each of these maps. To avoid confusion between negative exponents and inverses, we denote the inverse of  $z_n(\zeta)$  by  $\zeta_n(z)$  for  $n = 0, 1, 2, \dots, N$ .

### 5.3.3 Goursat Functions

The Goursat functions  $f$  and  $g$  are constructed using components associated with each boundary. That is, the Goursat functions are comprised of components evaluated in each of the  $\zeta_n$ -planes corresponding to the map  $z_n$ . The contribution to the flow from the outer boundary  $C_0$  is represented by

$$f_0(z_0(\zeta)) = F_0(\zeta) = \sum_{j=0}^{\infty} F_{0,j}\zeta_0^j(z),$$

$$g'_0(z_0(\zeta)) = G_0(\zeta) = \sum_{j=0}^{\infty} G_{0,j}\zeta_0^j(z).$$

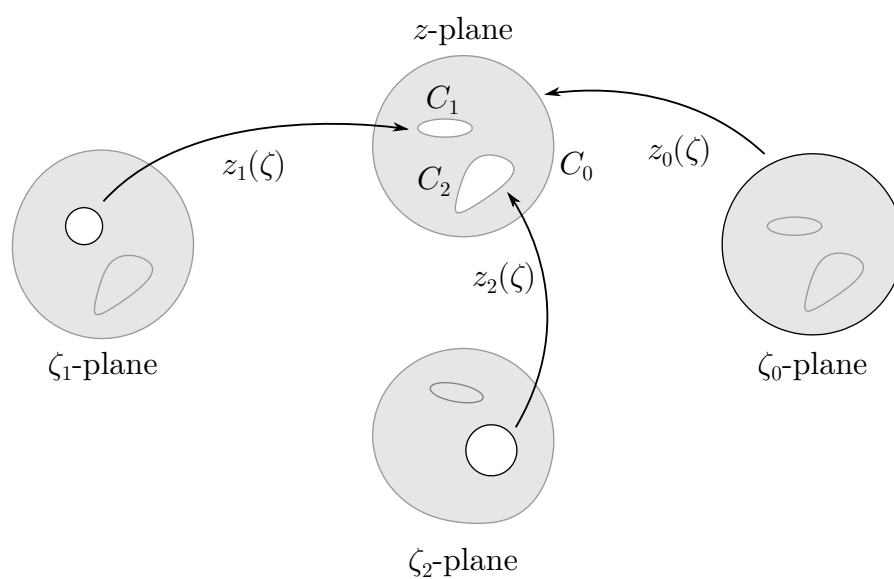


Figure 5.3.12: An example of the conformal maps used in the alternative spectral method that describe a domain in the  $z$ -plane with an outer boundary and two inner boundaries. The unit circle in each  $\zeta_n$ -plane is shown in black while all other boundaries are grey. The interior of the outer boundary  $C_0$  is mapped by  $z_0(\zeta)$  to the interior of the unit circle in the  $\zeta_0$ -plane. The exterior of each inner boundary  $C_n$ ,  $n = 1, 2$ , is mapped by  $z_n(\zeta)$  to the exterior of the unit circle in the  $\zeta_n$ -plane.

On each inner boundary  $C_n$  we take

$$f_n(z_n(\zeta)) = F_n(\zeta) = \sum_{j=1}^{\infty} F_{n,j} \zeta_n^{-j}(z),$$

$$g'_n(z_n(\zeta)) = G_n(\zeta) = \sum_{j=1}^{\infty} G_{n,j} \zeta_n^{-j}(z).$$

The Goursat functions are then given by

$$f(z) = \sum_{n=0}^N f_n(z_n(\zeta)) = \sum_{n=0}^N F_n(\zeta), \quad (5.3.11a)$$

$$g'(z) = \sum_{n=0}^N g'_n(z_n(\zeta)) = \sum_{n=0}^N G_n(\zeta). \quad (5.3.11b)$$

The components associated with each boundary may be simply summed provided the coefficients are solved for simultaneously, as described in the following subsection.

### 5.3.4 Boundary Conditions

Just as in the method of Section 5.2, the evolution of the fluid domain is computed by evolving the conformal maps. To start the method we specify a set of maps  $z_n$ ,  $n = 0, \dots, N$ , that take the unit circle in the  $\zeta_n$ -plane to boundary  $C_n$ . We then solve for the unknown coefficients in the Goursat functions (5.3.11) by substituting the series expression into the dynamic boundary condition (4.2.27). The resulting expressions are evaluated at a number of collocation points on each boundary, yielding a linear systems that is solved for the unknowns. With the Goursat functions known we can calculate the velocity of the fluid and so, by substituting into the kinematic condition (4.2.31), we are able to construct and solve a linear system for the reduced-time derivatives of the coefficients in the maps. With these known we integrate the map coefficients forward in

reduced time using a numerical method to find the new form of the maps. This process is repeated until the desired reduced time is reached.

The key difference lies in how the series are evaluated at the collocation points around each boundary. For each boundary  $C_n$  the collocation points are equally spaced around the unit circle in the  $\zeta_n$ -plane, and the relevant boundary condition is evaluated at these points; however, in order to evaluate the series we need to know the corresponding points in all of the other  $\zeta_n$ -planes. In order to determine these the collocation points are first mapped into the  $z$ -plane. For each map  $z_m$ ,  $m \neq n$ , we must compute the pre-image of the collocation points. Once these are known we are able to evaluate the boundary conditions and construct the linear system to solve. Determining the inverses is not trivial and is discussed further in the following subsection.

### 5.3.5 Inverting the Conformal Maps

In order to evaluate the Goursat functions in (5.3.11) at some point  $z$  we must first calculate  $\zeta_n(z)$  for each  $n$ . That is, we need the inverse of the maps  $z_n$ . In general these must be calculated numerically.

There are two classes of maps to consider: exterior–exterior (5.3.9) and interior–interior (5.3.10). For a map of the form (5.3.10) and given some point  $z$ , the problem is to find  $\zeta$  satisfying

$$z_n(\zeta) = z,$$

which may be written as

$$Z_{n,0} - z + \sum_{k=1}^{\infty} Z_{n,k} \zeta^k = 0.$$

This is a polynomial in  $\zeta$ , and since  $z_n$  is a conformal map there must be precisely one solution within the unit circle.

For an exterior–exterior map (5.3.9) we introduce the new variable  $\hat{\zeta} = 1/\zeta$  and conformal map  $\hat{z}_n = z_n(\hat{\zeta})$ , which takes the *interior* of the unit circle to the exterior of  $C_n$ . We then solve  $z = \hat{z}_n(\hat{\zeta})$  for  $\hat{\zeta}$ , which, after rearranging, may be written

$$Z_{n,1} + (Z_{n,0} - z)\hat{\zeta} + \sum_{k=1}^{\infty} Z_{n,-k}\hat{\zeta}^{k+1} = 0.$$

This is once again just a polynomial and we require the unique root that lies within the unit circle. With  $\hat{\zeta}$  known the solution to  $z = z_n(\hat{\zeta})$  is simply  $1/\hat{\zeta}$ .

Thus, in both cases we can invert the conformal map by finding the unique root within the unit circle of some polynomial. We investigated several methods for doing this:

- `roots` (MATLAB);
- companion matrices and eigenvalues;
- Newton’s method;
- the argument principle;
- `fsolve` (MATLAB); and
- `lsqnonlin` (MATLAB).

Note that the MATLAB function `roots` constructs a companion matrix and finds the eigenvalues using the function `eig` and we thus expect these two methods to produce similar results. These methods are described in Appendix B.

In determining the optimal method we considered three qualities: speed, accuracy and reliability (the method should be guaranteed to produce the correct result given any reasonable initial guess but should not rely upon the

initial guess being close to the solution). To test the method we need to generate polynomials of varying length that represent a conformal map from the unit disk to some bounded region. To do this we make use of the map given by Richardson (1992, p. 202, eqn (4.1)) for two unequal touching disks, which has the form

$$z(\zeta) = \frac{A\zeta}{a - \zeta} + \frac{B\zeta}{b + \zeta}. \quad (5.3.12)$$

The terms  $A$ ,  $a$ ,  $B$  and  $b$  are parameters that control the sizes of the touching disks. Using the formula for the sum of a geometric series we can approximate this by the degree  $K$  polynomial

$$p_K(\zeta) = A \sum_{k=1}^K \left(\frac{\zeta}{a}\right)^k - B \sum_{k=1}^K \left(-\frac{\zeta}{b}\right)^k.$$

For  $K \leq 6$  the polynomial approximation  $p_K(\zeta)$  corresponding to (5.3.12) does not represent a conformal map as the boundary self-intersects; however, for all larger  $K$  we can use  $p_K(\zeta)$  to test the performance of the proposed methods.

To test the accuracy and reliability of the methods we considered the polynomial  $p_{60}$ , generated 1000 points  $\tilde{\zeta}_m$  inside the unit disk and computed their images  $\tilde{z} = p_{60}(\tilde{\zeta}_m)$ . For each of the numerical methods listed above we attempted to solve the polynomial equation  $p_{60}(\tilde{\zeta}) - \tilde{z} = 0$  for  $\tilde{\zeta}$ . The solution was considered correct if it differed from  $\tilde{\zeta}$  by less than  $10^{-8}$ . The tolerances for Newton's method, `fsolve` and `lsqnonlin` were set to  $10^{-10}$  to ensure they met this requirement. Newton's method did not find the root in 18 (1.8%) of the trials, in each case converging to a root outside of the unit circle. Both `lsqnonlin` and the argument principle method failed in 1 (0.1%) of the trials, both finding the correct root but not within the required tolerance. All of the other methods met the tolerances in every trial.

The companion matrix and argument principle methods consistently found

the correct root to the desired tolerance and do not rely on initial guesses. These methods are the most desirable from the perspectives of accuracy and reliability. Newton's method, `fsolve` and `lsqnonlin` generally also produced accurate results; however, Newton's method sometimes converged to the wrong root. This behaviour was also displayed by `lsqnonlin` but much less frequently. This means that the methods are converging to a root outside of the unit disk. To overcome this we modified these methods so that if the root found had absolute value greater than 1 the `eig` method was called. To test the speed of the methods we randomly generated 200 points and images for each  $p_K$  for  $K = 10, \dots, 150$ , with the tolerances set as before. The solution times for each method were recorded and the mean computation times for each method are shown in Figure 5.3.13.

For polynomials of degree 39 or less the companion matrix method using `eig` is the fastest method, slightly ahead of `roots`; however, both of these companion matrix methods became slower as the degree increased. For polynomials of degree 40 or more Newton's method, which performs at a similar speed for polynomials of all degrees investigated, is fastest. Beyond 75 the companion matrix methods show a rapid increase in computational time and perform worse than `fsolve`, which is likely due to hardware limitations arising from the matrices used. Based on these results, we use `eig` for polynomials of degree 39 or less, while for higher-degree polynomials we use Newton's method, check the root is inside the unit circle and revert to `eig` if not.

### 5.3.6 Calculating Geometric Quantities

As for the previous spectral method we are interested in the total boundary length  $\Gamma$ , which is needed in the axial problem. Each boundary  $C_n$  can be

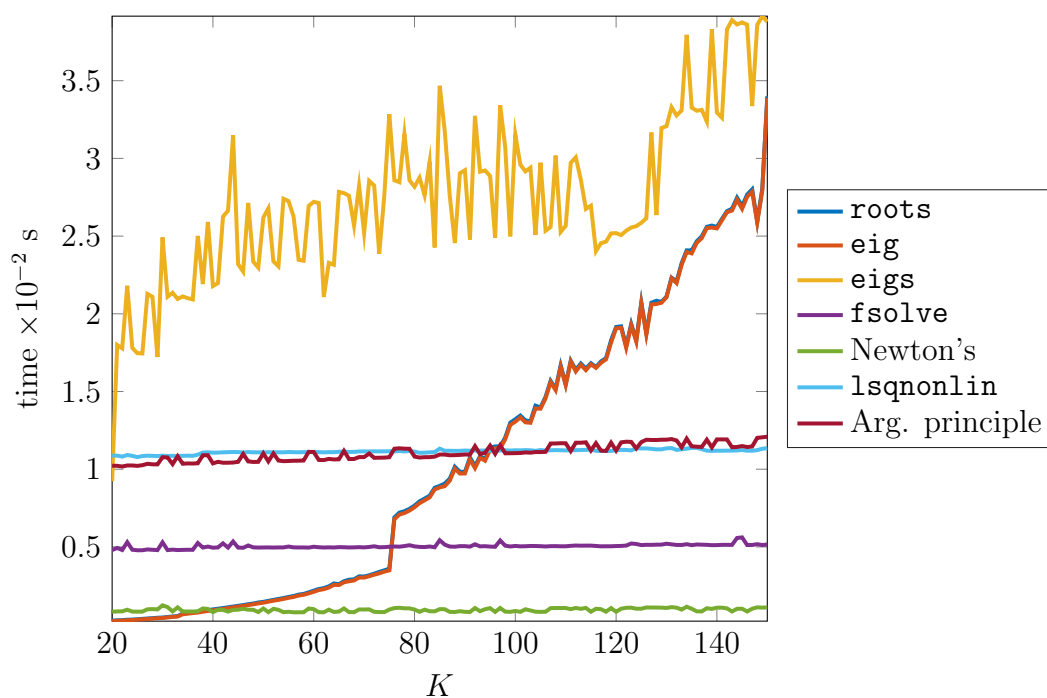


Figure 5.3.13: The mean computation times in seconds of the algorithms for finding the zeros of a polynomial of order  $K$ . The curves for the MATLAB functions `roots` and `eig` are almost identical as these are essentially the same method. For polynomials of degree 39 or less the companion matrix method using `eig` is the fastest method, while for polynomials of degree 40 or more Newton's method is fastest.

described by  $z = z_n(\zeta)$  for  $\zeta = e^{i\theta}$ ,  $\theta \in [0, 2\pi)$ . With this representation, we find that

$$\frac{\partial z_n}{\partial \theta} = i\zeta \frac{\partial z_n}{\partial \zeta}.$$

Using (4.2.34), the total boundary length is thus

$$\Gamma = \sum_{n=0}^N \int_0^{2\pi} \left| \frac{\partial z_n}{\partial \zeta} \right| d\theta,$$

while (4.2.35) shows that the area is

$$S = \int_0^{2\pi} \frac{\overline{z_0(\zeta(\theta))}}{z_0(\zeta(\theta))} \frac{\partial z_0}{\partial \zeta} i\zeta(\theta) d\theta - \sum_{n=1}^N \int_0^{2\pi} \frac{\overline{z_n(\zeta(\theta))}}{z_n(\zeta(\theta))} \frac{\partial z_n}{\partial \zeta} i\zeta(\theta) d\theta.$$

### 5.3.7 Convergence and Comparison with Known Solutions

Like the spectral method described in Section 5.2, the series used in this method are effectively Fourier series computed by satisfying the boundary conditions. As such, the error in this method again decreases, at least, geometrically as the number of terms in the truncated series increases. Due to this similarity we do not include an example of this convergence.

As a verification of this method we again compare the solution for an annulus with the exact solution. To match the previous comparison for the first spectral method we use an annulus with inner radius 0.5 and unit outer radius. The spectral method is integrated using the fourth-order Runge-Kutta method with a reduced-time step of  $10^{-2}$  up to  $\tau = 0.73$ , just before the internal hole closes. The exact and numerical solutions are plotted in Figure 5.3.14, where we observe that the two match to a high degree of accuracy.

Both the alternative spectral method and the method from Section 5.2 may be further validated by comparing the solutions found for the 3-hole preform

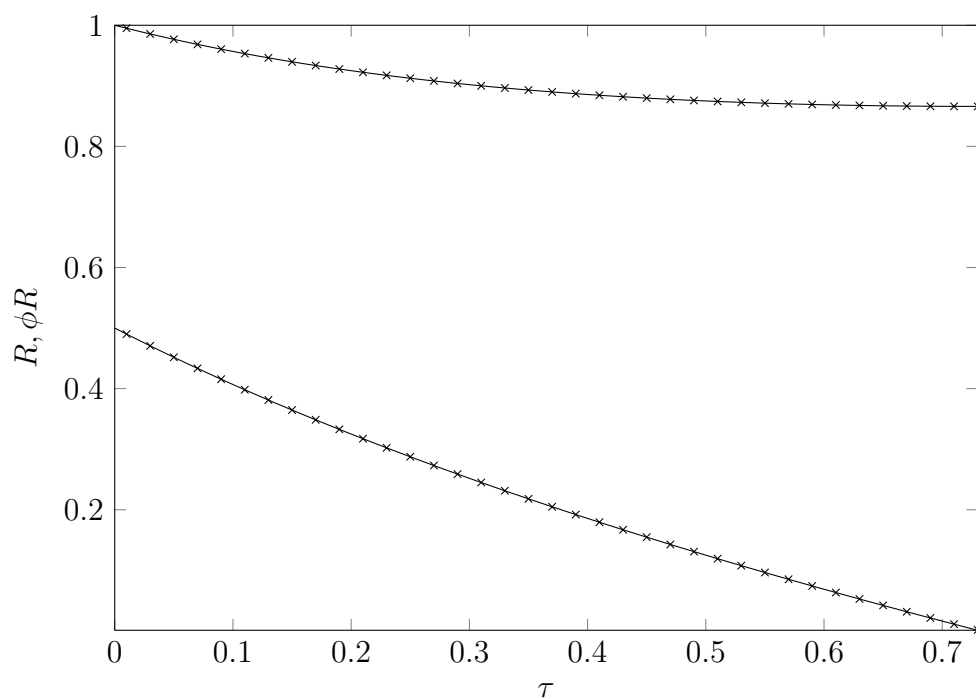


Figure 5.3.14: The inner radius  $\phi R$  and outer radius  $R$  of an annular region of fluid with initial inner radius 0.5 and unit outer radius. Shown are the exact radii (solid lines) and numerical solution calculated using the alternative spectral method (crosses). The spectral method was integrated using a fourth-order Runge-Kutta method with a reduced-time step of  $10^{-2}$  up to  $\tau = 0.73$ , just before the internal hole closes. The two solutions show very good agreement.

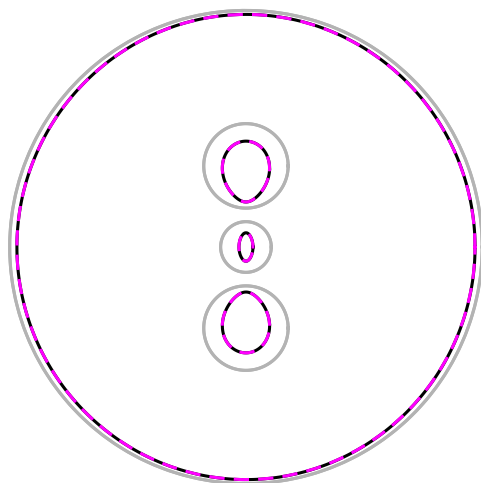


Figure 5.3.15: The solution for the 3-hole preform described in Table 5.2.1 at reduced time  $\tau = 0.06$ . Shown are the initial condition (grey), the solution from the first spectral method (black) and the solution from the alternative spectral method (purple). The two spectral methods show very good agreement.

described in Table 5.2.1, which, for comparison, are shown in Figure 5.3.15 at reduced time  $\tau = 0.06$ . We observe that both methods produce solutions that are identical to graphical accuracy, which suggests that both spectral methods are solving the problem correctly.

### 5.3.8 Application to Elliptical Boundaries

In certain MOF preforms initially circular boundaries become elliptical during the extrusion process. If such deformations are due to surface tension it could be possible to prevent this by starting with a geometry featuring ellipses with the opposite eccentricity. It is thus of interest to investigate geometries featuring elliptical inner boundaries. Applying the original spectral method to such examples would require the use of some method to generate a suitable

conformal map to describe the initial geometry. Using the alternative method developed here we need only find maps from the unit circle to each ellipse individually. We here show how this can be achieved analytically and present some sample cases to demonstrate the method.

### Mapping the Unit Circle to an Ellipse

We first consider mapping the exterior of the unit circle to the exterior of an ellipse. Let  $a, b \in \mathbb{R}$  with  $a > b$  and consider the Joukowski transformation

$$z(\zeta) = \frac{a+b}{2}\zeta + \frac{a-b}{2}\frac{1}{\zeta}.$$

Applying this to the unit circle  $\zeta = e^{i\theta}$ ,  $\theta \in [0, 2\pi]$ , gives

$$\begin{aligned} z(e^{i\theta}) &= \frac{a+b}{2}e^{i\theta} + \frac{a-b}{2}e^{-i\theta} \\ &= \frac{a+b}{2}(\cos(\theta) + i\sin(\theta)) + \frac{a-b}{2}(\cos(\theta) - i\sin(\theta)) \\ &= a\cos(\theta) + ib\sin(\theta). \end{aligned}$$

Thus, the Joukowski transformation takes the exterior of the unit circle to the exterior of an ellipse centred on the origin with major axis of length  $a$  aligned along the real axis and minor axis of radius  $b$  aligned along the imaginary axis. Multiplying by  $e^{i\phi}$  and adding  $z_c$  results in an ellipse with the same proportions but with centre  $z_c$  and with the major axis at an angle  $\phi$  to the real axis. This corresponds to the map

$$z(\zeta) = z_c + \frac{(a+b)e^{i\phi}}{2}\zeta + \frac{(a-b)e^{i\phi}}{2}\frac{1}{\zeta}.$$

This has the same form as the map (5.3.9) used in the alternative spectral method so can be used to construct initial maps with elliptical inner boundaries. The map has a singularity at  $\zeta = 0$  so cannot be used to map the interior of the

unit circle to the interior of an ellipse. This is a much more complicated problem and is not possible using only elementary functions (Ivanov and Trubetskov, 1994). For completeness we show how this may be done using the result derived by Nehari (1975), and attributed to Schwarz by Szegö (1950). Consider an ellipse in the  $z$ -plane with major radius  $a > 1$  and minor radius 1. This is mapped to the unit circle in the  $\zeta$ -plane by

$$\zeta(z) = \sqrt{k} \operatorname{sn} \left( \frac{2K(k)}{\pi} \sin^{-1} \left( \frac{z}{\sqrt{a^2 - 1}} \right), k \right).$$

Here,  $\operatorname{sn}(\cdot, k)$  is a Jacobi elliptic function and  $K(k)$  is the complete elliptic integral of the first kind, both with modulus  $k$ . We can write  $K(k) = F(1, k)$ , where

$$F(x, k) = \int_0^x \frac{1}{\sqrt{(1-t^2)(1-k^2t^2)}} dt$$

is the incomplete elliptic integral of the first kind. Following Karageorghis and Smyrlis (2008), this map may be inverted to give

$$z(\zeta) = \sqrt{a^2 - 1} \sin \left( \frac{\pi}{2K(k)} F \left( \frac{\zeta}{\sqrt{k}}, k \right) \right).$$

To use this map in the numerical method we would need to compute an expansion in the same form as the interior–interior map (5.3.10), which could be achieved by taking a discrete Fourier transform (see Chapter 8); however, MOFs typically do not feature elliptic outer boundaries and, as such, this is not of interest to the present problem.

### 5.3.9 3-Hole Preforms with an Elliptical Central Hole

As an example of the alternative spectral method we revisit the 3-hole geometries investigated in Subsection 5.2.10. From Figure 5.2.6 we observe that all three holes deform due to surface tension, with the central hole becoming

approximately elliptical due to the influence of the two outer holes. It was noted by Manning (2011, p. 205) that, while the two outer holes may vary in shape, the central hole must stay circular so as to fit the cane. We thus here consider a strategy for keeping the central hole circular.

At reduced time  $\tau = 0.06$  the central hole may be approximated by an ellipse with aspect ratio of approximately 2.0254. We thus take an initial condition in which the central circular hole has been replaced by an ellipse with the same aspect ratio but with the major and minor axes swapped. Note that an appropriate initial condition can be found directly using the results from above, which could not be achieved with the original spectral method. This geometry is then evolved forwards in reduced time until  $\tau = 0.06$ . The resulting geometry is shown in Figure 5.3.16a. The major and minor radii are, approximately,  $3.3447 \times 10^{-2}$  and  $2.8656 \times 10^{-2}$ , respectively, which correspond to the aspect ratio 1.1672. The mean of the major and minor radii is  $3.1051 \times 10^{-2}$ , and a circle with this radius is superimposed on the actual boundary in Figure 5.3.16b. We conclude that from this initial configuration we obtain a geometry with a central hole that is approximately circular.

## 5.4 Method of Fundamental Solutions

### 5.4.1 Motivation

The numerical methods described in Section 5.2 and Section 5.3 both construct solutions to the two-dimensional Stokes flow problem by describing the geometry using conformal mappings that are described by a set of parameters, and computing the reduced-time evolution of these parameters. Whilst both methods have been shown to agree with an exact solution, we also wish to test

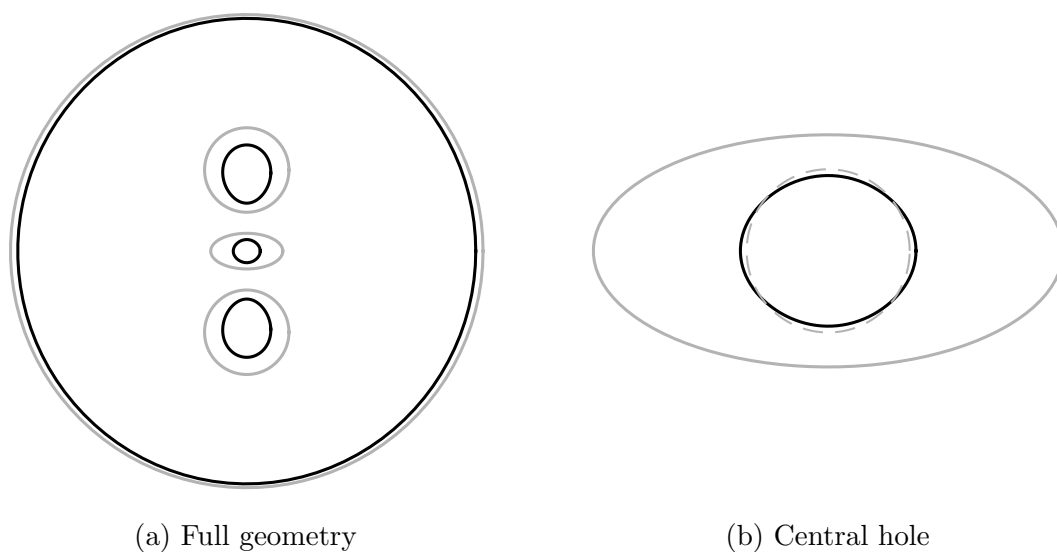


Figure 5.3.16: The 3-hole geometry starting with an elliptical central hole with aspect ratio 2.0254. The initial geometry is shown in grey and the geometry at  $\tau = 0.06$  in black. At the later reduced time the central hole has become approximately circular. The major and minor radii are  $3.3447 \times 10^{-2}$  and  $2.8656 \times 10^{-2}$ , respectively, which correspond to the aspect ratio 1.1672. Shown right is a magnification of the central hole. For comparison, a circle has been superimposed with radius  $3.1051 \times 10^{-2}$ , which is the mean of the major and minor radii (grey dashed).

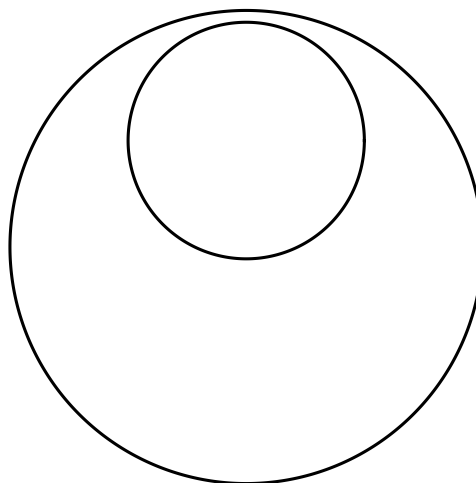


Figure 5.4.17: The initial condition for a two-dimensional Stokes flow problem solved by van de Vorst (1993). The outer boundary is a circle with unit radius centred on the origin, while the inner boundary has radius 0.5 and centre 0.45.

these methods against more complicated cases. In general, such cases will not admit an exact solution (or, at least, an exact solution has not yet been found) so we cannot provide a similar comparison as was done previously. There are two sources for solutions available: (1) solutions from the literature; and (2) solutions found by a fundamentally different numerical method. In this section we will explore both options.

As a comparison from the literature we consider a solution found by van de Vorst (1993) for a disk centred on the origin with unit radius and an off-centre circular interior boundary with radius 0.45 and centre 0.45, shown in Figure 5.4.17. This geometry also provides the opportunity to study the formation of cusp-like shapes. If such deformations can arise due to surface tension and a collapsing inner boundary we would expect an extreme case such as Figure 5.4.17 to display this behaviour.

As an alternative numerical method we will employ the method of funda-

mental solutions (MFS). This does not make use of conformal maps so provides a significantly different approach to the methods used so far. The MFS is outlined in the following subsection.

### 5.4.2 Overview of Method

Let  $\mathcal{L}$  be a partial differential operator and consider the homogeneous problem

$$\mathcal{L}u(z) = 0, \quad z \in \Omega. \quad (5.4.13)$$

A fundamental solution for  $\mathcal{L}$  is a function  $P(z, z_0)$ ,  $z_0 \notin \Omega$ , such that

$$\mathcal{L}P(z, z_0) = \delta(z_0).$$

A fundamental solution  $P$  is defined everywhere except for at the singularities  $z_0$ . The MFS attempts to construct a solution to (5.4.13) using a linear combination of fundamental solutions, which has the form

$$u(z) = \sum_{n=1}^N c_n P(z, z_n),$$

where the coefficients  $c_n$  are constants. The locations of the singularities can be fixed or determined as part of the solution process. The coefficients can be found by minimising the error in the boundary condition using a least squares fit.

### 5.4.3 Mathematical Formulation

We present a formulation of the MFS that makes use of the complex variable theory developed in this chapter and a novel set of singularities appropriate for the Stokes flow problem under consideration.

Suppose that the domain consists of  $N$  inner boundaries denoted  $C_n, n = 1 \dots N$ , and an outer boundary  $C_0$ . Each boundary is represented as a finite set of discrete points, rather than as a map from a canonical domain as was done for the previous numerical methods. At each reduced time the Goursat functions are constructed from a linear combination of fundamental solutions placed outside the fluid domain.

Typically, the fundamental solutions used are Stokeslets, which correspond to the Goursat functions

$$\begin{aligned} f(z) &= B \log(z - z_0), \\ g'(z) &= -\frac{B\bar{z}_0}{z - z_0} - \bar{B} \log(z - z_0). \end{aligned}$$

Physically, a Stokeslet represents a point force acting at  $z_0$ ; however, the Stokes equations imply that there is zero net force acting on the fluid. Instead, we use a stresslet, which corresponds to the limit as two Stokeslets of equal magnitude but opposite direction move closer together at a rate inversely proportional to their separation (Crowdy and Or, 2010). This ensures there is no net force within the fluid. Stresslets are placed around each boundary, while a source/sink is placed inside each interior boundary, as illustrated in Figure 5.4.18. This corresponds to the Goursat function representations

$$f(z) = \sum_{n=0}^N \sum_{j=1}^J \frac{B_{n,j}}{z - z_{n,j}}, \quad (5.4.14a)$$

$$g'(z) = \sum_{n=0}^N \sum_{j=1}^J \frac{B_{n,j} \bar{z}_{n,j}}{(z - z_{n,j})^2} + \sum_{n=1}^N \frac{Q_n}{z - c_n}, \quad (5.4.14b)$$

where  $z_{n,j}$  is a stresslet location, which lies around the outside of the  $n$ th boundary,  $B_{n,j}$  is a stresslet strength,  $c_n$  is a source/sink location and lies within the  $n$ th inner boundary and  $Q_n$  is a source/sink strength.

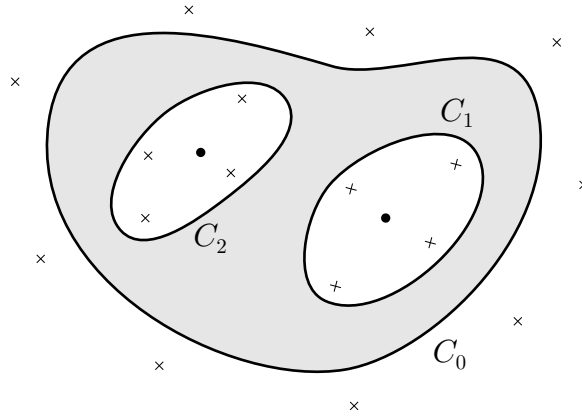


Figure 5.4.18: A sketch of the singularity locations using the method of fundamental solutions for a triply connected region. Stresslets (crosses) are placed around each boundary while a source/sink (dot) is placed inside each interior boundary. All of these singularities lie outside of the fluid.

The coefficients  $B_{n,j}$  and  $Q_n$  are determined by the dynamic boundary condition (4.2.27) which holds on the  $C_n, n = 0 \dots N$ , and states that

$$f + z\bar{f}' + \bar{g}' = -\frac{i}{2}z_s + A_n,$$

where the  $A_n$  are unknown constants that must be determined as part of the solution. This is achieved by evaluating this condition at a number of collocation points placed on the boundaries and finding the solution that minimises the square error. Substituting the expressions from (5.4.14) yields the equation

$$\sum_{n=0}^N \sum_{j=1}^J \frac{1}{z - z_{n,j}} B_{n,j} - \frac{z - z_{n,j}}{(z - z_{n,j})^2} \bar{B}_{n,j} + \sum_{n=1}^N \frac{1}{z - c_n} \bar{Q}_n - \sum_{n=0}^N A_n = -\frac{i}{2}z_s, \quad (5.4.15)$$

at each collocation point  $z$ . This condition specifies the solution up to an arbitrary rigid-body translation and rotation, which represent three degrees of freedom. In practice these are removed by fixing some point and an angle within the domain.

The precise solution method depends on how the locations  $z_{n,j}$  and  $c_n$  of the fundamental solutions are selected. The location of the singularities is of great importance as the choice affects both the convergence and accuracy of the solutions (Boselli *et al.*, 2012). The locations may either be predetermined (Young *et al.*, 2006; Aboelkassem and Staples, 2013) or set as part of the solution procedure (Karageorghis and Fairweather, 1987, 1989). By fixing the locations, condition (5.4.15) is linear in all the unknown terms, which is relatively simple to solve. If the locations are determined as part of the solution then (5.4.15) is non-linear in the unknowns. In this thesis we fix the location of the singularities, which allows the solution of (5.4.15) by a least-squares linear system. This is achieved by modifying the method presented by Young *et al.* (2006).

Let  $\delta$  be a small parameter that characterises the distance between the boundary and singularities. To each set of boundary points we fit a cubic spline interpolant with a periodic endpoint condition and use this to generate  $L$  points on each boundary,  $b_{n,l}, l = 1, \dots, L$ . The mean of the  $n$ th set of boundary points  $m_n$  is also calculated. On each inner boundary we set the locations by

$$z_{n,l} = b_{n,l} + \delta(m_n - b_{n,l}).$$

This shifts the points  $b_{n,l}$  towards the centre of the hole. On the outer boundary we take

$$z_{0,l} = b_{0,l} - \delta(m_0 - b_{0,l}),$$

which instead moves the points *away* from the centre. We here take  $\delta = 0.1$ , which has been found to provide accurate solutions. The sources inside each inner boundary are placed at the points  $m_n$ . For convex boundaries this method ensures that the singularities are located outside of the fluid domain. For concave regions we could instead shift the points  $b_{n,l}$  in the direction normal

to the boundary; however, this can result in singularities inside the domain as inner boundaries close. The problem of determining better algorithms for setting the singularity locations, including determining these locations as part of the solution process and making use of multiple layers of singularities, is left to future work. The cubic splines are also used to calculate the arc length derivative  $z_s$  used in (5.4.15). With the singularity locations fixed, (5.4.15) is linear in the unknowns  $B_{n,j}$ ,  $\bar{B}_{n,j}$  and  $\bar{Q}_n$ , so that evaluating this boundary condition at the collocation points yields a system of linear equations that may be written in the form  $M\mathbf{x} = \mathbf{b}$ , which is readily solved.

Once the coefficients in the Goursat functions (5.4.14) are known we can calculate the velocity at each of the boundary points. Using the kinematic boundary condition we can then integrate these points forward in reduced time to find the shape of the boundary at the next time step. The process is then repeated until the desired reduced time is reached.

The total boundary length  $\Gamma$  and area  $S$  are readily computed by substituting the cubic splines fitted to the boundary points into (4.2.34) and (4.2.35), respectively.

#### 5.4.4 Convergence

We define the error in the dynamic boundary condition by

$$e_s(J) = \|M\mathbf{x} - \mathbf{b}\|/\|\mathbf{b}\|,$$

which is a function of the number of stresslets  $J$  placed around each boundary. To illustrate the behaviour of this error we again consider the geometry from Figure 5.2.2 and compute  $e_s$  at reduced time  $\tau = 0$  for different values of  $J$ , as plotted in Figure 5.4.19. Like the spectral methods,  $e_s$  decreases geometrically

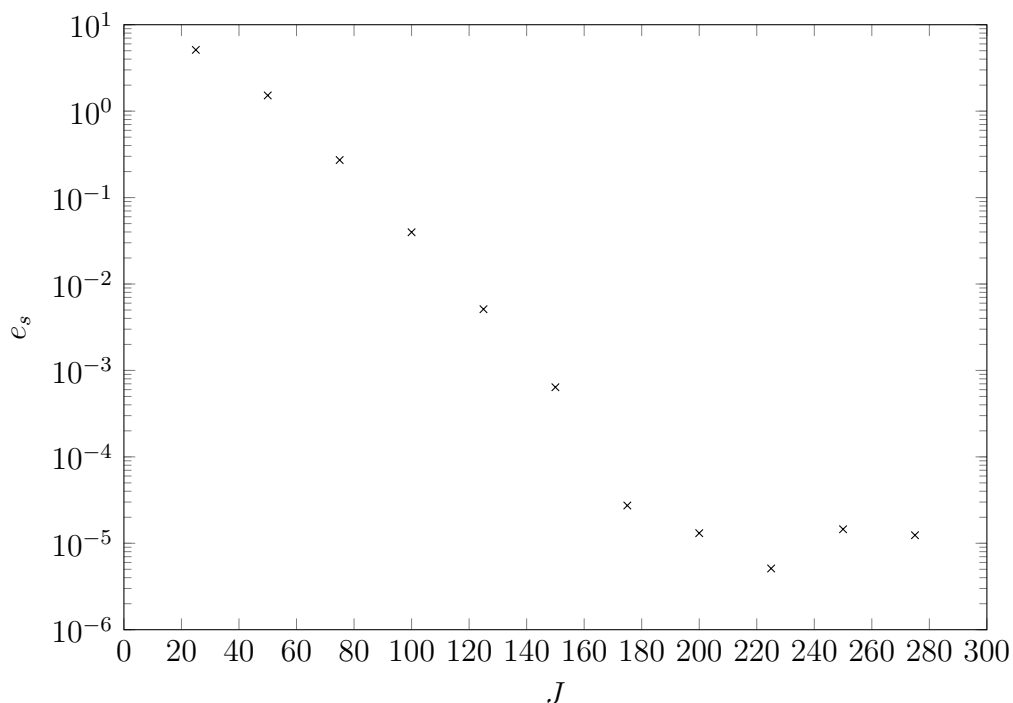


Figure 5.4.19: The error in the MFS dynamic boundary condition  $e_s$  at reduced time  $\tau = 0$  plotted against the number of stresslets  $J$  around each boundary. The error decreases at an approximately geometric rate.

as  $J$  increases; however, the rate of this decrease is an order of magnitude smaller, and does not reach the minimum until  $J \approx 200$ . Thus, the MFS is not as efficient as the spectral methods.

### 5.4.5 Comparison with Exact Solution

We first verify the MFS solution against the exact solution for an annulus with inner radius 0.5 and unit outer radius, with each boundary represented by 100 points. We place 100 stresslets around each boundary and perform the reduced-time integration using a fourth-order Runge-Kutta method with step

size  $10^{-2}$ . The radii from this solution are plotted along with the exact solution in Figure 5.4.20, from which we observe that the exact and numerical solutions show good agreement.

### 5.4.6 Van de Vorst Example and Comparison of Methods

We now return to the motivating example shown in Figure 5.4.17. The solutions at  $\tau = 0.25$  calculated using both the spectral method from Section 5.2 and the MFS are shown in Figure 5.4.21, along with the solution found by van de Vorst (1993). The solution using the spectral method is computed using 100 terms in each series on each boundary. The MFS solution was found using 200 points and 200 stresslets for each boundary, while the degrees of freedom were fixed by forcing points on the imaginary axis to stay purely imaginary, which removes the rotation, and fixing a point on the real axis, which removes the translation. We observe that the two numerical solutions computed here show very good agreement, which suggests that both are working correctly. The solution of van de Vorst features a more-pronounced cusp-like point where the outer and inner boundaries are nearest, which is not found in the other two solutions. Away from this region all three outer boundaries are similar.

In the context of fluid cylinders with surface tension, this result suggests that, even with the closure of a large interior hole, surface tension alone cannot cause the outer boundary to form cusp-like regions, such as those observed in extruded 3-hole preforms like that shown in Figure 1.1.3e.

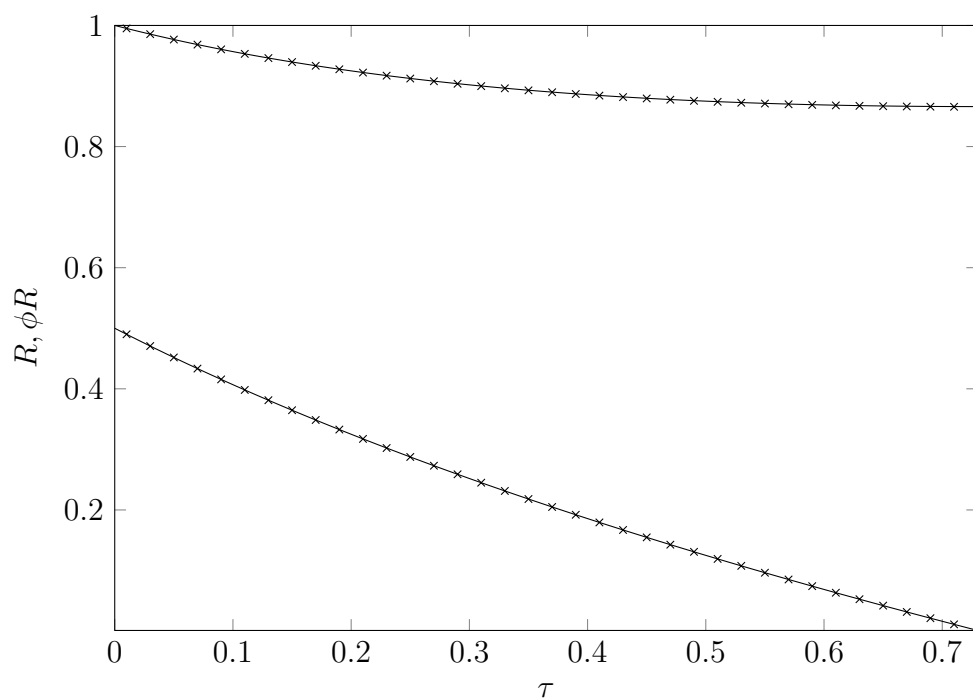


Figure 5.4.20: The evolution of the inner and outer radii  $\phi R$  and  $R$ , respectively, of an annulus with initial inner radius 0.5 and unit outer radius. Shown are the exact radii (solid lines) and numerical solution calculated using the method of fundamental solutions (crosses). The numerical solution used 100 points and 100 stresslets for each boundary. The time evolution was computed using a fourth-order Runge-Kutta method with a reduced-time step of  $10^{-2}$  up to  $\tau = 0.73$ , just before the internal hole closes. The two solutions show very good agreement.

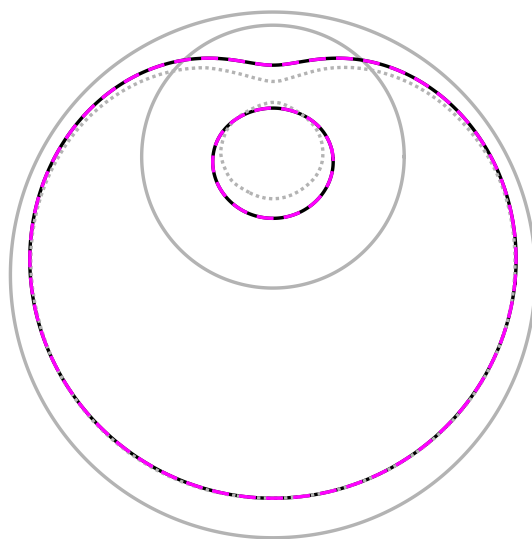


Figure 5.4.21: A comparison between the solutions at  $\tau = 0.25$  for the geometry shown in Figure 5.4.17 as found by van de Vorst (1993) (grey dots), the spectral method (solid black) and the method of fundamental solutions (purple dashes). The spectral and stresslet solutions are almost identical. The two boundaries from the van de Vorst solution show a greater deviation towards one another. Away from this region all three outer boundaries are similar.

## 5.5 Elliptical Pore Models

### 5.5.1 Overview of Method

We conclude by considering one final method for computing the evolution of Stokes flows under surface tension known as the elliptical pore model (EPM). The first version of this model was introduced by Crowdy (2004) and was based upon the earlier observation (Crowdy, 2003a) that elliptical bubbles in a linear Stokes flow remain elliptical as they evolve in reduced time. The model considers  $n$  such elliptical bubbles in an infinite fluid region. Under the above assumptions, the  $n$ th bubble can be described by a conformal map from the unit circle  $\zeta \in \mathbb{C}, |\zeta| = 1$  of the form

$$z = z_n(\zeta, \tau) = c_n(\tau) + \frac{\alpha_n(\tau)}{\zeta} + \beta_n(\tau)\zeta,$$

where  $\alpha_n(\tau) \in \mathbb{R}$  and  $\beta_n(\tau) \in \mathbb{C}$  are parameters that describe the dimensions of an ellipse centred at  $c_n(\tau) \in \mathbb{C}$ . The EPM models each boundary around the  $n$ th bubble as a point sink, and uses this assumption to calculate a system of ordinary differential equations for the reduced-time derivatives of  $c_n(\tau)$ ,  $\alpha_n(\tau)$  and  $\beta_n(\tau)$ . These are solved much more efficiently than the original moving boundary problem; however, it is important to note that the EPM is strictly only valid when the bubbles are sufficiently far apart and can become numerically unstable if this assumption is not met.

Motivated by the study of MOFs, the original model was extended by Buchak *et al.* (2015) to model the evolution of elliptical bubbles in a finite, circular fluid region. A stresslet singularity was added to each bubble, in addition to the sink, in order to give a more-accurate representation of the fluid flow. Under this model, the outer boundary is assumed to remain circular;

however, it has been shown to perform well for some typical MOF designs (Buchak *et al.*, 2015). In this thesis the extended model will also be referred to as the EPM.

Due to their complexity we do not record the evolution equations here and instead direct the reader to the original article by Buchak *et al.* (2015). We will, however, make use of the extended EPM to analyse some complicated geometries that would prove time consuming using one of the full numerical methods described previously in this chapter.

## 5.5.2 $n$ -Ring Preforms

### Overview

To illustrate the use of the EPM we here consider a family of preforms that feature circular holes arranged in concentric hexagonal layers. Following the notation of Ebendorff-Heidepriem and Monroe (2007), a preform of this type with  $n$  hexagonal rings shall here be denoted an  $n$ -ring preform. The geometry may be characterised by the distance between the centres of adjacent holes  $\Lambda$ , the diameter of the holes  $d$  and the outer radius  $R$ , which are illustrated in Figure 5.5.22 for the case  $n = 4$ . For fixed  $R$ , an  $n$ -ring preform may be described by the dimensionless ratio  $d/\Lambda$ .

### 4-Ring Preform

We first consider the 4-ring preform shown in Figure 5.5.22 with  $\Lambda = 3$  mm and  $d = 0.9$  mm, so that  $d/\Lambda = 0.3$ . The outer radius is taken to be  $R = 15$  mm and the domain is scaled to have unit area so as to match the transverse problem formulation. The evolution of the geometry is shown in Figure 5.5.23 at reduced

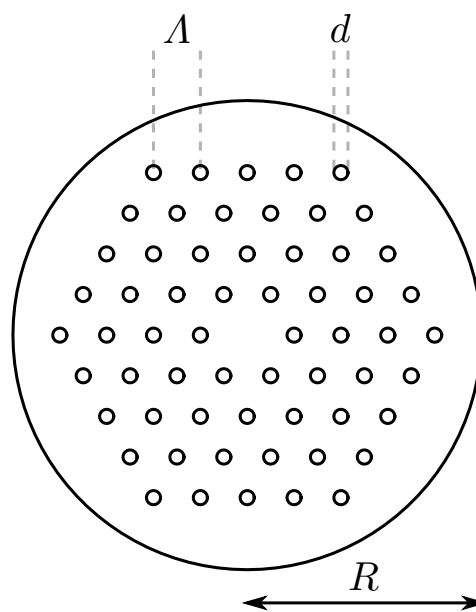


Figure 5.5.22: A schematic showing parameters for an  $n$ -ring preform (in this case  $n = 4$ ). The spacing between holes is denoted by  $\Lambda$  and the diameter of the holes by  $d$ . The notation and schematic used here is based upon that of Ebendorff-Heidepriem and Monro (2007).

times  $\tau = 0.005, 0.01, 0.015$  and  $0.02$ . Over this interval both the inner and outer boundaries reduce slightly in size. The inner holes also become elliptical, with this effect more pronounced in the outer rings than than the inner ring. These characteristics provide a good qualitative match to the experimental results of Ebendorff-Heidepriem and Monro (2007); however, in the latter each feature is much more pronounced.

Using this model we are able to investigate the effect of varying  $\Lambda$  on the final geometry, keeping both  $d$  and  $R$  fixed. We again consider a 4-ring preform with  $d = 0.9$  mm and  $R = 15$  mm, but take  $\Lambda = 1.2, 1.5, 2$  and  $2.5$ , which correspond to  $d/\Lambda = 3/4, 3/5, 9/20$  and  $9/25$ , respectively. For each of these designs we compute the geometry at reduced time  $\tau = 0.02$ , which are shown in Figure 5.5.24. From these we observe that as  $\Lambda$  decreases the inner holes become more elliptical. The orientation of the ellipses depends upon position. Boundaries in the inner ring have major axes tangential to the ring while on the corners of the outer ring the major axes are perpendicular to the ring. The sides of the outer ring are curved in shape, rather than straight. We note that the shape found for  $d/\Lambda = 3/4$  provides a very good qualitative match to the results of Ebendorff-Heidepriem and Monro (2007) for  $d/\Lambda = 0.3$ ; however, the ratio used in the model results in a more-densely packed collection of holes over a smaller area than the geometry used in the experiments.

### 7-Ring Preform

As a final example of an  $n$ -ring preform we consider the 7-ring geometry shown in Figure 5.5.25. Note that the six outermost holes have been removed leaving 162 holes. We take  $\Lambda = 2$  mm and  $d = 1$  mm, so that  $d/\Lambda = 0.5$ , with outer radius  $R = 15$  mm. The geometry is scaled to have unit area so as to match

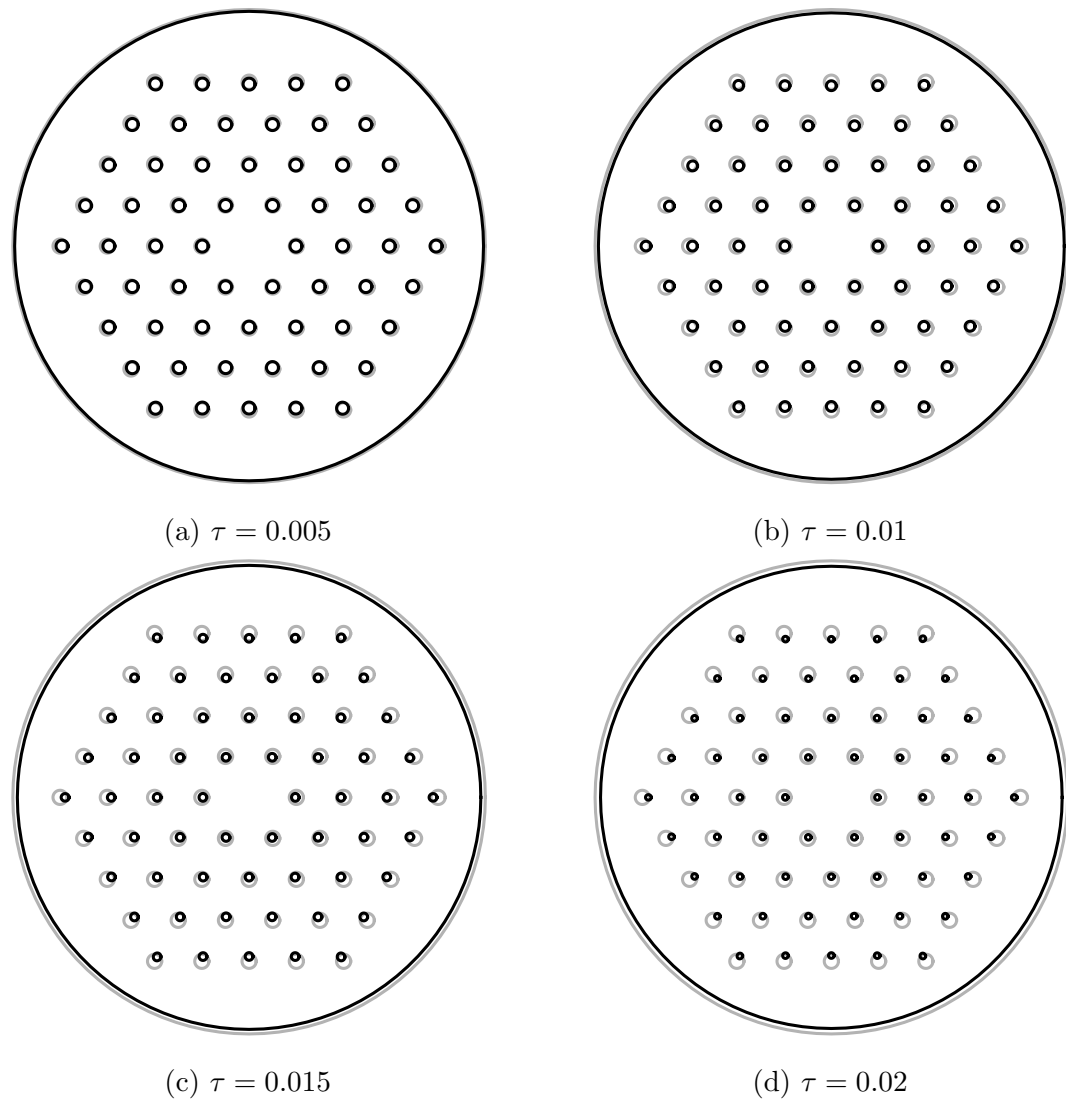


Figure 5.5.23: The evolution of the 4-ring preform geometry with  $\Lambda = 3$  mm,  $d/\Lambda = 0.3$  and  $R = 15$  mm at reduced times  $\tau = 0.005, 0.01, 0.015$  and  $0.02$ . The dark lines represent the geometry at the indicated reduced time while the light lines show the initial condition.

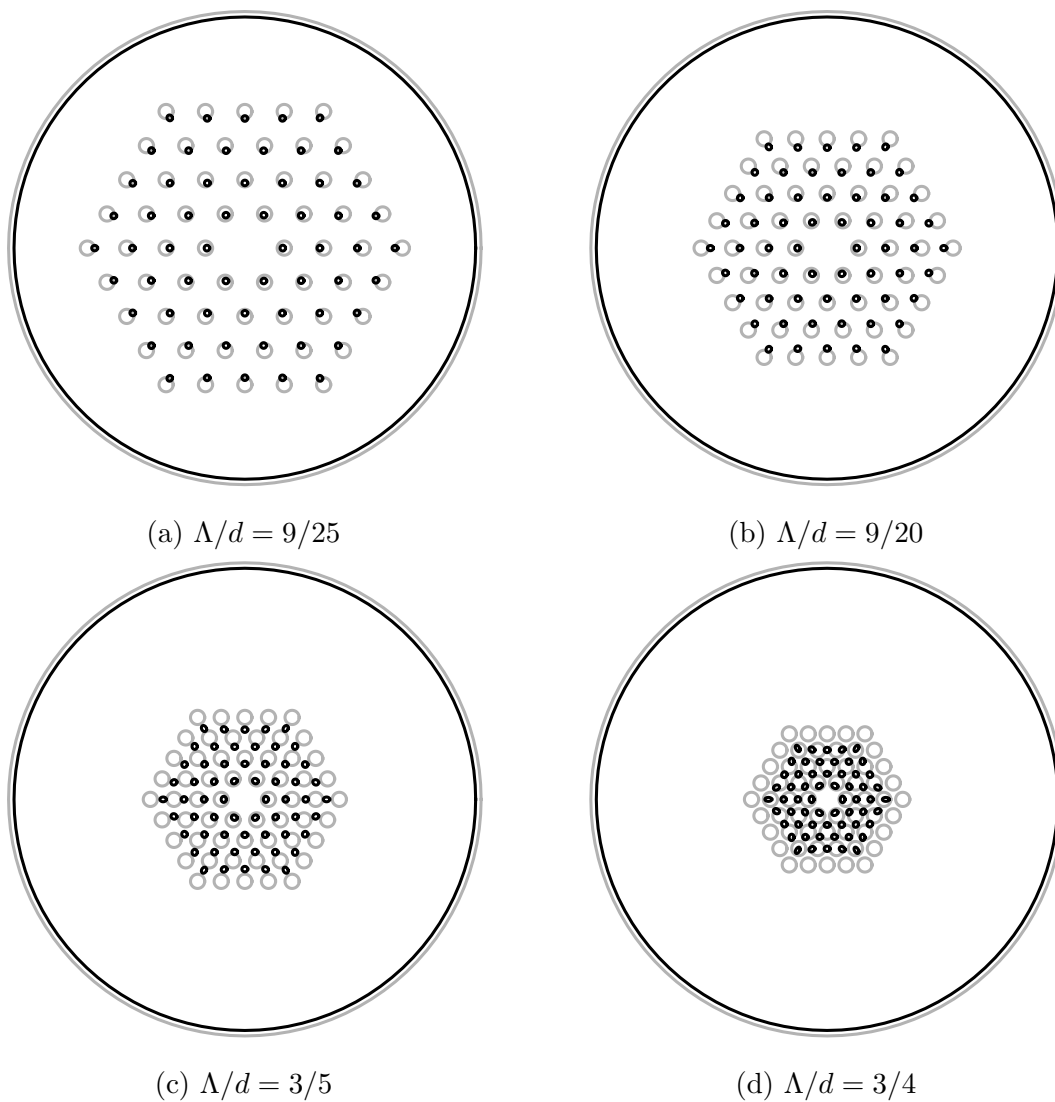


Figure 5.5.24: The evolution of the 4-ring preform geometry at reduced time  $\tau = 0.02$  for  $R = 15$  mm. Shown are geometries with  $\Lambda/d$  set to: (a)  $9/25$ , (b)  $9/20$ , (c)  $3/5$  and (d)  $3/4$ . The dark lines represent the geometry at the indicated reduced time while the light lines show the initial condition.

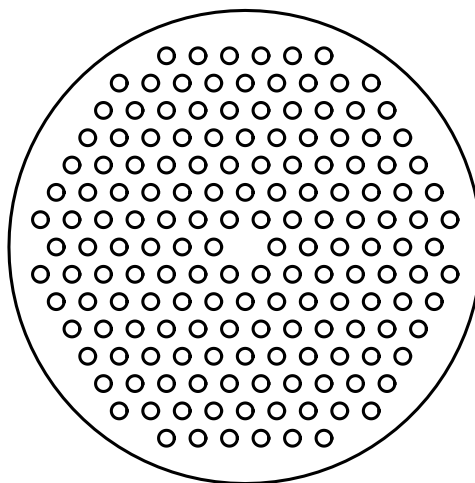


Figure 5.5.25: A 7-ring preform with  $\Lambda = 2$  mm,  $d/\Lambda = 0.5$  and  $R = 15$  mm. The six outermost holes have been removed leaving 162 holes.

the transverse problem formulation. The evolution of this design is shown in Figure 5.5.26 at reduced times  $\tau = 0.005, 0.01, 0.015$  and  $0.02$ . As in the 4-ring case, all the boundaries reduce in size. While the inner boundaries become somewhat elliptical all the holes remain close to circular. Like the 4-ring case, the model of the 7-ring design captures all of the experimental observations of Ebendorff-Heidepriem and Monroe (2007); however, each of these features are not as pronounced as in the experiments.

We conclude by considering two 7-ring designs again having  $d = 1$  mm and  $R = 15$  mm but with  $\Lambda = 1.5$  and  $\Lambda = 1.7$ , with ratios  $d/\Lambda$  of  $2/3$  and  $10/17$ , respectively. Each design is scaled so as to have unit area so as to match the transverse problem formulation. The geometries of both designs at reduced time  $\tau = 0.02$  are shown in Figure 5.5.27. As  $d/\Lambda$  increases the inner holes become more elliptical with orientations that depend upon location. Each corner of the outer ring features two ellipses with major axes directed towards the centre of the preform, while the major axes of the holes in the innermost ring are

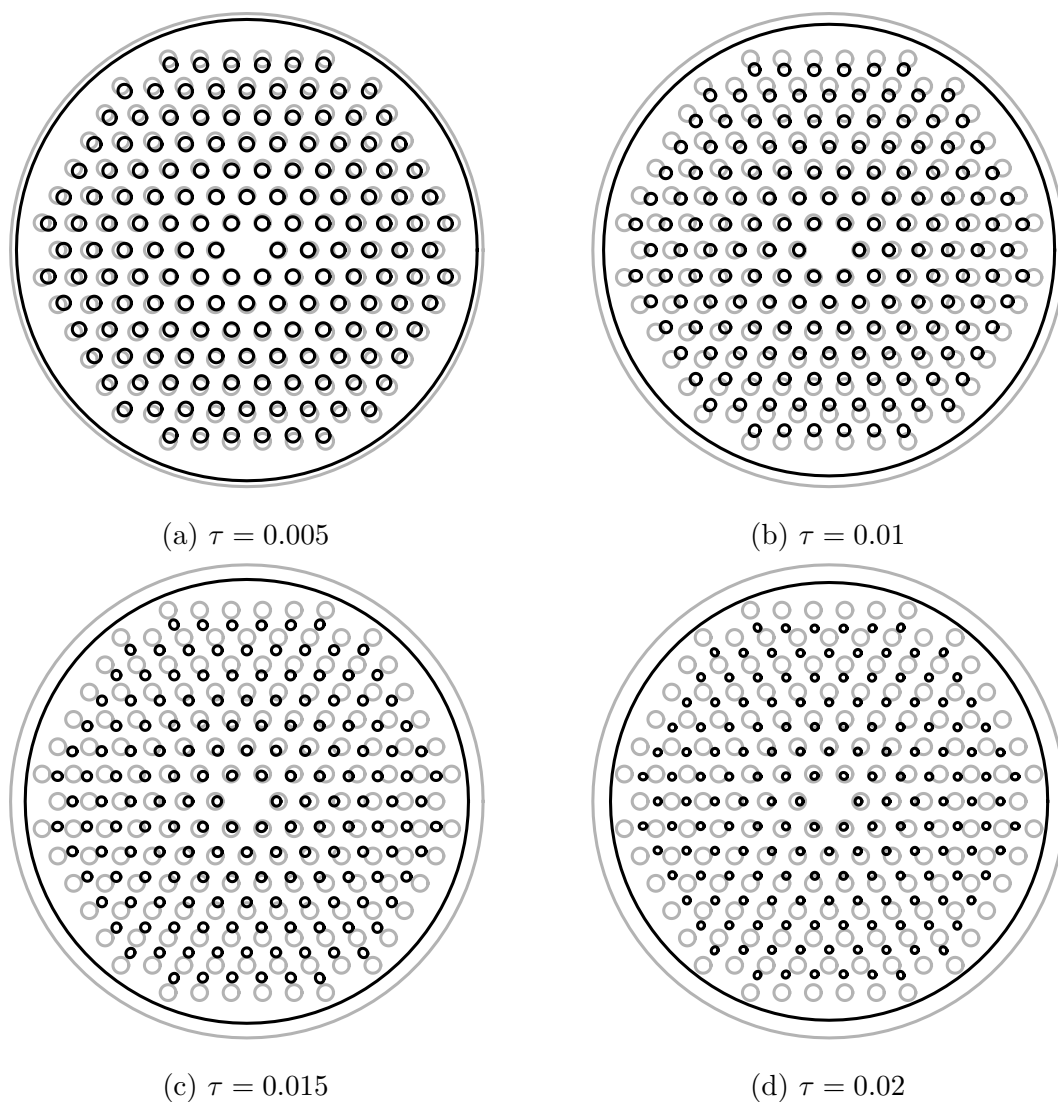


Figure 5.5.26: The evolution of the 7-ring preform geometry with  $\Lambda = 2$  mm,  $d/\Lambda = 0.5$  and  $R = 15$  mm, scaled to have unit area, at reduced times  $\tau = 0.005$ , 0.01, 0.015 and 0.02. The dark lines represent the geometry at the indicated reduced time while the light lines show the initial condition.

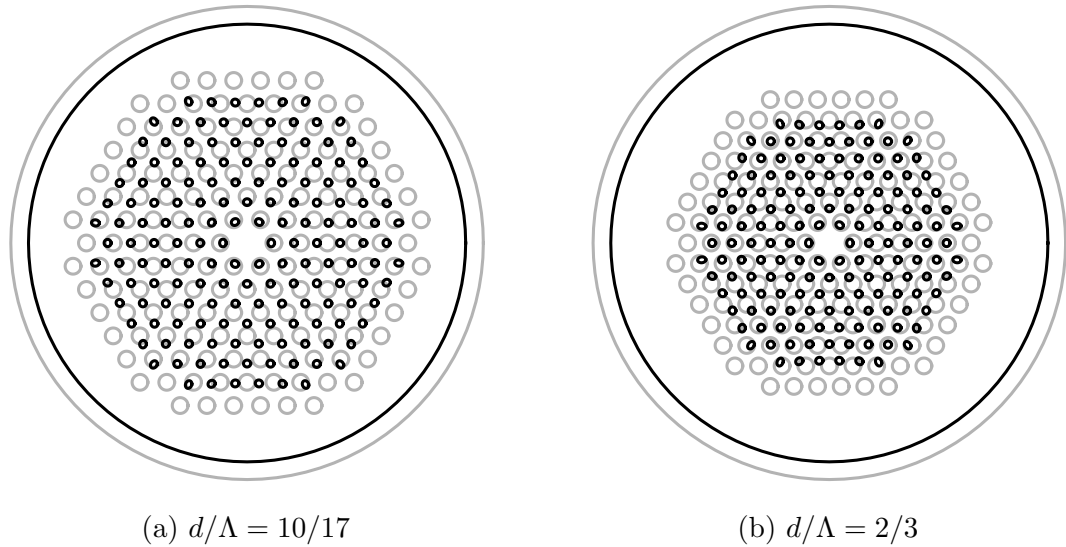


Figure 5.5.27: The evolution of 7-ring preform geometries for  $R = 15$  mm at reduced time  $\tau = 0.02$  with  $d/\Lambda$  equal to: (a)  $10/17$  and (b)  $2/3$ . The dark lines represent the geometry at the indicated reduced time while the light lines show the initial condition. As  $d/\Lambda$  increases the inner holes become more elliptical with orientations that depend upon location.

approximately tangential to the ring. Once again, increasing the value of  $d/\Lambda$  provides a better qualitative match to the results of Ebendorff-Heidepriem and Monro (2007) for  $d/\Lambda = 0.3$ ; however, the smaller ratio means that the pattern of internal holes is more-densely packed over a smaller area than in the experiment.

### Summary

The EPM provides an efficient solution to the transverse problem associated with MOF preform designs with many internal holes. Using this method we have investigated the evolution of cross sections corresponding to 4-ring

and 7-ring preforms. In both cases the surface-tension model captured all of the features observed in experiments; however, these features were not as pronounced. For each geometry, increasing the ratio  $d/\Lambda$  moved the internal holes closer together so that each felt a stronger influence from the others. This provided a better qualitative match to the original designs but produced geometries with a smaller scale. It thus appears that surface tension drives the observed deformations; however, in practice this effect may be modified by other factors not included in this model.

## 5.6 Summary

In general, the transverse problem (3.3.42) cannot be solved exactly and must instead be solved using numerical methods. We have considered four appropriate numerical methods, each of which is best suited to different cases. The first of these is a spectral numerical method that describes the domain using a conformal map from a multiply connected circle domain and may be applied to geometries of arbitrary connectivity. This method is both accurate and efficient, and, as such, will be the default numerical scheme used throughout this thesis. This method requires a suitable initial condition for the conformal map, which in some cases may be difficult to find. While methods based upon that of Fornberg (1980) can be used to generate appropriate initial conditions these still require an accurate initial guess in order to converge. The computation of appropriate initial conditions for some special cases of interest will be discussed in Chapter 8.

We have also developed an alternative spectral method for solving the transverse problem by extending the work of Cox and Finn (2007), which is

similar to the first spectral method but represents each boundary by a different conformal map. Because of this, the problem of finding the initial map is reduced to finding a map from the unit circle to each boundary individually. As an example, it was shown that the alternative spectral method can be given exact initial conditions for elliptical boundaries, which cannot be done with the first method.

In order to verify the two spectral methods we have developed a third numerical method using the method of fundamental solutions. The formulation given here is based upon the complex-variable representation described in Chapter 4, while the fundamental solutions used are stresslets and sources/sinks. We believe this is the first time the method has been formulated in this way. It was found that the MFS and spectral methods gave the same solutions.

The accuracy of the first spectral method and the MFS were compared using a test problem. It was shown that the error in the spectral method was minimised by using at least 30 terms in each series, while the MFS series required 200 terms to reach the minimum value, which is an order of magnitude larger. The alternative spectral method displays similar behaviour to the first spectral method but requires additional computation to invert the conformal maps. Thus, of these three methods the first spectral method provides the most efficient solution.

Finally, we described the elliptical pore method of Buchak *et al.* (2015). This method represents the inner boundaries using singularities, which is efficient for large numbers of inner boundaries, but only applies to geometries with elliptical inner boundaries and a circular outer boundary. The EPM was found to produce results similar to those seen in the extrusion of  $n$ -ring MOF preforms.

As discussed in Chapter 1, the deformations observed during MOF preform

extrusion can be classified broadly into three categories: changes in boundary shape; changes in interior hole location; and interior hole closure. The solutions and methods described in this chapter capture the first and second of these but some care must be taken with the third. The closure of an interior hole represents a significant change to the geometry; in particular, this represents a change to the connectivity. As such, this behaviour will typically require a modification to the solution method. In general, solutions will become singular at the point of closure so must be stopped once some condition representing closure is satisfied. Crowdy (2003*b*) considered a hole closed when its area was  $O(10^{-8})$ , while Richardson (2000) required the diameters to be  $O(10^{-10})$ , which corresponds to an area of  $O(10^{-20})$ . It is assumed that the hole is suitably small so that removing the hole does not significantly alter the dynamics. Thus, once the condition is met, we pause the method, replace the domain by an equivalent domain with the closed hole removed, and then restart the solution procedure. For example, in the case of the exact solution for an annulus, at the point in reduced time that the interior hole closes the domain must be replaced with a disk, which undergoes no further evolution. For the spectral numerical methods, a hole closure would require removing a boundary from the conformal map, while for the MFS we would need to delete a set of boundary points. In both cases the solution would need to be halted at the point of closure and the appropriate changes to the geometry made. As the MOF preforms under consideration here do not feature hole closure this problem will not be considered in this thesis.

Using the numerical methods we have solved the transverse problem for several geometries of interest. It was shown that the 6-hole, 7-hole and  $n$ -ring geometries all showed similar qualitative behaviour to that observed in

---

experiments. In some cases the features were not as pronounced as those seen in experiments, which may mean that there are additional effects that act in a similar manner to surface tension and enhance the deformations. While the inner boundaries of the 3-hole geometry also showed good qualitative agreement with typical experimental results, the transverse model did not capture the cusp-like deformation observed on the outer boundary. Furthermore, this cusp-like behaviour could not be reproduced even when using a single large interior hole. We thus conclude that surface tension is responsible, at least in part, for all of the deformations observed in experiments except for the cusp-like regions seen in the 3-hole geometry. This phenomenon will be discussed further in Chapter 7. The numerical methods from this chapter will be used in the models of stretching fluid cylinders in Chapter 6 and of extrusion in Chapter 7.



## Chapter 6

# Stretching Fluid Cylinders with Internal Structure

### 6.1 Introduction

In this chapter we apply the slenderness model developed in Chapter 3 to the stretching under gravity of a fluid cylinder with internal structure suspended at one end. This problem corresponds to the boundary condition  $w(0, t) = 0$ , so that the cross section initially at  $z = 0$  remains there for all time. It was shown in Chapter 3 that, under the slenderness approximation, the governing equations decompose into coupled axial and transverse systems. The latter is precisely the two-dimensional Stokes equations with unit surface tension and is independent of the axial problem. Such fluid flows were described using complex variables in Chapter 4, while in Chapter 5 numerical methods were developed to solve this problem on any domain of interest and for arbitrary connectivity. These solutions are now used to complete the solution to the axial problem.

A particular focus of this chapter is to analyse the interaction between gravitational and surface tension forces. Specifically, we wish to determine if and when surface tension effects are important. It has been shown by Wylie, Huang and Miura (2011) that for the pulling by a fixed force of a solid axisymmetric viscous thread with small inertia the effect of surface tension is negligible; however, experiments have shown that the interior structure of a stretching fluid cylinder undergoes deformation that could be the result of surface tension effects. We use the model developed to determine whether surface tension can indeed cause such deformations. Furthermore, we argue that the importance of surface tension depends upon both the relevant dimensionless parameters and the geometry under consideration. These results are validated by comparisons with experimental data for a cylinder with annular cross sections and a cylinder with three internal boundaries.

## 6.2 Governing Equations

### 6.2.1 Overview

We here show how the general model presented in Chapter 3 may be solved in the case  $w(0, t) = 0$ . As part of this process we set an appropriate velocity scale, verify the dimensionless parameters are of the correct order and incorporate the solution to the transverse problem into the axial solution.

### 6.2.2 Scales

Typical parameter values for the stretching cylinder problem are given in Table 6.2.1. The length scale  $\mathcal{L}$  is usually the initial length of the cylinder;

Table 6.2.1: Typical parameters values for the gravitational stretching and extrusion of a fluid cylinder.

Parameter	Symbol	Approximate value	Units
Surface tension	$\gamma$	0.2–0.3	$\text{N} \cdot \text{m}^{-1}$
Viscosity	$\mu_0$	$10^{6.5}–10^{8.5}$	$\text{Pa} \cdot \text{s}$
Density	$\rho$	$2.5 \times 10^3–6 \times 10^3$	$\text{kg} \cdot \text{m}^{-3}$
Cross-sectional area	$\mathcal{S}$	$5 \times 10^{-5}–8 \times 10^{-5}$	$\text{m}^2$
Initial length	$\mathcal{L}$	0.03–0.04	$\text{m}$
Thermal conductivity	$k$	1.3–2	$\text{W} \cdot \text{m}^{-1} \cdot \text{K}^{-1}$
Heat transfer coefficient	$h$	150–300	$\text{W} \cdot \text{m}^{-2} \cdot \text{K}^{-1}$
Thermal diffusivity	$\alpha$	$4.3 \times 10^{-7}–5.6 \times 10^{-7}$	$\text{m}^2 \cdot \text{s}^{-1}$

that is,  $\mathcal{L} = L_0$ . As  $g^*$  is assumed to be  $O(1)$ , the velocity scale  $\mathcal{U}$  is chosen by setting  $g^* = 1$ , which corresponds to setting  $\mathcal{U} = \rho g \mathcal{L}^2 / \mu_0$  and yields the dimensionless parameters

$$\text{Re} = \frac{\rho^2 g \mathcal{L}^3}{\mu_0^2}, \quad \gamma^* = \frac{\gamma}{\rho g \mathcal{L} \sqrt{\mathcal{S}}}, \quad \text{Pe} = \frac{\rho g \mathcal{L}^3}{\alpha \mu_0}. \quad (6.2.1)$$

Under this choice the parameter  $\gamma^*$  represents an inverse Bond number. Using the values from Table 6.2.1, we find that the velocity scale  $\mathcal{U}$  is  $6.9 \times 10^{-8}–2.9 \times 10^{-5} \text{ m} \cdot \text{s}^{-1}$ . The slenderness ratio  $\epsilon$  is  $O(10^{-1})$ , the Reynolds number  $\text{Re}$  is  $O(10^{-9})$  and the dimensionless surface tension  $\gamma^*$  is  $O(10^{-2})$ . Both the Péclet number  $\text{Pe}$  and the Biot number  $\text{Bi}$  are  $O(1)$ . These parameters satisfy all of the assumptions from Chapter 3 and we may thus make use of the equations derived therein. While we will eventually drop the inertial terms, these are retained for the time being and will be discussed later in Section 6.5.

### 6.2.3 Axial Problem and Lagrangian Co-ordinate

In Subsection 3.3.8 it was shown that by replacing the Eulerian axial co-ordinate  $z$  by a Lagrangian axial co-ordinate  $\tilde{z}$ , which labels each cross section, the transverse problem can be decoupled and solved independently of the axial problem. To incorporate this solution into the axial problem we first rewrite the axial momentum equation (3.3.32) in terms of this Lagrangian co-ordinate.

We are free to choose the particular Lagrangian co-ordinate used and so seek a definition that will make the resulting equations as straightforward as possible. To this end we define the Lagrangian co-ordinate to be the initial position of each cross section, which, due to the choice of axial length scale, will lie in the interval  $[0, 1]$ , as illustrated in Figure 6.2.1. So as to avoid confusion later when a different Lagrangian co-ordinate is used in Chapter 7, we denote this particular co-ordinate  $\xi$ . With this notation,  $\xi$  is defined as the solution to  $\xi = z(\xi, 0)$ . This co-ordinate has been used previously in several studies of extensional flows (Stokes, 2000; Wylie and Huang, 2007; Bradshaw-Hajek, Stokes and Tuck, 2007); however, some caution must be taken as this differs from the Lagrangian co-ordinate denoted by the same variable used by Wylie *et al.* (2011), which represents the initial dimensionless *mass* between each cross section and the origin. As per Stokes and Tuck (2004), applying conservation of mass to an arbitrary region of the cylinder, represented by the shaded region in Figure 6.2.1, shows that the Eulerian and Lagrangian co-ordinates are related by

$$S(\xi, t)dz = S_0(\xi)d\xi.$$

Rearranging and considering the limit as  $dz$  approaches zero yields

$$\frac{\partial z}{\partial \xi} = \frac{S_0(\xi)}{S(\xi, t)}, \quad (6.2.2)$$

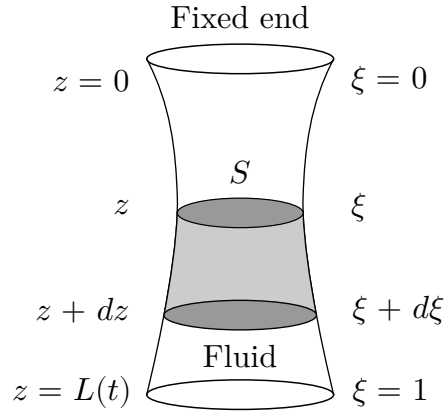


Figure 6.2.1: A sketch of the Eulerian and Lagrangian axial co-ordinates for a stretching fluid cylinder. The Eulerian co-ordinate  $z$ , shown on the left-hand side of the diagram, is converted to the Lagrangian co-ordinate  $\xi$ , shown on the right, defined by the initial position of each cross section so that  $\xi = z(\xi, 0)$ .

which may be integrated with respect to  $\xi$  subject to the condition  $z(0, t) = 0$  to give

$$z(\xi, t) = \int_0^\xi \frac{S_0(\xi')}{S(\xi', t)} d\xi'. \quad (6.2.3)$$

In converting to a Lagrangian reference frame we introduce the *material derivative*

$$\frac{D}{Dt} = \frac{\partial}{\partial t} + w_0 \frac{\partial}{\partial z},$$

which represents the rate of change in time following a particular cross section. Using this, the conservation of mass equation (3.3.33) is rewritten

$$\frac{\partial S}{\partial t} + w_0 \frac{\partial S}{\partial z} = \frac{DS}{Dt} = -S \frac{\partial w_0}{\partial z}.$$

and substituted into the axial momentum equation (3.3.32). Using (6.2.2) to convert derivatives with respect to  $z$  to derivatives with respect to  $\xi$  and making

use of the material derivative yields, finally,

$$\text{Re}S_0 \frac{Dw_0}{Dt} + \frac{\partial}{\partial \xi} \left( 3\mu^* \frac{DS}{Dt} \right) = S_0 + \frac{\gamma^*}{2} \Gamma_\xi. \quad (6.2.4)$$

Integrating this equation from 1 to  $\xi$  (that is, from the bottom end of the cylinder to cross section  $\xi$ ) yields

$$3\mu^* \frac{DS}{Dt} = \int_1^\xi S_0 \left( 1 - \text{Re} \frac{Dw_0}{Dt} \right) d\xi' + \frac{\gamma^*}{2} \Gamma - c(t). \quad (6.2.5)$$

The function  $c(t)$  is a time-dependent axial tension within the fluid. In the absence of any external pulling of the cylinder we assume that  $c(t) = 0$  and that any change in cross-sectional area at the very bottom of the cylinder is due to surface tension. As will be seen in Section 6.4, experiments show that the cross-sectional area at the very bottom of the cylinder changes very little with time. In some practical applications the cylinder is pulled with a constant force and  $c(t)$  will be a positive constant.

The first term from the integral on the right-hand side of (6.2.5) is

$$\int_1^\xi S_0 d\xi' = - \int_z^{L(t)} S(z', t) dz' = -V(\xi),$$

where  $V(\xi)$  is the dimensionless weight of fluid below cross section  $\xi$ . For a uniform initial geometry  $S(\xi, 0) \equiv 1$ , so that  $V(\xi) = 1 - \xi$ . Substituting this term into (6.2.5) we arrive at the axial equation

$$3\mu^* \frac{DS}{Dt} = \frac{\gamma^*}{2} \Gamma - V(\xi) - c(t) - \text{Re} \int_1^\xi \frac{Dw_0}{Dt} d\xi'. \quad (6.2.6)$$

For a solid axisymmetric cylinder with  $\text{Re} = 0$ , (6.2.6) is identical to that given by Stokes *et al.* (2011, p. 324, eqn (8)).

We also note that under the slenderness assumption the sides of the fluid region are taken to have small slope so that there is no axial contribution to

the curvature. At the free end of the cylinder  $\xi = 1$ , however, surface tension will work to round the sharp corners and this free end will no longer be flat. In this thesis we ignore this effect, which occurs over a long time relative to the stretching time, noting that it will have a negligible impact on the rest of the fluid away from  $\xi = 1$ .

At present (6.2.6) involves two interdependent unknown variables  $S$  and  $\Gamma$ . For a general geometry there is no simple relationship between the area of each cross section and the total boundary length and hence the problem is not closed. In order to relate these two quantities we must make use of the transverse problem of Subsection 3.3.8.

#### 6.2.4 Coupling the Axial and Transverse Problems

In Chapter 5 we saw how to solve the transverse problem, which yields  $\tilde{\Gamma}(\xi, \tau)$  in reduced time, while the boundary length is given by  $\Gamma(\xi, \tau) = \sqrt{S(\xi, \tau)} \tilde{\Gamma}(\xi, \tau)$ . To make use of this result to couple the transverse and axial models we convert the axial equation (6.2.6) to reduced time  $\tau$ . Aside from the above substitution for the  $\Gamma$  term we must consider two time-dependent terms: the time derivative on the left-hand side and  $c(t)$ .

Since the boundary length is given in terms of  $\sqrt{S}$  it is convenient to make a change of dependent variables by introducing  $\chi = \sqrt{S}$ . For a fixed  $\xi$ , the definitions of reduced time (3.3.39) and  $\chi$  show that the material derivatives with respect to  $t$  and  $\tau$  are related by

$$\frac{D}{Dt} = \frac{\gamma^*}{\mu^* \chi} \frac{D}{D\tau}.$$

Combining these results shows that

$$3\mu \frac{DS}{Dt} = 6\gamma^* \frac{D\chi}{D\tau}.$$

Since  $c(t)$  depends only upon time it must take the same value in each cross section for any given  $t$ ; however,  $\tau$  depends upon both  $t$  and  $\xi$ , meaning that at a given  $t$  each cross section may be at a different reduced time and thus  $c$  cannot be expressed as function of  $\tau$  alone. Formally, it is simple to show that  $t$  may be expressed as

$$t = \int_0^\tau \frac{\mu^* \chi(\xi, \tau')}{\gamma^*} d\tau',$$

which clearly shows that  $t$  is a function of both  $\tau$  and  $\xi$ . Thus, the time-dependent tension  $c(t)$  becomes a function  $C$  of both  $\xi$  and  $\tau$ ; at a given  $t$ , the reduced time  $\tau$  varies with  $\xi$  so that  $c(t) = C(\xi, \tau)$ . We define

$$6\sigma^*(\xi, \tau) = V(\xi) + C(\xi, \tau) \quad (6.2.7)$$

which represents the total dimensionless tension, due to gravity and any additional pulling, acting on cross section  $\xi$  at reduced time  $\tau$ . Using these results (6.2.6) becomes

$$\frac{D\chi}{D\tau} - \frac{1}{12}\chi\tilde{\Gamma} = -\frac{\sigma^*}{\gamma^*} - \frac{\text{Re}}{6} \int_\xi^1 \frac{1}{\mu^* \chi} \frac{Dw_0}{D\tau} d\xi'. \quad (6.2.8)$$

### 6.2.5 Solution for Small Inertia

The axial equation (6.2.8) is greatly complicated by the inclusion of inertia and no exact solution to this equation is known. In Subsection 6.2.2 it was shown that the Reynolds number  $\text{Re}$  was small so we are justified in dropping the inertial term from (6.2.8), which yields

$$\frac{D\chi}{D\tau} - \frac{1}{12}\chi\tilde{\Gamma} = -\frac{\sigma^*}{\gamma^*}. \quad (6.2.9)$$

This is a linear ordinary differential equation in  $\chi$ , which corresponds to that seen in fibre drawing (Stokes *et al.*, 2014, p. 8, eqn (2.17)) excepting that  $\sigma^*$  is

not constant but dependent on  $\xi$  and  $\tau$ . We have thus here demonstrated the key result that the inclusion of gravitational effects results in an equation of the same form as that of Stokes *et al.* (2014) but with  $\sigma^*$  a function of both  $\xi$  and  $\tau$ . This may now be solved using the integrating factor

$$H(\xi, \tau) = \exp\left(-\frac{1}{12} \int_0^\tau \tilde{\Gamma}(\xi, \tau') d\tau'\right), \quad (6.2.10)$$

which is similar to that employed by Stokes *et al.* (2014) but depends on both  $\xi$  and  $\tau$ . Upon multiplication of (6.2.9) by  $H$  we find that

$$\frac{D}{D\tau}(\chi H) = -\frac{\sigma^*}{\gamma^*} H,$$

which, for each value of  $\xi$ , may be integrated with respect to  $\tau$ , yielding

$$\chi(\xi, \tau) = \frac{1}{H} \left( \chi_0(\xi) - \frac{1}{\gamma^*} \int_0^\tau \sigma^* H d\tau' \right). \quad (6.2.11)$$

Here, we have introduced  $\chi_0(\xi) = \chi(\xi, 0)$ , which is the initial value of  $\chi$ . For a cylinder with initially-uniform cross section,  $\chi_0(\xi) = \sqrt{S_0(\xi)} \equiv 1$ . While equation (6.2.11) is similar in form to that previously obtained for the drawing of fibres (Stokes *et al.*, 2014, p. 183, eqn 2.19.), it differs significantly in that  $\sigma^*$  is not a constant but, in general, a function of both  $\xi$  and  $\tau$  because of the inclusion of gravity and the time-dependent tension  $C(\xi, \tau)$ . Ultimately we will assume that  $C(\xi, \tau)$  is constant, in which case (6.2.11) differs from the solution for fibre drawing only because  $\sigma^*$  and, possibly,  $\chi_0$  depend on  $\xi$  so that a different solution  $\chi$  is obtained for each  $\xi$ . In general (6.2.11) has no exact solution and we must compute the integrals in (6.2.10) and (6.2.11) numerically.

Given some cross section  $\xi$  and reduced time  $\tau$ , we use (6.2.11) to compute the area of the cross section, while the solution to the transverse problem determines the shape of the cross section. Thus, these two solutions together

completely describe how cross section  $\xi$  evolves in  $\tau$ . To determine the cylinder geometry at time  $t$  we require a relationship between  $t$  and  $\tau$  for each  $\xi$ . This is obtained by rearranging (3.3.41) to give

$$\int_0^\tau \chi d\tau' = \int_0^t \frac{\gamma^*}{\mu^*} dt' = \frac{\gamma^* t}{m(\xi, t)}, \quad (6.2.12)$$

where  $m(\xi, t)$  is the harmonic mean of  $\mu^*(\xi, t)$  at position  $\xi$  over time  $t$ ; that is,

$$m(\xi, t) = \frac{t}{\int_0^t \frac{1}{\mu^*(\xi, t')} dt'}.$$

As stated earlier, in this thesis we assume  $\mu^*$ , and hence  $m$ , to be known. We note that when  $\mu^* = \mu^*(\xi)$  we have  $m = m(\xi) = \mu^*(\xi)$ . Substituting (6.2.11) into (6.2.12) gives a relationship between  $t$  and  $\tau$  at each cross section  $\xi$ . At a given  $t > 0$  the dependence of (6.2.12) on  $\xi$  means that  $\tau$  will differ from cross section to cross section so that each will have a different shape, even in the case that  $\chi_0$  is independent of  $\xi$ . This is in contrast to previous models of fibre drawing (Stokes *et al.*, 2014) in which every cross section has the same initial geometry, evolves over the same reduced time  $\tau$  as it is drawn, and so has the same shape. If required, the Eulerian position  $z$  at any time  $t$  may be determined by substituting  $S = \chi^2$  into (6.2.3), which will typically need to be evaluated numerically.

Summarising, the general solution procedure is as follows:

- (1) solve the transverse flow problem for each  $\xi$ ;
- (2) calculate  $\tilde{\Gamma}(\xi, \tau)$  from the cross flow solution and, hence,  $H(\xi, \tau)$  from (6.2.10);
- (3) calculate  $\chi(\xi, \tau)$  from (6.2.11);
- (4) for each time  $t$  of interest:

- (a) find  $\tau$  for each cross section  $\xi$  using (6.2.12);
- (b) evaluate  $S(\xi, \tau)$  and  $x(\xi, \tau)$ .

The time dependence of  $c(t)$  greatly increases the difficulty of this problem. In typical MOF preform extrusion there is a constant pulling force and very often  $c(t) \equiv 0$ . From this point onwards we will assume that  $c(t) = C(\xi, \tau) = c$  is constant.

### 6.2.6 Solutions for Weak and Zero Surface Tension

In Subsection 3.3.4 it was assumed that  $\gamma^*$  was  $O(1)$  and a solution was derived that included the surface tension terms, which we will refer to as the full solution; however, in Subsection 6.2.2 it was observed that  $\gamma^*$  is  $O(10^{-2})$  or smaller, which suggests that surface tension has only a small effect on the solution. To investigate the importance of surface tension we here consider two approximations to the full problem. If  $\gamma^* \ll 1$ , the surface tension terms from the axial equation (6.2.6) may be dropped, so that this equation no longer depends upon the transverse problem. In addition, if  $\gamma^* = 0$  then (3.3.41) implies that  $\tau = 0$  and the transverse problem may be neglected. This agrees with results observed by Dewynne *et al.* (1994) for fibre drawing, namely that without surface tension the cross sections would change scale due to stretching but remain the same shape. We will refer to this as the zero-surface-tension (ZST) case. If, however,  $\gamma^* \ll 1$  but the area  $S$  is small or the geometry has large curvatures then even small values of  $\tau$  may make a significant change to the shape. We thus also consider the solution when surface tension terms are neglected in the axial problem but the transverse problem is retained, which is denoted the weak-surface-tension (WST) case.

Both the ZST and WST cases share the same axial equation (6.2.6) with the surface tension term removed. Integrating yields

$$S(\xi, t) = S_0(\xi) - \frac{2t\sigma^*(\xi)}{m(\xi, t)}. \quad (6.2.13)$$

We note that the ZST–WST solution for  $S$  does *not* depend on the cross-sectional shape, that is  $\Gamma(\xi, \tau)$ , which is in contrast to the solution of the full problem. For the WST case we can also obtain an expression for  $S$  at each  $\xi$  in terms of  $\tau$ . From (6.2.9), neglecting the term involving  $\tilde{\Gamma}$ , we find

$$\chi(\xi, \tau) = \chi_0(\xi) - \frac{\sigma^*(\xi)\tau}{\gamma^*}. \quad (6.2.14)$$

Equating with (6.2.13) gives the relationship between  $t$  and  $\tau$

$$\frac{t\gamma^*}{m(\xi, t)} = \tau \left( \chi_0 - \frac{\sigma^*\tau}{2\gamma^*} \right). \quad (6.2.15)$$

Writing (6.2.15) as a quadratic polynomial in  $\tau$  and solving for  $\tau$  gives

$$\tau = \frac{\gamma^*}{\sigma^*} \left[ \chi_0 - \left( \chi_0^2 - \frac{2\sigma^*t}{m} \right)^{\frac{1}{2}} \right], \quad (6.2.16)$$

where we must use the negative square root so that  $\partial\tau/\partial t > 0$  and  $\tau(\xi, 0) = 0$ . Thus, the WST solution, if appropriate, provides a straightforward relation between  $\tau$  and  $t$ . The term inside the parentheses in (6.2.16) is precisely (6.2.13) and is thus always initially positive. At a cross section  $\xi$  with positive  $\sigma^*$  this term decreases until the cross section reaches zero area, at which point the model no longer applies.

For the special case in which the viscosity  $\mu^*$  and initial area  $S_0$  are independent of  $\xi$  further progress can be made. For  $t > 0$ , substituting for  $S(\xi, t)$  in (6.2.3) and integrating yields

$$z(\xi, t) = \frac{3m}{t} \log \left( 1 + \frac{t\xi}{3m - t(1+c)} \right), \quad (6.2.17)$$

where  $m = m(t)$ . Setting  $\xi = 1$ , we find that the length of the fluid region is given by

$$z(1, t) = L(t) = \frac{3m}{t} \log \left( 1 + \frac{t}{3m - t(1+c)} \right).$$

Rearranging (6.2.17), it may be shown that

$$\left[ 1 - \frac{t(1+c)}{3m} \right] \exp \left( \frac{tz}{3m} \right) = 1 - \frac{t(1-\xi+c)}{3m}.$$

Observing that the right-hand side of this expression matches the right-hand side of (6.2.13) we may eliminate  $\xi$  to obtain

$$S(z, t) = \left[ 1 - \frac{t(1+c)}{3m} \right] \exp \left( \frac{tz}{3m} \right), \quad 0 \leq z \leq L(t).$$

This provides a full solution to the ZST case. For the WST case we must, in addition, solve the transverse problem and relate  $t$  to  $\tau$ . From (6.2.16),  $\tau$  is given by

$$\tau = \frac{\gamma^*}{\sigma^*(\xi)} \left[ 1 - \left( 1 - \frac{2\sigma^*(\xi)t}{m} \right)^{\frac{1}{2}} \right].$$

Again, this solution only applies up until some cross section reaches zero area.

## 6.3 Cylinders with No Internal Structure

### 6.3.1 Overview

In this section we consider some illustrative solutions for the stretching under gravity of cylinders with no internal structure. In Subsection 6.3.2 the full problem is first validated against a known solution for the stretching of an axisymmetric rod. Following this in Subsection 6.3.3 we compare solutions of the full problem with those obtained assuming zero and weak surface tension for two different geometries, namely a solid axisymmetric rod and a cylinder with a

non-circular cross section. In particular we will examine how well the ZST and WST solutions represent the full problem solution relative to the magnitude of the surface tension parameter  $\gamma^*$ . For generality solutions are derived as far as possible for a viscosity that varies with both Lagrangian co-ordinate  $\xi$  and time  $t$  but all results presented are for a constant viscosity.

### 6.3.2 Solution for a Solid Rod

Gravitational stretching of a slender solid axisymmetric cylinder hanging from a horizontal surface was considered by Stokes *et al.* (2011) and the solution obtained assuming a constant viscosity. We here summarise the solution method, extending it for a viscosity that depends on both time and axial position.

For a circular rod the relationship between cross-sectional area  $S$  and boundary perimeter  $\Gamma$  is  $\Gamma = 2\sqrt{\pi S}$ . Substituting for  $\Gamma$  in (6.2.6) and introducing  $\chi = \sqrt{S}$  yields

$$\mu^* \chi \frac{\partial \chi}{\partial t} = \delta \left( \chi - \frac{\sigma^*}{\delta} \right), \quad (6.3.18)$$

where  $\delta = \gamma^* \sqrt{\pi}/6$ . This is readily solved subject to the initial condition  $\chi(\xi, 0) = \chi_0(\xi)$ , giving

$$\chi - \chi_0 + \frac{\sigma^*}{\delta} \log \frac{\delta \chi - \sigma^*}{\delta \chi_0 - \sigma^*} = \frac{\delta t}{m(\xi, t)}. \quad (6.3.19)$$

Given values for  $\xi$  and  $t$ , (6.3.19) is an implicit equation for  $\chi$  that is readily solved by any suitable numerical method. Setting  $m(\xi, t) = 1$  for constant viscosity (6.3.19) is exactly equivalent to the solution given by Stokes *et al.* (2011, p. 326, eqn (12)). Wilson (1988) obtained a similar solution for fluid dripping from a circular capillary, again for constant viscosity.

We now solve this same problem using the reduced-time method detailed in Section 6.2. The transverse problem domain is scaled by  $\sqrt{S}$  and so remains

the unit disk for all time. If the radius from the transverse problem is  $\tilde{R}$  then we have  $\pi\tilde{R}^2 = 1$ , from which it is simple to show that the scaled boundary length is

$$\tilde{\Gamma}(\tau) = 2\pi\tilde{R} = 2\sqrt{\pi}.$$

Substituting this into the definition of  $H$  from (6.2.10) yields

$$H(\tau) = e^{-\frac{\tau\sqrt{\pi}}{6}},$$

and hence

$$\begin{aligned} \int_0^\tau H(\tau') d\tau' &= \frac{6}{\sqrt{\pi}} \left(1 - e^{-\frac{\tau\sqrt{\pi}}{6}}\right), \\ &= \frac{6}{\sqrt{\pi}} [1 - H(\tau)]. \end{aligned}$$

With these results established we substitute into the exact solution (6.2.11) to give, after some simplification,

$$\begin{aligned} \chi &= \left(\chi_0 - \frac{6\sigma^*}{\gamma^*\sqrt{\pi}}\right) \frac{1}{H} + \frac{6\sigma^*}{\gamma^*\sqrt{\pi}}, \\ &= \left(\chi_0 - \frac{\sigma^*}{\delta}\right) e^{\frac{\tau\sqrt{\pi}}{6}} + \frac{\sigma^*}{\delta}. \end{aligned} \quad (6.3.20)$$

To relate  $t$  and  $\tau$  we substitute  $\chi$  from (6.3.20) into (6.2.12), which yields the algebraic relationship

$$\frac{6}{\sqrt{\pi}} \left(\chi_0 - \frac{\sigma^*}{\delta}\right) \left(e^{\frac{\tau\sqrt{\pi}}{6}} - 1\right) + \frac{\sigma^*}{\delta} \tau = \frac{\gamma^*}{m(\xi, t)} t. \quad (6.3.21)$$

Thus, at any time  $t$  and position  $\xi$  we are able to calculate  $\tau(\xi)$  and hence also  $S(\xi, \tau) = \chi^2$ . Rearranging (6.3.20) shows that

$$e^{\frac{\tau\sqrt{\pi}}{6}} = \frac{\delta\chi - \sigma^*}{\delta\chi_0 - \sigma^*}$$

and hence

$$\tau = \frac{6}{\sqrt{\pi}} \log \left( \frac{\delta\chi - \sigma^*}{\delta\chi_0 - \sigma^*} \right).$$

Using these expressions to eliminate  $\tau$  from (6.3.21) recovers (6.3.19), and thus these two solutions agree exactly. Importantly, this shows that the reduced-time method is valid for this problem. Considering the form of each solution shows that the reduced-time method has the advantage of producing an *explicit* solution (6.3.20), albeit as a function of  $\tau$ , whereas using standard time produces only an *implicit* solution (6.3.19). This explicit form more readily reveals the evolution of  $S$  than the implicit solution. From (6.3.20) it is clear that  $\chi$ , and hence also  $S$ , increases at cross sections  $\xi$  for which  $\chi_0 > \sigma^*/\delta$  and decreases at cross sections with  $\chi_0 < \sigma^*/\delta$ .

This solution for the initial geometry  $\chi_0(\xi) \equiv 1$  with  $\gamma^* = 0.1$  is plotted in Figure 6.3.2. It is apparent that there is a particular value  $\xi_f$  for which  $S$  is constant. This point may be found by setting  $\chi_\tau = 0$  and  $\chi = \chi_0$  in either the implicit equation (6.3.18) or the reduced time equation (6.2.9) and solving for  $\xi$ , which yields

$$\chi_0(\xi_f) = \frac{\sigma^*}{\delta}.$$

In the special case  $\chi_0 \equiv 1$  this may be simplified further, giving

$$\xi_f = 1 + c - \gamma^* \sqrt{\pi}. \quad (6.3.22)$$

This is a linear equation in  $\gamma^*$  for the fixed point  $\xi_f$ . Thus, for initially uniform geometries, there is at most one fixed point for any given  $\gamma^*$ , the value of which decreases as  $\gamma^*$  increases. Since  $\xi \geq 0$  by definition, this fixed point will cease to exist when  $\gamma^* > (1 + c)/\sqrt{\pi}$ . For  $c \equiv 0$  this condition becomes  $\gamma^* > 1/\sqrt{\pi} \approx 0.56$  and the corresponding value of the fixed point is plotted in Figure 6.3.3. For  $\xi < \xi_f$  the value of  $S$  decreases with time, while for  $\xi > \xi_f$  the value of  $S$  increases. The existence of such a point has been considered

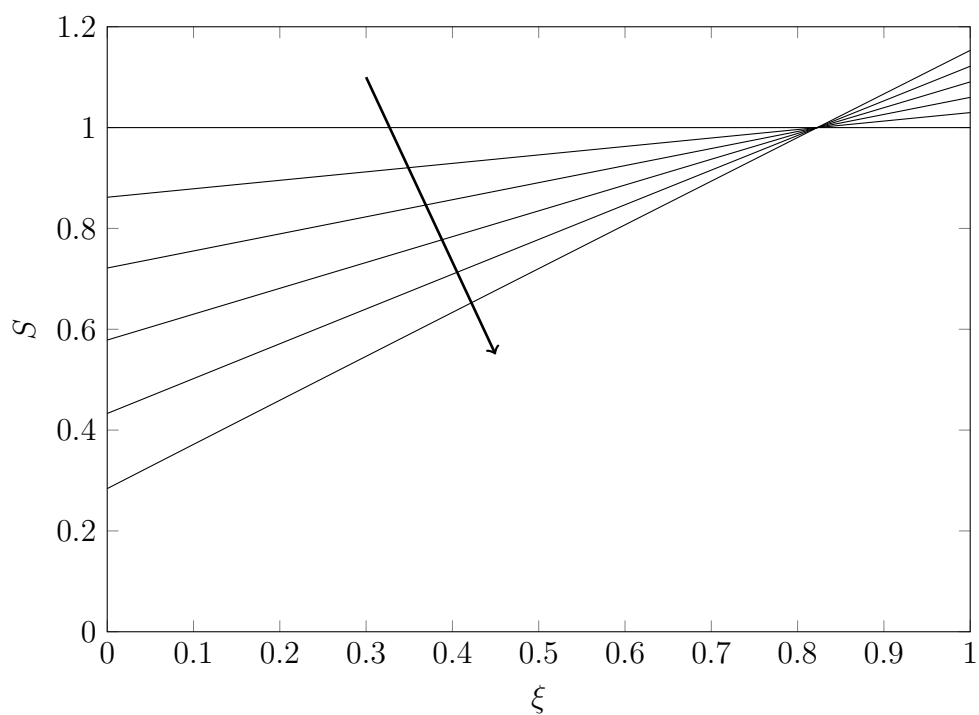


Figure 6.3.2: The area  $S(\xi, t)$  of a solid axisymmetric rod with  $S_0(\xi) = 1$  and  $\gamma^* = 0.1$  shown at times  $t = 0, 0.5, 1, 1.5, 2$  and  $2.5$ , with increasing time indicated by the arrow. The solutions show a fixed point  $\xi_f$  below which the area decreases and above which the area increases.

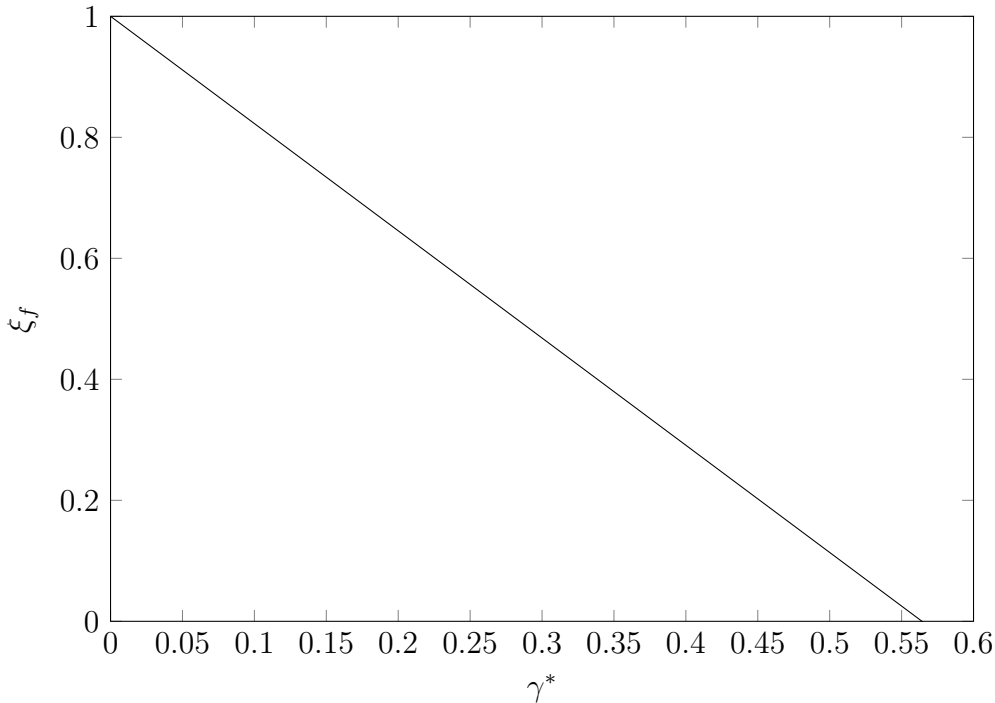


Figure 6.3.3: The fixed point  $\xi_f$  for a solid axisymmetric rod as a function of  $\gamma^*$  for the case  $c \equiv 0$ . The fixed point does not exist for  $\gamma^* > 1/\sqrt{\pi} \approx 0.56$ .

previously by Stokes *et al.* (2011), who also provided experimental evidence for the existence of such a fixed point in extending drops. Physically, this fixed point represents the position along the fluid at which the axial forces due to gravity and any applied force  $c$ , which stretch the fluid, are exactly balanced by surface tension, which, in this model, acts in the opposite direction to gravity. For  $\xi > \xi_f$  the compressive effect of surface tension is greater than the stretching due to gravity and the area of each cross section increases. Under the slenderness assumption this represents the first stages of a drop forming at the end of the cylinder.

For general geometries fixed points may be identified by setting  $S_t = 0$  in

(6.2.6), which yields the condition

$$V(\xi_f) = \frac{\gamma^*}{2}\Gamma(\xi_f, t) - c.$$

Since the left-hand side of this equation is independent of time, a fixed point can only exist if the right-hand side is also independent of time. This shows that, for constant  $c$ , a fixed point can only occur if  $\gamma^* = 0$  or  $\Gamma$  is constant, which both imply that there is no transverse flow. For non-zero  $\gamma^*$  the total boundary length  $\Gamma$  can only be constant if the external boundary is a circle and there are no interior boundaries.

### 6.3.3 Influence of Surface Tension and Geometry

We now consider some examples to compare the full, ZST and WST solutions as both  $\gamma^*$  and the geometry vary. The effect of surface tension is investigated by considering solutions for  $\gamma^* = 10^{-3}, 10^{-2}$  and  $10^{-1}$ , while the influence of geometry is illustrated by considering two representative cases: a solid circular rod and an epicycloid, the latter of which is shown in Figure 6.3.4. The circular rod does not evolve in the transverse flow problem, while an exact solution to the transverse problem for the evolution of an epicycloid was given by Hopper (1990). We here set  $c = 0$ .

Figure 6.3.5 shows the area  $S$  plotted against  $\xi$  at times  $t = 1$  and 2 for each of the values of  $\gamma^*$  for the ZST–WST problem (in which  $S$  is independent of the cross-sectional geometry) and for the full problem, where the cross section is a circle and an epicycloid. From these curves it can be seen that when  $\gamma^* = 10^{-3}$  all three solutions are identical to graphical accuracy at both times. This suggests that for this value of  $\gamma^*$  surface tension does not have a significant effect, regardless of the geometry under consideration. For  $\gamma^* = 10^{-2}$

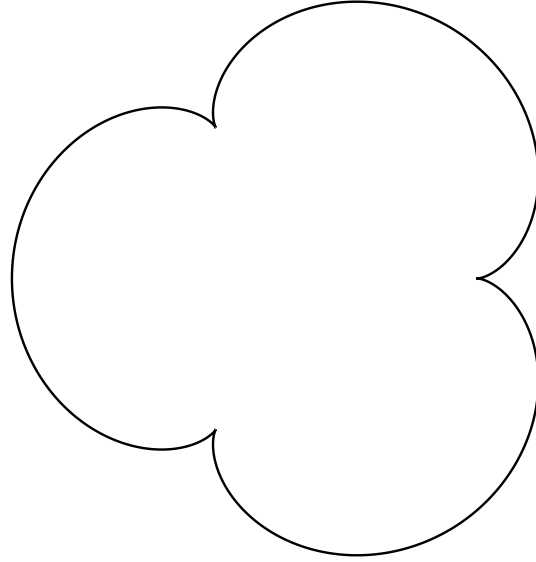


Figure 6.3.4: The epicycloid used as an initial cross section geometry.

the three solutions show qualitative but not quantitative agreement. At  $t = 1$  the ZST–WST solution and solid-rod solution are similar, while the epicycloid solution has a larger area at all values of  $\xi$ . By time  $t = 2$ , the rod has deviated from the ZST–WST solution by more, while the epicycloid solution is further away again. Finally, with  $\gamma^* = 10^{-1}$ , the differences are even more pronounced and are clearly visible at both times. Once again, the epicycloid solution is larger than that for the rod, which is in turn larger than the ZST–WST solution. The differences between the rod and epicycloid may be explained by the difference in the boundary lengths. The initial boundary length of the epicycloid is greater than that of the circle and remains larger over the course of this simulation. Inspecting (6.2.6), it is clear that the larger  $\tilde{\Gamma}$ , the greater the influence of surface tension on the axial problem. The ZST–WST solution is smallest as it has no boundary length term. As these differences accumulate with time the deviation is greater at  $t = 2$  than at  $t = 1$ .

Within the transverse problem surface tension works to reduce the total boundary length, so that as  $\tau$  increases  $\tilde{\Gamma}$  decreases towards  $2\sqrt{\pi}$ , which is the total boundary length for a disk of unit area. In addition, as a given cross section  $\xi$  becomes smaller due to axial stretching the unscaled boundary length  $\Gamma$  must also decrease, so that the influence of surface tension on  $S$  decreases with time. In regions near the end of the cylinder  $\xi = 1$ , where there is little stretching,  $S$  increases with time, which is most noticeable for larger  $\gamma^*$ . The scaled boundary length  $\tilde{\Gamma}$  still decreases with  $\tau$  but  $\Gamma = \sqrt{S}\tilde{\Gamma}$  may increase due to the increase in  $S$ . Differentiating (3.3.41) with respect to  $t$  we observe that as  $S$  increases the rate of increase in  $\tau$  reduces. Thus, surface tension works to slow the rate of change of  $\tau$ .

The influence of surface tension may also be observed in the cross section profiles. In the case of the rod the shape of each cross section remains the same in the transverse problem and can only change in scale due to axial stretching. Figure 6.3.6 shows cross sections through the rod at  $\xi = 0.5$  at  $t = 2$  for  $\gamma^* = 10^{-2}$  and  $10^{-1}$ . For the smaller value of  $\gamma^*$  the ZST, WST and full solutions have all changed in scale due to axial stretching but are otherwise indistinguishable. For  $\gamma^* = 10^{-1}$  the ZST and WST solutions still appear identical, while the full solution is noticeably larger. These results all agree with the corresponding plots of  $S$  shown in Figure 6.3.5d and Figure 6.3.5f, respectively. Thus, without any transverse evolution the cross section is completely described by the axial solution. For  $\gamma^* \leq 10^{-2}$  there is no noticeable difference between the solutions, while by  $\gamma^* = 10^{-1}$  the full solution differs due to reduced axial stretching on account of the surface tension term in the axial equation.

In the case of the epicycloid there are some notable differences in behaviour due to surface tension driven flow in the cross section. Again, we consider cross

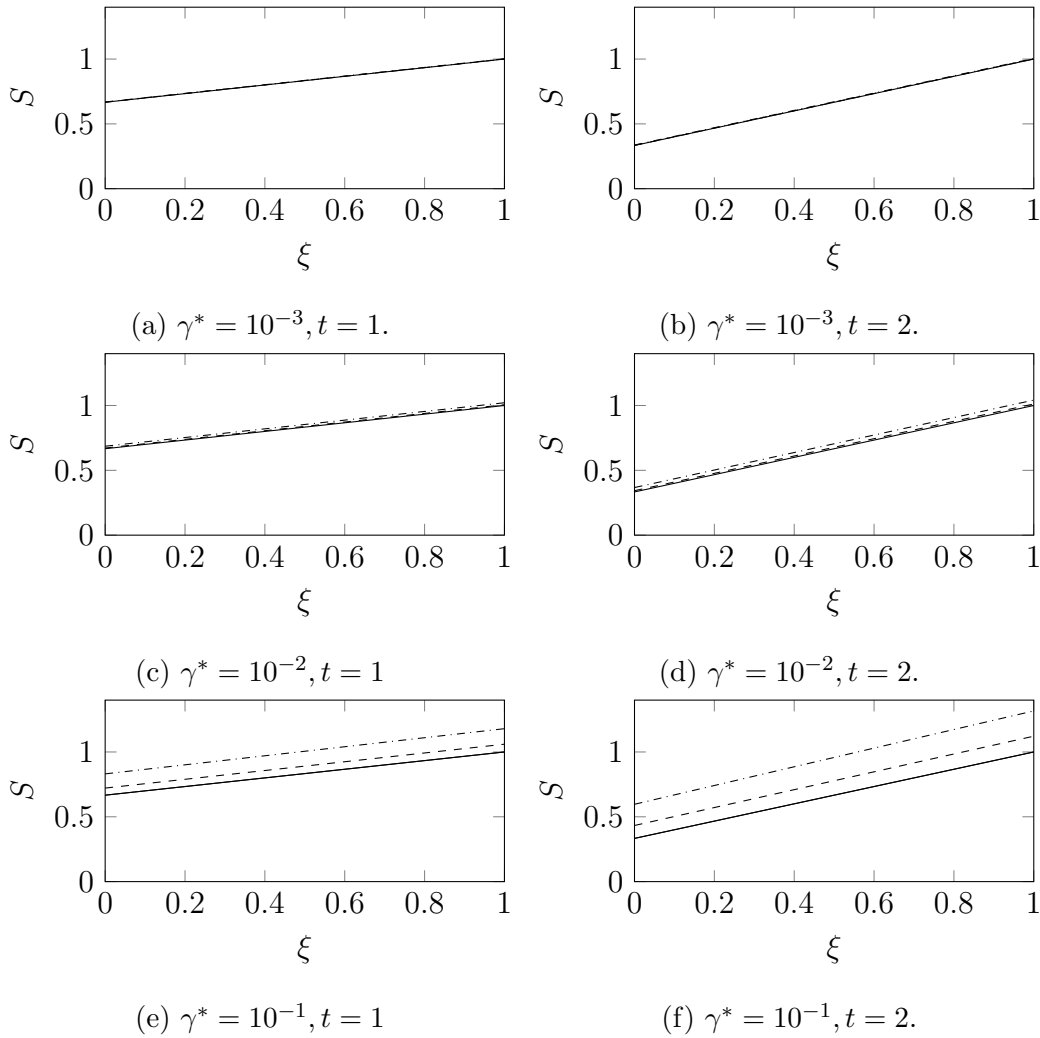


Figure 6.3.5: The areas  $S(\xi, t)$  corresponding to the ZST–WST solution (solid curve), and the full problem for each of the rod (dashed curve) and epicycloid (dash–dot curve). The solutions have been computed with dimensionless surface tensions  $\gamma^* = 10^{-3}$ ,  $10^{-2}$  and  $10^{-1}$ , and are shown at times  $t = 1$  and  $2$ . For  $\gamma^* = 10^{-3}$  the three solutions are indistinguishable to graphical accuracy at both times shown. For  $\gamma^* = 10^{-2}$  the epicycloid solution is slightly larger for all  $\xi$ , while the rod and ZST–WST solutions remain similar to each other. For  $\gamma^* = 10^{-1}$  the three solutions differ noticeably.

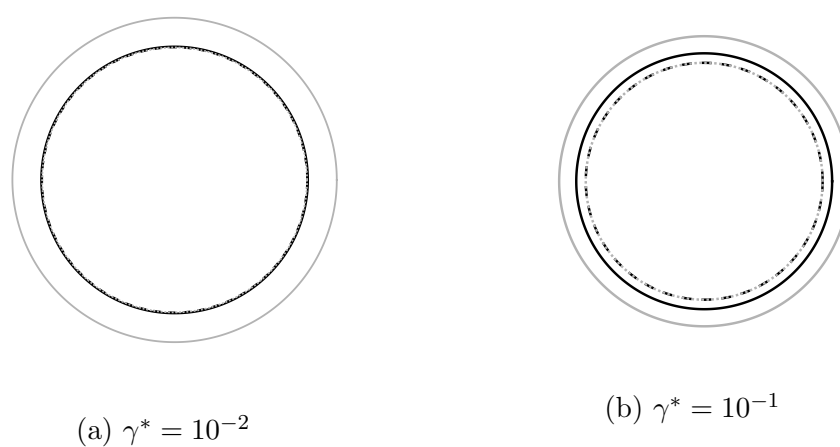


Figure 6.3.6: The cross section at  $\xi = 0.5$  for the stretching circular cylinder. The initial condition is shown in solid grey. At  $t = 2$  we have the full solution (solid black), the WST solution (black dashed) and the ZST solution (grey dotted). The solutions are indistinguishable at  $\gamma^* = 10^{-2}$  while for  $\gamma^* = 10^{-1}$  the full solution is significantly different from the ZST and WST solutions, which are identical.

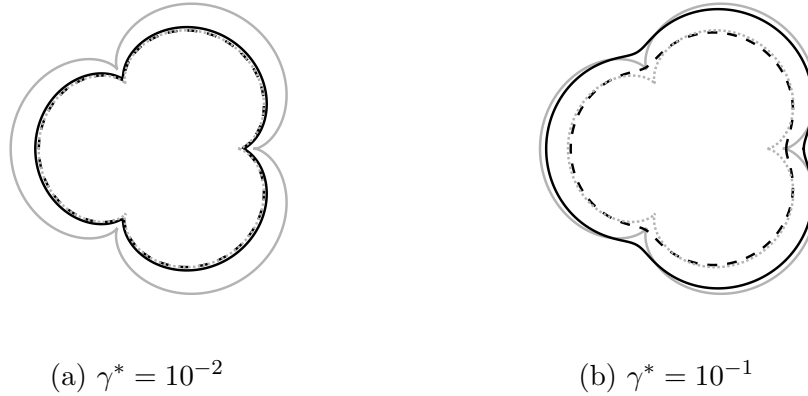


Figure 6.3.7: The cross section at  $\xi = 0.5$  for the stretching cylinder with initial cross sections in the shape of an epicycloid. The initial condition is shown in solid grey. At  $t = 2$  we have the full solution (solid black), the WST solution (black dashed) and the ZST solution (grey dotted). The solutions are similar for  $\gamma^* = 10^{-2}$  but are all distinct for  $\gamma^* = 10^{-1}$ .

sections at  $\xi = 0.5$  and  $t = 2$ , which are plotted in Figure 6.3.7. At  $\gamma^* = 10^{-2}$  the ZST and WST solutions are practically identical, while the full solution shows some smoothing at the cusps and is larger in the regions between. For  $\gamma^* = 10^{-1}$  the three solutions are all distinct. The full solution shows further smoothing and has not reduced much in area. The WST solution shows similar smoothing but, without the resistance to gravity provided by surface tension in the axial problem, has reduced in scale. While the ZST solution has the same area as the WST solution it has a noticeably different shape as there is no surface tension driven flow in the transverse direction to smooth the cusps.

The effect of surface tension can be further highlighted by comparing the domains from the transverse problem so that they each have unit area, which allows a comparison between the solutions without the effect of axial stretching.

Figure 6.3.8a shows such a comparison for the epicycloid at  $t = 2$  and  $\gamma^* = 10^{-1}$ , from which it is evident that the full and WST solutions show almost identical behaviour, while the ZST and initial condition are necessarily identical. To see why the full and WST solutions agree, the values of  $\tau$  from these two solutions are plotted against  $\xi$  in Figure 6.3.8b. While the two curves clearly differ at the plotted scale this difference is never more than  $3.0927 \times 10^{-2}$ , which occurs at  $\xi = 0$ , and the WST solution is at most 14% larger relative to the full solution. The shapes for the full and WST are thus effectively the same. Hence, even though  $\tau$  depends upon  $S$ , as can be seen from (3.3.41), the different axial solutions from the full and WST problems make little difference to the value of  $\tau$  and hence the shape observed; rather, the shape differs depending on the magnitude of surface tension in the transverse problem.

For the two cylinders considered in this subsection we have seen that for  $\gamma^* O(10^{-3})$  surface tension does not have a significant impact on either the axial or transverse systems and the ZST model provides a good approximation to the full problem. If  $\gamma^*$  is  $O(10^{-2})$  the ZST–WST axial model shows small differences from the full model but still provides a useful approximation. At this value of  $\gamma^*$  all three transverse models show close agreement; the ZST model differs in regions of large curvature. For  $\gamma^*$  of  $O(10^{-1})$  the WST transverse model still provides a good approximation to the full problem; however, the ZST–WST axial model and ZST transverse model show significant differences and are no longer appropriate.

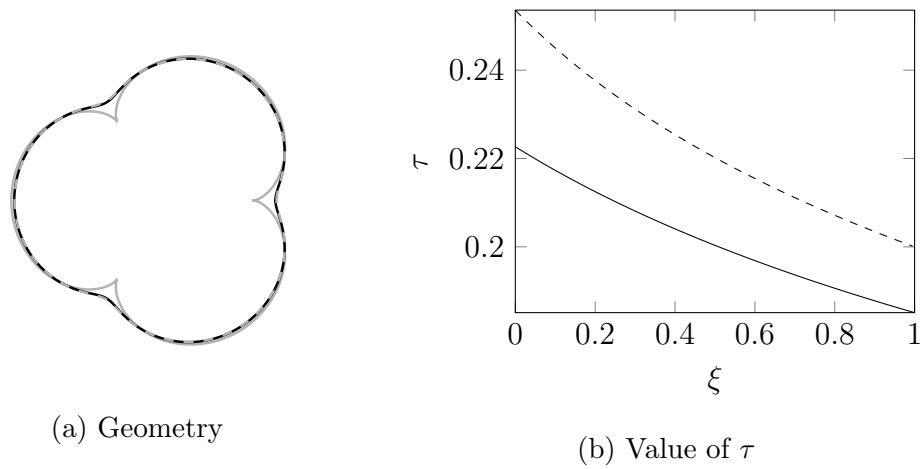


Figure 6.3.8: A comparison between the solutions to the transverse (scaled) problem for an epicycloid with  $\gamma^* = 10^{-1}$ . (a) Cross sections at  $\xi = 0.5$  and  $t = 2$  for the initial condition (grey solid), which is also the ZST solution, the full solution (solid black) and the WST solution (grey dashed); the full and WST solutions appear almost identical. (b) The values of  $\tau$  for the full (solid black) and WST (black dashed) problems, which differ by at most  $3.0927 \times 10^{-2}$ . The WST solution is at most 14% larger relative to the full solution.

## 6.4 Cylinders with Internal Structure

### 6.4.1 Overview

In this section we solve for the gravitational stretching, with no additional forcing (that is,  $c = 0$ ), of fluid cylinders with internal structure; that is, having interior boundaries. Two cases are considered: (1) a cylinder with an annular cross section for which an exact solution exists, and (2) a circular cylinder with three circular holes having collinear centres on a diameter of the cross section, for which a numerical solution is obtained.

Experimental data are available for both of these cases, consisting of the initial and final geometries of, and the weight below, a number of cross sections. From the weight below a cross section, the corresponding Lagrangian co-ordinate  $\xi$  may be determined. The known values of  $\sigma(\xi)$  and  $\gamma$  allow the computation of the ratio  $\sigma^*/\gamma^* = \sigma/(6\gamma\sqrt{\mathcal{S}})$ , which is needed in the model. We do not need to compute  $\sigma^*$  or  $\gamma^*$  explicitly. The experimental setup is shown in Figure 6.4.9, while further details and experimental measurements are given in Appendix C. As we will see, comparison of each experiment with the model demonstrates that the shape of the interior boundaries can be explained only with the inclusion of the surface-tension-driven transverse problem. Comparisons are made with the full and WST models.

We here note that experimental information on the viscosity (or temperature) of the glass, the exact initial length  $\mathcal{L}$  of the cylinder and the physical time from the commencement of deformation to the end of the experiment are not available to enable a comparison of the experimental deformation time with that predicted by the model. Instead, comparisons are made using reduced time  $\tau$ , which incorporates information from both the physical time and the

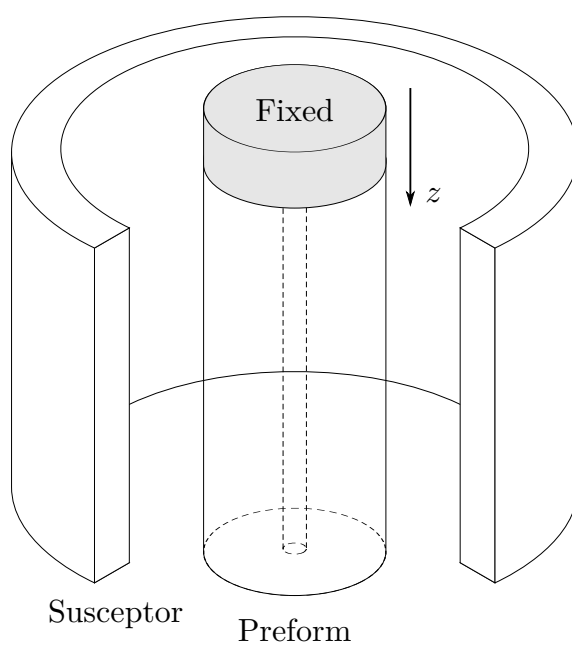


Figure 6.4.9: A schematic showing the set-up for the annular tube experiment. The upper end of a glass tube was held fixed while the lower end was free. The glass was heated by the surrounding electromagnetically-heated susceptor and allowed to stretch under gravity. In the diagram a section of the susceptor has been removed for clarity. The lower portion of the cylinder that deforms has a length somewhat less than the length of the susceptor.

viscosity profile.

### 6.4.2 Stretching Tube

As a first example of a geometry with internal structure we consider a cylinder in which each cross section is an annulus. Both the size and aspect ratio of the annulus are allowed to vary with  $\xi$ . It has been shown previously (Stokes *et al.*, 2014) that the associated transverse problem (3.3.42) can be solved exactly, yielding the scaled boundary length

$$\tilde{\Gamma}(\xi, \tau) = \frac{2}{\alpha_0} \left( \frac{\tau}{2\alpha_0} + 1 \right)^{-1},$$

where  $\alpha_0(\xi)$  is the difference between the scaled outer and inner radii at position  $\xi$  and reduced time  $\tau = 0$ . Substituting this expression into (6.2.11) yields the exact solution

$$\chi = \left( \frac{\tau}{2\alpha_0} + 1 \right)^{\frac{1}{3}} \left\{ \chi_0(\xi) - \frac{3\alpha_0\sigma^*}{\gamma^*} \left[ \left( \frac{\tau}{2\alpha_0} + 1 \right)^{\frac{2}{3}} - 1 \right] \right\}. \quad (6.4.23)$$

Using (6.2.12) it may be shown that  $t$  and  $\tau$  at cross section  $\xi$  are related by the algebraic equation

$$\frac{2\gamma^*}{3\alpha_0 m(\xi, t)} t = \left( \chi_0(\xi) + \frac{3\alpha_0\sigma^*}{\gamma^*} \right) \left[ \left( \frac{\tau}{2\alpha_0} + 1 \right)^{\frac{4}{3}} - 1 \right] - \frac{\sigma^*\tau}{\gamma^*} \left( \frac{\tau}{2\alpha_0} + 2 \right).$$

With this solution we are now in a position to investigate the influence of surface tension on a stretching tube. For this we again assume a constant viscosity, so that  $\mu \equiv m \equiv 1$ , and consider a cylinder with  $\chi_0(\xi) = 1$  and constant  $\alpha_0(\xi)$ . Although the axial solution (6.4.23) is best expressed in terms of the parameter  $\alpha_0$ , extruded annular preforms are more commonly described by the aspect ratio  $\phi$  of the inner to outer radii. Hence, we here use  $\phi(\xi, t)$  to characterise the

shape of a given annular tube. The quantities  $\alpha_0$  and  $\phi_0 = \phi(\xi, 0)$  are related by

$$\alpha_0^2 = \frac{1 - \phi_0}{\pi(1 + \phi_0)}.$$

We consider annuli with initial aspect ratios  $\phi_0$  between 0.2 and 0.9 in steps of 0.1. For each  $\phi_0$  we compute the geometry at  $t = 1$  for  $\gamma^* = 10^{-2}$  and  $10^{-1}$ . The computed areas  $S$  are plotted in Figure 6.4.10. Although the aspect ratio varies with  $\xi$  and  $t$ , the mass below each cross section  $\xi$  remains unchanged over time, allowing a comparison of surface-tension effects alone. For both values of  $\gamma^*$  the area at  $t = 1$  increases with the initial aspect ratio. This is because the surface tension component  $(\gamma^*\Gamma/2)$  in (6.2.6) that opposes gravitational stretching increases with  $\phi$ , since  $\Gamma$  increases with  $\phi$ . Clearly a larger surface tension  $\gamma^*$  also increases  $S(\xi, t)$ .

The corresponding ratios  $\phi(\xi, 1)$  from the transverse flow are plotted in Figure 6.4.11. These describe the shape of each cross section independent of any change of scale due to stretching. For  $\gamma^* = 10^{-2}$  the ratios do not change significantly and show no discernible dependence upon  $\xi$ . Thus, at this value of  $\gamma^*$  surface tension has little influence on the transverse flow. For  $\gamma^* = 10^{-1}$  all the ratios have decreased by approximately 0.1 and show only a slight increase as  $\xi$  increases. Thus, even though the value of  $\tau$  depends upon  $S$  via (3.3.41), which from Figure 6.4.10 changes significantly with  $\xi$ , the shape of each cross section shows little dependence upon  $\xi$ . The transverse flow is influenced largely by the value of  $\gamma^*$  alone.

To conclude our examination of the stretching annular tube we compare our model with experimental data. As described in Appendix C, an annular tube with initial aspect ratio  $\phi_0 = 0.168$  and a nominal initial external radius of 5 mm was fixed in a drawing tower, heated, and allowed to stretch under

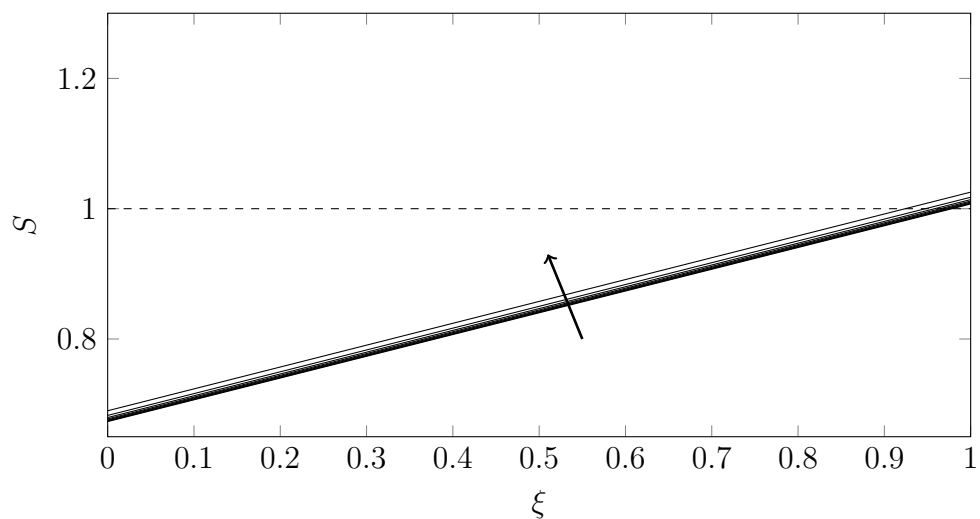
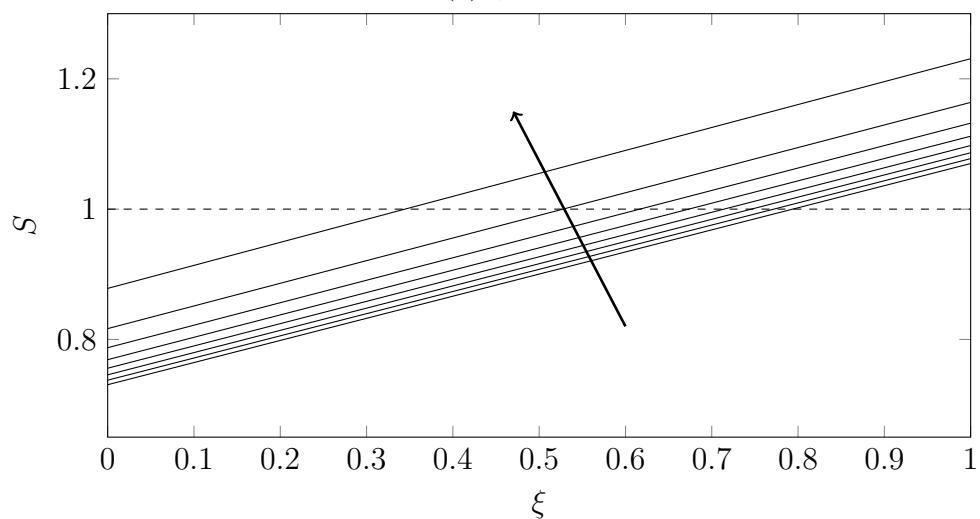
(a)  $\gamma^* = 10^{-2}$ (b)  $\gamma^* = 10^{-1}$ 

Figure 6.4.10: The area  $S(\xi, t)$  plotted against  $\xi$  for a tube with  $S_0(\xi) = 1$ . Solutions are shown at time  $t = 1$  for initial aspect ratios  $\phi_0 = 0.2, 0.3, \dots, 0.9$ , and  $\gamma^* = 10^{-2}$  and  $10^{-1}$ . The initial condition is shown as a dashed line while the arrows indicate the direction of increasing  $\phi_0$ . At every value of  $\xi$  the area increases with  $\phi_0$ , and this increase is greater for larger  $\gamma^*$ .

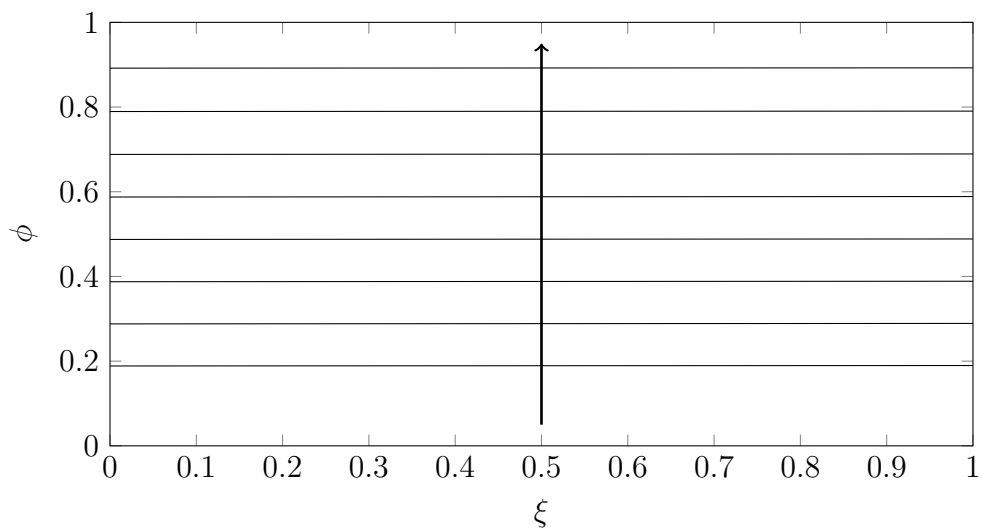
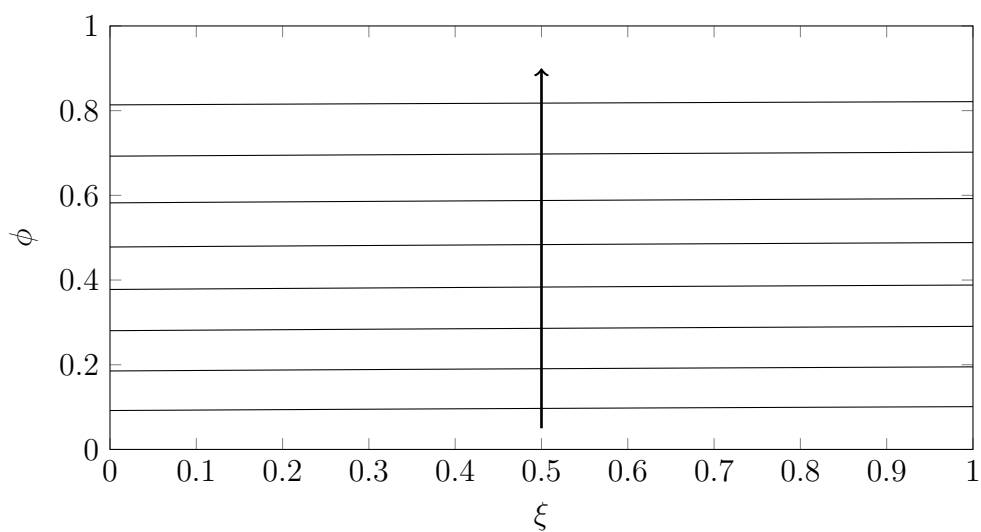
(a)  $\gamma^* = 10^{-2}$ (b)  $\gamma^* = 10^{-1}$ 

Figure 6.4.11: The aspect ratios  $\phi(\xi, 1)$  of the annuli from the transverse problem at  $t = 1$  for initial values  $\phi_0 = 0.2, 0.3, \dots, 0.9$ . The arrows indicate the direction of increasing  $\phi_0$ . For  $\gamma^* = 10^{-2}$  the ratios do not change significantly and show no discernible dependence upon  $\xi$ . For  $\gamma^* = 10^{-1}$  all the ratios have decreased by approximately 0.1 and increase by a small amount as  $\xi$  increases.

gravity, as illustrated in Figure 6.4.9. Matching experimentally measured cross-sectional areas to the model we find the value  $\tau$  corresponding to each cross section and this is used in the transverse model to predict the cross-section geometry. That is, we are able to calculate the shape of each cross section given the predicted area and compare the shape with that seen experimentally. The experimental external and internal radii scaled with  $\sqrt{\mathcal{S}\mathcal{S}(\xi, t)}$ , denoted  $R$  and  $\phi R$ , are plotted for some different values of  $\xi$  in Figure 6.4.12 along with the theoretical radii from the transverse problem for both the full and WST solutions. Since the scaled radii from the experimental data differ from their initial value, while in the absence of surface tension these should remain unchanged, we conclude that surface tension is having a significant effect. This deformation is larger as  $\xi$  decreases, which is due to two effects: (1) the cross sections with smaller label  $\xi$  spent longer in the heated susceptor region and hence had more chance to deform; and (2) due to stretching under a larger gravitational force they became smaller, giving rise to higher curvatures and hence a stronger surface-tension effect. For both the inner and outer radii the models match the data very well. In the region  $\xi < 0.4$  the tube has become so thin that there is only a small difference in the mass below each cross section, and hence only a small difference in the axial force, so that the radii change very little with  $\xi$ .

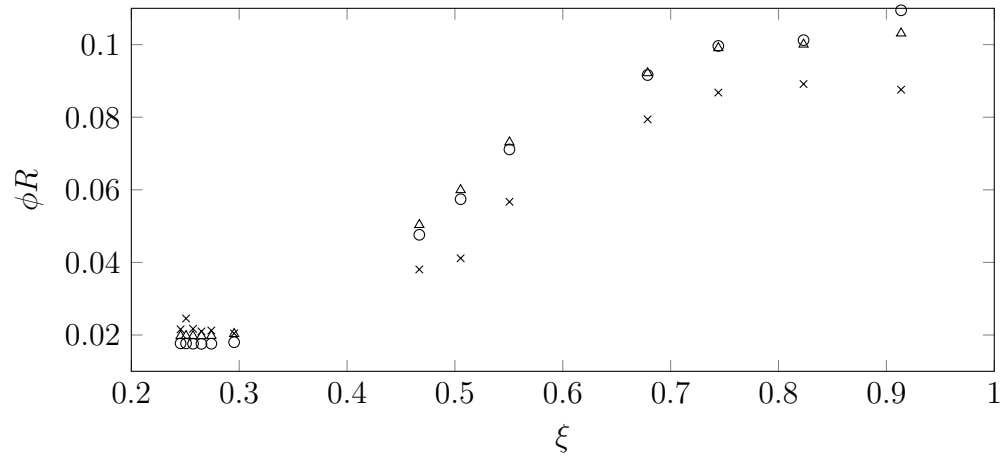
Figure 6.4.13 shows the aspect ratio  $\phi$  from the data and as predicted by the full and WST models. Unlike the examples in Figure 6.4.11,  $\phi$  shows a strong dependence upon  $\xi$ . This is due to changes in viscosity that occur as the glass cools.

There are several potential sources of error in the experimental data. Both boundaries are not perfectly circular so that the diameters measured vary

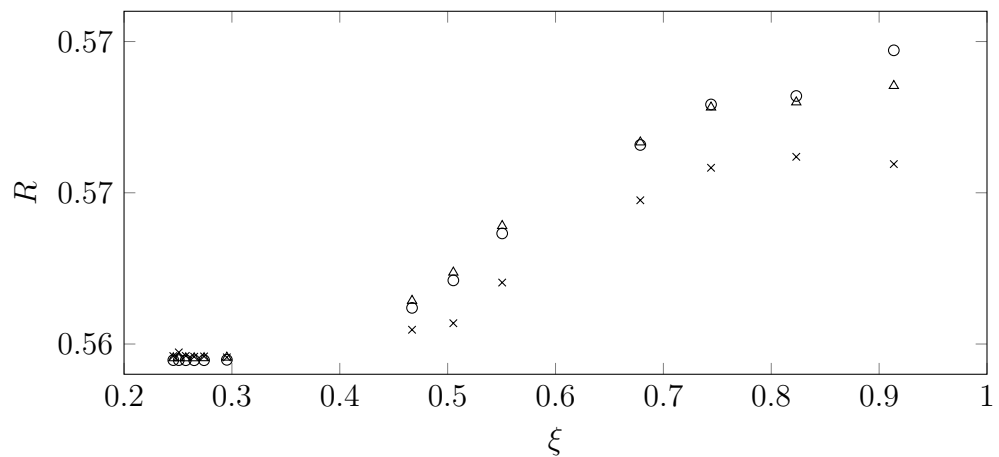
depending on the orientation of the cross section. It is also difficult to identify the precise location of the boundary, particularly when measuring the internal hole. Values measured using photographs can be incorrect if the camera is not correctly aligned, resulting in a skewed image. This is of particular importance for  $\xi < 0.4$  for which both diameters were measured using photographs. Taking into account these possible errors, the theoretical and observed values show good qualitative agreement. From this we conclude that the model is capturing the important physics in the problem. Importantly, the reduction in radius observed in Figure 6.4.12, when axial stretching has been removed, can only be explained by surface tension. Thus, we must include surface tension in order to capture the correct shape in each cross section.

### 6.4.3 3-Hole Experiment

We now consider a similar experiment to that in the previous section but with the multiply connected cross section geometry shown in Figure 6.4.14. This has a circular outer boundary with three circular inner holes and is of interest as it is similar to the shape of MOF preform jackets used for electro-optic fibre designs (Manning, 2011). The cylinder was produced by drilling the three internal channels into a solid rod. The top and bottom of the drilled cylinder are shown overlaid in Figure 6.4.14. Unfortunately, the axes of the channels were not exactly parallel to the axis of the cylinder, while in neither the top nor the bottom cross section was the centre of the middle hole at the centre of the outer boundary. As the experimental data recorded corresponded to a portion of the cylinder at the bottom, the lower geometry was used as the initial condition for the model. Evaluation of (6.2.11), as well as determination of the cross-sectional shape, required the solution of the transverse flow problem



(a) Inner radius



(b) Outer radius

Figure 6.4.12: A comparison of the dimensionless (a) inner radius  $\phi R$  and (b) outer radius  $R$  from the transverse flow model for the stretching tube. Shown are the experimental data (crosses), and the predictions by the full (circles) and WST (triangles) models. Both models produce similar results and provide a very good match to the data. In the absence of surface tension the cross section in the transverse flow model will not change over time so that the reduction in radius can only be explained by surface tension.

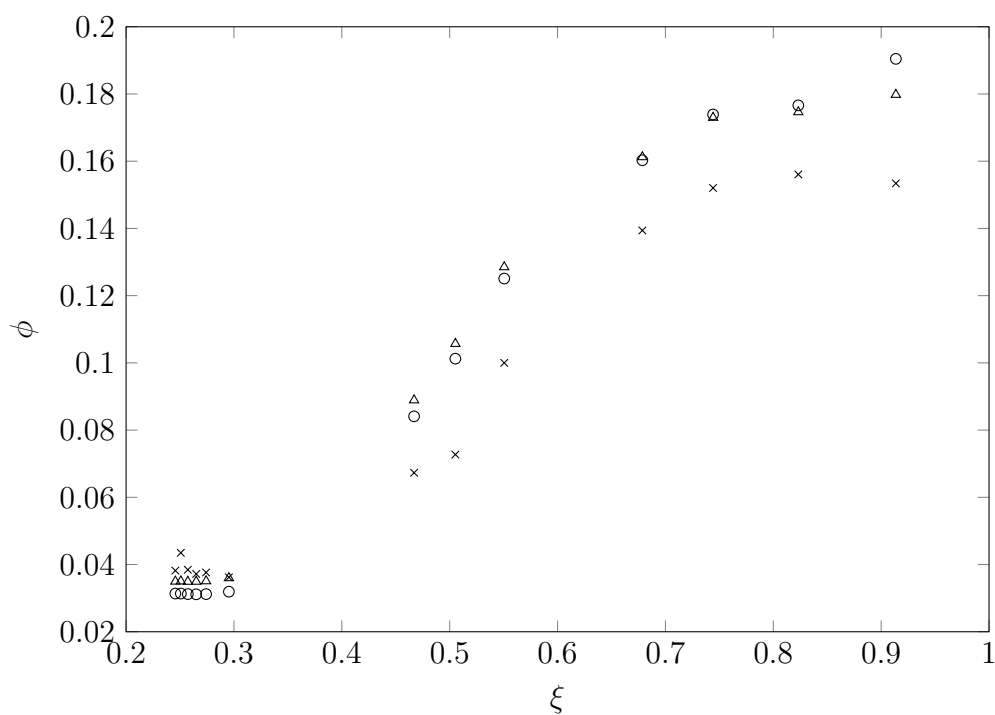


Figure 6.4.13: A comparison of the aspect ratio  $\phi$  for the stretching annular tube problem. Shown are the experimental data (crosses), and the predictions by the full (circles) and WST (triangles) models. The value of  $\phi$  shows a strong dependence upon  $\xi$ , which is due to a varying viscosity.

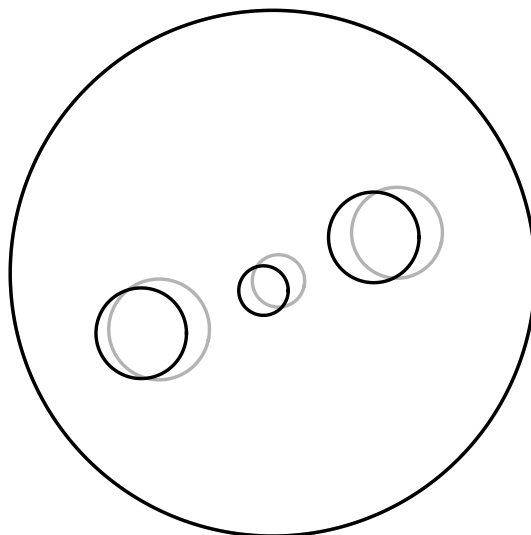


Figure 6.4.14: The initial configuration for the three-channel cylinder. Traces of the bottom (dark) and top (light) cross sections are shown overlaid. The bottom geometry was used as the initial condition in the transverse problem.

and with no exact solution available, this was done numerically using the complex-variable-based spectral method from Section 5.2

To provide a representative example of this process we here consider the predicted cross section at  $\xi = 0.30204$ . Using the method described in Appendix C yields the value  $\tau \approx 9.1026 \times 10^{-2}$ , corresponding to the geometry shown in Figure 6.4.15a, while the WST model predicts the reduced time  $\tau = 8.9207 \times 10^{-2}$ , which corresponds to an almost identical geometry (not shown). The two outer holes are almost circular but have decreased in size, while the central hole has both decreased in size and also become elliptical. This shows very good qualitative agreement to the observed geometry, also shown in Figure 6.4.15a; however, the model predicts a smaller central hole than that observed in the experiment.

By comparing the solution to the transverse problem with the experimental

result graphically, the best match occurs at the reduced time  $\tau = 0.08$ , which is shown in Figure 6.4.15b. At this value of  $\tau$  the interior holes predicted by the model are of similar size and shape to those observed in the experiment. Allowing for experimental error and the method used for determining  $\tau$ , the model captures the correct behaviour very well.

This comparison of model and experiment demonstrates the importance of surface tension. Without surface tension the cross sections will change in scale only but will undergo no other deformation. Experimentally, however, the central hole is seen to become elliptical in shape, matching the expected shape produced by the model with surface tension driving the transverse flow. Thus, surface tension must be included in order to correctly model the transverse flow. This is particularly important for the smaller central hole, which has the highest curvature of the four boundaries.

## 6.5 Including Inertia

It was seen that the inclusion of inertia resulted in a seemingly intractable form of the axial equation (6.2.8), which included an integral of the inertial term. It was shown in Subsection 6.2.2 that the Reynolds number was sufficiently small and from Subsection 6.2.5 onwards the inertial terms in the axial problem were neglected. (Recall that, provided  $\epsilon^2 \text{Re}$  is not  $O(1)$ , there are no inertia terms in the leading-order transverse problem.) While this assumption is appropriate for the typical parameter values considered here there may be cases in which this is no longer valid. For example, Wylie and Huang (2007) have shown that if a solid, axisymmetric thread is drawn with a force above some critical value, and in the absence of gravity and surface tension, then inertia must be included in

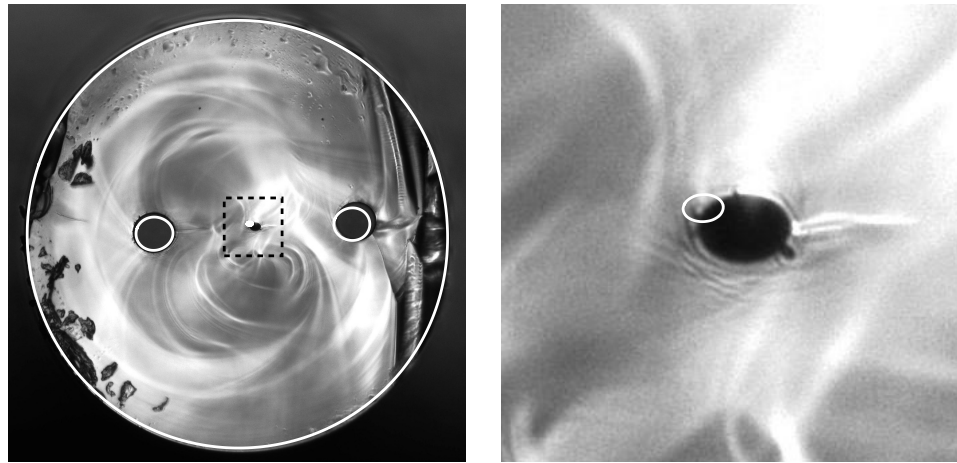
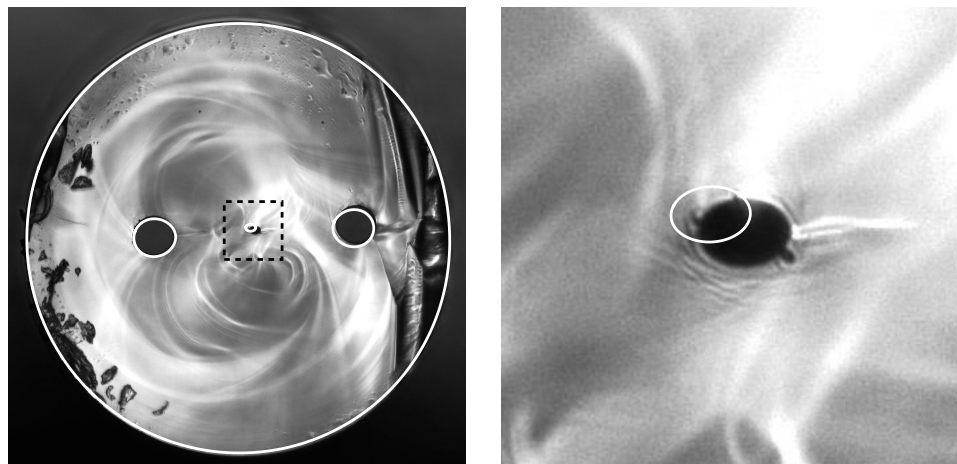
(a)  $\tau = 9.1026 \times 10^{-2}$ (b)  $\tau = 0.08$ 

Figure 6.4.15: A comparison between the experiments and model for the 3-hole cylinder. Shown top is as photograph of cross section  $\xi = 0.30204$  with the predicted shape from the model, corresponding to  $\tau = 9.1026 \times 10^{-2}$ , overlaid in white. The two outer holes show good agreement. The region inside the square is shown enlarged on the right, which shows that the predicted central hole is too small but does capture the correct qualitative behaviour. Shown below is a better match found by choosing  $\tau = 0.08$ .

order to find a solution. Near to the pinch-off of a fibre, the original length and velocity scales are no longer appropriate and may cause the Reynolds number to increase, meaning that inertial effects become important (Stokes and Tuck, 2004). Similarity solutions may be found near to the pinch-off time (Eggers and Villermaux, 2008). To conclude this chapter we here consider how the results of Stokes and Tuck (2004) may be extended to model the extension under gravity of a fluid cylinder with internal structure.

If we assume that the viscosity does not depend upon time so that  $\mu^* = \mu^*(\xi)$ , we can write (6.2.4) as

$$\frac{D}{Dt} \left[ \text{Re} S_0 w_0 + (3\mu^* S)_\xi \right] = S_0 g^* + \frac{\gamma^*}{2} \Gamma_\xi,$$

which is integrated with respect to  $t$  subject to the condition  $w_0(\xi, 0) = 0$  to give

$$\text{Re} S_0 w_0 + 3(\mu^* S - \mu^* S_0)_\xi = S_0 g^* t + \frac{\gamma^*}{2} \int_0^t \Gamma_\xi dt'.$$

Dividing by  $S_0$ , rearranging and differentiating with respect to  $\xi$  gives

$$\frac{\partial}{\partial \xi} \left[ \frac{3}{S_0} \frac{\partial}{\partial \xi} (\mu^* S - \mu^* S_0) - \frac{\gamma^*}{2S_0} \int_0^t \Gamma_\xi dt' \right] = -\text{Re} \frac{\partial w_0}{\partial \xi}.$$

Differentiating (6.2.2) with respect to  $t$  shows that

$$\frac{\partial w_0}{\partial \xi} = -\frac{S_0}{S^2} \frac{\partial S}{\partial t},$$

so that, after multiplying by  $S^2/S_0$ , the axial equation may be written as

$$\text{Re} \frac{\partial S}{\partial t} = \frac{S^2}{S_0} \frac{\partial}{\partial \xi} \left[ \frac{3}{S_0} \frac{\partial}{\partial \xi} (\mu^* S - \mu^* S_0) - \frac{\gamma^*}{2S_0} \int_0^t \Gamma_\xi dt' \right]. \quad (6.5.24)$$

The solution of this equation is complicated by the inclusion of the term with coefficient  $\gamma^*$  on the right-hand side, which represents the effects of surface tension and was not present in the work of Stokes and Tuck (2004). To proceed

would require knowledge of the relationship between  $S$  and  $\Gamma$ , which requires a transformation to reduced time. If, however,  $\gamma^*$  is small it is possible to use the ZST or WST approximations, in which case the surface-tension terms may be neglected and (6.5.24) reduces to

$$\text{Re} \frac{\partial S}{\partial t} = \frac{S^2}{S_0} \frac{\partial}{\partial \xi} \left[ \frac{3}{S_0} \frac{\partial}{\partial \xi} (\mu S - \mu S_0) \right]. \quad (6.5.25)$$

This has the form of a nonlinear diffusion equation with  $S$  in place of the concentration and a diffusion coefficient proportional to  $S^2$ . A similar equation was found first by Kaye (1991, p. 72, eqn (4.3.20)) for a cylinder of Newtonian fluid with uniform initial geometry and constant viscosity. This equation was extended by Stokes and Tuck (2004) for an arbitrary initial condition. In both of these studies the respective equations were solved numerically using finite difference methods.

The derivation given here shows that, for zero or weak surface tension, it is possible to include inertia in the solution of the axial problem. In the WST case the evolution of the transverse problem could still be computed by first solving (6.5.25) for  $S$  and then substituting  $\sqrt{S} = \chi$  into (6.2.12) to compute the corresponding values of  $\tau$ . With  $\tau$  known at each  $\xi$  the shape of the corresponding cross sections is given by evaluating the transverse solution at each  $\tau$  in the same manner as above when inertia was neglected.

Since inertia is not important in preform extrusion this modification is not discussed here further and is left to future work.

## 6.6 Summary

We have developed a model for the gravitational stretching of a very viscous fluid cylinder with internal structure. This model can be applied to any cross

section geometry provided it is possible to solve the associated transverse Stokes flow problem. For some cases, such as those illustrated in Section 6.3 and the annulus from Section 6.4, exact solutions exist, otherwise this problem must be solved using numerical methods.

While the full model includes surface-tension effects in both the axial and transverse problem it is possible to derive simplified models with surface tension featuring only in the transverse problem (the WST case) or neglected altogether (the ZST case). For typical values of the surface tension parameter  $\gamma^*$  of size  $O(10^{-2})$  it has been shown that surface tension does not have a strong influence on the axial problem. For the transverse flow surface tension is important. When  $\gamma^*$  is  $O(10^{-1})$  surface tension is important in the axial problem. This theoretical result is supported by the experimental data. To capture the correct behaviour it was essential to include surface tension in the transverse problem. The reduced-time model provided a convenient mechanism for estimating the transverse flow without knowledge of the viscosity.

The stretching under gravity of a fluid cylinder with internal structure and surface tension was investigated here because it closely resembles the conditions experienced by a MOF preform after the material exits the die. Due to this similarity, it is likely that surface tension is also important to understanding the extrusion of MOFs. To further investigate this hypothesis we will next extend this model by including the addition of material at the top of the cylinder, with the ultimate aim of developing a model of the MOF extrusion process.

This study has concerned only situations in which inertia is not important, and we emphasise that inertia is not important in the experiments described above. Given sufficient time, however, a cylinder may stretch and thus reduce sufficiently in diameter so that the original length scales are no longer appro-

---

priate and accelerations become large. In this case the problem enters a new regime in which the Reynolds number may no longer be assumed small, so that inertial effects become important. Wylie and Huang (2007) have studied this phenomenon in some detail, while the inclusion of inertia has also been investigated in the absence of surface tension by Stokes and Tuck (2004). It is possible to extend the methods discussed here by retaining the inertial terms in the axial problem; however, this leads to a more complicated equation that has no known explicit solution and presents significant challenges even for a numerical solution. Under a ZST or WST approximation it is possible to derive a diffusion-like axial equation similar to that of Stokes and Tuck (2004). The investigation of such a modification is left to future work.



# Chapter 7

## Modelling Extrusion

### 7.1 Introduction

In Chapter 6 we considered the stretching under gravity of a fluid cylinder with internal structure and surface tension, which was modelled using the slenderness equations from Chapter 3 with the axial velocity boundary condition  $w(0, t) = 0$ . With an appropriate axial Lagrangian co-ordinate, it was shown that the axial problem admitted an exact solution that depended upon the solution to the transverse flow. Using this solution it was concluded that surface tension can have a significant effect on the fluid flow.

In this chapter we build upon this work to construct a model for the extrusion of a fluid from a die, as occurs in MOF preform extrusion. This model again uses the equations from Chapter 6 but takes  $w(0, t)$  to be non-zero. To simplify the analysis a different axial Lagrangian co-ordinate will be employed in order to account for the increasing mass of fluid. We discuss the transition that occurs as the fluid leaves the die but do not include this effect. The model developed will be used to analyse some examples from MOF

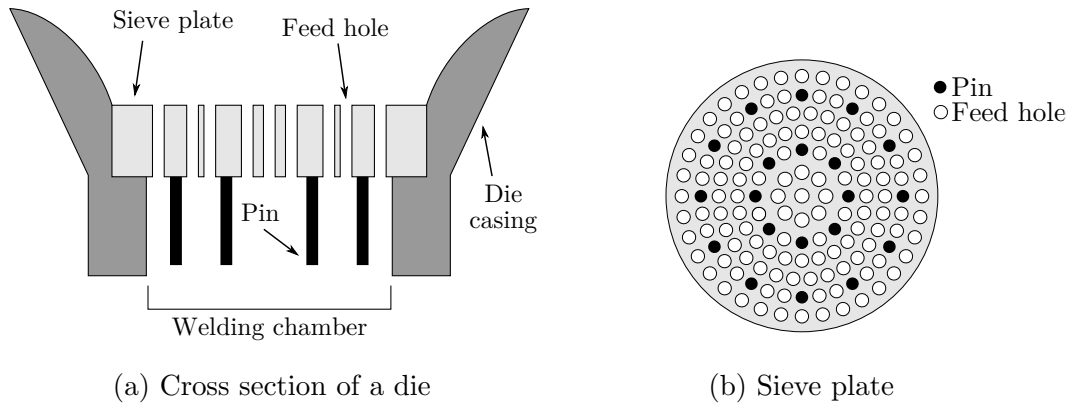


Figure 7.2.1: A schematic of a typical extrusion die design. Modified from Ebendorff-Heidepriem and Monroe (2012).

preform extrusion.

## 7.2 Die Effects

The problem of preform extrusion is made difficult by two phenomena that arise due to the passage of the fluid through the die: start-up effects and extrudate swell.

Start-up effects arise as the molten glass is first pushed through the die. A typical die, such as is sketched in Figure 7.2.1, consists of three key components: the die casing, the sieve plate and the pins. The sieve plate is a thin disk with a number of punctures known as feed holes that allow the molten material to flow through. The pins are fixed to the underside of the sieve plate and block the molten material, giving rise to the pattern of air channels within the preform (Ebendorff-Heidepriem and Monroe, 2007). The sieve plate and pins sit within the die casing, into which the molten material is forced. The region at the lower end of the die casing is known as the welding chamber. In this

region the strands of molten material passing through the feed holes must fuse together to fill the region around the pins. This requires that the material be extruded at sufficiently low speeds so as to give the molten material enough time to fuse. In the very early stages of an extrusion the material typically does not fuse together, resulting in fingers of unjoined filaments at the end of the preform (see Figure 7.2.2). This section of the preform cannot be used and is removed before the preform is drawn into a fibre. For the purposes of this analysis we will ignore this initial stage, and any effects the unfused filaments may have, and assume that the preform exits the die fully fused.

Of the two die-related effects, extrudate swell poses the most significant challenge. This phenomenon, known also as die swell, arises from the change in boundary conditions from no slip or partial slip at surfaces within the die to free surfaces once the material exits the die, which results in a transition of the axial flow from a non-uniform to a uniform profile with an accompanying increase in the preform diameter. This is perhaps best illustrated for circular dies; see Figure 7.2.3. Suppose that the flow is fully developed, with the no-slip boundary condition in the die and a free surface outside the die. Upstream, and within the die, we expect Poiseuille flow (a parabolic velocity profile), while downstream outside of the die the fluid displays plug flow (a uniform velocity profile). Between these two extremes the fluid exits the die and swells.

For Newtonian fluids extruded from circular dies this increase has been observed to be between 1.06 and 1.13 times the initial area (Middleman and Gavis, 1961; Horsfall, 1973), while for annular regions numerical studies have predicted this swell to be between 1.13 and 1.18, depending on the initial radii (Mitsoulis, 1986; Huynh, 1998). The effects of die swell during preform extrusion have been investigated using finite element methods for the case of

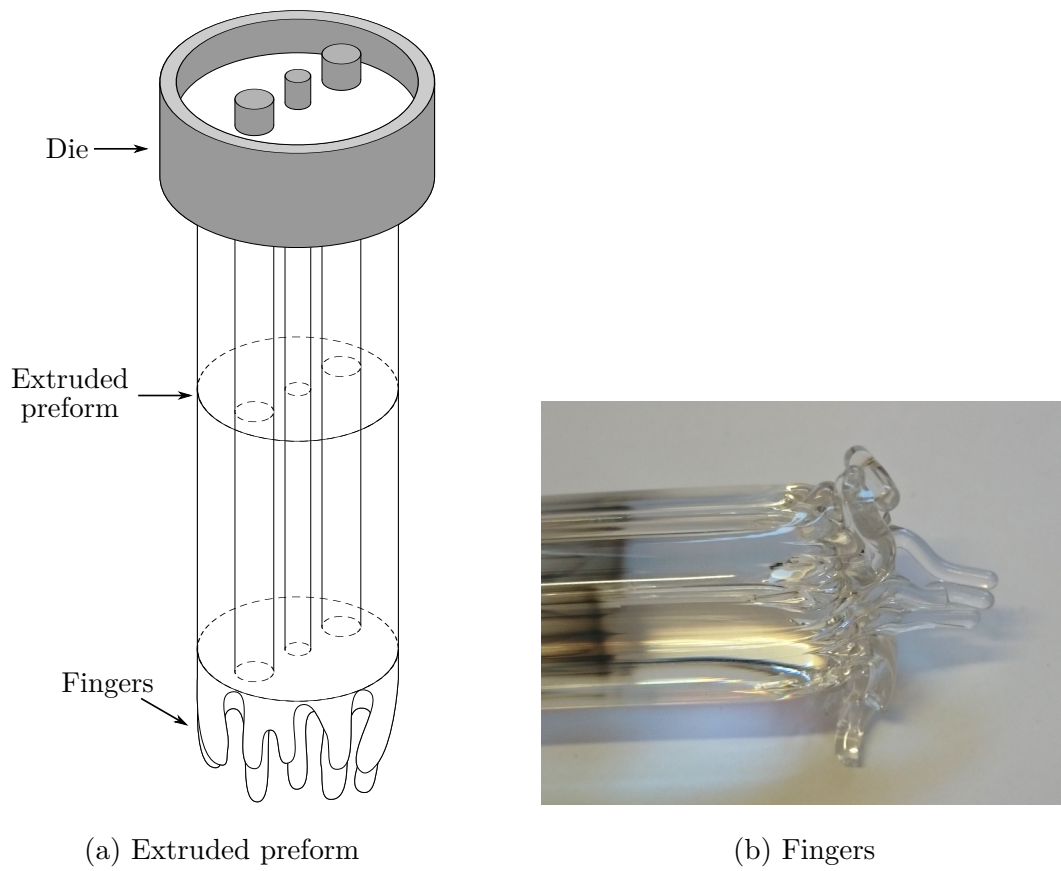


Figure 7.2.2: A sketch of a die and extruded preform, and a photo of the end of an extruded preform.

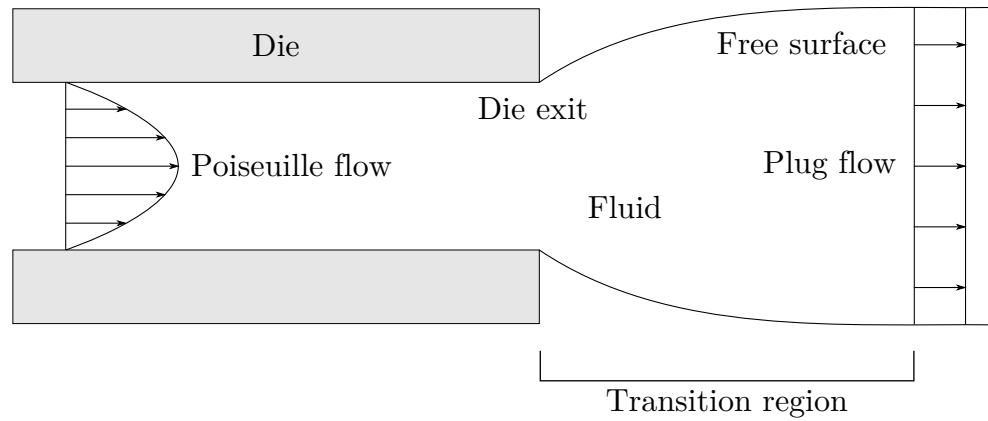


Figure 7.2.3: A cross section through a circular die showing extrudate swell.

an annular preform Trabelssi *et al.* (2014) and a 3-ring preform Trabelssi *et al.* (2015), with the results matched to experimental data by adjusting parameters within the model. Ebendorff-Heidepriem and Monro (2012) have analysed some basic models relating flux and friction through dies during extrusion. As a first step to creating a model of preform extrusion we ignore the effects of extrudate swell.

## 7.3 Extrusion Model

Using the assumptions made thus far we here construct a basic model for the extrusion of a fluid cylinder with internal structure. Much of the analysis is similar to that for a stretching fluid cylinder so use will be made of this earlier analysis where appropriate.

Table 7.3.1: Typical parameter values for extrusion.

Parameter	Symbol	Approx. value	Units
Surface tension	$\gamma$	0.2–0.3	$\text{N} \cdot \text{m}^{-1}$
Viscosity	$\mu_0$	$10^{6.5}$ – $10^{8.5}$	$\text{Pa} \cdot \text{s}$
Density	$\rho$	$2.5 \times 10^3$ – $6 \times 10^3$	$\text{kg} \cdot \text{m}^{-3}$
Die area	$\mathcal{S}$	$5 \times 10^{-5}$ – $8 \times 10^{-5}$	$\text{m}^2$
Representative flux	$\mathcal{Q}$	$10^{-11}$ – $1.6 \times 10^{-10}$	$\text{m}^3 \cdot \text{s}^{-1}$
Extrusion speed	$\mathcal{U}$	$1.7 \times 10^{-7}$ – $3.3 \times 10^{-6}$	$\text{m} \cdot \text{s}^{-1}$
Thermal conductivity	$k$	1.3–2	$\text{W} \cdot \text{m}^{-1} \cdot \text{K}^{-1}$
Heat transfer coefficient	$h$	150–300	$\text{W} \cdot \text{m}^{-2} \cdot \text{K}^{-1}$
Thermal diffusivity	$\alpha$	$5.6 \times 10^{-7}$ – $4.3 \times 10^{-7}$	$\text{m}^2 \cdot \text{s}^{-1}$

### 7.3.1 Parameters and Governing Equations

Consider a die with an arbitrary number of pins distributed throughout the cross section, through which is forced molten glass at some volumetric flux denoted  $Q(t)$ . Under the assumptions in Chapter 2, molten glass is a Newtonian fluid with a temperature-dependent viscosity. Typical values for the material properties and other associated parameters during MOF preform extrusion are given in Table 7.3.1, which, where appropriate, match those used previously for the stretching problem. Here, the characteristic area  $\mathcal{S}$  is the area of the die geometry and  $\mathcal{Q}$  is a representative volumetric flux through the die exit. The axial length scale is denoted  $\mathcal{L}$  and will be set below. The velocity scale  $\mathcal{U}$  is defined to be the axial velocity at the die exit and is related to the characteristic flux and area by  $\mathcal{Q} = \mathcal{S}\mathcal{U}$ . This corresponds to the time scale  $\mathcal{L}/\mathcal{U} = \mathcal{L}\mathcal{S}/\mathcal{Q}$ .

As per Chapter 3, we initially consider a Cartesian co-ordinate system with

the  $z$ -axis oriented parallel to the flow of fluid out of the die, and with the  $x$ - and  $y$ -axes perpendicular to the die exit. The corresponding velocity vector is  $(u, v, w)$ . The variables are scaled as per (3.3.7), while the dimensionless flux is defined by  $Q = \mathcal{Q}\hat{Q}$ . From this point onwards we drop carets from dimensionless variables but will retain asterisks on scaled parameters for later convenience. The governing equations are the Navier–Stokes, continuity and heat equations, given in (3.3.5), while the boundary conditions at the die are

$$S(0, t) = 1, \quad u(0, t) = 1, \quad T(x, y, 0, t) = 1.$$

With the given scales the Reynolds number, Péclet number, Biot number, dimensionless surface tension and gravity are, respectively,

$$\text{Re} = \frac{\rho\mathcal{Q}\mathcal{L}}{\mu_0\mathcal{S}}, \quad \text{Pe} = \frac{\mathcal{L}\mathcal{Q}}{\alpha\mathcal{L}}, \quad \text{Bi} = \frac{h\mathcal{L}}{k}, \quad \gamma^* = \frac{\gamma\mathcal{L}\sqrt{\mathcal{S}}}{\mu_0\mathcal{Q}}, \quad g^* = \frac{\rho g\mathcal{L}^2\mathcal{S}}{\mu_0\mathcal{Q}}. \quad (7.3.1)$$

In the stretching problem the natural axial length scale  $\mathcal{L}$  was the initial cylinder length  $L_0$ , while, in the absence of a suitable characteristic speed, the velocity scale  $\mathcal{U}$  was set by requiring  $g^* = 1$ . In the extrusion problem the situation is reversed: the extrusion speed provides a natural velocity scale but there is no initial axial length from which to define  $\mathcal{L}$ . We thus again set the final scale by fixing  $g^* = 1$ , so that the length scale, Reynolds number, surface tension

parameter, Péclet number, Biot number and time scale are, respectively,

$$\mathcal{L} = \sqrt{\frac{\mu_0 \mathcal{Q}}{\rho g \mathcal{S}}} \quad (7.3.2a)$$

$$\text{Re} = \sqrt{\frac{\rho \mathcal{Q}^3}{\mu_0 g \mathcal{S}^3}} \quad (7.3.2b)$$

$$\gamma^* = \frac{\gamma}{\sqrt{\mu_0 \rho g \mathcal{Q}}} \quad (7.3.2c)$$

$$\text{Pe} = \sqrt{\frac{\mu_0 \mathcal{Q}^3}{\alpha^2 \rho g \mathcal{S}^3}} \quad (7.3.2d)$$

$$\text{Bi} = \frac{h}{k} \sqrt{\frac{\mu_0 \mathcal{Q}}{\rho g \mathcal{S}}} \quad (7.3.2e)$$

$$\frac{\mathcal{L}}{\mathcal{U}} = \sqrt{\frac{\mu_0 \mathcal{S}}{\rho g \mathcal{Q}}}. \quad (7.3.2f)$$

As in Chapter 6, the parameter  $\gamma^*$  is an inverse Bond number. Using the typical values from Table 7.3.1 yields a length scale  $\mathcal{L}$  of  $O(10^{-1})$ . The slenderness ratio  $\epsilon$  is  $O(10^{-2})$ , the Reynolds number  $\text{Re}$  is  $O(10^{-11})$ , the dimensionless surface tension  $\gamma^*$  is  $O(10^{-1})$ , the Péclet number  $\text{Pe}$  is  $O(1)$  and the Biot number  $\text{Bi}$  is  $O(1)$ . These values satisfy the assumptions of the slenderness model developed in Chapter 3.

For small times  $t$  the extruded cylinder will be shorter than the length  $\mathcal{L}$ , so that the slenderness ratio  $\epsilon = \sqrt{\mathcal{S}}/\mathcal{L}$  is not a true measure of the geometry. As such, initially the extruded cylinder cannot be considered slender. We here assume that the error introduced by applying the slenderness approximation for early times is small. In practice, the lower end of a MOF preform, which is extruded first, is discarded due to the fingers of material. A consequence of this is that the region above this, which is retained, may be considered slender for all times.

Given this assumption, we again make use of the slenderness approximation

so that the analysis is identical to that of Chapter 3. In particular: the heat model is neglected; it is assumed that the viscosity is known; and the model reduces to coupled axial and transverse systems. The analysis is then similar to that used in Chapter 6; however, in the case of an extruded fluid we make some adjustments to this formulation that relate primarily to the Lagrangian co-ordinate and reduced time. These are described in the following subsection.

### 7.3.2 Lagrangian Co-ordinate and Reduced Time

For the stretching cylinder an axial Lagrangian co-ordinate was introduced that labelled each cross section by the initial axial position of the cross section (Subsection 6.2.3). While it would be possible to define an initial position for each cross section of an *extruding* cylinder we find it simpler to follow the method used by Wilson (1988) and introduce an axial Lagrangian co-ordinate  $\eta$  that labels each cross section by the time at which it leaves the die, illustrated in Figure 7.3.4. Thus,  $\eta$  is defined as the solution to  $z(t, t) = 0$  where  $z = z(\eta, t)$ . In order to relate  $\eta$  and  $z$  we must consider the flux of material through the die, shown in Figure 7.3.4. Then, in the region between  $\eta$  and  $\eta + d\eta$  we have that

$$Q d\eta = -S dz,$$

so that in the limit as  $d\eta$  and  $dz$  go to zero we have

$$\frac{\partial z}{\partial \eta} = -\frac{Q}{S}. \quad (7.3.3)$$

Integrating (7.3.3) with the condition that  $z(t, t) = 0$  yields

$$z(\eta, t) = \int_{\eta}^t \frac{Q(t')}{S(\eta, t')} d\eta'. \quad (7.3.4)$$

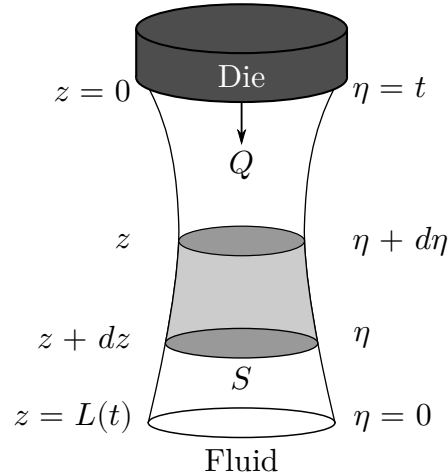


Figure 7.3.4: An illustration of the Eulerian and Lagrangian co-ordinates for an extruded fluid cylinder. Fluid is extruded from the die at the volumetric flow rate  $Q$  and has cross-sectional area  $S(z)$ . By enforcing conservation of mass within the shaded region we find that  $Q d\eta = -S dz$ .

The other significant difference between the formulation of the stretching and extrusion problems lies in the use of reduced time  $\tau$ . While  $\tau$  plays the same role in both problems there are some variations in the definitions used in each. For a stretching fluid region  $\tau$  was defined as the solution to (3.3.39), which states that

$$\frac{\partial \tau}{\partial t} = \frac{\gamma^*}{\mu \sqrt{S}},$$

subject to the condition  $\tau(\xi, 0) = 0$ , so that at physical time  $t$  every cross section is at reduced time  $\tau = 0$ . Physically, this condition means that at  $t = 0$  every cross section has no deformation. This condition is enforced by the limits of integration used in the definition (3.3.41).

In the extrusion problem this condition is replaced by the requirement that the cross sections are not deformed when they leave the die. In terms of reduced

time, this condition states that at  $t = \eta$ , cross section  $\eta$ , which is at the die exit, must have associated reduced time  $\tau(\eta, \eta) = 0$ . Solving (3.3.39) subject to this condition yields

$$\tau = \int_{\eta}^t \frac{\gamma^*}{\mu\chi} dt'. \quad (7.3.5)$$

Once again, in reduced time  $\tau$  the flow within any cross section is a two-dimensional Stokes flow with unit surface tension, so is governed by the transverse system (3.3.42), which is independent of the axial flow. Since  $\tau = \tau(\eta, t)$  for  $t \geq \eta$ , each cross section is associated with a different reduced time, as for the stretching problem; however, as each cross section has the same initial geometry, being the negative of the die, every cross section has the same associated transverse problem. This is in contrast to the stretching problem in which each cross section could, in general, have a different initial geometry and hence a different associated transverse problem.

With this definition made, the analysis of the axial problem continues as per Chapter 6 up to Subsection 6.2.3. Following the method but using the new Lagrangian co-ordinate  $\eta$ , we introduce the total boundary length  $\Gamma(\eta, t)$  and material derivative, which yields

$$-\text{Re}Q \frac{Dw_0}{Dt} + \frac{\partial}{\partial \eta} \left( 3\mu \frac{DS}{Dt} \right) = -Q + \frac{\gamma^*}{2} \frac{\partial \Gamma}{\partial \eta}.$$

Integrating with respect to  $\eta$  over the length of the cylinder at time  $t$ , which ranges from 0 to  $\eta$ , results in

$$3\mu \frac{DS}{Dt} = - \int_0^{\eta} Q - \text{Re}Q \frac{Dw_0}{Dt} d\eta' + \frac{\gamma^*}{2} \Gamma - c(t),$$

where  $c(t)$  represents a time-dependent axial tension. The first term of the integrand on the right-hand side is just

$$\int_0^{\eta} Q(\eta) d\eta' = \int_z^{L(t)} S dS = V(\eta),$$

where  $V(\eta)$  is the dimensionless weight of material below cross section  $\eta$ . In the case of a constant flux  $Q \equiv 1$  and this mass is simply  $V(\eta) = \eta$ .

As the Reynolds number  $Re$  is small, from this point onwards the inertial terms will be neglected. Introducing the total fibre tension

$$6\sigma^*(\eta, t) = V(\eta) + c(t)$$

results in the axial equation

$$3\mu \frac{DS}{Dt} = -6\sigma^* + \frac{\gamma^*}{2}\Gamma. \quad (7.3.6)$$

At present this equation involves two unknown quantities  $S$  and  $\Gamma$ , which, for a general geometry, have no simple relationship. In a manner identical to that used on (6.2.6), we overcome this by transforming to reduced time  $\tau$  and introducing  $\chi = \sqrt{S}$ . In reduced time, the boundary length is given by

$$\Gamma(\eta, \tau) = \chi(\eta, \tau)\tilde{\Gamma}(\tau),$$

where  $\tilde{\Gamma}(\tau)$  is the boundary length from the solution to the transverse problem. Note that, unlike the stretching problem, each cross section has the same associated transverse problem so that  $\tilde{\Gamma}$  is a function of  $\tau$  only. Introducing this into (7.3.6), the resulting differential equation may be solved using the integrating factor

$$H(\tau) = \exp\left(-\frac{1}{12} \int_0^\tau \tilde{\Gamma}(\tau') d\tau'\right),$$

which is similar to (6.2.10) but is independent of the Lagrangian co-ordinate  $\eta$ . Similar to (6.2.11), using this integrating factor yields the axial solution

$$\chi(\eta, \tau) = \frac{1}{H(\eta)} \left(1 - \frac{1}{\gamma^*} \int_0^\tau \sigma^* H(\tau) d\tau'\right). \quad (7.3.7)$$

Finally, we can relate  $t$  and  $\tau$  in a manner similar to that of (6.2.12), giving

$$\chi \frac{\partial \tau}{\partial t} = \frac{\gamma^*}{\mu}.$$

For any cross section  $\eta$  we note that at the time of extrusion  $t = \eta$  we must have  $\tau = 0$ . Thus, integrating the above expression with respect to  $t$  from  $\eta$  to  $t$  results in the relationship

$$\int_0^\tau \chi d\tau' = \int_\eta^t \frac{\gamma^*}{\mu} dt' = \frac{\gamma^*(t - \eta)}{m(\eta, t)}, \quad (7.3.8)$$

where

$$m(\eta, t) = \frac{t - \eta}{\int_\eta^t \frac{1}{\mu^*(\eta, t')} dt'}$$

is the harmonic mean of  $\mu^*(\eta, t)$  for cross section  $\eta$  between the times  $\eta$  and  $t \geq \eta$ . This provides a complete general solution to the extrusion problem. For the remainder of this chapter this solution is used to explore a selection of example problems. From this point onwards we assume that  $c(t)$  is constant.

### 7.3.3 Solutions for Zero and Weak Surface Tension

Similar to the solutions found in Subsection 6.2.6, we here consider two approximations to the full extrusion solution found in Subsection 7.3.2 for cases in which the surface tension parameter  $\gamma^*$  is small. When  $\gamma^* \ll 1$  and  $\chi$  is not too small we may drop the surface tension terms from both the axial and transverse problems. In this case the cross sections only vary in scale due to the axial equation, which no longer depends upon the transverse flow. Setting  $\gamma^* = 0$  in (7.3.5) shows that  $\tau = 0$  so that the transverse problem may be neglected entirely. This is denoted the zero-surface-tension (ZST) case. For geometries in which there are large curvatures or small area  $S$ , small changes in  $\tau$  may still be important. For such situations we neglect the surface tension

terms from the axial equation but still include the transverse problem. This is denoted the weak-surface-tension (WST) case.

For both the ZST and WST cases, we set  $\gamma^* = 0$  in (7.3.6) and integrate, yielding

$$S(\eta, t) = 1 - \frac{2(t - \eta)\sigma^*(\eta)}{m(\eta, t)}. \quad (7.3.9)$$

This is identical in form to the equivalent result for stretching (6.2.13). As before, (7.3.9) does not depend upon the cross-sectional shape. The WST axial equation may also be solved in reduced time, which gives

$$\chi(\eta, \tau) = 1 - \frac{\sigma^*(\eta)\tau}{\gamma^*}.$$

Equating  $\chi^2$  to  $S$  as given by (7.3.9) yields a quadratic equation for  $\tau$ , which may be solved to give

$$\tau = \frac{\gamma^*}{\sigma^*} \left[ 1 - \left( 1 - \frac{2(t - \eta)\sigma^*}{m} \right)^{\frac{1}{2}} \right].$$

As in Subsection 6.2.6, the negative root must be chosen so that  $\partial\tau/\partial t > 0$  and  $\tau(t, t) = 0$ . The term inside the parentheses in this relationship is precisely (7.3.9) and is thus always initially positive. For positive  $\sigma^*$  the area of cross section  $\eta$  decreases with increasing  $t$  and eventually reaches 0, at which point the solution is no longer applicable. This is discussed further in Section 7.7.

If the viscosity  $\mu^*$  is independent of  $\eta$  further progress can be made. For

$t > \eta$ , we substitute  $S$  from (7.3.9) into (7.3.4) and integrate to yield

$$z(\eta, t) = \begin{cases} \frac{6m}{\sqrt{12m - (c+t)^2}} \left[ \arctan \left( \frac{2\eta + c - t}{\sqrt{12m - (c+t)^2}} \right) \right]_{\eta}^t, & 12m > (c+t)^2, \\ \frac{-6m}{\sqrt{(c+t)^2 - 12m}} \left[ \operatorname{artanh} \left( \frac{2\eta + c - t}{\sqrt{(c+t)^2 - 12m}} \right) \right]_{\eta}^t, & 12m < (c+t)^2, \\ \frac{-2}{2\eta + c - t}, & 12m = (c+t)^2. \end{cases} \quad (7.3.10)$$

The length is given by  $L(t) = z(0, t)$ . Unlike the stretching case in Subsection 6.2.6, the complexity of this solution means we cannot find a closed-form expression for  $S(z, t)$ .

## 7.4 Geometries with No Internal Holes

### 7.4.1 Solution for a Solid Rod

For a solid rod the area and boundary length are related by  $\Gamma = 2\sqrt{\pi S}$ . Substituting into the governing equation (7.3.6) and introducing  $\chi = \sqrt{S}$  yields

$$\mu^* \chi \frac{\partial \chi}{\partial t} = \delta \left( \chi - \frac{\sigma^*}{\delta} \right),$$

where, as before,  $\delta = \gamma^* \sqrt{\pi}/6$ . As this is a separable differential equation, we may solve this directly subject to  $\chi(\eta, \eta) = 1$  to give

$$\chi - 1 + \frac{\sigma^*}{\delta} \log \left( \frac{\delta \chi - \sigma^*}{\delta - \sigma^*} \right) = \frac{\delta(t - \eta)}{m(\eta, t)}. \quad (7.4.11)$$

This is an implicit equation for  $\chi$  that may be solved numerically for given values of  $t$  and  $\eta$ , and is the extension of the solution for a stretching cylinder (6.3.19) to an extruded fluid cylinder.

In the case that  $c = 0$  and  $\mu \equiv 1$ , (7.3.6) is precisely the equation found by Wilson (1988, p. 564, eqn (15)), and (7.4.11) the same solution.

Using the reduced-time approach, the solution may be written

$$\begin{aligned}\chi &= \left(1 - \frac{6\sigma^*}{\gamma^*\sqrt{\pi}}\right) \frac{1}{H} + \frac{6\sigma^*}{\gamma^*\sqrt{\pi}}, \\ &= \left(1 - \frac{\sigma^*}{\delta}\right) e^{\frac{\tau\sqrt{\pi}}{6}} + \frac{\sigma^*}{\delta}.\end{aligned}\quad (7.4.12)$$

Substituting (7.4.12) into (7.3.8) then yields

$$\frac{6}{\sqrt{\pi}} \left(1 - \frac{\sigma^*}{\delta}\right) \left(e^{\frac{\tau\sqrt{\pi}}{6}} - 1\right) + \frac{\sigma^*}{\delta} \tau = \frac{\gamma^*(t - \eta)}{m(\eta, t)}.\quad (7.4.13)$$

Using (7.4.12) it is readily shown that

$$e^{\frac{\tau\sqrt{\pi}}{6}} = \frac{\delta\chi - \sigma^*}{\delta - \sigma^*}$$

and

$$\tau = \frac{6}{\sqrt{\pi}} \log \left( \frac{\delta\chi - \sigma^*}{\delta - \sigma^*} \right).$$

Substituting these into (7.4.13) recovers (7.4.11) precisely.

## 7.4.2 Influence of Surface Tension and Geometry

In Subsection 6.3.3 we considered the influence of the dimensionless surface tension  $\gamma^*$  on the stretching of a fluid cylinder with no internal structure. This analysis is now repeated for an *extruded* fluid cylinder. We again consider solutions of the full axial problem for both a solid axisymmetric rod and an epicycloid, along with the ZST–WST axial solution, which is independent of the cross-sectional geometry.

Figure 7.4.5 shows solutions for the three cases for  $\gamma^* = 10^{-3}$ ,  $10^{-2}$  and  $10^{-1}$ , shown at times  $t = 1$  and 2. At  $\gamma^* = 10^{-3}$  the axisymmetric rod, epicycloid

and ZST–WST solutions are almost identical to graphical accuracy at both times shown. The free ends of the fluid regions  $\eta = 0$  have area near or equal to 1. For  $\gamma^* = 10^{-2}$  the three solutions differ noticeably. At both times the epicycloid has a larger area than the rod, which in turn has a larger area than the ZST–WST solution. This difference is greater near the free end, which has been outside the die longest and experiences no gravitational stretching, while all three solutions meet at the die end, at which the boundary conditions require the area to be 1. The case  $\gamma^* = 10^{-1}$  shows similar qualitative behaviour to  $\gamma^* = 10^{-2}$  but with greater differences between the solutions. In particular, the free ends of the rod and epicycloid solutions both show areas significantly greater than 1, which is due to the compressive effect of surface tension.

## 7.5 Controlling Deformation and Exact Solution for an Annulus

### 7.5.1 Overview

In this section we investigate the relationship between  $\gamma^*$ , defined by (7.3.2c), and the amount of deformation in an extruded fluid cylinder. To facilitate this analysis we introduce measures of the level of both axial and transverse deformation. In order to illustrate these measures on a geometry with an internal boundary we derive an exact solution for extrusion through an annular die, similar to that for a stretching annulus in Section 6.3. Through this example we show how  $\gamma^*$  may be used to control the deformation.

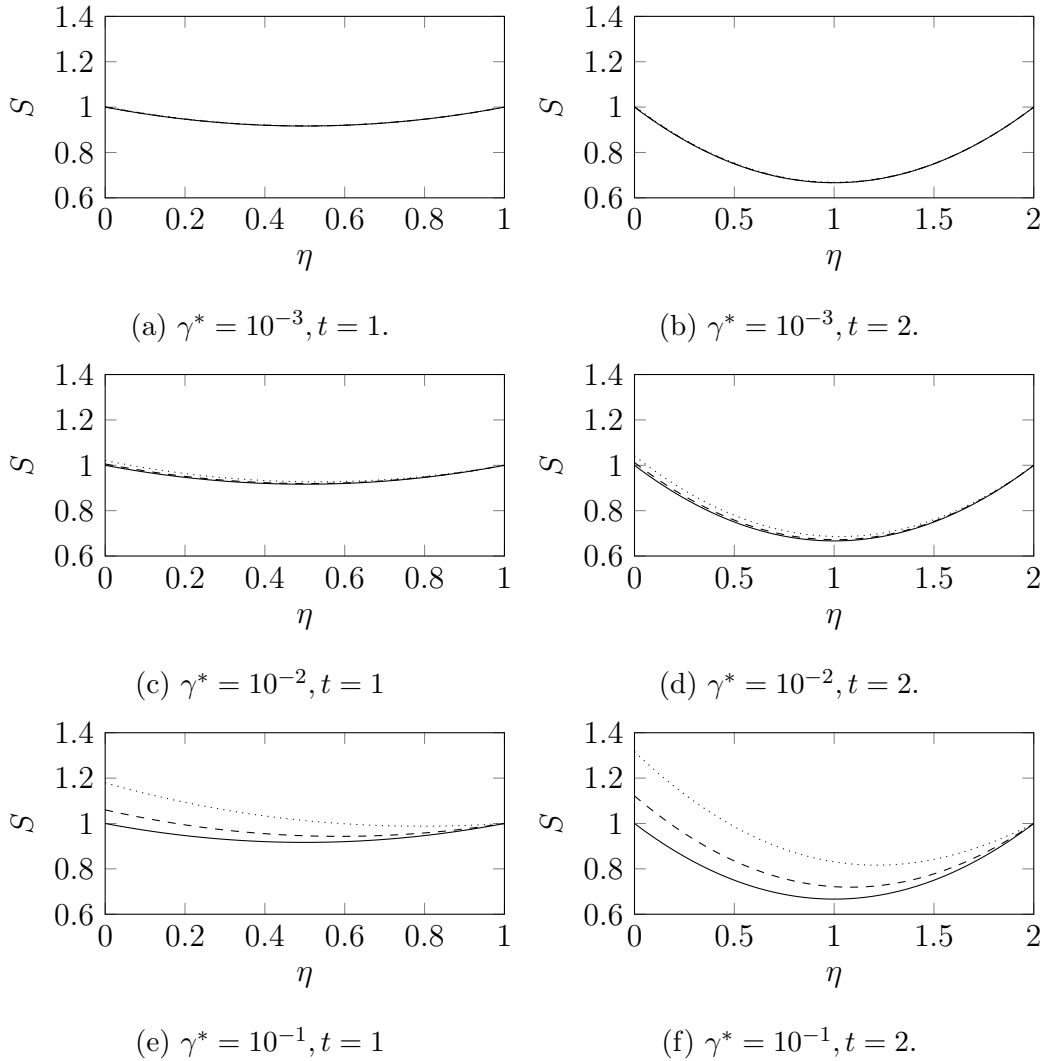


Figure 7.4.5: The solutions  $S(\xi, t)$  corresponding to the ZST–WST solution (solid curve), and the full problem for each of the rod (dashed curve) and epicycloid (dotted curve). The solutions have been computed with dimensionless surface tensions  $\gamma^* = 10^{-3}$ ,  $10^{-2}$  and  $10^{-1}$ , and are shown at times  $t = 1$  and 2. For  $\gamma^* = 10^{-3}$  the three solutions are indistinguishable to graphical accuracy at both times shown. For  $\gamma^* = 10^{-2}$  the epicycloid solution is slightly larger for all  $\xi$ , while the rod and ZST–WST solutions remain similar to each other. For  $\gamma^* = 10^{-1}$  the three solutions differ noticeably.

### 7.5.2 Measuring Deformation

To properly understand the effect of  $\gamma^*$  we first need a quantitative method to measure the deformation of an extruded fluid cylinder. We note that the state of any cross section  $\eta$  may be described by the area  $S$  and reduced time  $\tau$ . Thus, one possible measure of axial deformation up to time  $t$  is

$$S_d(t) = \max_{\eta} |S - 1|,$$

which measures the maximum deviation of the area from the initial area of 1. Similarly, larger  $\tau$  corresponds to greater change in geometry, so that the transverse deformation may be measured by

$$\tau_d(t) = \max_{\eta} |\tau|.$$

Both  $S_d(t)$  and  $\tau_d(t)$  are non-decreasing. While it would be possible to define average or integrated measures of the deformation, we choose the above forms as they provide an upper bound on the deformation, so are easily related to specified manufacturing tolerances.

### 7.5.3 Solution for an Annulus

To provide an example of the defined measures we consider extrusion through an annular die. Defining  $\alpha_0$  to be the difference between the outer and inner radii in the associated transverse problem, the area is given by

$$S(\eta, \tau) = \left( \frac{\tau}{2\alpha_0} + 1 \right)^{\frac{2}{3}} \left\{ 1 - \frac{3\alpha_0\sigma^*}{\gamma^*} \left[ \left( \frac{\tau}{2\alpha_0} + 1 \right)^{\frac{2}{3}} - 1 \right] \right\}^2,$$

while the relationship between  $t$  and  $\tau$  is

$$\frac{2\gamma^*}{3\alpha_0 m} (t - \eta) = \left( 1 + \frac{3\alpha_0\sigma^*}{\gamma^*} \right) \left[ \left( \frac{\tau}{2\alpha_0} + 1 \right)^{\frac{4}{3}} - 1 \right] - \frac{\sigma^*\tau}{\gamma^*} \left( \frac{\tau}{2\alpha_0} + 2 \right).$$

These equations are identical to those for stretching in Chapter 6 with  $t$  replaced by  $t - \eta$  and  $\chi_0 = 1$ . The solution process is identical to the stretching case.

### 7.5.4 Controlling Deformation

Using the solution for an annulus we wish to investigate how adjusting the extrusion parameters effects the magnitude of the observed deformations. While the material properties are fixed,  $\gamma^*$  may be controlled experimentally by adjusting the flux  $\mathcal{Q}$ , or by altering the temperature to change  $\mu_0$ . We consider extrusion through three annular dies with aspect ratios  $\phi = 0.3, 0.5$  and  $0.7$ . For each die geometry we run the model until time  $t = 1$  for a range of surface tension  $\gamma^*$  from 0 to 1. The corresponding deformations  $S_d(1)$  and  $\tau_d(1)$  are plotted against  $\gamma^*$  in Figure 7.5.6. For each of the aspect ratios considered we observe that  $\tau_d(1)$  shows an approximately linear increase as  $\gamma^*$  increases. This is because larger  $\gamma^*$  increases the rate at which the transverse problem evolves, which leads to greater deformations. The value of  $S_d(1)$  initially decreases, reaches a minimum at  $\gamma_m^*(\phi)$ , and then increases. The value  $\gamma_m^*(\phi)$  decreases with  $\phi$ . The behaviour of  $S_d(1)$  can be explained by considering the balance between axial stretching and surface tension in (7.3.6). In the region  $0 \leq \gamma^* < \gamma_m^*(\phi)$  the largest deformation in the area is due to gravitational stretching; that is,  $S_d(1)$  corresponds to a cross section  $\eta$  at which  $S(\eta, 1) < 1$ . For  $\gamma^* > \gamma_m^*(\phi)$ , the largest area deformation occurs near the free end  $\eta = 0$  of the extruded cylinder where surface tension causes the area to increase, so that the largest deformation now corresponds to a cross section  $\eta$  at which  $S(\eta, 1) > 1$ . The value of  $\gamma_m^*(\phi)$  increases with  $\phi$  because a larger  $\phi$  results in larger boundary lengths and hence a stronger contribution from the surface tension terms in (7.3.6).

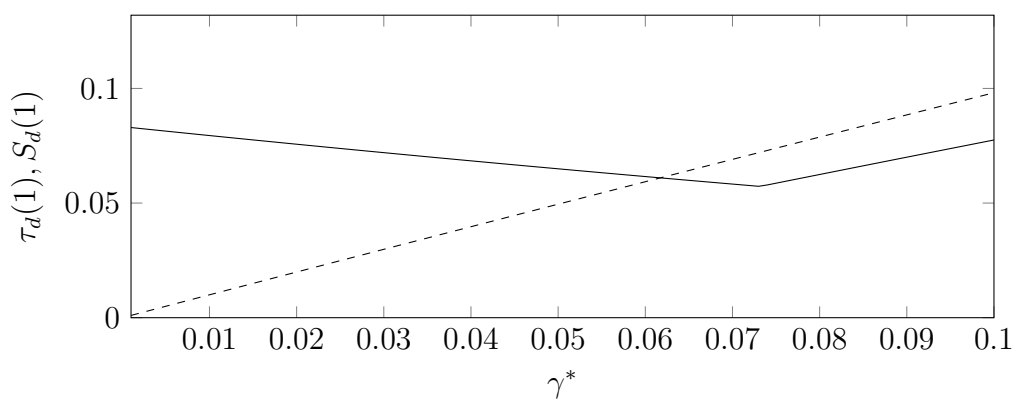
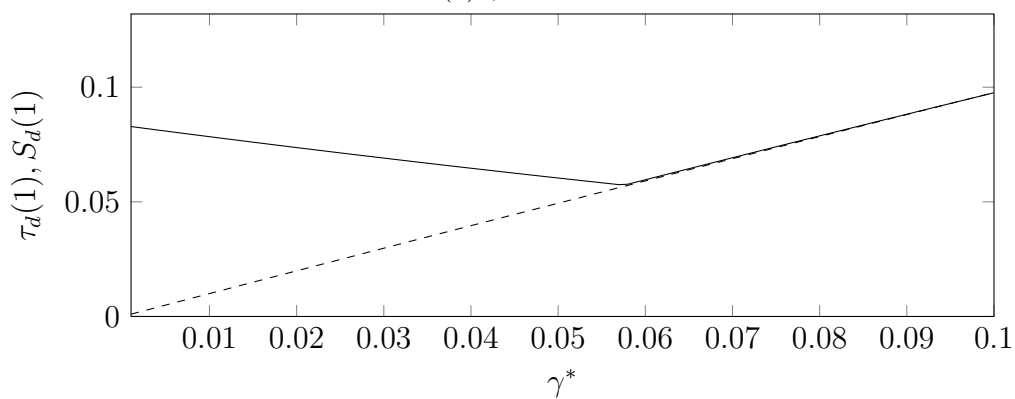
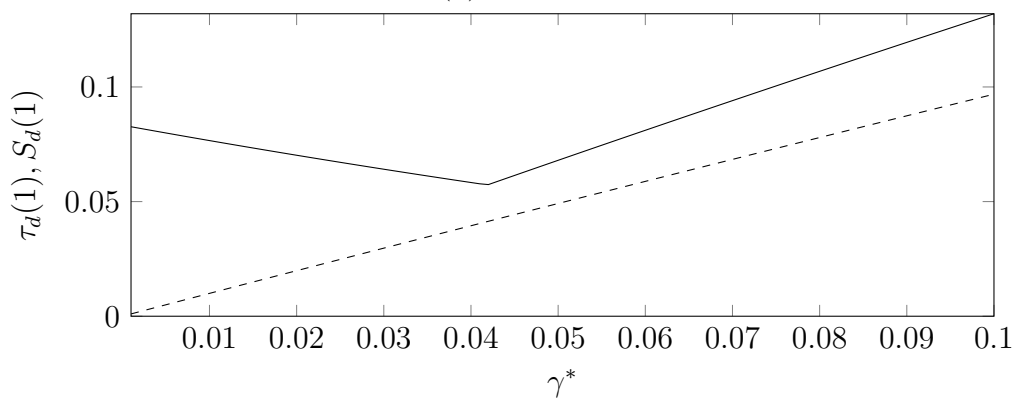
(a)  $\phi = 0.3$ (b)  $\phi = 0.5$ (c)  $\phi = 0.7$ 

Figure 7.5.6: The deformation errors  $S_d(1)$  (solid black) and  $\tau_d(1)$  (black dashed) plotted against the dimensionless surface tension  $\gamma^*$  for annuli with initial aspect ratios (a)  $\phi = 0.3$ ; (b) 0.5; and (c) 0.7.

These results have important implications for MOF preform extrusion. Typically, the area of each cross section is not important as this can be adjusted automatically by the force applied when the preform is drawn into a fibre. In contrast, the shape of each cross section must have a precise pattern and any deformations cannot be corrected during drawing. Indeed, studies have shown that during drawing the cross-sectional shape again evolves as a two-dimensional Stokes flow with unit surface tension and thus, assuming there is no pressurisation of the channels, deformations in the preform will only become worse during drawing (Stokes *et al.*, 2014). While surface-tension-driven deformations arising during drawing can, in theory, be controlled by pressurising the channels, in practice this is difficult to achieve (Chen *et al.*, 2015). It is thus more important to minimise  $\tau_d$ , while the value of  $S_d$  is less important. Given a particular material,  $\gamma^*$  may be reduced by increasing either  $\mathcal{Q}$  or  $\mu_0^*$ . That is, both a faster extrusion speed or larger viscosity result in smaller deformations in the transverse geometry.

## 7.6 MOF Preform Examples

### 7.6.1 Overview

In Chapter 5 we computed solutions to the transverse problem for three MOF preform geometries: a 3-hole preform; a 7-hole preform; and a 7-ring preform. The solutions for the 7-hole and 7-ring preforms were both similar to experimental results, and while it was shown that surface tension alone could not generate the cusp-like regions in the outer boundary of the 3-hole preform the solution correctly captured the behaviour of the inner boundaries. Thus, it was concluded that surface tension could explain much of the observed

deformation.

While the transverse solutions describe the range of shapes the cross sections may attain, these solutions alone cannot be used to determine the precise shape of each cross section at a particular time without information from the axial problem. Stated in terms of the extrusion model developed here, we must solve the axial problem and determine  $\tau(\eta, t)$  in order to be able to evaluate the transverse solution at the correct reduced time. We thus here make use of the three transverse solutions listed above to simulate MOF preform extrusion. While  $\tau$  necessarily increases with time  $t$ , if this increase is small then the deformations from the transverse solution will be minimal in practice. Our goal is to determine the range of  $\tau$  values likely to be associated with preform extrusion and, in particular, whether  $\tau$  becomes large enough for surface-tension-driven deformations of the cross sections to be observed.

The values for the surface tension and density for a typical preform extrusion are stated in Table 7.6.2. The flux is taken to be constant so that  $Q(t) \equiv 1$ , while we also assume that the viscosity is constant so that  $\mu \equiv m \equiv 1$ . The billet sizes are based on the values used by Ebendorff-Heidepriem and Monroe (2007). For the three- and 7-hole preforms we use a billet with diameter 30 mm, which means that the billet has cross-sectional area  $\mathcal{S}_b = 2.25\pi \times 10^{-4} \text{ m}^2$ . For the 7-ring preform we use a billet with diameter 50 mm and hence cross-sectional area  $\mathcal{S}_b = 6.25\pi \times 10^{-4} \text{ m}^2$ . The height of each billet is taken to be  $\mathcal{L}_b = 30 \text{ mm}$ . The velocity at the die is typically set by the ram speed, here taken to be  $\mathcal{U}_b = 0.1 \text{ mm} \cdot \text{min}^{-1} \approx 1.66 \times 10^{-2} \text{ m} \cdot \text{s}^{-1}$ . By conservation of mass, the flux scale is

$$Q = S\mathcal{U} = \mathcal{S}_b\mathcal{U}_b.$$

Table 7.6.2: Parameter values used for the three extrusion examples. These represent typical values observed during MOF preform extrusion.

Parameter	Symbol	Value	Units
Surface tension	$\gamma$	0.23	$\text{N} \cdot \text{m}^{-1}$
Density	$\rho$	$3.6 \times 10^6$	$\text{kg} \cdot \text{m}^{-3}$
Ram speed	$\mathcal{U}_b$	0.1	$\text{mm} \cdot \text{min}^{-1}$

Rearranging this expression shows that the corresponding extrusion velocity is

$$\mathcal{U} = \frac{\mathcal{S}_b \mathcal{U}_b}{\mathcal{S}},$$

We assume that extrusion continues until all of the material has been used up, so that the extrusion time is

$$t_f = \frac{\mathcal{L}_b}{\mathcal{U}_b}.$$

In practice some of the glass remains inside the die and cannot be forced out by the ram but this will not significantly change the results. The scales and dimensionless parameters for each example are given in Table 7.6.3.

Table 7.6.3: The area scales, axial length scales and dimensionless parameters used for the three extrusion examples. These are calculated using (7.3.2) and the values from Table 7.6.2.

Parameter	Symbol	3-hole	7-hole	7-ring
Area	$\mathcal{S}$ (m)	$1.4235 \times 10^{-4}$	$9.1106 \times 10^{-5}$	$5.7962 \times 10^{-4}$
Length	$\mathcal{L}$ (m)	$5.4324 \times 10^{-2}$	$7.6191 \times 10^{-2}$	$3.9990 \times 10^{-2}$
Flux	$\mathcal{Q}$ ( $\text{m}^3 \cdot \text{s}^{-1}$ )	$1.1781 \times 10^{-9}$	$1.1781 \times 10^{-9}$	$3.2725 \times 10^{-9}$
Billet area	$\mathcal{S}_b$ ( $\text{m}^2$ )	$7.0686 \times 10^{-4}$	$7.0686 \times 10^{-4}$	$1.9635 \times 10^{-3}$
Viscosity	$\mu_0$ ( $\text{Pa} \cdot \text{s}$ )	$10^{7.1}$	$10^{7.2}$	$10^7$
Reynolds number	Re	$1.2856 \times 10^{-10}$	$2.2379 \times 10^{-10}$	$8.1281 \times 10^{-11}$
Slenderness ratio	$\epsilon$	$2.1963 \times 10^{-1}$	$1.2528 \times 10^{-1}$	$6.0203 \times 10^{-1}$
Surface tension	$\gamma^*$	$1.0051 \times 10^{-2}$	$8.9583 \times 10^{-3}$	$6.7667 \times 10^{-3}$
Extrusion time	$t_f$	2.7421	3.0549	2.5413

### 7.6.2 3-Hole Preform

The extruded 3-hole preform is shown in Figure 7.6.7 along with three cross sections from the top, middle and bottom. The length of the preform is 27.545 cm, which is similar to the lengths observed in experiments. The area  $S$  and reduced time  $\tau$  are plotted in Figure 7.6.8. The area is larger than 1 at  $\eta = 0$ , which is due to the compressive effect of surface tension in the axial direction. The maximum reduced time is  $\tau = 2.7397 \times 10^{-2}$ , which occurs at the free end  $\eta = 0$  of the preform. Over half of the preform has a reduced time greater than  $1 \times 10^{-2}$ , indicating that this region has undergone noticeable deformation. The value of  $\tau$  decreases with  $\eta$  until reaching 0 at the die. From the plotted cross sections we see that the preform has sufficiently large  $\tau$  values for the interior holes to display surface-tension-driven deformation.

### 7.6.3 7-Hole Preform

The 7-hole preform is plotted in Figure 7.6.9, while the area and reduced time are plotted in Figure 7.6.10. The length of the preform is 57.738 cm. At the middle of the preform the area has reduced to less than half of the area at the die, while the area at the free end  $\eta = 0$  is slightly greater than the initial value. The largest reduced time  $\tau$  is  $2.7113 \times 10^{-2}$ , which occurs at  $\eta = 0$ , and approximately three quarters of the preform has a reduced time  $\tau > 10^{-2}$ , indicating significant deformation in this region. These values are sufficiently large for surface-tension-deformations to occur along this section of the preform. The shape of the  $\tau$  curve is similar to the 3-hole preform.

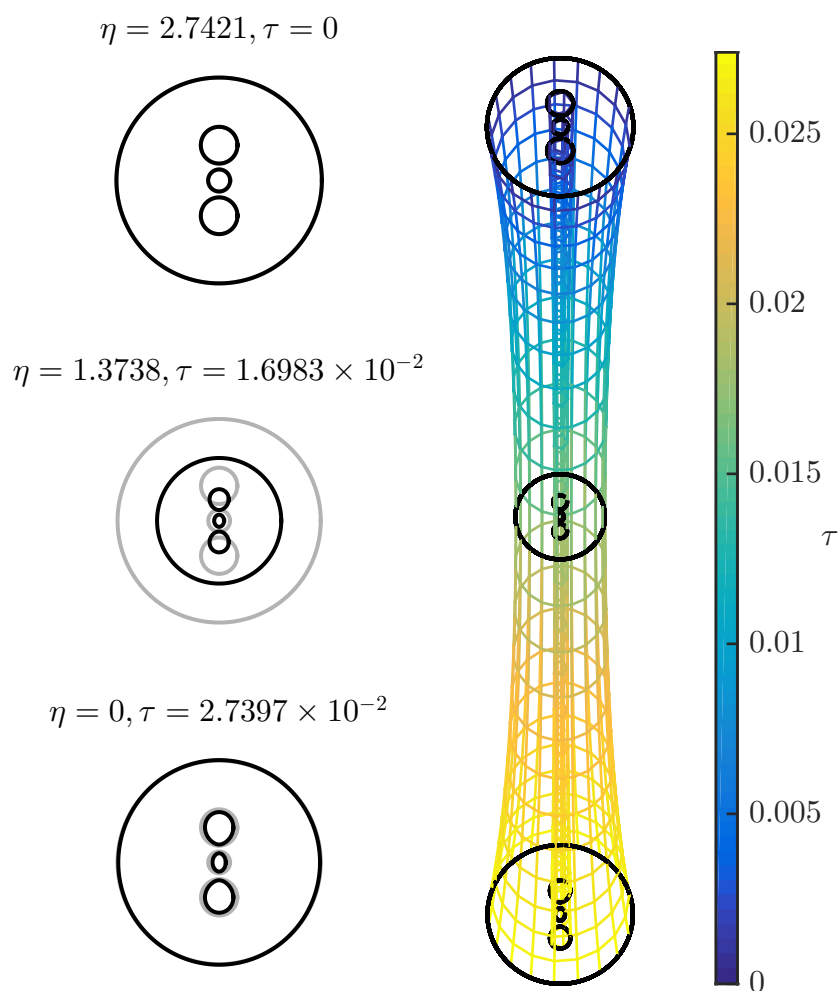


Figure 7.6.7: The extruded 3-hole preform with cross sections at three values of  $\eta$ . The preform is plotted in Eulerian co-ordinates and the colour represents the value of  $\tau$ . The length of the preform is 27.545 cm. The largest reduced time is  $2.7397 \times 10^{-2}$ , which occurs at the free end  $\eta = 0$  of the preform.

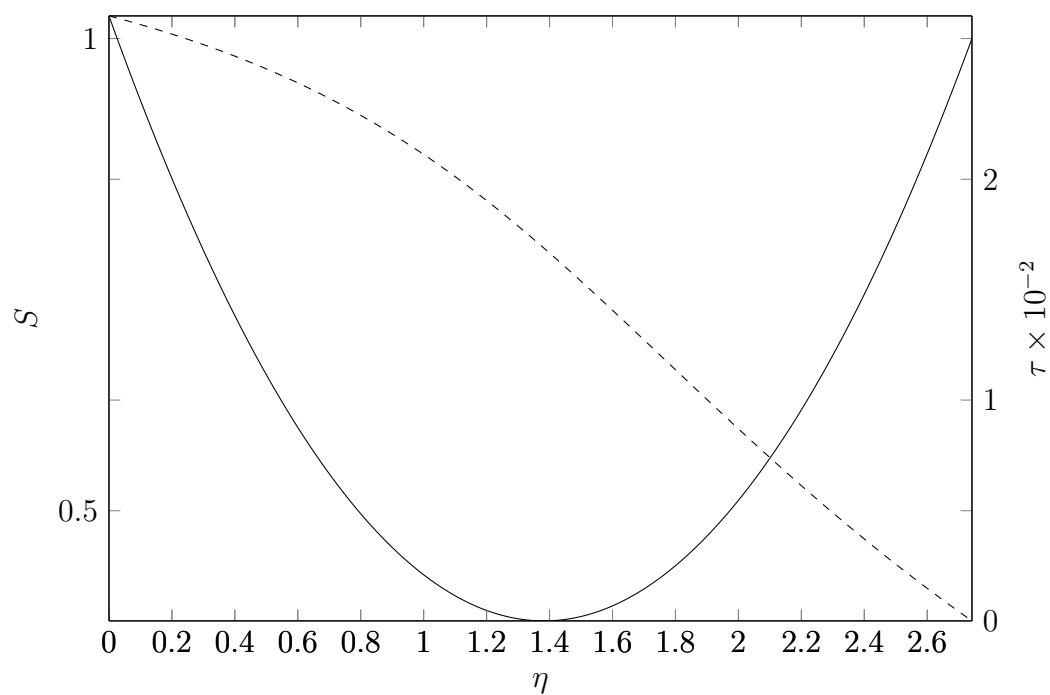


Figure 7.6.8: The area  $S$  (solid) and reduced time  $\tau$  (dashed) plotted against position  $\eta$  for the extruded 3-hole preform. The area is larger than 1 at  $\eta = 0$ , while the value of  $\tau$  decreases with  $\eta$ . Over half of the preform has a reduced time greater than  $1 \times 10^{-2}$ , indicating noticeable deformation.

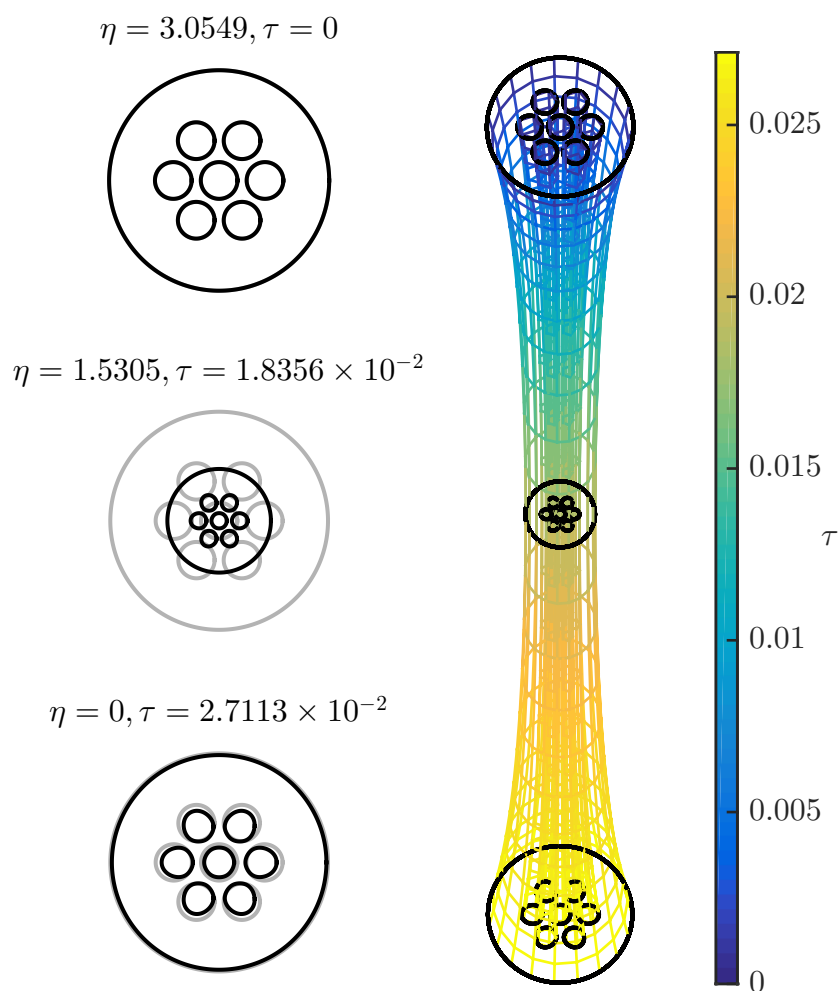


Figure 7.6.9: The extruded 7-hole preform with cross sections at three values of  $\eta$ . The preform is plotted in Eulerian co-ordinates and the colour represents the value of  $\tau$ . The length of the preform is 57.738 cm with maximum reduced time  $\tau = 2.7113 \times 10^{-2}$ .

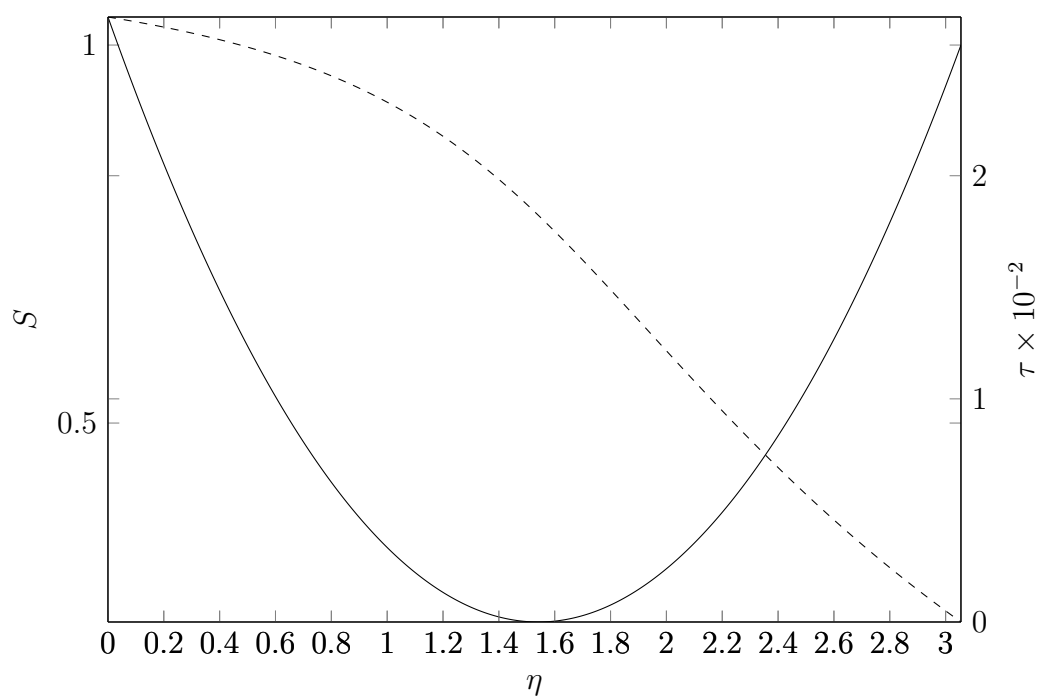


Figure 7.6.10: The area  $S$  (solid) and reduced time  $\tau$  (dashed) plotted against position  $\eta$  for the extruded 7-hole preform. The area at the middle of the preform is less than half the area of the die, while the area has increased near cross section  $\eta = 0$ . Approximately three quarters of the preform has a reduced time  $\tau > 10^{-2}$ , indicating significant deformation in this region.

### 7.6.4 7-Ring Preform

The 7-ring preform geometry is shown in Figure 7.6.11 while the area and reduced time are plotted against position in Figure 7.6.12. This preform is only 16.023 cm long, which is smaller than the previous two examples despite having a billet with a larger radius. The maximum reduced time is  $\tau = 1.6937 \times 10^{-2}$ , which occurs at  $\eta = 0$ . This is the smallest maximum of the three examples but is still large enough for surface-tension-driven deformation to occur. Approximately half of the preform has a reduced time greater than  $10^{-2}$ , indicating significant deformation in this region.

### 7.6.5 Cooling After Extrusion

In the extrusion examples considered above we assumed that the viscosity was constant. In practice, however, as the preform is extruded the cross sections move out of the heated region and cool down, while once all the material is extruded the heating elements are turned off. The temperature thus depends upon both axial position and time, and hence so too does the viscosity. Both of these dependencies enter into the model through the harmonic mean of the viscosity  $m(\eta, t)$ , which appears in (7.3.8) and influences the relationship between  $t$  and  $\tau$ . To illustrate the inclusion of a time-varying viscosity we conclude this section by considering the cooling of a preform after extrusion. In particular we are interested in determining how much additional deformation occurs as the preform cools and how this depends upon the cooling time.

Suppose that a preform is extruded at a constant temperature, which is used as the temperature scale  $\mathcal{T}$ . After some time  $t_f$  all the billet material will have been used up, at which point the heating elements are switched off. The

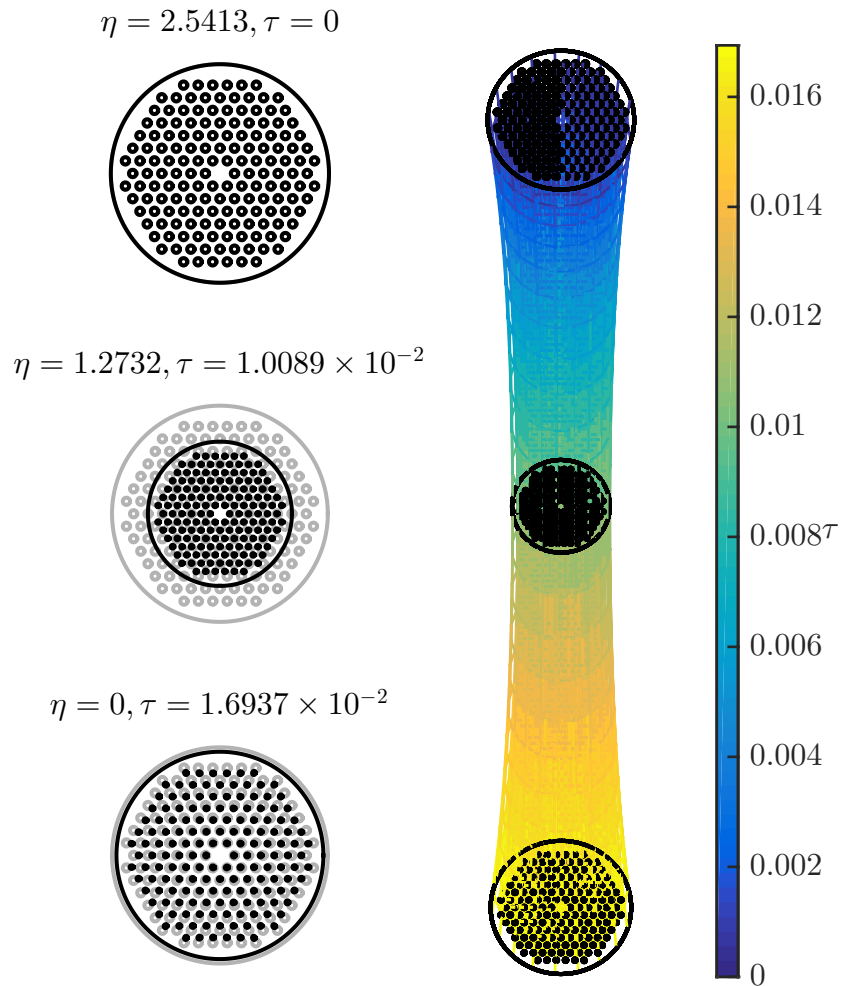


Figure 7.6.11: The extruded 7-ring preform with cross sections at three values of  $\eta$ . The preform is plotted in Eulerian co-ordinates and the colour represents the value of  $\tau$ . The length of the preform is 16.023 cm with maximum reduced time  $\tau = 1.6937 \times 10^{-2}$ .

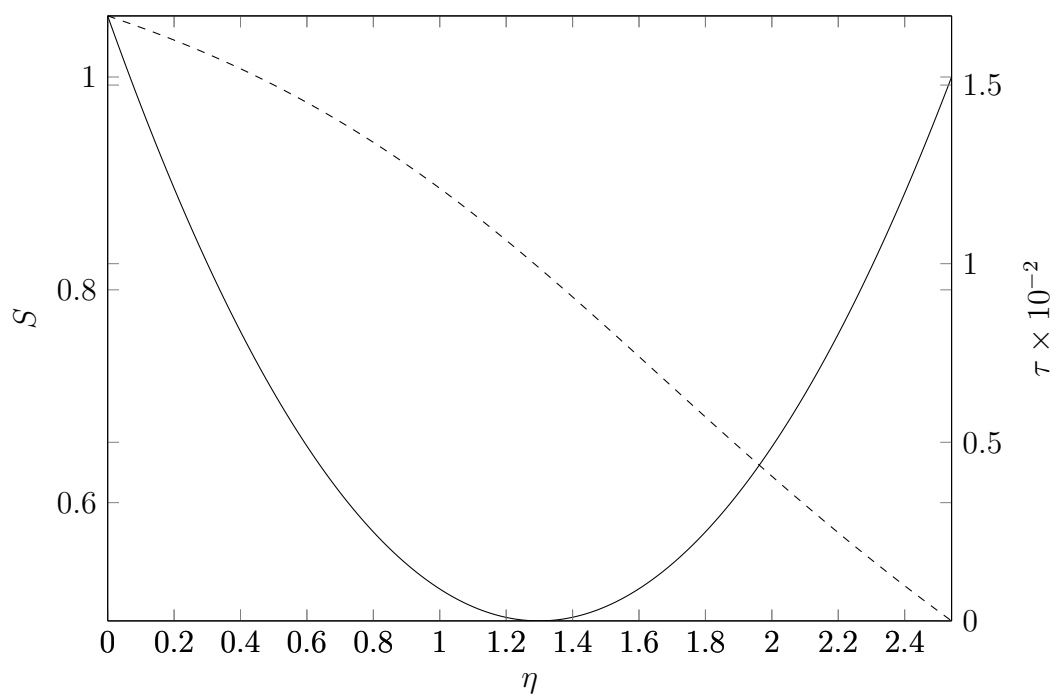


Figure 7.6.12: The area  $S$  (solid) and reduced time  $\tau$  (dashed) plotted against position  $\eta$  for the extruded 7-ring preform. Approximately half of the preform has a reduced time greater than  $10^{-2}$ , indicating significant deformation in this region.

extruded preform then cools uniformly until the temperature of the material reaches the atmospheric temperature  $T_a$  at time  $t_a$ . The preform evolves like a stretching fluid region from Chapter 6. For simplicity we assume that the temperature decreases linearly for  $t > t_f$  so is described by the function

$$T(t) = \begin{cases} 1, & t \leq t_f, \\ a(t - t_f) + 1, & t > t_f, \end{cases} \quad (7.6.14)$$

where the coefficient  $a$  is given by

$$a = \frac{T_a - 1}{t_a - t_f}.$$

To relate the temperature and viscosity we use the (dimensional) VFTH equation (2.2.1), which we scale by  $\mu_0$ . Multiplying the temperature (7.6.14) by  $\mathcal{T}$  to give a dimensional quantity and substituting this into the VFTH equation yields

$$\mu(t) = \begin{cases} 1, & t \leq t_f, \\ \frac{1}{\mu_0} 10^{-A + \frac{B}{\mathcal{T}T(t) - T_0}}, & t > t_f. \end{cases} \quad (7.6.15)$$

The harmonic mean of  $\mu$  is thus

$$m(t) = \begin{cases} 1, & t \leq t_f, \\ \frac{t - \eta}{t_f - \eta + I(t)}, & t > t_f, \end{cases}$$

where

$$I(t) = \frac{\mu_0 10^A}{a\mathcal{T}} \left[ e^{-\frac{B \ln(10)}{\mathcal{T}T(t) - T_0}} (\mathcal{T}T(t) - T_0) + B \ln(10) \operatorname{Ei} \left( -\frac{B \ln(10)}{\mathcal{T}T(t) - T_0} \right) \right]_{t_f}^t$$

and  $\operatorname{Ei}(x)$  is the exponential integral

$$\operatorname{Ei}(x) = - \int_{-x}^{\infty} \frac{e^{-t}}{t} dt.$$

In MATLAB this function is implemented as  $\text{Ei}(x) = -\text{expint}(-x)$ . With this  $m(t)$ , the relationship between  $t$  and  $\tau$  (7.3.8) becomes

$$\int_0^\tau \chi d\tau' = M(\eta, t) = \begin{cases} \gamma^*(t - \eta), & t \leq t_f, \\ \gamma^*(t_f - \eta + I(t)), & t > t_f. \end{cases} \quad (7.6.16)$$

To demonstrate this model we consider the 3-hole preform extrusion and associated parameters from Subsection 7.6.2, along with the low temperature range VFTH parameters from Table 2.2.3. Using this relationship, the extrusion viscosity  $\mu_0 = 10^{7.1} \text{ Pa} \cdot \text{s}$  corresponds to the temperature  $573.46^\circ\text{C}$ . We take the final temperature to be  $20^\circ\text{C}$  and, based on experimental observations, assume that the preform takes 7 hours to cool, giving  $t_a = 6.5812$ . The value of  $M(\eta, t)$  is plotted in Figure 7.6.13 up to time  $t = t_a$  for five values of  $\eta$  between 0 and  $t_f$ . At each  $\eta$  the corresponding  $M$  grows linearly up until the heat is turned off at time  $t = t_f$ , while beyond  $t_f$  the value of  $M$  increases but at a decreasing rate. At time  $t_e = 3.2148$ ,  $M$  reaches 99% of its final value for all  $\eta$ . Thus, beyond  $t_e$  the preform undergoes little additional deformation.

Figure 7.6.14 shows the area  $S$  and reduced time  $\tau$  at times  $t = t_f, t_e$  and  $t_a$ . The values at  $t_e$  and  $t_a$  are almost indistinguishable to graphical accuracy. Between  $t_f$  and  $t_a$  the preform undergoes significant additional deformation. The area  $S$  decreases for  $\eta > 2.1981 \times 10^{-2}$  and changes by an average of  $4.9859 \times 10^{-2}$ , with a maximum decrease of 0.10015 at the end of the preform nearest the die  $\eta = 2.7421$ . On average, the reduced time  $\tau$  increases by  $1.5334 \times 10^{-3}$ , with a maximum increase of  $1.8598 \times 10^{-3}$  at  $\eta = 1.4123$ . At  $t_f$  the preform has length 27.545 cm, while this has increased to 30.668 cm at  $t_e$  and 30.702 cm by  $t_a$ . This represents an increase in length of approximately 11%.

This analysis indicates that an extruded preform undergoes significant

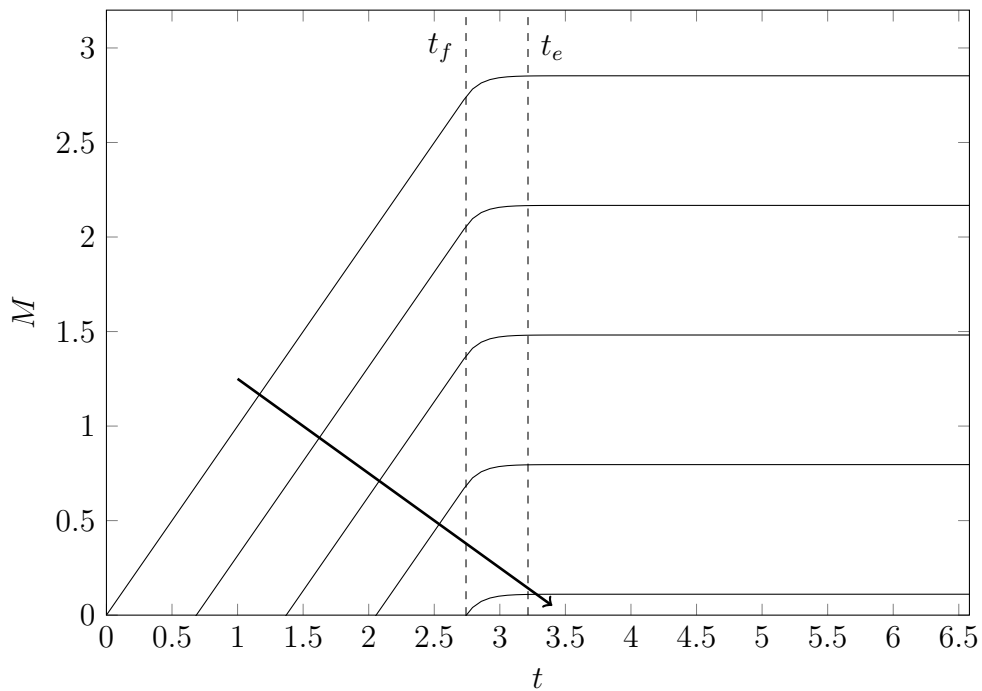


Figure 7.6.13: The value of  $M(\eta, t)$  up to time  $t_a = 6.5812$  for five values of  $\eta$  between 0 and  $t_f$ . The arrow indicates the direction of increasing  $\eta$ . At each  $\eta$  the corresponding  $M$  grows linearly up until the heat is turned off at time  $t_f = 2.7421$ , while beyond  $t_f$  the value of  $M$  increases but at a decreasing rate. At time  $t_e = 3.2148$ ,  $M$  reaches 99% of its final value for all  $\eta$ .

additional deformation during cooling, which must be accounted for in order to produce accurate models of preform extrusion. While this deformation can be reduced by cooling the preform faster this may not always be possible. Glass must be cooled slowly in order to relieve internal stresses (Shelby, 2005) through a process known as *annealing*. Glass that is not annealed may be brittle and break easily, which limits the cooling rate. Thus, deformations arising during cooling can only be controlled by altering the die geometry or adjusting  $\gamma^*$ .

## 7.7 Pinch-Off

### 7.7.1 Overview

Although not related to MOF preform extrusion, the model described in this chapter can also be used to analyse the formation of drops from a filament of viscous fluid. Suppose a viscous fluid is flowing out of a nozzle of arbitrary shape with gravity acting in the direction of fluid flow. Given enough time, the cross-sectional area at some point will go to zero and a drop will break off from the filament. This event is referred to as *pinch-off*, while the time at which the filament breaks is called the *crisis time*.

Near the crisis time the acceleration of the fluid increases and inertial terms become important, which means the Reynolds number will increase and may no longer be considered small. As such, the inertialess solutions derived throughout this chapter are no longer applicable and do not describe the mechanics of pinch-off (Stokes *et al.*, 2011). Nevertheless, it has been noted that inertia is only important close to the crisis time (Stokes and Tuck, 2004), by which point the filament will have become thin near the pinch-off point. Thus, while an inertialess model does not describe the shape of the drop near the crisis time

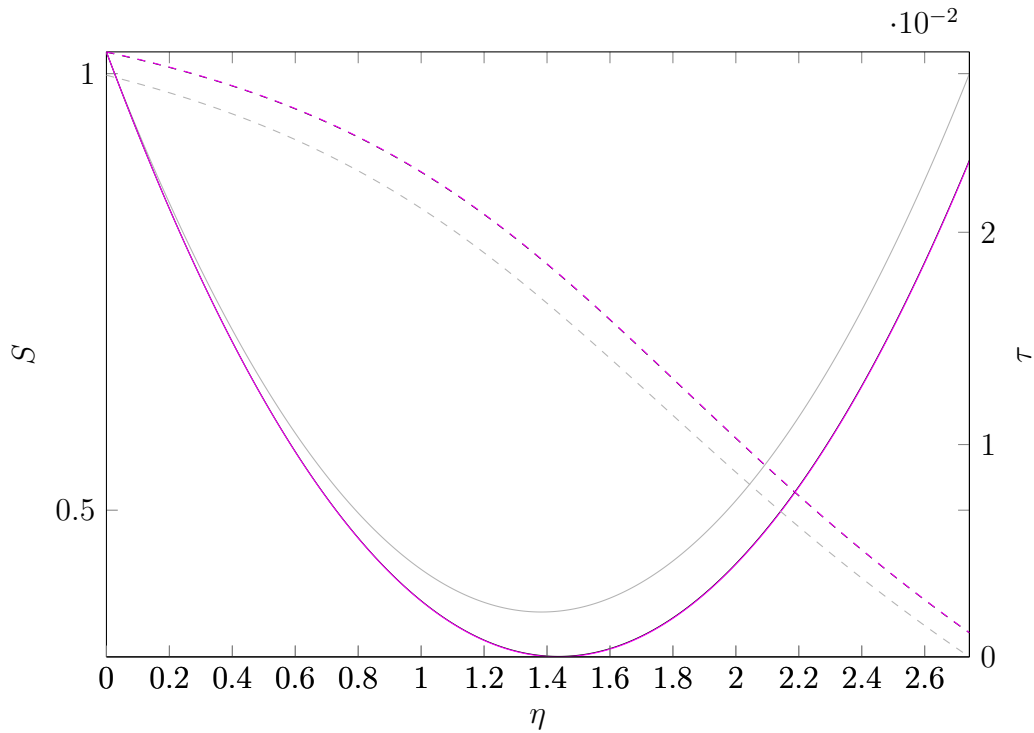


Figure 7.6.14: The area  $S$  (solid) and reduced time  $\tau$  (dashed) at times  $t = t_f$  (grey),  $t_e$  (black) and  $t_a$  (purple). The values at  $t_e$  and  $t_a$  are almost indistinguishable to graphical accuracy. Between  $t_f$  and  $t_a$  the area  $S$  changes by an average of  $4.9859 \times 10^{-2}$ , with a maximum decrease of  $0.10015$  at the end of the preform nearest the die  $\eta = 2.7421$ . On average, the reduced time  $\tau$  increases by  $1.5334 \times 10^{-3}$ , with a maximum increase of  $1.8598 \times 10^{-3}$  at  $\eta = 1.4123$ . The preform increases in length by approximately 11%.

it does provide a good estimate of the drop volume. Using this observation, Wilson (1988), derived exact expressions for the Lagrangian co-ordinate at which pinch-off occurs  $\eta_c$  and the crisis time  $t_c$  using both a ZST–WST model, which is independent of the cross-sectional shape, and for an axisymmetric solid rod with surface tension. We here use the extrusion model developed in this chapter to derive pinch-off volumes for general geometries with surface tension and compare these with the exact expressions of Wilson (1988). Throughout this section we will assume the viscosity is constant and there is no additional tension so that  $\mu \equiv m \equiv 1$  and  $c \equiv 0$ .

For the following analysis we require the additional condition that, given some area  $S_c < 1$ , the first point to reduce to  $S_c$  must be a local minimum as a function of  $\eta$ ; that is, the first cross section  $\eta$  to reach  $S_c$  must do so in the shortest time. Thus, at the critical point  $\eta_c$  and crisis time  $t_c$  we must have

$$\left. \frac{\partial t}{\partial \eta} \right|_{(\eta_c, t_c)} = 0. \quad (7.7.17)$$

### 7.7.2 Exact Solution for Zero Surface Tension

Setting  $S = 0$  in the ZST–WST solution (7.3.9) and rearranging yields

$$t = \frac{3}{\eta} + \eta.$$

Note that pinch-off cannot occur at the end of the cylinder so  $\eta \neq 0$ . Differentiating this result with respect to  $\eta$  and applying (7.7.17) shows that

$$\eta_c = \sqrt{3},$$

while the associated crisis time is

$$t_c = 2\eta_c.$$

The expressions for  $\eta_c$  and  $t_c$  are equivalent to the dimensional equations of Wilson (1988, eq (10) and (11)).

### 7.7.3 Exact Solution for a Solid Rod

It is possible to derive an exact expression including surface tension for the pinch-off time of a solid rod with circular cross section. Given some value  $\chi_c < 1$ , substituting into the exact solution (7.4.11) yields

$$t = \eta + \frac{2}{\delta} \left[ \chi_c - 1 + \frac{\eta}{\delta} \log \left( \frac{\delta \chi_c - \eta}{\delta - \eta} \right) \right]. \quad (7.7.18)$$

This expression describes the time at which cross section  $\eta$  has area  $S_c = \chi_c^2$ . Differentiating (7.7.18) and applying the condition (7.7.17) yields, after some simplification,

$$\eta_c^2 = \frac{6}{\delta} \left( \frac{1}{\lambda} \log \frac{1 - \lambda}{1 - \lambda \chi_c} + \frac{1 - \chi_c}{(1 - \lambda \chi_c)(1 - \lambda)} \right),$$

where  $\lambda = \delta/\eta$ . This is most-easily solved by choosing a value for  $\lambda$ , solving for  $\eta_c$  and then calculating the corresponding  $\delta = \lambda \eta_c$ , similar to the method of Wilson (1988). Of particular interest is the case  $\chi_c = 0$ , which corresponds to pinch-off, in which case the critical point and time are related by

$$\eta_c^2 = \frac{6}{\delta} \left( \frac{1}{\lambda} \log (1 - \lambda) + \frac{1}{1 - \lambda} \right).$$

This is precisely the result found by Wilson (1988, p. 565, eqn (19)).

### 7.7.4 Solution for General Geometries

For general geometries, substituting  $\chi = 0$  into (7.3.7) and rearranging yields

$$\gamma^* \chi_0(\eta) = \sigma^*(\eta) \int_0^\tau H(\tau') d\tau', \quad (7.7.19)$$

which relates each cross section  $\eta$  and the reduced time  $\tau$  at which the cross-sectional area is zero. For a given  $\eta$ , (7.7.19) is solved numerically for  $\tau$ . Using (7.3.8), the corresponding times  $t$  are given by

$$t = \eta + \frac{1}{\gamma^*} \int_0^\tau \chi d\tau'. \quad (7.7.20)$$

For a given solution to the transverse problem both (7.7.19) and (7.7.20) are readily evaluated using numerical integration. The first cross section  $\eta$  to pinch off can be approximated by finding the minimum of the computed  $t$ .

The solutions  $\eta_c$  found by this method for a solid rod and an epicycloid, along with the exact ZST–WST and rod solutions, are plotted in Figure 7.7.15. The numerical solution for a rod agrees well with the exact solution, which validates the numerical method. The solution for a rod increases approximately (but not exactly) linearly with  $\gamma^*$  and approaches the ZST–WST solution as  $\gamma^*$  approaches zero. The points  $\eta_c$  for an epicycloid are larger than those for both a rod and the ZST–WST solution. This is because surface tension resists the reduction in area caused by gravitational stretching and this resistance is greater for larger boundary length, such as that for an epicycloid compared with a circle. This result has the interesting consequence that the drop volume may be controlled by adjusting the boundary length of the die geometry. The problem of determining an appropriate shape given  $\gamma^*$  and a desired drop volume is left to future work.

## 7.8 Summary

By introducing the alternative Lagrangian co-ordinate  $\eta$ , we have shown that the slenderness model for a stretching fluid cylinder with internal structure is readily extended to model the extrusion of fluid through a die. The model

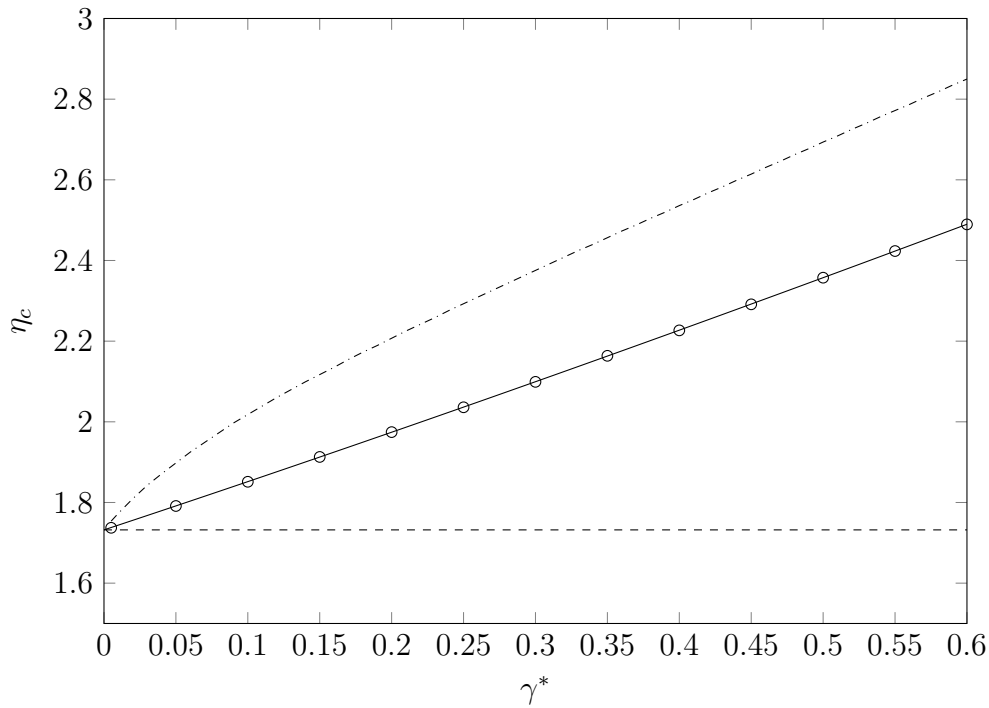


Figure 7.7.15: The points  $\eta_c$  at which pinch-off occurs plotted against  $\gamma^*$ . Exact solutions are shown for the ZST–WST limit (dashed line) and for a rod using the full model including surface tension (solid curve). Numerical results computed using the full model are plotted for a solid rod (circles) and an epicycloid (dash-dot curve). The exact and numerical results for the solid rod show good agreement. The solutions with surface tension approach the ZST–WST solution as  $\gamma^*$  decreases. Because surface tension resists stretching and is greater for large boundary length the epicycloid results in a larger  $\eta_c$ .

developed here includes the effect of surface tension and allows for the viscosity to vary with time and space. The model does not include die effects, such as extrudate swell, the addition of which is left to future work.

Through the examples in Section 7.6, it has been shown that this model captures many of the features seen in MOF preform extrusion but does not always provide an exact match to experimental results. A particular example of this is the 3-hole preform from Subsection 7.6.2. In this case the model predicted similar deformation of the interior holes as is seen in experiments but did not capture the cusp-like regions in the outer boundary. This suggests that, while surface tension alone can explain the deformation of the interior holes, there is some piece of physics important to the deformations that is missing from the model. The likely element is the effect of the die, which will be tested briefly in Chapter 8.

By including a time-dependent viscosity, we have shown that an extruded preform undergoes significant additional deformation while cooling. This deformation must be considered when constructing models of preform extrusion. While this deformation can be reduced by increasing the cooling rate this can interfere with annealing, resulting in a brittle, and hence unusable, preform.

The model has been used to predict drop volumes for pinch-off and shows good agreement to previous exact results. Further work could consider how to select the appropriate geometry so as to obtain a given drop mass.



# Chapter 8

## Preform Stacking and Cusp-Like Deformations

### 8.1 Introduction

In this chapter we use the theory developed in this thesis to analyse two problems that arise in MOF preform fabrication: the coalescence of stacked tubes and the cusp-like deformations that arise during 3-hole preform extrusion. Both of these problems feature non-circular outer boundaries, complicating the solution of the transverse problem.

In the first problem we model the coalescence of a collection of tubes stacked in a circular array, which gives rise to an associated transverse problem consisting of touching annuli. We investigate the stretching of these collections using the model from Chapter 6, with a particular focus on the level of deformation in the transverse problem. This is related to the capillary stacking method of MOF preform fabrication.

In the second problem we revisit the extrusion of 3-hole MOF preforms. In

Chapters 5 and 7 it was shown that while surface tension could account for the distortion of the interior boundaries this effect alone could not give rise to the cusp-like regions observed in experiments. Based on further experimental observations, we here consider the hypothesis that the cusp-like regions develop inside the die and thus are already present as the fluid leaves the die. To investigate this we assume that the extruded fluid leaves the die with circular inner boundaries and cusp-like deformations in the outer boundary, and consider how such a geometry would evolve under the extrusion model from Chapter 7.

The associated transverse systems for each of these problems do not possess exact solutions and thus we must use one of the spectral methods described in Chapter 5; however, in order to do so we first require an appropriate map to describe the initial configuration. In all of the examples considered thus far the exterior boundary has been circular, while the inner boundaries were ellipses and often also circular. This allowed the initial map to be written down in a simple exact form using one or both of the spectral methods. Geometries with initially non-circular boundaries, such as in the two problems outlined above, do not, in general, have a simple form and hence cannot be constructed directly. In such cases the map coefficients may be computed using numerical methods referred to as Fornberg methods. These are named after the work of Fornberg (1980), who developed a method for computing the coefficients of maps from the unit disk to a region bounded by a Jordan curve (a simple closed curve). This method used a quadratically convergent outer iteration, similar to Newton's method, and a super linearly-convergent inner iteration. Extensions of Fornberg's method have been applied to map the unit disk to regions exterior to a single Jordan curve (DeLillo and Pfaltzgraff, 1998), an annulus to a bounded doubly connected region (Fornberg, 1984; DeLillo and

Pfaltzgraff, 1998), regions exterior to a finite collection of disks to a region exterior to the same number of Jordan curves (DeLillo, Horn and Pfaltzgraff, 1999; Benchama, DeLillo, Hrycak and Wang, 2007), and from circle domains to the interior of a Jordan curve with holes bounded by Jordan curves Kropf (2009). All of these methods require initial values for the map parameters, with convergence relying upon finding sufficiently accurate guesses. A review of some other methods for simply connected regions was given by DeLillo (1994). Determining appropriate initial values is a significant challenge, particularly for multiply connected regions in which changing a parameter associated with one boundary affects all of the others.

As an alternative to Fornberg methods, we here demonstrate how we can generate the required initial conditions using maps that possess similar features. Specifically, we generate maps for touching annuli using maps for two touching disks developed by Hopper (1990), and for multiple touching disks by Richardson (2000) and Crowdy (2003*b*). The maps for the 3-hole preform problem can also be generated using solutions given by Hopper (1990). After deriving the appropriate initial conditions the maps are then used to analyse the stated problems.

Finally, we consider whether the cusp-like deformations in the outer boundary of the 3-hole preform could arise within the transition region outside the die in which the fluid changes from a non-uniform to a uniform axial velocity profile. As a first examination of this hypothesis we construct a basic model of the fluid flow inside the die. This model is solved for some typical geometries, revealing the areas that undergo large changes in the axial velocity within the transition region and hence may experience deformation during the transition.

## 8.2 Coalescing Tubes

### 8.2.1 Map for Two Tubes

#### Method

We first derive a set of map parameters from an appropriate circle domain to two coalescing tubes, as illustrated in Figure 8.2.1. It was shown by Hopper (1990) that two coalescing *solid* disks can be described by a conformal map from the unit disk of the form

$$z(\zeta) = \frac{A(t)\zeta}{a(t)^2 - \zeta^2}, \quad (8.2.1)$$

where  $A(t)$  and  $a(t) > 1$  are real parameters that control the area and separation of the disks, respectively. For notational clarity we will suppress this time dependence from hereon. The cusp-like regions are mapped from the points  $\zeta = \pm e^{i\pi/2} = \pm i$ . Substituting into (8.2.1) shows that the cusp-like points are located at  $z = \pm iA/(a^2 + 1)$ . Thus, the parameter  $a$  controls the locations of these points and hence also the width of the region joining the two tubes. The disks have centres  $\pm d = z(\pm a^{-1})$ , so the outer radius is

$$z(1) - z(1/a) = \frac{A(a^2 - a + 1)}{a^4 - 1}.$$

If we set

$$A = \frac{a^4 - 1}{(a^2 - a + 1)} \quad (8.2.2)$$

then the outer radius is always 1 and as  $a$  approaches  $1^+$  the two disks move further apart, finally touching only at the origin.

We use (8.2.1), along with the condition (8.2.2), to determine an appropriate map representing two coalescing *tubes* in the form of (5.2.1). That is, we modify the map by adding circular inner boundaries to each of the cylinders. In order

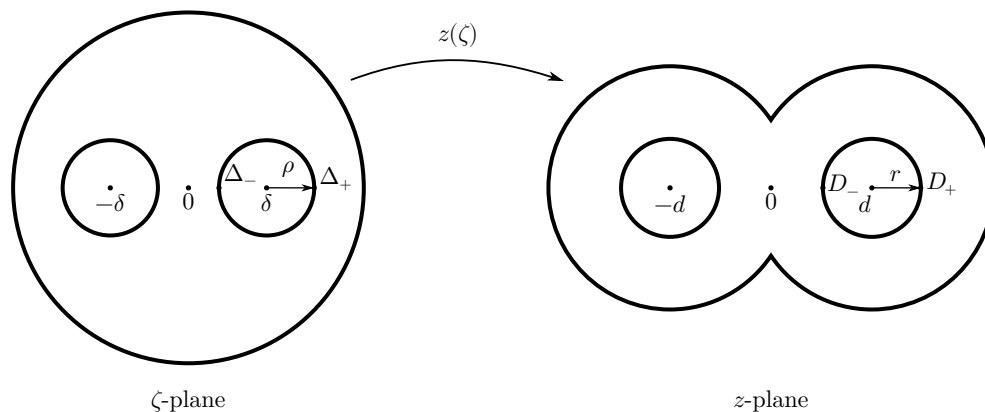


Figure 8.2.1: A conformal map from a circle domain in the  $\zeta$ -plane to a pair of coalescing tubes in the  $z$ -plane. The inner circles in the  $\zeta$ -plane have centres  $\pm\delta$  and radii  $\rho$ , with boundary points  $\Delta_{\pm} = \delta \pm \rho$  that lie on the real axis. These circles are mapped to circles in the  $z$ -plane with centres  $\pm d$  and radii  $r$ , with boundary points  $D_{\pm} = d \pm r$  also on the real axis. We require that  $z(K_+) = D_+$  and  $z(K_-) = D_-$ .

to do this we make the key observation that the map (8.2.1) will map circles inside the unit disk to shapes very close to circles inside the domain in the  $z$ -plane. Thus, the process of constructing an appropriate map can be divided into two steps:

- (1) determine the centres  $\delta_j$  and radii  $\rho_j$  of circles in the  $\zeta$ -plane so that (8.2.1) maps these to the inner boundaries in the  $z$ -plane;
- (2) determine the series coefficients for a map of the form (5.2.1) that approximates (8.2.1).

In step (1) we calculate the locations of the circles in the  $\zeta$ -plane by requiring that certain points are mapped to known locations in the  $z$ -plane. Note that the centres of the inner boundaries in the  $\zeta$ -plane  $\pm\delta$  do not necessarily map

to the centres of the inner boundaries in the  $z$ -plane  $\pm d$  (recall instead that  $\pm d = z(\pm a^{-1})$ ). We instead use the following observations to derive equations for  $\rho$  and  $\delta$ . By symmetry we expect that the circles in the  $\zeta$ -plane are located at  $\pm\delta$  and have radius  $\rho$ , with both parameters real. Suppose that these are mapped to circles in the  $z$ -plane with corresponding centres  $\pm d$  and radii  $r$ , again both real. We define points  $\Delta_{\pm} = \delta \pm \rho$ , which lie on the boundary of the right-hand side circle in the  $\zeta$ -plane, with corresponding points  $D_{\pm} = d \pm r$  in the  $z$ -plane on the right-hand side inner boundary. Both of these are known from the specified values of  $d$  and  $r$ . The relevant quantities are shown in Figure 8.2.1. We require that

$$z(\Delta_+) = D_+ \quad \text{and} \quad z(\Delta_-) = D_-.$$

Using (8.2.1), we find that these conditions correspond to

$$D_{\pm} = \frac{A\Delta_{\pm}}{a^2 - \Delta_{\pm}^2},$$

which may be rearranged to yield

$$D_{\pm}\Delta_{\pm}^2 + A\Delta_{\pm} - D_{\pm}a^2 = 0.$$

These are both quadratics in  $\Delta_{\pm}$ , so have solutions

$$\Delta_+ = \frac{-A \pm \sqrt{A^2 + 4a^2 D_+^2}}{2D_+}, \quad (8.2.3a)$$

$$\Delta_- = \frac{-A \pm \sqrt{A^2 + 4a^2 D_-^2}}{2D_-}. \quad (8.2.3b)$$

Due to the choice in sign there are two possible solutions for each of  $\Delta_-$  and  $\Delta_+$ . We thus need some extra conditions to choose the correct roots. The new inner boundaries cannot intersect the existing boundaries, nor can they intersect each other. We thus require  $0 < \delta + \rho < 1$  and  $0 < \delta - \rho < 1$ , equivalent to

$0 < \Delta_{\pm} < 1$ . These two conditions together are sufficient to ensure the correct map is found and are satisfied by taking the positive roots in (8.2.3). With  $\Delta_{\pm}$  known we can easily calculate

$$\delta = \frac{\Delta_+ + \Delta_-}{2}, \quad (8.2.4a)$$

$$\rho = \frac{\Delta_+ - \Delta_-}{2}. \quad (8.2.4b)$$

With  $\rho$  and  $\delta$  determined it remains to deduce the coefficients  $Z_{j,k}$  in the map (5.2.1). To do so, we first note that we can write

$$z(\zeta) = \frac{A(t)\zeta}{a^2 - \zeta^2} = \frac{A\zeta}{a^2} \frac{1}{1 - \left(\frac{\zeta}{a}\right)^2}.$$

The second term in this product is the sum of a geometric series in the variable  $\zeta/a$ . As  $a > 1$ , this series converges for  $|\zeta| \leq 1$  and thus, using the result for the sum of a geometric series, we can write

$$z(\zeta) = \frac{A\zeta}{a^2} \sum_{n=0}^{\infty} \left(\frac{\zeta}{a}\right)^{2n} = A \sum_{n=0}^{\infty} \frac{\zeta^{2n+1}}{a^{2n+2}}.$$

That is, we can represent  $z(\zeta)$  as the Taylor series

$$z(\zeta) = A \left( \frac{\zeta}{a^2} + \frac{\zeta^3}{a^4} + \dots \right)$$

Comparing this with (5.2.1), this corresponds to the coefficients

$$Z_{j,k} = \begin{cases} \frac{A}{a^{k+1}} & \text{if } j = 0, k \text{ odd} \\ 0 & \text{if } j = 0 \text{ and } k \text{ even, or } j \geq 1. \end{cases}$$

In practice this is truncated after some finite number of terms.

As a final remark, we observe that the series form of the map, which includes only positive odd powers of  $\zeta$ , is not unexpected. Since the map takes the interior of the unit circle to the interior of a Jordan curve and  $z(0) = 0$  the

series can only include positive powers of  $\zeta$ . Since both the domain and image are the same when rotated by  $180^\circ$ , corresponding to multiplication by  $i^2 = -1$ , we must have that

$$z(-\zeta) = -z(\zeta). \quad (8.2.5)$$

Equating coefficients shows that there can be no even powers of  $\zeta$ . Because of this we measure the number of terms in these series by the number of non-zero terms  $T$ .

As an example of this map we consider two tubes of radius 1 and internal holes of radius 0.2. The value of  $a$  is chosen to be 1.2 so that the tubes are initially fused together but still have circular boundaries away from the points of contact. These values will be used as default parameters throughout the following analysis.

### Accuracy

Having developed a method for finding conformal maps to describe two coalescing tubes we now analyse the accuracy. There are two components to the accuracy:

- (1) How well does the series approximation match the original map?
- (2) How close are the new inner boundaries in the  $z$ -plane to circle of radius  $r$  with centres  $z = \pm d$ ?

We denote the truncated series form of the map by  $\hat{z}$ . To measure (1) for some number of non-zero terms  $T$  we place 100 equispaced points around each of the four boundaries in the  $\zeta$ -plane, denoted  $\zeta_b$ ,  $b = 1, 2, \dots, 400$ , and define the truncation error

$$e_t(T) = \max_{\zeta_b} \frac{|z(\zeta_b) - \hat{z}(\zeta_b)|}{|z(\zeta_b)|}. \quad (8.2.6)$$

To measure (2) we place 100 points along one of the new inner boundaries in the  $\zeta$ -plane, denoted  $\zeta_c, c = 1, 2, \dots, 100$ , and define the inner boundary circularity error

$$e_i(r) = \max_{\zeta_c} \frac{|\hat{z}(\zeta_c) - d| - r}{r}. \quad (8.2.7)$$

Only one inner boundary need be checked as the symmetry of the map means that each inner boundary is identical in shape. Note also that we define this error using the series form of the map  $\hat{z}(\zeta)$  rather than the exact map  $z(\zeta)$  as it is the former that is of greater interest in practical applications.

To investigate (1) we fix  $r = 0.2$  and evaluate  $e_t(T)$  for various values of  $T$ , which is plotted in Figure 8.2.2. From this we see that  $e_t(T)$  decreases exponentially as  $T$  increases, with the error dropping to machine precision after approximately 100 non-zero terms.

To investigate (2) we set  $T = 100$  and evaluate  $e_i(r)$  for various values of  $r$  between 0 and 1, which is plotted in Figure 8.2.3. From this we see that the inner boundaries are close to circles of radius  $r$  centred at  $\pm d$  for smaller values of  $r$  and become less so as  $r$  increases. To illustrate the circularity, Figure 8.2.4 shows the maps computed for  $r = 0.2$  and  $r = 0.8$  with truncation  $T = 100$ . For  $r = 0.2$  the inner boundaries are indistinguishable to graphical accuracy, while for  $r = 0.8$  the inner boundaries are noticeably non-circular. Since the tubes typically used in capillary stacking have small aspect ratio  $\phi < 0.2$  our method for finding a conformal map is sufficiently accurate for the problems of interest.

### Example

To demonstrate the use of these maps we consider the coalescence of two tubes made from F2 glass having length 10 cm, outer radius 1 cm and inner radius

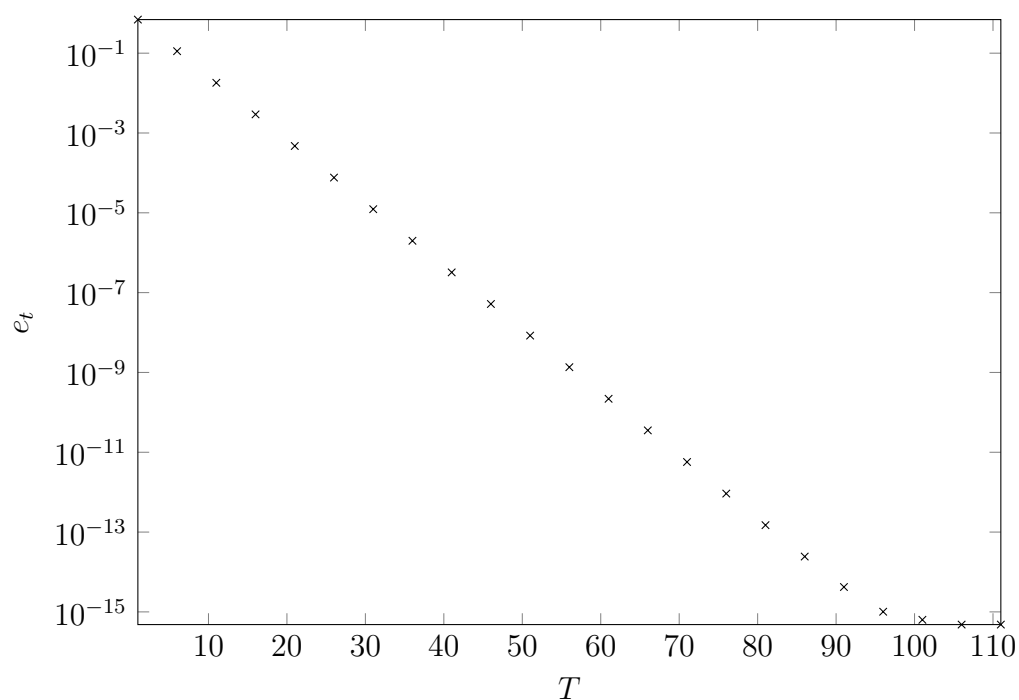


Figure 8.2.2: The truncation error  $e_t(T)$  (8.2.6) plotted against the number of non-zero terms  $T$  for a conformal map describing two coalescing tubes with  $r = 0.2$ . The vertical axis uses a logarithmic scale. The error decays exponentially and reaches machine precision at  $T \approx 100$ .

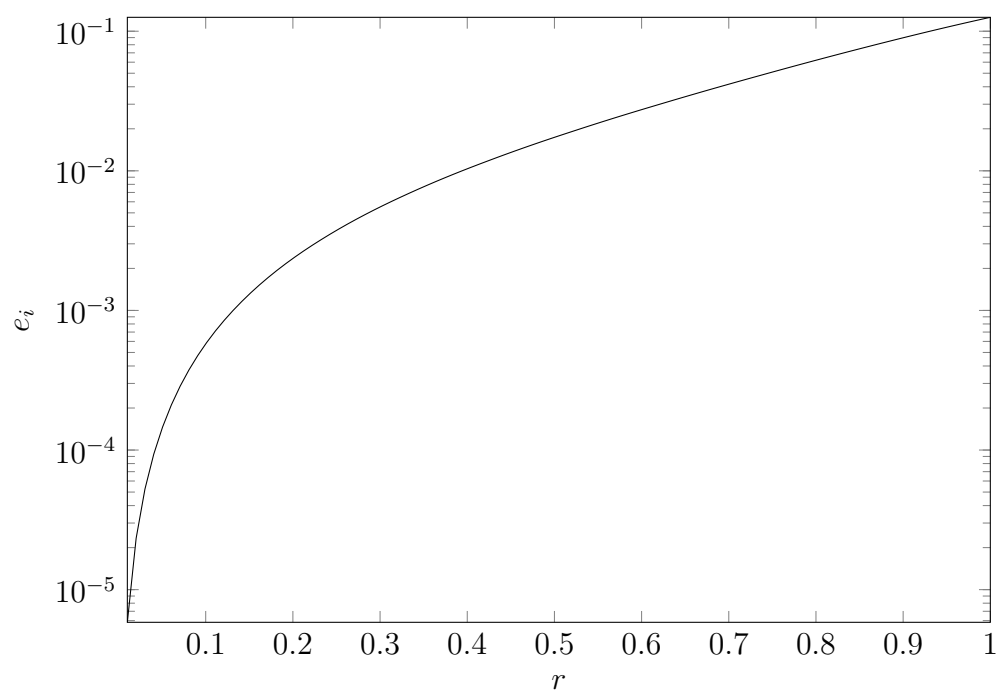


Figure 8.2.3: The inner boundary error circularity  $e_i(r)$  (8.2.7) plotted against the radius  $r$  for a conformal map describing two coalescing tubes with  $T = 100$  non-zero terms. The vertical axis uses a logarithmic scale. The error increases with  $r$ . For  $r = 0.2$  the error is  $O(10^{-3})$ .

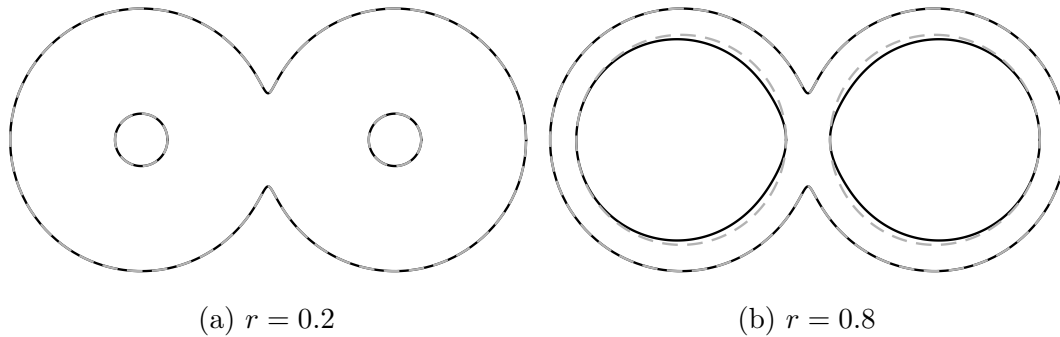


Figure 8.2.4: A comparison of the exact geometry (solid black) and the computed map (grey dashed) for two tubes with  $T = 100$  and  $a = 1.2$  for (a)  $r = 0.2$  and (b)  $r = 0.8$ . The inner boundary circularity errors for the two geometries are  $O(10^{-3})$  and  $O(10^{-2})$ , respectively. For  $r = 0.2$  the inner boundaries are indistinguishable to graphical accuracy, while for  $r = 0.8$  the inner boundaries are noticeably not circular.

2 mm, so that the initial cross-sectional geometry is that shown in Figure 8.2.4a. The tubes are taken to be fixed at one end as per the stretching model from Chapter 6 and initially fused so that  $a = 1.2$ . The tubes are then heated so that the viscosity is  $\mu = 10^{7.5} \text{ Pa} \cdot \text{s}$  and allowed to coalesce for five hours. From the above error analysis we find that  $e_i(0.2)$  is  $O(10^{-3})$ , while taking  $T = 100$  non-zero terms means that  $e_t(100)$  is  $O(10^{-16})$ , so the initial map is suitably accurate. We use the spectral method from Section 5.2 to solve the associated transverse problem, taking  $J = 200$  terms in the Goursat function series for each boundary, while  $T = 100$  corresponds to taking  $K = 200$  terms in each of the map series. This solution is then used in combination with the stretching model (Chapter 6) to find the evolution of the tubes. The relevant parameters are given in Table 8.2.1. The final geometry is shown in Figure 8.2.5, while the final area  $S$  and reduced time  $\tau$  are plotted against Lagrangian position  $\xi$

Table 8.2.1: The area scale, axial length scale and dimensionless parameters for two coalescing tubes. These are calculated using (6.2.1).

Parameter	Symbol	Value
Area	$\mathcal{S}$ (m)	$6.0292 \times 10^{-6}$
Length	$\mathcal{L}$ (m)	$10^{-1}$
Viscosity	$\mu_0$ (Pa · s)	$10^{7.5}$
Surface tension	$\gamma$ (N · m <sup>-1</sup> )	$2.3 \times 10^{-1}$
Density	$\rho$ (kg · m <sup>-3</sup> )	$3.6 \times 10^3$
Reynolds number	Re	$1.2709 \times 10^{-10}$
Slenderness ratio	$\epsilon$	$2.4554 \times 10^{-2}$
Dimensionless surface tension	$\gamma^*$	$2.6532 \times 10^{-2}$
Scaled stretching time	$t_f$	2.0095

in Figure 8.2.6. The final length of the tubes is 15.417 cm, while  $\tau$  varies by  $1.3587 \times 10^{-2}$  along the length of the tubes. At the top of the tube the area is less than half the initial value, while at the free end the area is little larger than 1.

## 8.2.2 Map for More Than Two Tubes

### Method

Crowdy (2003*b*) showed that regions with  $N \geq 3$  touching cylinders of equal radius, arranged in a ring, could be represented by a conformal map from an annulus with unit outer radius and inner radius  $\rho$  of the form

$$z(\zeta) = A(t)\zeta \frac{P_N(\zeta\rho^{2/N}a(t)^{-1}, \rho)}{P_N(\zeta a(t)^{-1}, \rho)}, \quad (8.2.8)$$

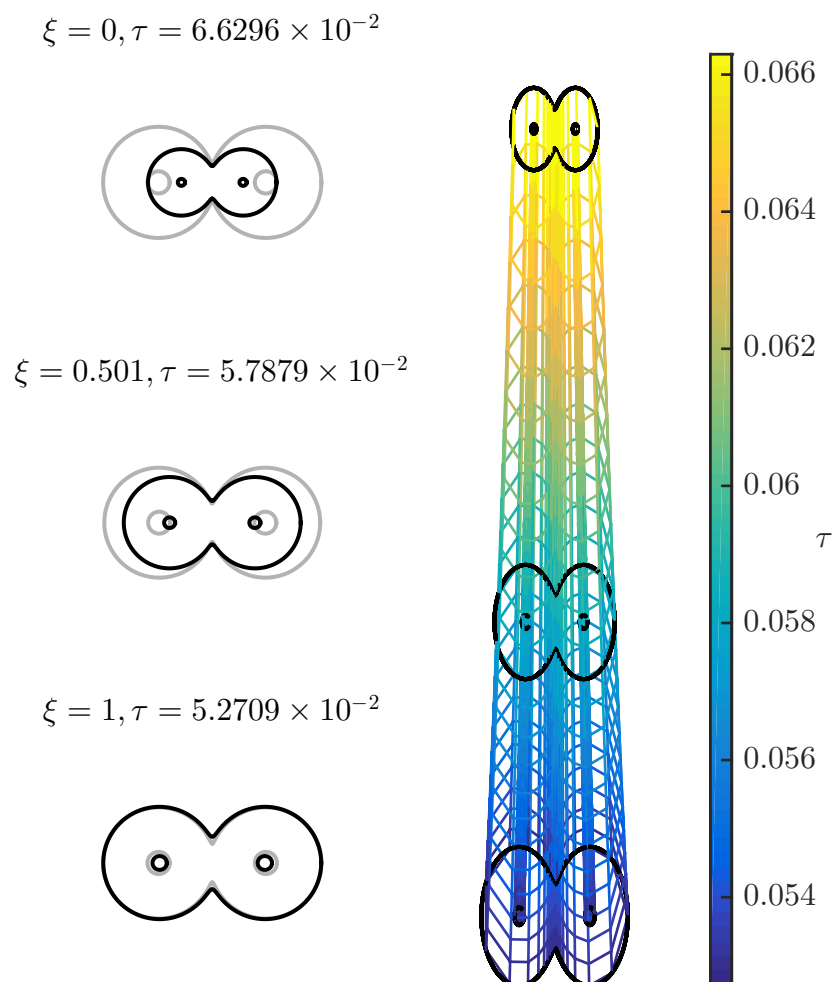


Figure 8.2.5: The coalescence of two stretching tubes each having unit outer radius and inner radius 0.2 with cross sections at three values of  $\xi$ . The final length of the tubes is 15.417 cm.

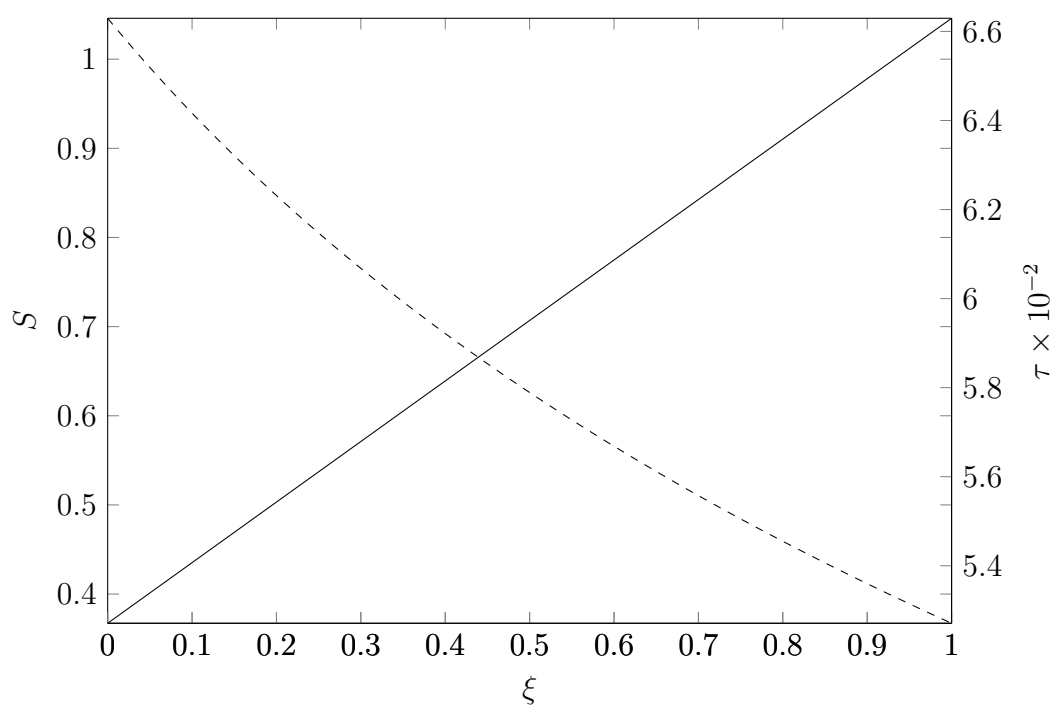


Figure 8.2.6: The final area  $S$  (solid) and reduced time  $\tau$  (dashed) plotted against Lagrangian position  $\xi$  for the coalescence of two tubes with unit outer radius and inner radius 0.2. At the top of the tube the area is less than half the initial value, while at the free end the area is little larger than 1, while the reduced time  $\tau$  varies by  $1.3587 \times 10^{-2}$  along the length of the tubes.

where

$$P_N(\zeta, \rho) = (1 - \zeta^N) \prod_{k=0}^{N-1} (1 - \rho^{2kN} \zeta^N)(1 - \rho^{2kN} \zeta^{-1}),$$

and both  $A(t)$  and  $a(t)$  are real-valued functions of time. Using the form of these maps we can extend the method used in the previous subsection to examples with  $N \geq 3$  identical coalescing tubes arranged in a ring. These cases have two additional complications: (1) the touching cylinders give rise to an additional central hole that does not occur in the  $N = 2$  case; and (2) the initial map is not given in a closed form. To illustrate how we can modify the method from above we here consider the case for  $N = 3$  such as is sketched in Figure 8.2.7; however, we emphasise that this method applies for all  $N \geq 3$ .

For this case, the geometry in the  $z$ -plane contains  $N + 1 = 4$  inner boundaries: the medial hole between the tubes and the three lateral holes in the tubes themselves. These tubes are centred at the points  $de^{2\pi ij/3}$ ,  $j = 0, 1, 2$ , which are the 3rd roots of unity multiplied by  $d > 0$ . In general,  $N$  tubes will have centres at the  $N$ th roots of unity multiplied by  $d$ . The circle domain in the  $\zeta$ -plane consists of the unit circle with four disks removed. The disk with radius  $\rho_m > 0$  centred on the origin is mapped to the medial hole in the  $z$ -plane, while the three outer disks each have radius  $\rho_l > 0$  with centres  $\delta e^{2\pi ij/3}$ ,  $j = 0, 1, 2$ , again multiples of the roots of unity.

The form of the map (8.2.8) means that one of the tubes in the  $z$ -plane will have its centre on the real axis so that the inner boundary of this tube will map from a circle in the  $\zeta$ -plane also centred on the real axis. We thus again introduce  $\Delta_{\pm} = \delta \pm \rho_l$  and  $D_{\pm} = d \pm r$ , as sketched in Figure 8.2.7, with the requirement that

$$z(\Delta_{\pm}) = D_{\pm}. \quad (8.2.9)$$

Since both  $z(\zeta)$  and the  $D_{\pm}$  are known, (8.2.9) represents two real non-linear

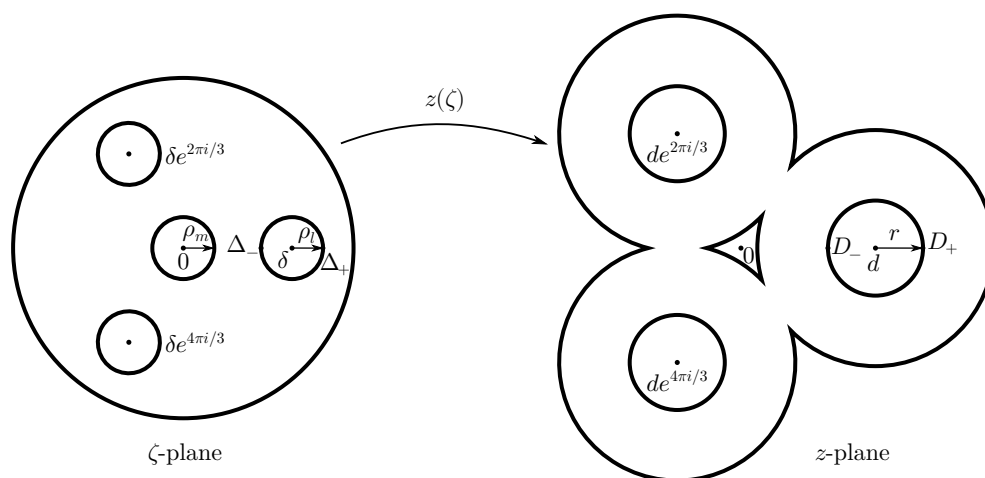


Figure 8.2.7: An illustration of a conformal map from a circle domain in the  $\zeta$ -plane to three coalescing tubes in the  $z$ -plane. The three outer circles in the  $\zeta$ -plane have centres  $\delta e^{2\pi ij/3}$ ,  $j = 0, 1, 2$ , which are multiples of the roots of unity. We assume that the points  $\Delta_{\pm} = \delta \pm \rho_l$  lie on the real axis. The medial hole in the  $\zeta$ -plane of radius  $\rho_m$  is mapped to the medial hole in the  $z$ -plane. The lateral holes in the  $\zeta$ -plane with radii  $\rho_l$  are mapped to the lateral holes in the  $z$ -plane with centres  $d e^{2\pi ij/3}$ ,  $j = 0, 1, 2$ , and radii  $r$ . We assume that the points  $D_{\pm} = d \pm r$  lie on the real axis and specify that  $z(\Delta_{\pm}) = D_{\pm}$ .

equations that are readily solved for  $\Delta_{\pm}$  using a suitable numerical method. As in the  $N = 2$  case, (8.2.9) has multiple solutions and we thus require additional conditions in order to select the correct solution. We specify that the new boundaries cannot intersect the existing boundaries or each other, which implies that  $\rho_m < \delta - \rho_l < \delta + \rho_l < 1$ . These conditions are equivalent to requiring that  $\rho_m < \Delta_{\pm} < 1$ . While these could be enforced through a constrained optimisation method it has been found that the MATLAB zero-finding method `fzero` with the initial guesses  $\Delta_{\pm} = 0.7$  produces the appropriate solution. Once  $\Delta_{\pm}$  are known, the values of  $\rho_l$  and  $\delta$  are determined by (8.2.4).

With these parameters fixed, it remains only to determine the coefficients for a conformal map of the form of (5.2.1) that approximates  $z(\zeta)$ . Since the initial map features an outer boundary with one inner boundary centred on the origin we seek an approximation of the form

$$\hat{z}(\zeta) = \sum_{k=0}^K Z_{0,k} \zeta^k + \sum_{k=1}^K Z_{1,k} \left( \frac{\rho_m}{\zeta} \right)^k \quad (8.2.10)$$

for some number  $K$ , corresponding to  $2K + 1$  coefficients to be determined. For the case of two tubes this could be done exactly; however, this is not possible in this case due to the form of the map (8.2.8). Instead, we use a discrete Fourier transform to approximate the coefficients  $Z_{j,k}$  in (8.2.10). This is readily achieved using MATLAB's fast Fourier transform function `fft`. To do this, we generate  $I$  points  $\zeta_i, i = 1, \dots, I$ , around the unit circle and compute the discrete Fourier transform of  $z(\zeta_i)$ , yielding the coefficients of the non-negative powers  $Z_{0,k}$ . We then take the transform of  $z(\rho_m \zeta_i)$ , which yields the coefficients  $Z_{1,k}$  of the negative powers of  $\zeta$ . As a general rule we use  $I = 3n$  points to ensure an accurate result.

The rotational symmetry of both the domain and image impose restrictions

upon the form of  $\hat{z}(\zeta)$ . For a given number of tubes  $N$  both the domain and image must have the same shape when rotated by  $2\pi/N$ . This corresponds to multiplication by the complex number  $\omega_N = \exp(2\pi i/N)$ , which is the  $N$ th root of unity with the smallest positive argument. The rotational symmetry condition may then be expressed as

$$z(\omega_N \zeta) = \omega_N z(\zeta).$$

Note that (8.2.5) is a special case of this equation with  $N = 2$ , so that  $\omega_2 = -1$ .

Using (8.2.10) to express this as a condition on  $\hat{z}(\zeta)$ , we can write

$$\sum_{k=0}^n Z_{0,k} \omega_N^k \zeta^k + \sum_{k=1}^n Z_{1,k} \omega_N^{-k} \left(\frac{\rho_m}{\zeta}\right)^k = \sum_{k=0}^n Z_{0,k} \omega_N \zeta^k + \sum_{k=1}^n Z_{1,k} \omega_N \left(\frac{\rho_m}{\zeta}\right)^k.$$

Equating the coefficients of powers of  $\zeta$ , it is clear that a given coefficient can be non-zero only if

$$\omega_N^k = \omega_N, \quad k = -n, \dots, -1, 0, 1, \dots, n.$$

Taking the complex logarithm in base  $\omega_N$  we find that this equation holds for  $k = 1 + MN$ ,  $M \in \mathbb{Z}$ . That is, the coefficient of  $\zeta^k$  can be non-zero only when

$$k \equiv 1 \pmod{N}.$$

This means that only every  $N$ th term in the series can be non-zero. This agrees with the result for  $N = 2$ , since requiring  $k \equiv 1 \pmod{2}$  is equivalent to restricting  $k$  to be odd. It is important to take this into account when computing the coefficients and analysing the accuracy of the map  $\hat{z}$ .

### Accuracy

Just as for the  $N = 2$  case we are interested in the accuracy of both the series form of the map and the circularity of the holes in the tubes. The former is

measured by  $e_t(T)$ , defined as per (8.2.6) with 100 terms around each of the five boundaries, where  $T$  represents the number of non-zero terms in each series. The latter is measured by  $e_i(r)$ , defined in (8.2.7), where  $r$  is the inner radius of each tube.

To illustrate the performance of this method we analyse the errors for the case  $N = 3$ , with  $r = 0.2$ ,  $\rho_m = 0.08$ ,  $T = 35$  and  $a = 1.4$  as default values. The logarithm of the truncation error  $e_t(T)$  is plotted against  $T$  in Figure 8.2.8, which shows that the error decays exponentially as  $T$  increases, reaching machine precision at  $T \approx 35$ . The logarithm of the inner boundary circularity error is plotted against the inner radius  $r$  in Figure 8.2.9, which shows that this error increases with  $r$ . Figure 8.2.10 shows comparisons between the exact geometry and computed map for  $r = 0.2$  and  $r = 0.8$ . From these we see that there is very good agreement for  $r = 0.2$  but the case  $r = 0.8$  features inner boundaries that are noticeably non-circular. We are primarily interested in  $r < 0.2$ , for which  $e_i(r)$  is  $O(10^{-3})$  and the maps provide a good approximation. The errors for  $N > 3$  show similar qualitative behaviour but these cases are not considered in this thesis.

### Three Tube Example

To illustrate the coalescence of multiple tubes we here consider three tubes each with inner radius 0.2 and unit outer radius with  $a = 1.4$ , as shown in Figure 8.2.10a. The maps are computed with  $T = 35$  and the transverse problem solved using the spectral method from Section 5.2. This example differs from the case with two tubes due to the existence of a central hole, which is not initially circular, formed by the meeting of the outer boundaries of the tubes. For MOF preform fabrication it is of interest whether this central

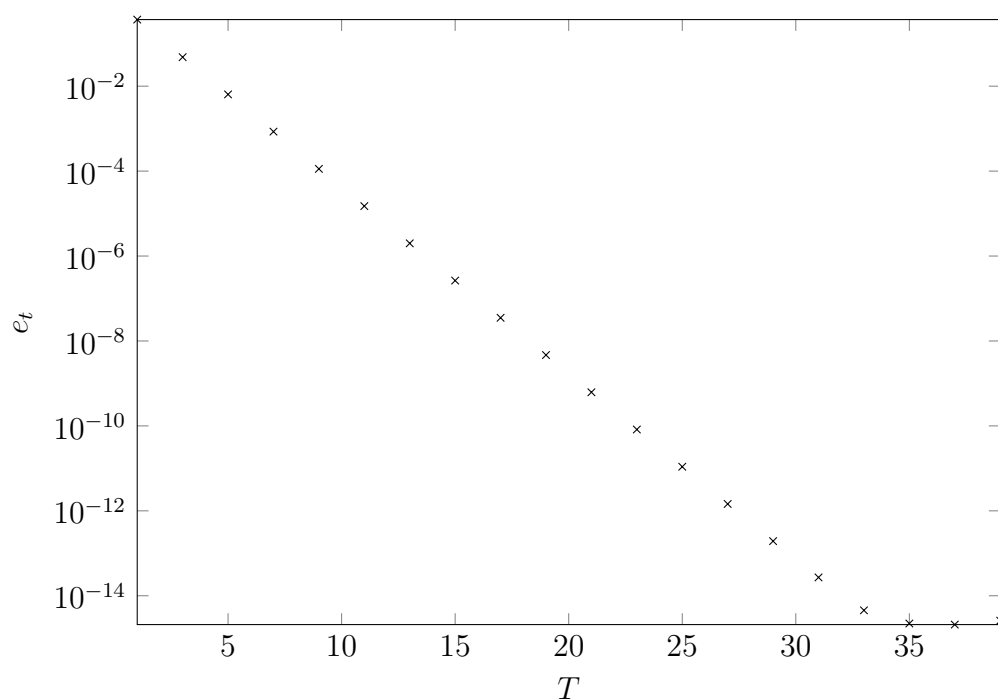


Figure 8.2.8: The truncation error  $e_t(T)$  plotted against  $T$  for a conformal map with  $T$  non-zero terms describing three coalescing tubes with  $r = 0.2$  and  $a = 1.4$ . The vertical axis uses a logarithmic scale. The error decays exponentially and reaches machine precision at  $T \approx 35$ .

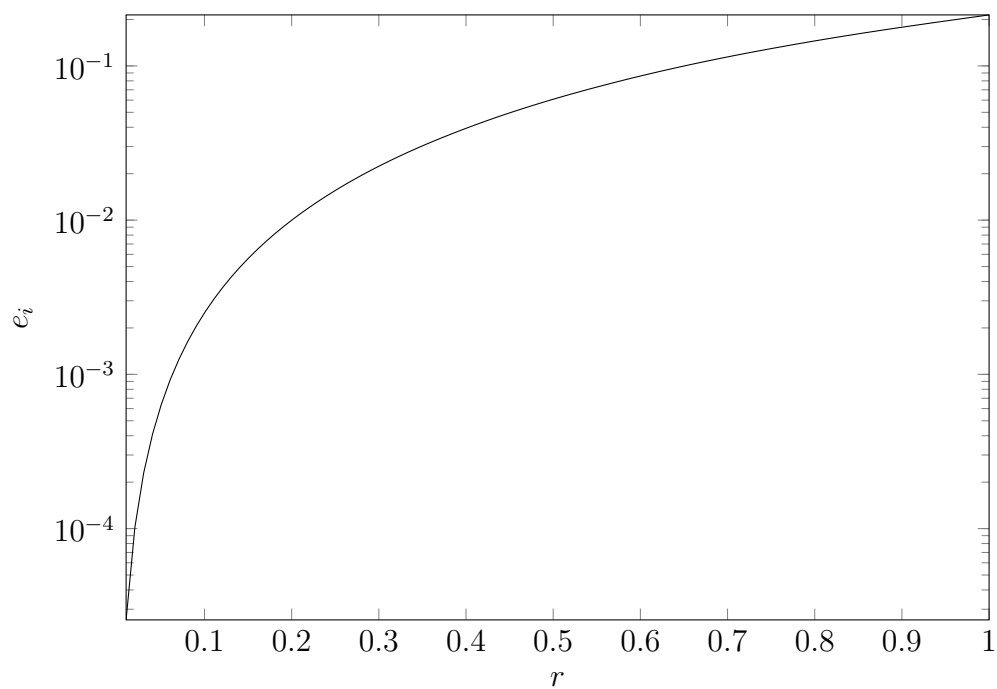


Figure 8.2.9: The inner boundary error  $e_i(r)$  plotted against the radius  $r$  for a conformal map describing three coalescing tubes with  $T = 35$  non-zero terms. The vertical axis uses a logarithmic scale. The error increases with  $r$ .

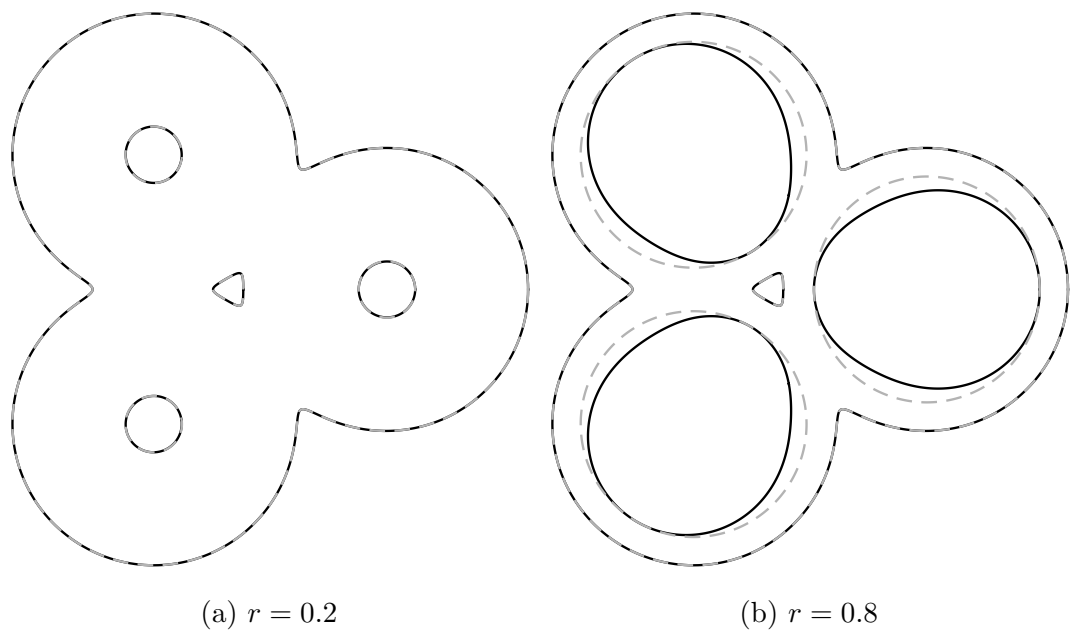


Figure 8.2.10: A comparison of the exact geometry (solid black) and the computed map (grey dashed) for three tubes with  $T = 35$  and  $a = 1.4$  for (a)  $r = 0.2$  and (b)  $r = 0.8$ . The inner boundary circularity errors are  $O(10^{-3})$  and  $O(10^{-1})$ , respectively. For  $r = 0.2$  the inner boundaries are indistinguishable to graphical accuracy, while for  $r = 0.8$  the inner boundaries are noticeably not circular.

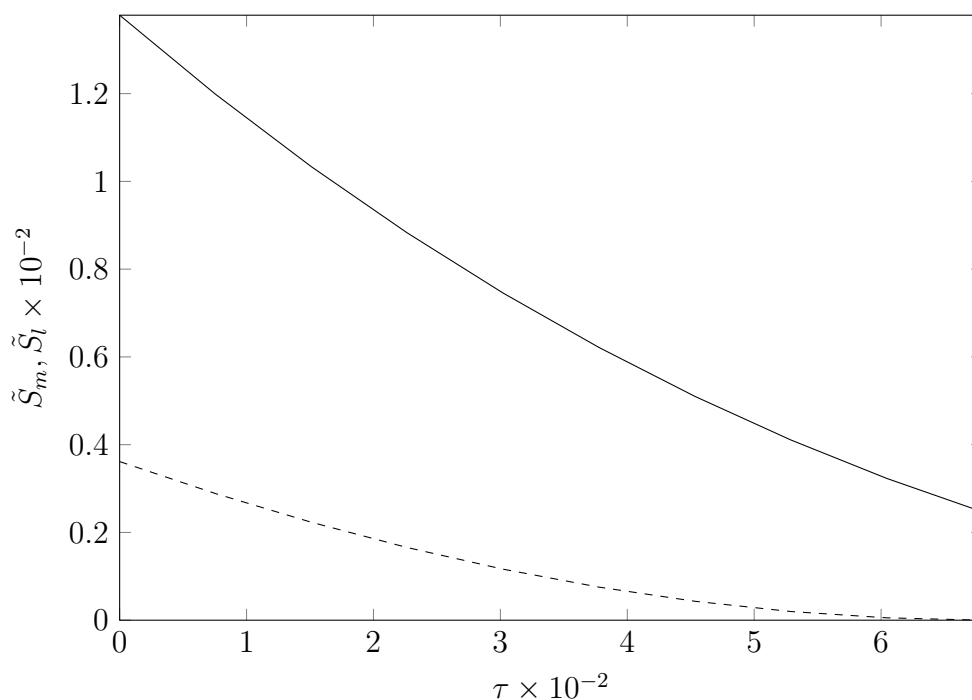


Figure 8.2.11: The areas of the medial hole  $S_m(\tau)$  (dashed) and a lateral hole  $S_l(\tau)$  (solid) from the transverse problem corresponding to three coalescing tubes with inner radius 0.2, unit outer radius and  $a = 1.4$ .

hole closes before the three lateral holes. The closure of the medial and lateral holes can be described by the areas of the holes in the transverse problem, which are denoted  $\tilde{S}_m(\tau)$  and  $\tilde{S}_l(\tau)$ , respectively. These areas are plotted in Figure 8.2.11, from which we observe that the medial hole closes at  $\tau \approx 0.068$ . This shows that, provided the lateral holes have suitably large initial radii, it is possible to fuse the tubes together such that the medial hole closes and the lateral holes remain open.

Using the stretching model from Chapter 6 we may also investigate how the areas of the internal holes vary along the length of three coalescing tubes. We consider three tubes of F2 glass fused together so that the initial cross sections

Table 8.2.2: The area scale, axial length scale and dimensionless parameters for three coalescing tubes. These are calculated using (6.2.1).

Parameter	Symbol	Value
Area	$\mathcal{S}$ (m)	$9.0239 \times 10^{-6}$
Length	$\mathcal{L}$ (m)	$10^{-1}$
Viscosity	$\mu_0$ (Pa · s)	$10^{7.5}$
Surface tension	$\gamma$ (N · m <sup>-1</sup> )	$2.3 \times 10^{-1}$
Density	$\rho$ (kg · m <sup>-3</sup> )	$3.6 \times 10^3$
Reynolds number	Re	$1.2709 \times 10^{-10}$
Slenderness ratio	$\epsilon$	$3.0040 \times 10^{-2}$
Dimensionless surface tension	$\gamma^*$	$2.1687 \times 10^{-2}$
Scaled stretching time	$t_f$	2.0095

are all as in Figure 8.2.10a. The tubes are kept at a viscosity of  $10^{7.5}$  Pa · s for five hours. We denote the areas of the medial and lateral holes by  $S_m(z, t)$  and  $S_l(z, t)$ , respectively, both of which vary with axial position  $z$  and time  $t$ . The areas after 2.5 and 5 hours, along with the initial areas, are plotted in Figure 8.2.12. Both  $S_m$  and  $S_l$  are non-decreasing as functions of  $z$ , while  $S_l > S_m$  for all  $z$  at every time  $t$ . After five hours the medial hole at  $z = 0$  has almost closed but is still open along the rest of the cylinder; however, this area is at most  $5.3540 \times 10^{-4}$ .

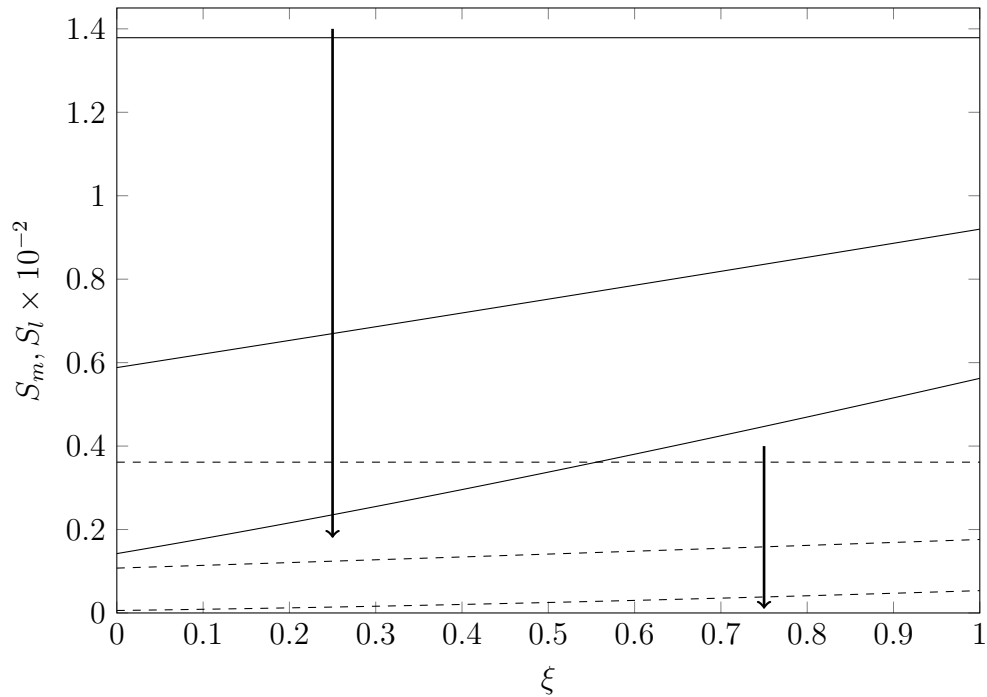


Figure 8.2.12: The areas of the medial hole  $S_m(z, t)$  (dashed) and lateral holes  $S_l(z, t)$  (solid) along the length of three coalescing tubes. Shown are the initial areas and areas after 2.5 and 5 hours, with arrows indicating the direction of increasing time. The tubes are held at a viscosity of  $10^{7.5}$  Pa · s. Both  $S_m$  and  $S_l$  are non-decreasing as functions of  $z$ , while  $S_l > S_m$  for all  $z$  at every time  $t$ . After five hours the medial hole at  $\xi = 0$  ( $z = 0$ ) has almost closed but is still open along the rest of the cylinder; however, this area is at most  $5.3540 \times 10^{-4}$ .

## 8.3 Deformed 3-Hole Preforms

### 8.3.1 Geometry at the Die Exit

In Chapter 5 we considered the evolution of the transverse problem for the 3-hole preform that features three circular internal boundaries. It was shown that, given enough time, surface tension caused the inner boundaries to deform in a manner similar to that observed in experiments; however, the outer boundary showed little deformation and did not develop the cusp-like regions seen in the physical preforms. In Chapter 7 we considered some typical extrusion conditions from which it was concluded that surface tension could explain the deformation of the internal boundaries but not that of the external boundary, and thus the latter must be due to effects not included in the model.

Shown in Figure 8.3.13 is a section from an extruded 3-hole preform following cooling, solidification of the glass and removal of the die. The top of this piece was just at the die exit and the lower end a small distance below it. We observe that the three interior boundaries, being still in contact with or just below the pins, are still approximately circular while the outer boundary already features cusp-like deformations. Based on these observations we propose the hypothesis that the external boundary shape develops during the sintering of the glass strands coming through the feed holes into the welding chamber within the die (see Figure 7.2.1).

Constructing a detailed model of the fluid flow inside the die is a complicated problem that is beyond the scope of this thesis and so is left to future work. Instead, as a first test of this hypothesis, we here investigate whether the extrusion model from Chapter 7 produces deformations similar to those observed in experiments when given an initial geometry like Figure 8.3.13. In particular,



Figure 8.3.13: A section from an extruded 3-hole preform that was at the die exit when the material solidified. The top of this piece was just at the exit and the lower end outside. The interior boundaries are still circular while the outer boundary features the cusp-like regions. This suggests that these deformations formed inside the die.

we seek to determine whether: (1) the outer boundary retains the cusp-like regions or if these become smooth due to surface tension; and (2) whether the internal holes still develop the correct pattern when the outer boundary starts as the irregular shape with cusp-like regions rather than a circle, or if the irregular outer boundary results in a modified hole geometry.

### 8.3.2 Computing Initial Maps

#### Method

In order to proceed we require a suitable conformal map of the form (5.2.1) from a circle domain to the shape from Figure 8.3.13 to use as the initial condition in the transverse problem. Such a map is illustrated in Figure 8.3.14. The circle domain must have three interior boundaries: two outer circles of radii  $\rho_l$  with centres  $\pm\delta$  that map to the outer circles in the  $z$ -plane, and one inner circle of radius  $\rho_m$  centred on the origin that maps to the inner circle in the  $z$ -plane.

Similar to the procedure used in Section 8.2, we attempt to find such a map using a known map for a similar domain. It was noted by Hopper (1990) that an epitrochoid with  $N$  cusps can be represented by a map from the unit circle  $|\zeta| = 1$  of the form

$$z(\zeta) = A \left( \zeta + \frac{\zeta^{N+1}}{N+1} \right),$$

where the real positive number  $A$  controls the area of the domain in the  $z$ -plane. We here consider the case  $N = 2$  and introduce an additional real positive parameter  $a$  to give the more-general map

$$z(\zeta) = A \left( \zeta + \frac{\zeta^3}{a} \right).$$

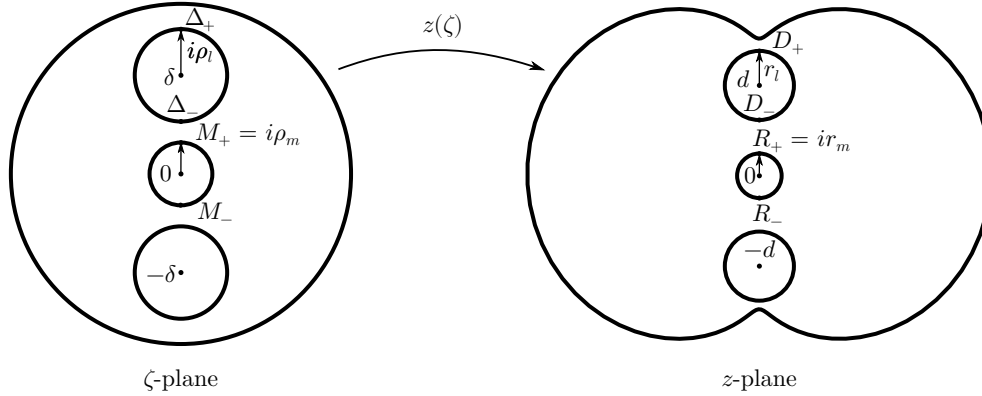


Figure 8.3.14: An illustration of a conformal map from a circle domain to the deformed 3-hole preform domain. The points  $M_{\pm} = \pm i\rho_m$  are mapped to  $R_{\pm} = \pm ir_m$ , while the points  $\Delta_{\pm} = \delta \pm \rho_l$  are mapped to  $D_{\pm} = d \pm ir_l$ .

This map provides a starting point for generating the deformed 3-hole preform map. It may be verified that the first derivative has zeros at  $\zeta = \pm i\sqrt{a/3}$ , which lie outside the unit circle if  $a > 3$ . Furthermore, this map satisfies

$$z(\pm i) = \pm \frac{A(a-1)}{a}i; \quad (8.3.11)$$

that is, the points  $\pm i$  are mapped onto the imaginary axis in the  $z$ -plane and thus are the tips of the (near) cusps. Thus, up to the scale  $A$ , the locations of these points are controlled by the parameter  $a$ , and as  $a$  increases these two points move further apart along the imaginary axis. We also note that

$$z(\pm 1) = \pm A \left( 1 + \frac{1}{a} \right), \quad (8.3.12)$$

so that the points  $\zeta = \pm 1$  are mapped to the real axis in the  $z$ -plane and lie on the longest diameter through the geometry. Together, (8.3.11) and (8.3.12) are used to set  $a$  and  $A$  by fixing the level of cusping and width of the geometry.

By symmetry we expect the centres of the outer circles in the  $\zeta$ -plane to lie on the imaginary axis, so that  $\delta$  is purely imaginary. To assist in determining

the required parameters we introduce  $\Delta_{\pm} = \delta \pm i\rho_l$  and  $D_{\pm} = d \pm ir_l$ , which represent points at the top and bottom of the top outer circle in the  $\zeta$ - and  $z$ -planes, respectively, as illustrated in Figure 8.3.14. We specify that

$$z(\Delta_{\pm}) = D_{\pm},$$

which yields cubic equations in  $\Delta_{\pm}$ ,

$$\Delta_{\pm}^3 + a\Delta_{\pm} - \frac{aD_{\pm}}{A} = 0,$$

each having three solutions. These are readily solved using a numerical method, with the appropriate solutions identified using the additional condition  $|\Delta_{\pm}| < 1$ .

We then compute

$$\begin{aligned}\delta &= \frac{\Delta_+ + \Delta_-}{2}, \\ \rho_l &= \frac{\Delta_+ - \Delta_-}{2i}.\end{aligned}$$

The radius of the medial circle is found by introducing  $M_{\pm} = \pm i\rho_m$  and  $R_{\pm} = \pm ir_m$ , shown in Figure 8.3.14. Requiring

$$z(M_{\pm}) = R_{\pm}$$

yields the cubic equations

$$M_{\pm}^3 + aM_{\pm} - \frac{aR_{\pm}}{A} = 0,$$

which are the same cubic equations as before but with  $\Delta_{\pm}$  replaced by  $M_{\pm}$  and  $D_{\pm}$  replaced by  $R_{\pm}$ . Once again these are solved and the correct root identified by the condition  $|M_{\pm}| < 1$ . We then compute

$$\rho_m = \frac{M_+ - M_-}{2i}.$$

Table 8.3.3: Parameter values for the deformed 3-hole preform map. The size and location of the interior boundaries match those from Table 5.2.1 in the investigation of 3-hole preforms in Subsection 5.2.10. The corresponding geometry is shown in Figure 8.3.16b.

Parameter	$A$	$a$	$d$	$r_l$	$r_m$
Value	5.6	4	$2.4i$	1.25	0.75

Since this circle is centred on the origin we expect that  $M_+ + M_- = 0$ ; that is, these two values should be complex conjugates.

Finally, we note that the map can be written as

$$z(\zeta) = A\zeta + \frac{A}{a}\zeta^3,$$

which is already in the form (5.2.1) required by the spectral method. Thus we can make use of this map directly in this numerical method with no need for approximation.

The parameter values used are given in Table 8.3.3. The values of  $A$  and  $a$  are chosen so that the largest diameter of the outer boundary is the same as that of the die and the geometry features cusping similar to that observed in experiments. The size and location of the interior boundaries used match those from Table 5.2.1 in the investigation of 3-hole preforms in Subsection 5.2.10.

### Accuracy

As the map is already in the form required for the spectral method there is no truncation error arising from a series expansion, such as occurred for the tube maps in Section 8.2. To measure how close the internal boundaries are to

circular we generate 100 points  $\zeta_b$  around each of the medial and lateral holes in the  $\zeta$ -plane and introduce the medial and lateral error measures

$$e_m(r_m) = \max_{\zeta_b} \frac{|z(\zeta_b) - r_m|}{r_m},$$

$$e_l(r_l) = \max_{\zeta_b} \frac{||z(\zeta_b) - d| - r_l|}{r_l}.$$

These are plotted in Figure 8.3.15 for  $r_m \in [0.2, 1]$  and  $r_l \in [0.5, 1.5]$ . In each case all other parameters are set as per Table 8.3.3. From these we observe that both errors increase with the radius, which means that the holes are more circular for smaller radii. The largest error arises as the lateral hole nears the cusp-like region of the outer boundary, which has the opposite curvature to the lateral inner boundary. Figure 8.3.16 shows a comparison between the exact geometry and two illustrative maps with  $a = 4$  and  $A = 5.6$  for the radii:  $r_m = 0.25$  and  $r_l = 0.6$ ; and  $r_m = 0.75$  and  $r_l = 1.25$ . At the smaller radii the map and exact solution are almost identical. For the larger radii, which correspond to the parameters from Table 8.3.3, the outer holes are noticeably non-circular. Even at these values, however, the map is suitably accurate for our examination of the effect of a cusped external boundary with both errors at most  $O(10^{-1})$ .

### 8.3.3 Extrusion Example

Using the method described above we are able to construct conformal maps, suitable for use in the spectral method from Section 5.2, that describe deformed 3-hole preforms that have circular inner boundaries and cusp-like regions on the outer boundary. Using these maps we now investigate whether a preform leaving the die with this geometry yields a final geometry similar to that observed in experiments. Specifically, we wish to determine whether: (1) the

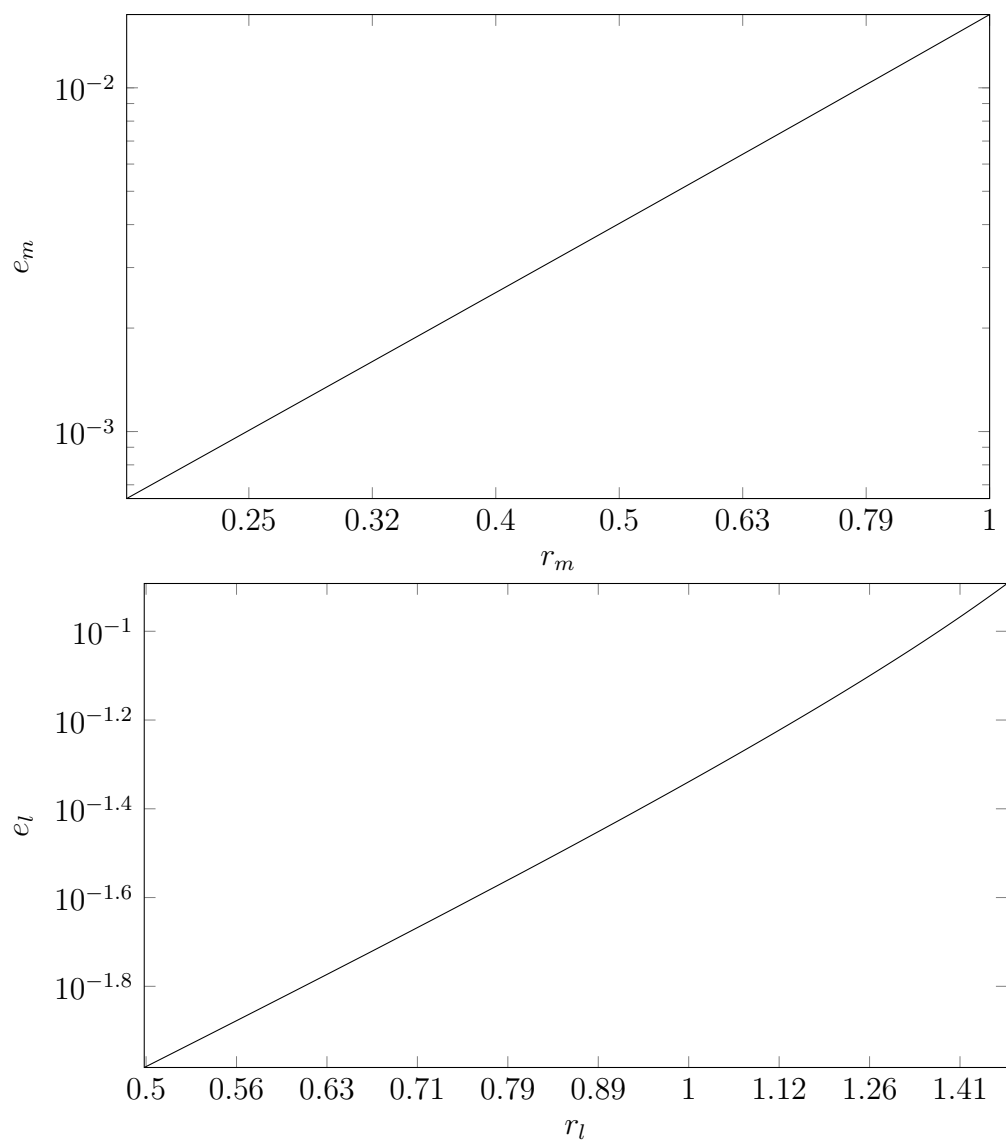


Figure 8.3.15: The errors  $e_m$  and  $e_l$  for the deformed 3-hole preform maps. All axes are drawn on a logarithmic scale. Both holes become more circular as the radius decreases.

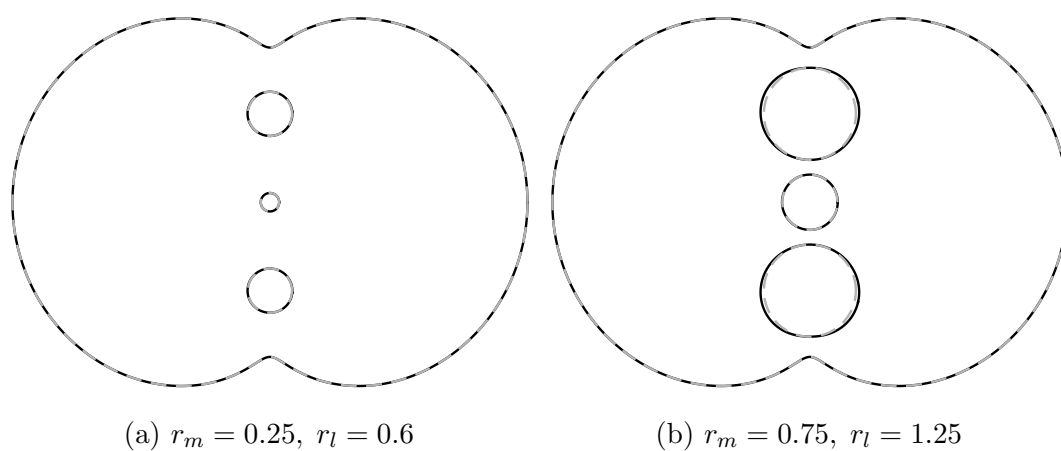


Figure 8.3.16: A comparison between the exact geometry with  $a = 4$  and  $A = 5.6$  (solid black) and the computed map (grey dashed) for the deformed 3-hole preform for the radii: (a)  $r_m = 0.25$  and  $r_l = 0.6$ ; and (b)  $r_m = 0.75$  and  $r_l = 1.25$ . For the smaller radii the inner boundaries are almost exactly circular. For the larger radii the inner boundary is still approximately circular but the two outer boundaries show greater deviations; however, even at these values the map is suitably accurate.

deformation of the inner holes matches that observed in experiments; and (2) the cusp-like regions of the outer boundary remain or become smooth. While meeting these two criteria does not provide definitive proof that the cusp-like regions form inside the die it does indicate that this hypothesis is consistent with observations.

To test this hypothesis we use the geometry shown in Figure 8.3.16b and described above by the parameters given in Table 8.3.3. Using the spectral method from Section 5.2 we solve the associated transverse problem, in this case taking  $J = 100$  terms in each of the series for the Goursat functions and  $K = 100$  terms in each of the series in the conformal map. The computed solution is then coupled with the extrusion model from Chapter 7 to find the preform geometry. The extrusion parameters are given in Table 8.3.4 and, where possible, are the same as in the 3-hole extrusion example from Subsection 7.6.2.

The final preform geometry is shown in Figure 8.3.17. From this we note that the cusp-like regions present at the die persist along the length of the preform, meaning that surface tension is not strong enough to smooth these before the extrusion finishes. Figure 8.3.19 shows the geometry at the lower end of the 3-hole preform with cusped external boundary along with the solution from the lower end of the preform with circular external boundary found in Subsection 7.6.2. We note that the interior holes are similar in both size and shape, although in the case of the cusped external boundary the holes nearer the cusps are a little more elliptical. This suggests that, for these geometries, the outer boundary has only a small influence over the evolution of interior boundaries. Importantly, this means that the interior boundaries still display the characteristic deformation observed in experiments, while the external boundary provides a much better match than that found with a circular

Table 8.3.4: Area scale, axial length scale and dimensionless parameters for the deformed-preform extrusion example. These are calculated using (7.3.2) and the values from Table 7.6.2.

Parameter	Symbol	Value
Area	$\mathcal{S}$ (m)	$1.0459 \times 10^{-4}$
Length	$\mathcal{L}$ (m)	$6.3377 \times 10^{-2}$
Flux	$\mathcal{Q}$ ( $\text{m}^3 \cdot \text{s}^{-1}$ )	$1.1781 \times 10^{-9}$
Billet area	$\mathcal{S}_b$ ( $\text{m}^2$ )	$7.0686 \times 10^{-4}$
Viscosity	$\mu_0$ ( $\text{Pa} \cdot \text{s}$ )	$10^{7.1}$
Reynolds number	Re	$2.0414 \times 10^{-10}$
Slenderness ratio	$\epsilon$	$1.6137 \times 10^{-1}$
Surface tension	$\gamma^*$	$1.0051 \times 10^{-2}$
Scaled extrusion time	$t_f$	3.1991

external boundary. The final area and reduced time are plotted against the Lagrangian co-ordinate  $\eta$  in Figure 8.3.18, which we again note show similar behaviour to the 3-hole extrusion solution with a circular outer boundary shown in Figure 7.6.8. The preform has length 63.989 cm, which is longer than the original example due to the smaller area of the fluid as it exits the die.

These observations are consistent with the hypothesis that the cusps are present at the die exit. It is thus likely that the deformation of the inner boundaries is due to surface tension acting on the fluid once outside the die, while the cusp-like regions in the outer boundary are due to the fluid flow inside the die. Consequently, this suggests that the extrusion model developed in Chapter 7 correctly captures the behaviour of the fluid below the die and, given the correct initial condition at the die exit, yields a solution that matches the deformations observed in experiments.

## 8.4 Fluid Flow Inside the Die

### 8.4.1 Motivation

In the previous section we considered whether the deformation of the 3-hole preform is consistent with cusp-like regions forming inside the welding chamber of the die. Using the extrusion model from Chapter 7, it was shown that this hypothesis is consistent with experimental observations.

An alternative hypothesis is that the cusp-like regions form due to extrudate swell in the transition region between the die exit and the point at which the fluid reaches plug flow (illustrated in Figure 7.2.3). As the extrusion model developed in this thesis neglects extrudate swell a thorough examination of this alternative hypothesis is beyond the scope of this thesis. Instead, we consider

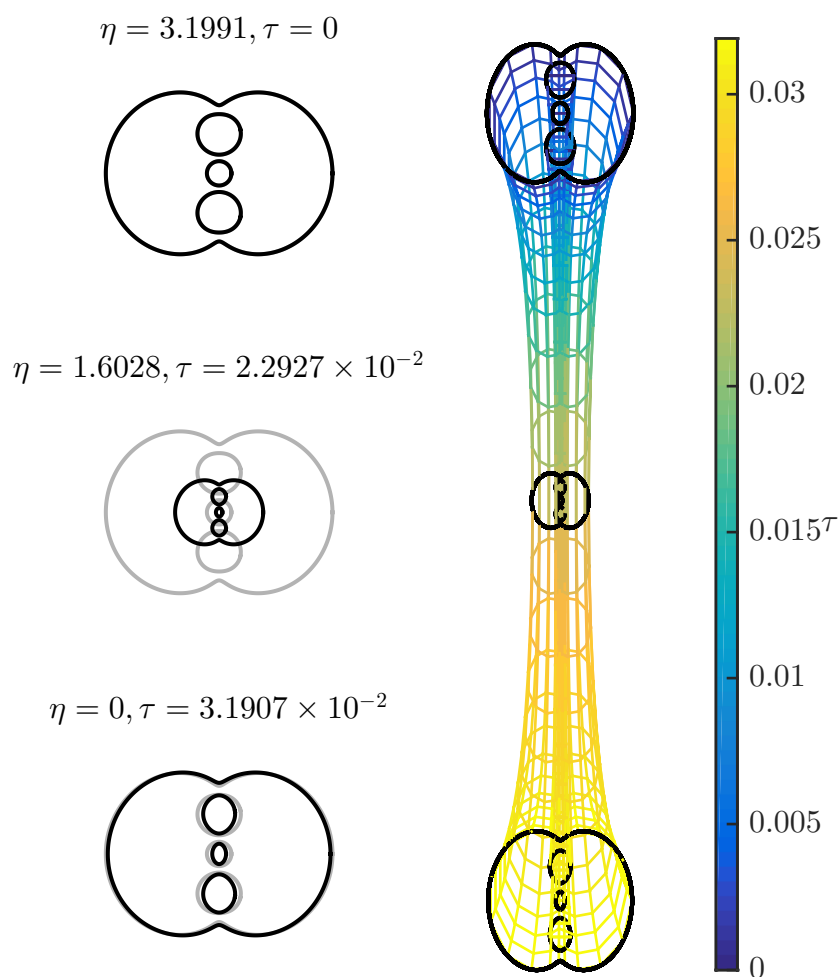


Figure 8.3.17: The geometry of the deformed 3-hole preform with cross sections shown at three values of  $\eta$ . The cusp-like regions present at the die exit persist throughout the extrusion while the inner holes show deformations similar to those observed in experiments. The deformation of the inner boundaries is similar to the deformation observed with a circular outer boundary shown in Figure 7.6.7.

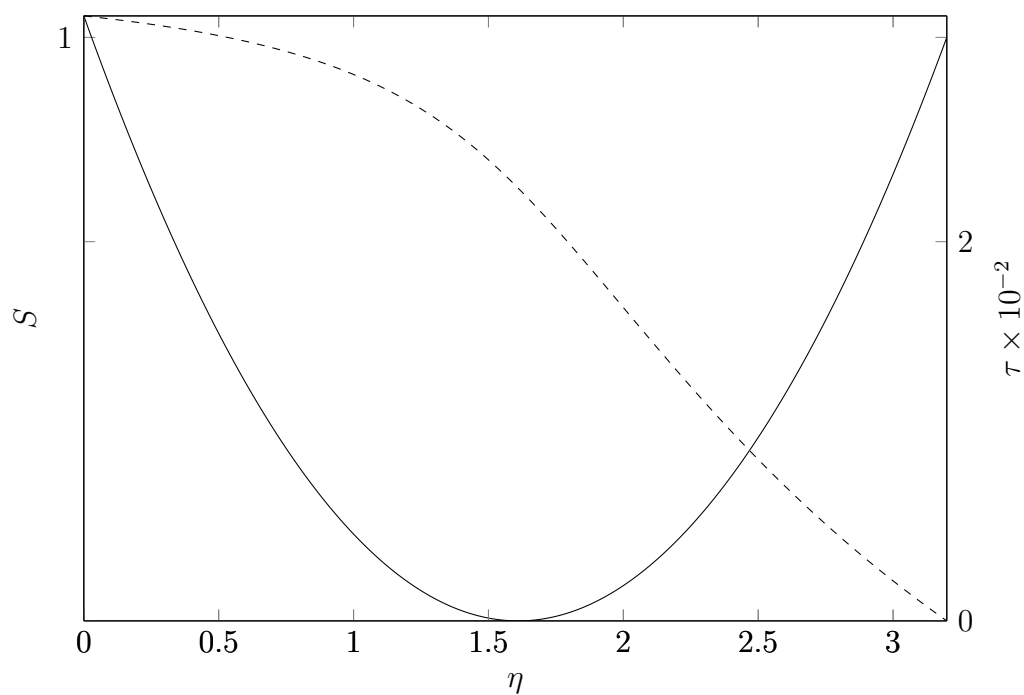


Figure 8.3.18: The area  $S$  (solid) and reduced time  $\tau$  (dashed) for the deformed 3-hole preform. Note that  $\eta = 0$  is the lower end of the preform that first exited the die. The behaviour is similar to that observed in the original 3-hole extrusion example shown in Figure 7.6.8.

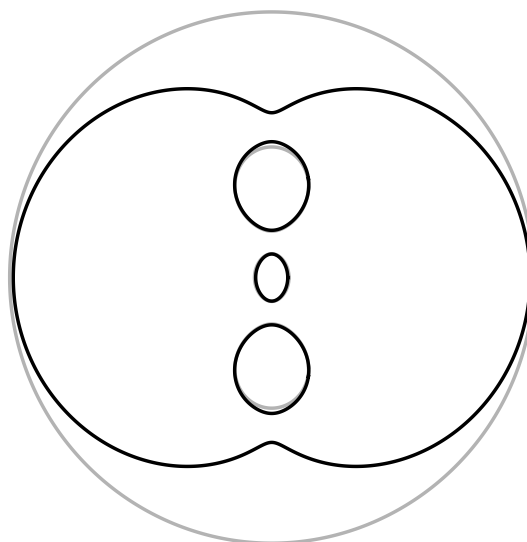


Figure 8.3.19: A comparison between the geometry at the end of the 3-hole preform from Subsection 7.6.2 (grey) and the deformed 3-hole preform (black). The interior holes in each solution are similar in both size and shape.

a basic model of the axial velocity inside the die away from the die exit. It has been noted previously (Richardson, 1970) that the presence of the die exit influences the fluid flow both upstream and downstream, and thus the velocity profile at the die exit will be different to the profile predicted by this model; however, for the purposes of this investigation the two flow profiles are assumed to be similar enough to give a qualitative understanding of the profile at the die exit. Using this model we investigate whether the 3-hole geometry displays a significantly different flow profile to the other geometries considered and whether any such differences could lead to the formation of the cusp-like regions.

### 8.4.2 Model

Following Chapter 2 and Chapter 6, the fluid is assumed to be very viscous and so is modelled by the Stokes and continuity equations. The no-slip condition is applied on the boundaries, which includes the outer boundary and the  $N \geq 0$  pins within the die. Similar to the extrusion model we consider a Cartesian co-ordinate system in which the axial co-ordinate  $z$  is aligned with the die axis while the  $x$ - and  $y$ -axes lie in the cross plane. It is assumed that:

- (1) the flow is steady;
- (2) there is no transverse flow;
- (3) the die exit has no effect on the flow; and
- (4) the flow is fully developed.

For a solid axisymmetric geometry, these assumptions are precisely those of Poiseuille flow. Under these assumptions, the Stokes equations show that the pressure is a function of the axial co-ordinate  $z$  only. The continuity equation implies that the axial velocity  $w$  is also independent of  $z$ . Lengths are scaled by  $\mathcal{L}$ , which is chosen so that the cross section has unit area so as to match the transverse problem (3.3.42). The viscosity is scaled by  $\mu_0$ , pressure by  $\mathcal{P}$  and velocities by  $\mathcal{U} = \mathcal{L}\mathcal{P}/\mu_0$ . Applying these scales yields the governing equation

$$\nabla_{\perp}^2 w = -1,$$

which is Poisson's equation. Using the complex-variable theory from Chapter 4, this may be written as

$$\frac{\partial^2 w}{\partial z \partial \bar{z}} = \frac{1}{4}.$$

Integrating with respect to  $z$  and  $\bar{z}$ , this has the general real solution

$$w = \Re(f(z)) + \frac{1}{4}|z|^2,$$

where  $f(z)$  is an unknown analytic function. In a similar fashion to the spectral method in Section 5.2, we map the geometry to a circle domain with unit outer radius and inner boundaries of radius  $\rho_j$  and centre  $\delta_j$ . The function  $f(z)$  can then be approximated by the composed form

$$f(z(\zeta)) = F(\zeta) = \sum_{j=0}^J F_{0,j} \zeta^j + \sum_{n=1}^N \left[ F_{n,0} \log(\zeta - \delta_n) + \sum_{j=1}^J F_{n,j} \left( \frac{\rho_n}{\zeta - \delta_n} \right)^j \right]. \quad (8.4.13)$$

Substituting into the no-slip boundary condition yields

$$\Re(F(\zeta)) = -\frac{1}{4}|z(\zeta)|^2. \quad (8.4.14)$$

Evaluating this expression at a number of collocation points on the boundary in the  $\zeta$ -plane yields a system of linear equations for the unknowns  $F_{j,k}$  and their complex conjugates, which may be written in the form

$$\Re(A)\Re(\mathbf{x}) - \Im(A)\Im(\mathbf{x}) = \mathbf{b},$$

where  $\mathbf{x}$  is a vector of the unknowns  $F_{j,k}$  and  $\mathbf{b}$  is a real vector composed of the right-hand side of (8.4.14). We use 100 collocation points around each boundary. This system is readily solved for the real and imaginary parts of  $\mathbf{x}$ , which are then used to compute  $w$ . In practice, we use (8.4.13) with  $J = 30$ , which has been found to give suitable accuracy.

### 8.4.3 Examples

To illustrate the different behaviour that may be encountered we consider the dies corresponding to the 3-hole, 7-hole and 7-ring preform designs from

Section 7.6. For the 3-hole die, shown in Figure 8.4.20, the maximum welding chamber axial velocity is  $2.5 \times 10^{-2}$ . The largest velocities occur between the imaginary axis and the outer boundary, away from the pins. In particular, the velocities either side of the line of pins are around twice those between the two lateral pins and the outer boundary. Between the pins the velocity is close to zero. The velocity in the 7-hole die, shown in Figure 8.4.21, displays similar behaviour, with almost zero velocity between the pins and the largest velocities between the pins and the outer boundary. In this case, however, the velocities are at most approximately  $1.1 \times 10^{-2}$ , which is lower than for the 3-hole geometry. While the 7-ring die, shown in Figure 8.4.22, again features similar qualitative behaviour, the maximum velocity in this case is only  $3.8 \times 10^{-3}$ . The velocity is close to uniform between the pins, which cover a large proportion of the geometry.

The axial flow in each of the geometries may be compared by considering the axial velocities along the  $x$ - and  $y$ -axes, which are plotted in Figure 8.4.23. As all three geometries are symmetric about both axes only the velocity along the non-negative portion of each axis is plotted. Along the  $x$ -axis the 3-hole geometry has only one pin, located in the centre of the die, so displays a large change in velocity. The velocities in the 7-hole and 7-ring geometries are much lower due to the presence of pins on or near this axis. Along the  $y$ -axis both the 3-hole and 7-hole geometries feature velocities of similar magnitudes; however, in this direction the 3-hole geometry has a central pin and an outer pin while the 7-hole geometry has only a central pin. The 7-ring geometry again has much smaller velocities due to the close proximity of the pins.

In the transition from flow inside the die to plug flow we expect fluid particles with higher than average velocities to decelerate and fluid particles

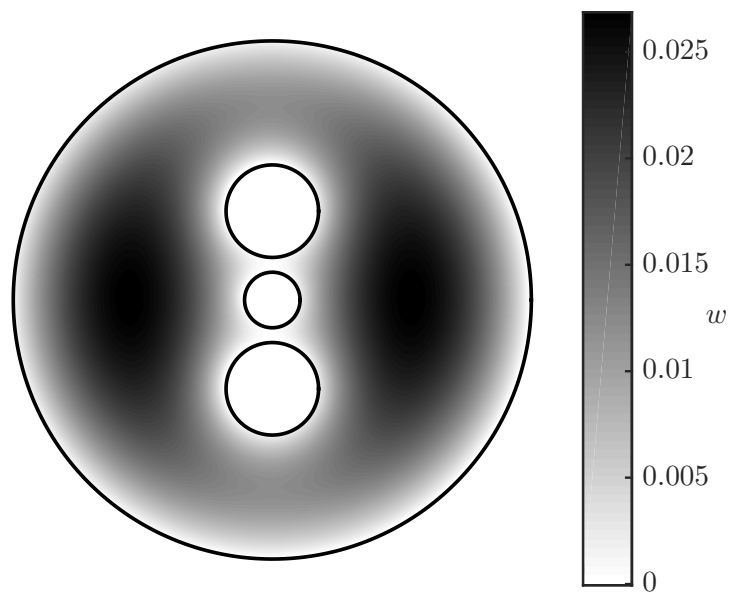


Figure 8.4.20: The welding chamber axial flow for the 3-hole die. The largest velocities occur off of the imaginary axis away from the pins. The maximum velocity is  $2.5 \times 10^{-2}$ .

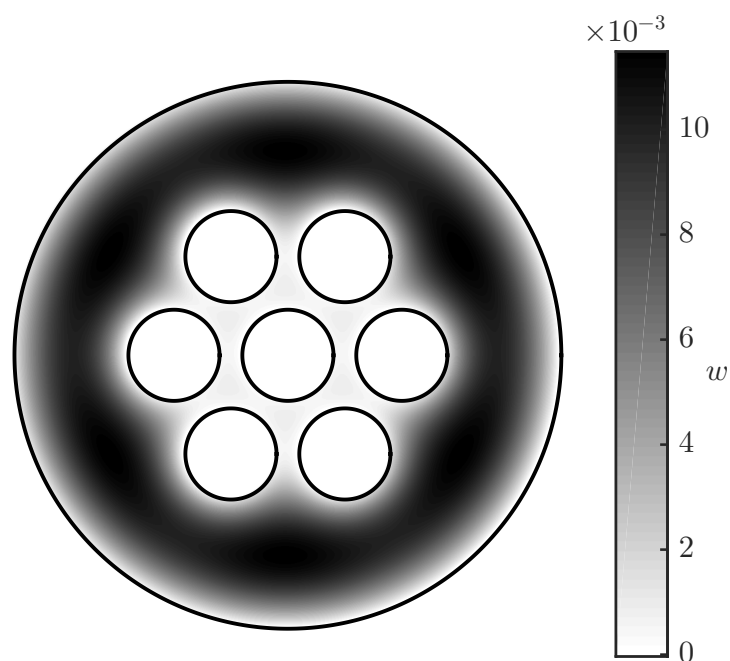


Figure 8.4.21: The welding chamber axial flow for the 7-hole die. The largest velocities occur between the imaginary axis and the outer boundary, away from the pins. The velocity is close to uniform between the interior holes. The maximum velocity is approximately  $1.1 \times 10^{-2}$ .

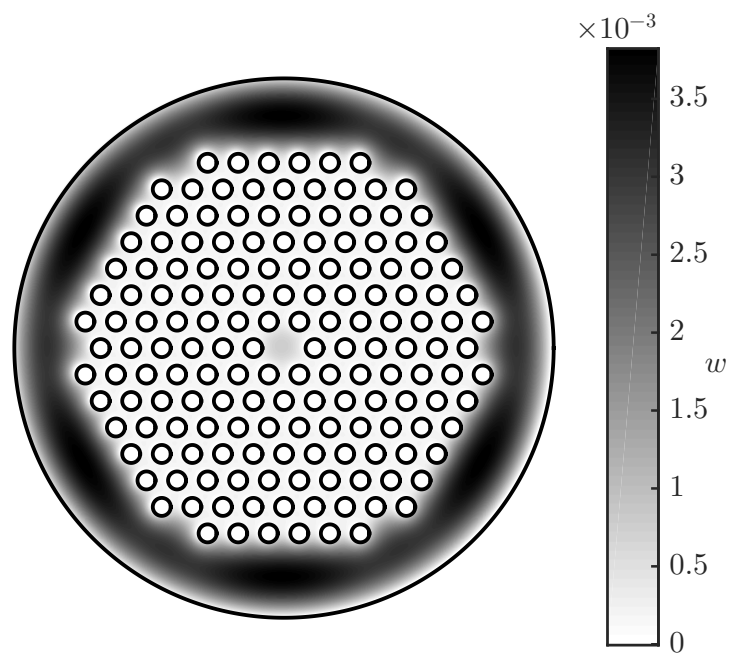


Figure 8.4.22: The welding chamber axial flow for the 7-ring die. The largest velocities occur between the outer ring of holes and the outer boundary. The velocity is close to uniform between the interior holes. The maximum velocity is approximately  $3.8 \times 10^{-3}$ .

with lower than average velocities to accelerate. For the 3-hole geometry this would mean that particles above and below the outer holes would increase in velocity. Viewed at some cross section inside the transition region at a fixed distance outside the die this increase in velocity would appear like fluid leaving the cross-sectional domain, which could lead to the formation of the cusp-like regions. Conversely, in regions of large flow velocity deceleration of the fluid implies fluid being pulled into the cross-sectional domain. This effect would be smaller in the 7-hole and 7-ring geometries due to the smaller differences in velocity over the domains.

In addition to large differences in the order of magnitude of the velocity, the 3-hole geometry has only 2-fold rotational symmetry, with the  $y$ -axis as the axis of symmetry, and it is along this axis that the cusp-like regions form during preform extrusion. Both the 7-hole and 7-ring geometries have 6-fold rotational symmetry, which means a more-uniform change in the velocity around the external boundary and, consequently, no cusping.

From these observations we conclude that the axial velocity inside the welding chamber is significantly different for the 3-hole geometry compared with the 7-hole and 7-ring geometries. As the number of pins in the design increases the maximum axial velocity within the welding chamber reduces and the velocity profile becomes closer to uniform. Thus, the hypothesis considered here seems plausible; however, these results do not provide evidence that the change in the axial velocity profile to plug flow does distort the geometry once it leaves the die. This hypothesis must be investigated using more-advanced models of the axial velocity inside the die and in the transition region, along with experimental data. This investigation is left to future work.

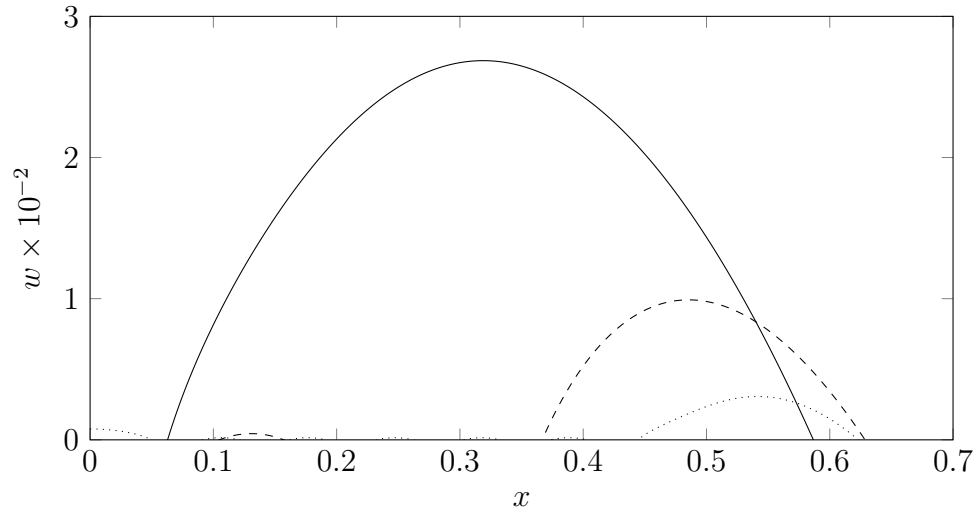
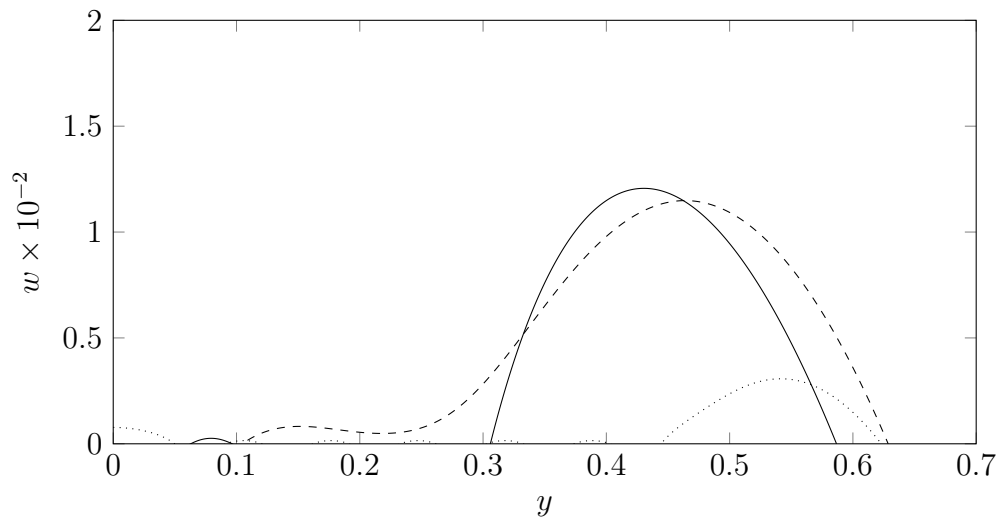
(a)  $x$ -axis(b)  $y$ -axis

Figure 8.4.23: The axial velocity  $w$  for the 3-hole (solid), 7-hole (dashed) and 7-ring (dotted) dies along the non-negative portions of the  $x$ - and  $y$ -axes. Along the  $x$ -axis the 3-hole geometry has much larger velocities. Along the  $y$ -axis both the 3-hole and 7-hole geometries have similar profiles except for an additional pin in the 3-hole geometry. The 7-ring geometry has smaller velocities along both axes due to a larger number of pins.

## 8.5 Summary

We have presented a method for computing the parameters for conformal maps written in the form of (5.2.1) using existing exact maps for similar geometries. These maps have been shown to be suitably accurate for the problems of interest here.

Using the computed maps and the stretching model from Chapter 6 we considered the coalescence of two and three tubes. In the case of three tubes it was shown that the tubes may be fused together such that the medial hole closes while the lateral hole remains open.

By examining images of an extruded 3-hole preform we hypothesised that the cusp-like deformations in the outer boundary are present at the time the fluid leaves the die. To test this hypothesis we modelled the extrusion of such a geometry and found that the results provided a qualitative match to experimental observations. This match was much better with respect to the cusped boundaries than that found in Chapter 7 using the die geometry as the initial condition. Based on these observations we conclude that it is likely that the cusp-like deformations form inside the die.

We also discussed the transition from a non-uniform axial flow within the die to plug flow downstream of the die as a possible mechanism for the formation of the cusp-like regions. Using a simple model of the flow in the die we found that the 3-hole design features larger velocity gradients inside the welding chamber than the 7-hole and 7-ring designs. The 3-hole design has only 2-fold rotational symmetry and features large regions with no pins. As a consequence the axial velocity is an order of magnitude larger along the horizontal axis than along the vertical axis. This asymmetry in the velocity profile could explain why the cusp-like regions form along the vertical axis. The 7-hole and 7-ring designs

---

have 6-fold symmetry and relatively uniform velocities around the external boundary. The differences between the designs may be why cusp-like regions are found in the 3-hole design but not the others. Further modelling is required to determine whether the change in the axial velocity profile within the transition region can lead to the formation of cusp-like regions.

It is also left to future work to investigate whether a combination of the two mechanisms considered in this chapter work together to form the cusp-like regions.



# Chapter 9

## Conclusions

We have developed a model for the stretching under gravity of a fluid cylinder with surface tension. Using a slenderness approximation, the governing equations and boundary conditions decompose into independent transverse problems for each cross section and an axial problem that depends upon the transverse solutions. A basic energy model with a Newton cooling boundary condition was used to argue that the leading-order temperature may vary with both axial position and time but must be constant within any cross section. It followed that, to leading order, the viscosity must also be independent of the transverse co-ordinates and both quantities were assumed known. The solutions developed apply to cylinders with arbitrary cross sections and include both gravity and surface-tension effects. The development of these solutions is a novel result.

Using a Lagrangian co-ordinate system and transforming to reduced time, the axial problem admits an exact solution that depends upon the solution to the transverse problem. In reduced time, the latter is precisely a classical two-dimensional Stokes flow with a moving boundary driven by unit surface

tension. While this problem admits exact closed-form solutions for a limited number of geometries, in general the solution must instead be computed using numerical methods. The geometries considered in this thesis are of high connectivity and have irregular boundaries, making it important to use efficient numerical techniques. To this end we used complex variables to represent the transverse flow, which reduced the system of PDEs in two spatial dimensions to the simpler problem of finding complex analytic functions that satisfied the boundary conditions. We developed two spectral methods for solving this problem that make use of conformal mapping techniques. Both of these methods represent the unknown functions as complex series that converge geometrically as the number of terms increases. To validate these methods we have also developed a third scheme based upon the method of fundamental solutions, which we believe is novel due to the use of stresslet singularities and the complex-variable formulation. These three methods have been verified against known exact solutions and produce solutions that closely agree for geometries without exact solutions. We have also made use of the elliptical pore model, which applies to geometries with elliptical inner boundaries and a circular outer boundary. This approximation provides an efficient solution method for geometries with high connectivity.

The model has been used to analyse the importance of surface tension on a stretching fluid cylinder. To isolate the effect of surface tension two approximations to the model were derived: the zero-surface-tension (ZST) case in which surface tension was neglected entirely; and the weak-surface-tension (WST) case in which surface tension was included in the transverse problem only. When the dimensionless surface tension is  $O(10^{-2})$ , which represents a typical value, surface tension does not significantly impact the axial solution

but does have an influence over the transverse problem and so cannot be neglected. This important result indicates that even though surface tension effects appear small they must be included in order to correctly predict the cross-sectional geometry. This conclusion was verified by comparing the model with experimental data for a cylinder with an annular cross section, and a cylinder with three circular interior boundaries and a circular outer boundary. It was observed that both the WST and full models provided a good match to the data while the ZST model did not correctly capture the cross-sectional geometry.

Using a non-zero velocity boundary condition, the model has also been used to study MOF preform extrusion. We have considered three typical MOF preform designs, referred to as the 3-hole, 7-hole and 7-ring geometries. For both the 7-hole and 7-ring cases the model predicted similar geometries to those observed in experiments, and we thus concluded that surface tension could, at least in part, explain the deformations observed in these two cases. It was also shown how the system parameters could be adjusted to minimise the cross-sectional deformation. For the 3-hole geometry the shape of the interior boundaries predicted by the model matches those observed in experiments, suggesting that surface tension could also explain these deformations; however, the experimental results displayed large cusp-like deformations in the outer boundary not observed in the model. This suggests that these are not the result of gravitational stretching or surface tension.

Based on observations of a die used to extrude a 3-hole preform, it was hypothesised that the cusp-like deformations developed inside the die. To test this hypothesis we applied the model to a geometry similar to the 3-hole geometry but with the cusp-like regions already present. It was found that the

final geometry included all of the key features observed in experiments and we thus concluded that this hypothesis provided a reasonable explanation of these deformations. We also considered the alternative hypothesis that the cusp-like regions develop due to the transition in flow profiles that occurs as the fluid leaves the die. We presented a basic model of the axial flow inside the die that showed that the 3-hole geometry results in larger velocity gradients and a velocity profile inside the die that might explain why this geometry only develops cusp-like deformations. These results are only preliminary and both hypotheses require further investigation.

In the analysis of the cusp-like regions we had to determine appropriate conformal maps that described the initial geometry. We developed a novel technique for doing so that generated the map from known maps that represent similar geometries. The same technique was used to construct maps that represent coalescing tubes that, combined with the stretching model, were used to predict the size of the channels along the length of the array of tubes.

There is, at present, no consensus on the appropriate energy model to use, and many variations may be found in the literature. As such, we instead focused on the fluid flow problem, assuming the temperature was known. Investigating the role of temperature, particularly in the context of MOF preform fabrication, is a vital but challenging problem that must be undertaken in future work. Once an appropriate model has been developed, the higher-order terms from the energy equations may be used to develop an axial temperature model that would couple to the axial fluid flow problem. This would, for example, provide insight into the cooling of an extruded preform outside the die and, in particular, the dependence of the geometry on cooling. Furthermore, numerical analysis by Xue *et al.* (2007) suggests that, with a uniform atmospheric temperature,

the temperature within each cross section becomes uniform on a time scale of the order of minutes, and that this occurs more rapidly with the inclusion of intra-boundary radiative heat transfer. Given that the viscosity is sensitive to even small changes in temperature, future work might also consider the effect of a non-constant temperature and, hence, viscosity, in the cross section.

The extrusion model presented in this thesis ignores the effect of extrudate swell. Numerical studies have shown that, in the case of an annulus, this can result in an outer diameter up to 13% larger than that of the die (Mitsoulis, 1986). Numerical simulations have also been used to argue that extrudate swell can account for the deformation observed in preform extrusion (Trabelssi *et al.*, 2015). A consideration of the relative importance of surface tension and extrudate swell in order to determine whether one or both of these are important and how the two interact would be of value. As MOF preforms may have a large number of internal boundaries, future models used to study extrudate swell must be highly efficient and could, under suitable assumptions, again make use of the complex-variable formulation employed here.

A thorough theoretical understanding of MOF preform fabrication will guide modifications of the process so as to obtain the desired geometries. Once the additional effects discussed above have been incorporated into this model (or dismissed as unimportant), and the modified model verified against experimental data, we will be able to predict the final geometry of a preform given the die geometry and system parameters. With this understanding we will be in a position to address the more-difficult inverse problem of selecting an appropriate die geometry and choosing the system parameters so as to give a desired final geometry. This work will ultimately result in both the development and, crucially, the realisation of novel optical fibre technology.



# Appendix A

## Transport Theorems

In the analysis of the axial equations in Chapter 3 we have made use of two transport theorems. These state that, for a region  $\Omega \in \mathbb{R}^2$  with boundary  $\partial\Omega$  on which  $G = 0$  and a twice-differentiable function  $\phi(x, y, t)$ , we have (Dewynne *et al.*, 1992)

$$\frac{\partial}{\partial t} \iint_{\Omega} \phi \, dx \, dy = \iint_{\Omega} \frac{\partial \phi}{\partial t} \, dx \, dy - \oint_{\partial\Omega} \frac{\phi}{|\nabla_{\perp} G|} \frac{\partial G}{\partial t} \, ds, \quad (\text{A.1})$$

$$\frac{\partial}{\partial z} \iint_{\Omega} \phi \, dx \, dy = \iint_{\Omega} \frac{\partial \phi}{\partial z} \, dx \, dy - \oint_{\partial\Omega} \frac{\phi}{|\nabla_{\perp} G|} \frac{\partial G}{\partial z} \, ds. \quad (\text{A.2})$$

These are derived from Reynolds' transport theorem (Leal, 2007), which may be stated

$$\frac{d}{dt} \iint_{\Omega} \mathbf{f} \, dx \, dy = \iint_{\Omega} \frac{\partial \mathbf{f}}{\partial t} \, dx \, dy + \oint_{\partial\Omega} (\mathbf{v} \cdot \mathbf{n}) \mathbf{f} \, ds,$$

where  $\mathbf{f}(x, y, t)$  is a function,  $\mathbf{v}$  is the velocity of the area element and  $\mathbf{n}$  is the outwards-pointing unit normal to  $\Omega$ .



# Appendix B

## Numerical Methods for Solving Polynomial Equations

### B.1 Overview

This appendix describes the numerical methods for solving polynomial equations investigated in Chapter 5. To illustrate these methods we will refer to the polynomial

$$p(\zeta) = \sum_{k=0}^K a_k \zeta^k. \quad (\text{B.1})$$

## B.2 Companion Matrix

The companion matrix of (B.1) is defined to be

$$C = \begin{bmatrix} 0 & 0 & \dots & 0 & -\frac{a_0}{a_k} \\ 1 & 0 & \dots & 0 & -\frac{a_1}{a_k} \\ 0 & 1 & \dots & 0 & -\frac{a_2}{a_k} \\ \vdots & \vdots & \ddots & \vdots & \vdots \\ 0 & 0 & \dots & 1 & -\frac{a_{k-1}}{a_k} \end{bmatrix}$$

It may be verified that  $p$  is the characteristic polynomial of  $C$ , so that the zeros of  $p$  are precisely the eigenvalues of  $C$ . Hence, we can use any suitable algorithm to calculate the eigenvalues of  $C$ , then select the appropriate root from these.

Within MATLAB there are two main methods for doing this: `eig` and `eigs`. The command `eig(C)` returns all the eigenvalues of  $C$ . From this we select the eigenvalue that lies within the unit circle. The function `eigs` uses the Lanczos algorithm to find eigenvalues, and can find a specified number of these. For this case, we specify to find the eigenvalue closest to zero in magnitude. The MATLAB function `roots` also works by constructing  $C$  and calling `eig`, making use of checks on the polynomial to avoid numerical errors. This method is also used by the MATLAB function `roots`.

## B.3 Newton's Method

Given some initial guess for the root  $\zeta_0$ , Newton's method states that better approximations are given by iterating

$$\zeta_{j+1} = \zeta_j - \frac{p(\zeta_j)}{p'(\zeta_j)}.$$

In practice, we iterate until successive iterates differ by less than some tolerance. Newton's method can suffer from the need to select an appropriate initial guess. Since  $p$  comes from a conformal map we expect that  $p'$  is non-zero within the unit circle and thus expect to find some neighbourhood of the solution in which all initial guesses will converge to that solution; however, there is no guarantee that a given initial guess will lie in this neighbourhood. This method has the advantage that, since  $p$  is a polynomial and thus has a continuous second derivative, we expect Newton's method to converge quadratically.

## B.4 Argument Principle

Suppose that  $f$  is a meromorphic function on  $\Omega$  with no zeros or poles on the boundary  $\partial\Omega$ , and define  $n(\partial\Omega, z)$  to be the winding number of  $\partial\Omega$  around  $z$ . Given a function  $g(z)$  that is analytic in  $\Omega$ , the argument principle states that

$$\frac{1}{2\pi i} \oint_{\partial\Omega} g(z) \frac{f'(z)}{f(z)} dz = \sum_a n(\partial\Omega, a)g(a) - \sum_b n(\partial\Omega, b)g(b),$$

where the first sum is over all the zeros of  $f$  including multiplicities, and the second over all the poles of  $f$  include their order. Taking  $\Omega$  to be the unit circle, polynomial  $p$  should have exactly one zero and no poles within  $\Omega$ . Furthermore, the winding number about the zero must be 1. Taking  $g(z) = z$  and applying the argument principle we find that the root is given by

$$r = \frac{1}{2\pi i} \oint_{\partial\Omega} \frac{zp'(z)}{p(z)} dz.$$

To evaluate this integral we parameterise the unit circle by  $\zeta(t) = e^{it}$  where  $t \in [0, 2\pi]$ . Using this we find that  $\zeta'(t) = ie^{it}$ , so we write the above expression as

$$r = \frac{1}{2\pi} \int_0^{2\pi} e^{2it} \frac{p'(e^{it})}{p(e^{it})} dt.$$

In practice, these integrals are performed using the Chebfun package, which first approximates the integrand by a Chebyshev series and uses this to compute the integral. Compared with other integration schemes tried, this results in a drastic improvement in both the speed and accuracy of this method.

## B.5 Other Methods

The remaining two methods are both in-built MATLAB functions. The function `fsolve` uses the trust-region dogleg method, based upon the work of Powell (1970). The function `lsqnonlin` uses the trust-region reflective algorithm. In both methods the complex values must be split into real and imaginary parts. While `fsolve` may find any root of  $p$ , `lsqnonlin` can be supplied with bounds to restrict the search region. Both algorithms require an initial guess for the root.

# Appendix C

## Experimental Set-Up and Measurements

### C.1 General method

A glass cylinder of known geometry was placed into an optical fibre drawing tower with the top end fixed and the bottom end free, as shown for an annular tube in Figure 6.4.9. The cylinder was surrounded by an electromagnetically-heated susceptor that was initially at room temperature and then heated to 930 °C so that the glass softened and the tube stretched under gravity, with no additional pulling. After some minutes the cylinder had deformed such that a drop was suspended by a thin filament, several metres in length, extending back to the remainder of the cylinder at the top of the draw tower. The bottom metre or so, which by this time had cooled sufficiently to solidify and handle, was broken off. All data were obtained from this piece, which consisted of a drop connected to a tapered filament and which we hereafter simply call ‘the drop’.

When completely cold, the drop was weighed and then divided into segments as illustrated in Figure C.1. The segments closest to the free end of the drop were each approximately 5 mm thick and were cut using a mechanical device. Some material was lost during each cut making it difficult to accurately measure the weight of each segment. To minimise any error, the weight below each cut was instead calculated by subtracting from the original weight the weight remaining after each segment was removed.

As the cutting process left rough edges, each segment was polished on both sides to ensure accurate measurement of the diameters. After being polished the segments were approximately 1–2 mm thick. Images of the cross sections were taken with a digital camera and the outer diameters were measured with a digital calliper. The inner diameters were then calculated from the known outer diameter and the measured ratio. In the thin-filament region segments were snapped off rather than cut. As these had smaller outer diameters, photographs of the cross sections were taken with a digital camera through an optical microscope. The diameters were measured using image processing software built into the microscope.

The viscosity  $\mu$  depends upon temperature, which varies in general with both axial position and time, so that  $\mu = \mu(x, t)$ . Although the susceptor temperature is known we do not know the temperature within the glass and thus do not know the viscosity. Additionally, once the glass leaves the susceptor even the temperature of the surrounding atmosphere is not known (Kostecki *et al.*, 2014). Thus, we have no knowledge of the glass viscosity during the experiment and hence also do not know the length  $\mathcal{L}$  of the deforming cylinder. Experimental observation shows that  $\mathcal{L}$  is somewhat less than the 45 mm length of the susceptor. Because the viscosity is not known it is also difficult to

determine the time over which the deformation takes place.

From the measured weights, the known initial geometry and assuming  $\mathcal{L} = 40$  mm, the coordinate  $\xi$  at each cut was calculated.

In the absence of experimental viscosity and time data we compare model output with experimental data using reduced time  $\tau$ , which incorporates information on the unknown time and viscosity, along with the surface tension. Matching experimentally measured final cross-sectional areas to the model, results in a nonlinear equation for the value of  $\tau$  at each cross section, which is readily solved. This match can be performed using the reduced time solution to the WST axial problem (6.2.14) or the solution to the full axial problem (6.2.11). With  $\tau$  known we can use the transverse model to compute the predicted transverse geometry. That is, we are able to calculate the predicted *shape* of each cross section given the observed *area*. In effect, this process removes the axial stretching from both the model and the data, allowing a comparison of the transverse surface-tension-driven flow. If surface tension is not important, the data should show no change in the shape of the transverse domain (as all the change would be due to stretching, which is limited to the axial problem). Any deviation in shape will reflect the effect of surface tension.

## C.2 Tube

The initial aspect ratio was  $0.168 \pm 10^{-2}$ . While this ratio was constant along the 177 mm length of the tube, the manufacturing process resulted in a taper in the tube so that the outer radius varied linearly from 5.03 mm at the top to 5.295 mm at the bottom, as sketched in Figure C.2. Other relevant physical quantities are given in Table C.1. Segments 5 and 9 were lost during

Table C.1: Physical parameters for the stretching tube experiment. The area scale  $\mathcal{S}$  is calculated from the larger end of the tube, so that the initial dimensionless areas are all between 0 and 1.

Quantity	Value	Units
$\rho$	$3.6 \times 10^3$	$\text{kg} \cdot \text{m}^{-3}$
$\gamma$	0.25	$\text{N} \cdot \text{s}$
$\mathcal{S}$	$8.559 \times 10^{-5}$	$\text{m}^2$

the polishing process while segment 11 was broken, which meant the diameters of these segments could not be measured. The data are recorded in Table C.2.

From the measurements taken, the outer radius in metres can be approximated by the function  $\bar{R}(\xi) = a\xi + b$  where  $a = 5.988 \times 10^{-5} \text{ m}$ ,  $b = 5.235 \times 10^{-3} \text{ m}$  and the bar denotes a dimensional quantity. Using these measurements and the aspect ratio 0.168, the area of each cross section  $\xi$  in square metres is given by

$$\bar{S}(\xi) = \pi(1 - 0.168^2)\bar{R}^2(\xi). \quad (\text{C.1})$$

Integrating this expression with respect to  $\xi$  and accounting for the length scale shows that the total volume below any point  $\xi$  is given by

$$\bar{V}(\xi) = \mathcal{L}\pi(1 - 0.168^2) \left[ \frac{a^2}{3}(1 - \xi^3) + ab(1 - \xi^2) + b^2(1 - \xi) \right]. \quad (\text{C.2})$$

Dividing the known masses from Table C.2 by the density yields the measured volume below each cut. Equating these values to the theoretical expression (C.2) gives a cubic equation for  $\xi$ . Once the value of  $\xi$  corresponding to each segment is determined it is simple to calculate the initial area of each cross section, and hence also  $\chi_0(\xi)$ , from (C.1). It should be emphasised that, although each

Table C.2: Data recorded from the stretching tube experiment. The mass below each segment  $M$  was calculated by removing the segment and subtracting the remaining mass from the initial mass. For  $\xi > 0.4$  the outer diameters  $d_{\text{out}}$  were measured using a calliper and the inner diameters  $d_{\text{in}}$  calculated from digital photos of each segment. The diameters of the remaining segments were measured using a digital photo taken under a microscope.

Segment	$\xi$	$M$ (g)	$d_{\text{out}}$ (mm)	$d_{\text{in}}$ (mm)
1	0.913 63	1.060	10.61	1.627
2	0.823 20	2.160	10.58	1.651
3	0.744 18	3.113	10.54	1.602
4	0.678 61	3.898	10.18	1.419
5	–	4.819	–	–
6	0.550 56	5.416	8.68	0.8680
7	0.505 28	5.948	7.46	0.5425
8	0.466 99	6.396	6.41	0.4314
9	–	6.754	–	–
10	0.295 31	8.383	1.653	0.059 86
11	–	8.515	–	–
12	0.274 20	8.625	1.335	0.050 28
13	0.265 02	8.730	1.215	0.045 19
14	0.257 23	8.819	1.119	0.043 06
15	0.250 75	8.893	1.049	0.045 61
16	0.245 67	8.951	0.984	0.037 59

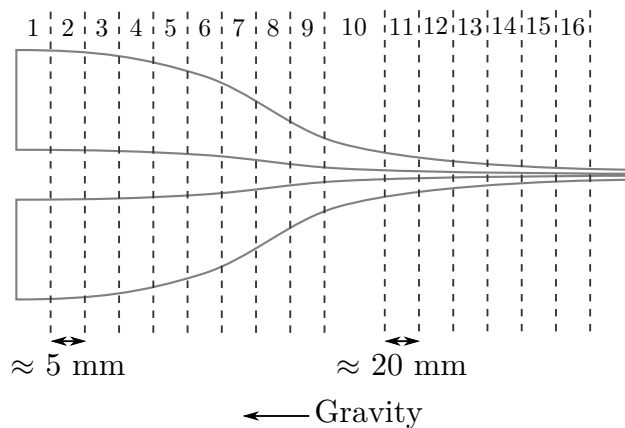


Figure C.1: A schematic of the drop after stretching under gravity. The drop was cut into 16 segments. The first nine were each approximately 5 mm in width, while the remaining segments were approximately 20 mm in width. The drop is not shown to scale.

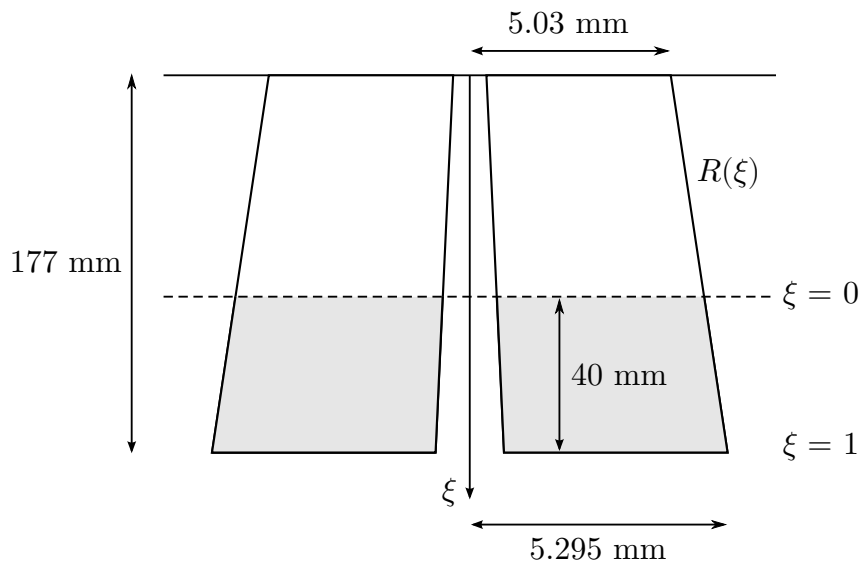


Figure C.2: The initial shape of the cylinder used in the stretching tube experiment. The radii are smaller at  $\xi = 0$  than at  $\xi = 1$  but are in the same ratio along the length of the tube.

cross section started with a different area, the radii in each were in the same ratio. Thus, every cross section corresponds to the same transverse problem.

### C.3 3-Hole Cylinder

The density and surface tension were the same as for the annular drop (Table C.1), while the area scale was taken to be  $\mathcal{S} = 1.69 \times 10^{-4} \text{ m}^2$ . The drop was cut into 38 segments. The pieces with  $\xi > 0.4$  were larger and so were cut mechanically, while the remaining pieces had smaller outer diameters and so were snapped off. The areas of all the cross sections were calculated by fitting circles over the boundaries in the photographs using image processing software. While the boundaries were not perfectly circular this method provided a reasonable approximation. Typically, the central hole was furthest from circular but, due to its small size, this did not have a significant effect on the results. A summary of the data is given in Table C.3. Segment 3 was damaged during the measurement process so that no area could be recorded.

Since each cross section was assumed to have the same initial area  $\mathcal{S}$ , the volume below any cross section  $\xi$  is given by

$$\bar{V}(\xi) = \mathcal{L}\mathcal{S}(1 - \xi).$$

Equating this to the volumes calculated from the measured masses and density yields a linear equation for the value of  $\xi$  for each segment.

Table C.3: Data recorded from the three-channel stretching experiment. Listed are the Lagrangian co-ordinates  $\xi$ , the masses  $M$  below each segment and the cross-sectional areas  $A$ . Segment 3 was lost during the measurement process.

Seg.	$\xi$	$M$ (g)	$A$ (mm <sup>2</sup> )	Seg.	$\xi$	$M$ (g)	$A$ (mm <sup>2</sup> )
1	0.958 57	1.012	156.635 68	14	0.347 18	15.948	2.462 256 6
2	0.898 03	2.491	169.647 87	15	0.335 79	16.226	1.467 426 6
3	–	3.963	–	16	0.328 80	16.397	1.306 086 1
4	0.780 47	5.363	162.753 12	17	0.322 53	16.550	0.948 823 27
5	0.708 67	7.117	155.340 71	18	0.318 50	16.648	0.713 388 61
6	0.655 50	8.416	132.268 83	19	0.316 11	16.706	0.626 089 09
7	0.580 67	10.244	118.422 18	20	0.313 38	16.773	0.512 021 80
8	0.528 68	11.514	80.458 745	21	0.311 40	16.821	0.517 249 99
9	0.474 20	12.845	50.995 111	22	0.309 42	16.870	0.452 893 20
10	0.442 84	13.611	25.258 58	23	0.307 13	16.926	0.426 887 72
11	0.418 32	14.210	14.711 88	24	0.305 30	16.971	0.404 408 92
12	0.356 84	15.712	9.029 541 8	25	0.303 84	17.006	0.378 082 07
13	0.362 37	15.577	4.394 739 7	26	0.302 04	17.050	0.353 721 38

# Bibliography

- Aboelkassem, Y. and Staples, A. E. (2013), ‘Stokeslets-meshfree computations and theory for flow in a collapsible microchannel’, *Theoretical and Computational Fluid Dynamics* **27**(5), 681–700.
- Airy, G. B. (1863), ‘On the strains in the interior of beams’, *Philosophical Transactions of the Royal Society of London* **153**, 49–79.
- Amano, K. (1994), ‘A charge simulation method for the numerical conformal mapping of interior, exterior and doubly-connected domains’, *Journal of Computational and Applied Mathematics* **53**(3), 353–370.
- Antanovskii, L. K. (1994), ‘A plane inviscid incompressible bubble placed within a creeping viscous flow: formation of a cusped bubble’, *European Journal of Mechanics - B/Fluids* **13**(4), 491–509.
- Babcock, C. L. (1940), ‘Surface tension measurements on molten glass by a modified dipping cylinder method’, *Journal of the American Ceramic Society* **23**(1), 12–17.
- Balk, M. B. and Zuev, M. F. (1970), ‘On polyanalytic functions’, *Russian Mathematical Surveys* **25**(5), 201–223.

- Barton, G., van Eijkelenborg, M. A., Henry, G., Large, M. C. J. and Zagari, J. (2004), ‘Fabrication of microstructured polymer optical fibres’, *Optical Fiber Technology* **10**(4), 325–335.
- Batchelor, G. K. (1967), *An Introduction to Fluid Mechanics*, Cambridge University Press.
- Belwalkar, A., Xiao, H., Misiolek, W. Z. and Toulouse, J. (2010), ‘Extruded tellurite glass optical fiber preforms’, *Journal of Materials Processing Technology* **210**(14), 2016–2022.
- Benchama, N., DeLillo, T. K., Hrycak, T. and Wang, L. (2007), ‘A simplified Fornberg-like method for the conformal mapping of multiply connected regions—Comparisons and crowding’, *Journal of Computational and Applied Mathematics* **209**(1), 1–21.
- Berkemeier, F., Voss, S., Árpád W. Imre and Mehrer, H. (2005), ‘Molar volume, glass-transition temperature, and ionic conductivity of Na- and Rb-borate glasses in comparison with mixed Na–Rb borate glasses’, *Journal of Non-Crystalline Solids* **351**(52–54), 3816–3825.
- Biros, G., Ying, L. X. and Zorin, D. (2004), ‘A fast solver for the Stokes equations with distributed forces in complex geometries’, *Journal of Computational Physics* **193**(1), 317–348.
- Boselli, F., Obrist, D. and Kleiser, L. (2012), ‘A multilayer method of fundamental solutions for Stokes flow problems’, *Journal of Computational Physics* **231**(18), 6139–6158.
- Boyd, J. P. (2000), *Chebyshev and Fourier Spectral Methods*, second edn, Dover Publications, Inc.

- Boyd, K., Ebendorff-Heidepriem, H., Monro, T. M. and Munch, J. (2012), ‘Surface tension and viscosity measurement of optical glasses using a scanning CO<sub>2</sub> laser’, *Optical Materials Express* **2**(8), 1101–1110.
- Bradshaw-Hajek, B. H., Stokes, Y. M. and Tuck, E. O. (2007), ‘Computation of extensional flow of slender viscous drops by a one-dimensional Eulerian method’, *SIAM Journal on Applied Mathematics* **67**(4), 1166–1182.
- Buchak, P., Crowdy, D. G., Stokes, Y. M. and Ebendorff-Heidepriem, H. (2015), ‘Elliptical pore regularisation of the inverse problem for microstructured optical fibre fabrication’, *Journal of Fluid Mechanics* **778**, 5–38.
- Buckmaster, J. D. and Flaherty, J. E. (1973), ‘The bursting of two-dimensional drops in slow viscous flow’, *Journal of Fluid Mechanics* **60**, 625–639.
- Carrier, G. F., Krook, M. and Pearson, C. L. (1966), *Functions of a Complex Variable*, McGraw-Hill Book Company.
- Chakravarthy, S. S. and Chiu, W. K. S. (2009), ‘Boundary integral method for the evolution of slender viscous fibres containing holes in the cross-section’, *Journal of Fluid Mechanics* **621**, 155–182.
- Chanshetti, U. B., Shelke, V. A., Jadhav, S. M., Shankarwar, S. G., Chondhekar, T. K., Shankarwar, A. G., Sudarsan, V. and Jogad, M. S. (2011), ‘Density and molar volume studies of phosphate glasses’, *Facta Universitatis, Series: Physics, Chemistry and Technology* **9**(1), 29–36.
- Chen, M. J., Stokes, Y. M., Buchak, P., Crowdy, D. G. and Ebendorff-Heidepriem, H. (2015), ‘Microstructured optical fibre drawing with active channel pressurisation’, *Journal of Fluid Mechanics* **783**, 137–165.

- Clarke, N. S. (1968), ‘Two-dimensional flow under gravity in a jet of viscous liquid’, *Journal of Fluid Mechanics* **31**(03), 481–500.
- Coleman, C. J. (1981), ‘A contour integral formulation of plane creeping newtonian flow’, *The Quarterly Journal of Mechanics and Applied Mathematics* **34**(4), 453–464.
- Cox, S. M. and Finn, M. D. (2007), ‘Two-dimensional Stokes flow driven by elliptical paddles’, *Physics of Fluids* **19**(11), 113102.
- Crowdy, D. G. (1999), ‘A note on viscous sintering and quadrature identities’, *European Journal of Applied Mathematics* **10**(6), 623–634.
- Crowdy, D. G. (2002a), ‘Exact solutions for the viscous sintering of multiply-connected fluid domains’, *Journal of Engineering Mathematics* **42**(3–4), 225–242.
- Crowdy, D. G. (2002b), ‘On a class of geometry-driven free boundary problems’, *SIAM Journal on Applied Mathematics* **62**(3), 945–964.
- Crowdy, D. G. (2003a), ‘Compressible bubbles in Stokes flow’, *Journal of Fluid Mechanics* **476**, 345–356.
- Crowdy, D. G. (2003b), ‘Viscous sintering of unimodal and bimodal cylindrical packings with shrinking pores’, *European Journal of Applied Mathematics* **14**(4), 421–445.
- Crowdy, D. G. (2004), ‘An elliptical-pore model for late-stage planar viscous sintering’, *Journal of Fluid Mechanics* **501**, 251–277.
- Crowdy, D. G. and Or, Y. (2010), ‘Two-dimensional point singularity model of a low-Reynolds-number swimmer near a wall’, *Physical Review E* **81**(3), 036313.

- Crowdy, D. G. and Tanveer, S. (1998), ‘A theory of exact solutions for annular viscous blobs’, *Journal of Nonlinear Science* **8**(4), 375–400.
- Crowdy, D. G., Tanveer, S. and Vasconcelos, G. L. (2005), ‘On a pair of interacting bubbles in planar Stokes flow’, *Journal of Fluid Mechanics* **541**, 231–261.
- Cummings, L. J. and Howell, P. D. (1999), ‘On the evolution of non-axisymmetric viscous fibres with surface tension, inertia and gravity’, *Journal of Fluid Mechanics* **389**, 361–389.
- Cummings, L. J., Howison, S. D. and King, J. R. (1997), ‘Conserved quantities in Stokes flow with free surfaces’, *Physics of Fluids* **9**(3), 477–480.
- Cummings, L. J., Howison, S. D. and King, J. R. (1999), ‘Two-dimensional Stokes and Hele-Shaw flows with free surfaces’, *European Journal of Applied Mathematics* **10**(6), 635–680.
- de Gennes, P. G., Brochard-Wyart, F. and Quéré, D. (2013), *Capillarity and Wetting Phenomena: Drops, Bubbles, Pearls, Waves*, Springer New York.
- Deang, J. and Gunzburger, M. (1998), ‘Issues related to least-squares finite element methods for the Stokes equations’, *SIAM Journal on Scientific Computing* **20**(3), 878–906.
- DeCusatis, C. M. and DeCusatis, C. J. S. (2006), *Fiber Optic Essentials*, Academic Press, Burlington.
- DeLillo, T. K. (1994), ‘The accuracy of numerical conformal mapping methods: a survey of examples and results’, *SIAM Journal on Numerical Analysis* **31**(3), 788–812.

- DeLillo, T. K., Horn, M. A. and Pfaltzgraff, J. A. (1999), ‘Numerical conformal mapping of multiply connected regions by Fornberg-like methods’, *Numerische Mathematik* **83**(2), 205–230.
- DeLillo, T. K. and Pfaltzgraff, J. A. (1998), ‘Numerical conformal mapping methods for simply and doubly connected regions’, *SIAM Journal on Scientific Computing* **19**(1), 155–171.
- Denn, M. M. (1980), ‘Continuous drawing of liquids to form fibers’, *Annual Review of Fluid Mechanics* **12**, 365–387.
- Dewynne, J. N., Howell, P. D. and Willmot, P. (1994), ‘Slender viscous fibres with inertia and gravity’, *The Quarterly Journal of Mechanics and Applied Mathematics* **47**(4), 541–555.
- Dewynne, J. N., Ockendon, J. R. and Wilmott, P. (1992), ‘A systematic derivation of the leading-order equations for extensional flows in slender geometries’, *Journal of Fluid Mechanics* **244**, 323–338.
- Dewynne, J., Ockendon, J. R. and Wilmott, P. (1989), ‘On a mathematical model for fiber tapering’, *SIAM Journal on Applied Mathematics* **49**(4), 983–990.
- Ebendorff-Heidepriem, H. (2011), personal communication.
- Ebendorff-Heidepriem, H. and Monro, T. M. (2007), ‘Extrusion of complex preforms for microstructured optical fibers’, *Optics Express* **15**(23), 86–92.
- Ebendorff-Heidepriem, H. and Monro, T. M. (2009), Soft glass microstructured optical fibers: recent progress in fabrication and opportunities for novel

- optical devices, in ‘Communications and Photonics Conference and Exhibition (ACP), 2009 Asia’, pp. 1–2.
- Ebendorff-Heidepriem, H. and Monroe, T. M. (2012), ‘Analysis of glass flow during extrusion of optical fiber preforms’, *Optical Materials Express* **2**(3), 304–320.
- Ebendorff-Heidepriem, H., Moore, R. C. and Monroe, T. M. (2008), ‘Progress in the fabrication of the next-generation soft glass microstructured optical fibers’, *AIP Conference Proceedings* **1055**(1), 95–98.
- Eggers, J. and Dupont, T. F. (1994), ‘Drop formation in a one-dimensional approximation of the Navier–Stokes equation’, *Journal of Fluid Mechanics* **262**, 205–221.
- Eggers, J. and Villiermaux, E. (2008), ‘Physics of liquid jets’, *Reports on Progress in Physics* **71**(3), 036601.
- Ehrlich, L. W. and Gupta, M. M. (1975), ‘Some difference schemes for the biharmonic equation’, *SIAM Journal on Numerical Analysis* **12**(5), 773–790.
- El-Hadp, Z. A., Khalida, F. A., El-Kheshen, A. A. and Moustaffa, F. A. (1995), ‘Density and molar volume of some high lead silicate’, *Communications, Faculty Of Science, University of Ankara Series B: Chemistry and Chemical Engineering* pp. 33–50.
- Fairweather, G. and Karageorghis, A. (1998), ‘The method of fundamental solutions for elliptic boundary value problems’, *Advances in Computational Mathematics* **9**(1–2), 69–95.

- Finn, M. D. and Cox, S. M. (2001), ‘Stokes flow in a mixer with changing geometry’, *Journal of Engineering Mathematics* **41**(1), 75–99.
- Finn, M. D., Cox, S. M. and Byrne, H. M. (2003a), ‘Chaotic advection in a braided pipe mixer’, *Physics of Fluids* **15**(11), L77–L80.
- Finn, M. D., Cox, S. M. and Byrne, H. M. (2003b), ‘Topological chaos in inviscid and viscous mixers’, *Journal of Fluid Mechanics* **493**, 345–361.
- Fitt, A. D., Furusawa, K., Monro, T. M., Please, C. P. and Richardson, D. J. (2002), ‘The mathematical modelling of capillary drawing for holey fibre manufacture’, *Journal of Engineering Mathematics* **43**(2), 201–227.
- Fornberg, B. (1980), ‘A numerical method for conformal mappings’, *SIAM Journal on Scientific and Statistical Computing* **1**(3), 386–400.
- Fornberg, B. (1984), ‘A numerical method for conformal mapping of doubly connected regions’, *SIAM Journal on Scientific and Statistical Computing* **5**(4), 771–783.
- Fulcher, G. S. (1925), ‘Analysis of recent measurements of the viscosity of glasses’, *Journal of the American Ceramic Society* **8**(6), 339–355.
- Garabedian, P. R. (1966), ‘Free boundary flows of a viscous liquid’, *Communications on Pure and Applied Mathematics* **19**(4), 421–434.
- Glowinski, R. and Pironneau, O. (1979), ‘Numerical methods for the first biharmonic equation and for the two-dimensional Stokes problem’, *SIAM Review* **21**(2), 167–212.
- Goursat, É. J.-B. (1898), ‘Sur l’équation  $\Delta\Delta u = 0$ ’, *Bulletin de la S.M.F.* **26**, 233–237.

- Greenbaum, A., Greengard, L. and Mayo, A. (1992), ‘On the numerical solution of the biharmonic equation in the plane’, *Physica D: Nonlinear Phenomena* **60**(1–4), 216–225.
- Greengard, L. and Kropinski, M. (2004), ‘Integral equation methods for Stokes flow in doubly-periodic domains’, *Journal of Engineering Mathematics* **48**(2), 157–170.
- Greengard, L., Kropinski, M. C. and Mayo, A. (1996), ‘Integral equation methods for Stokes flow and isotropic elasticity in the plane’, *Journal of Computational Physics* **125**(2), 403–414.
- Greenspan, D. and Schultz, D. (1972), ‘Fast finite-difference solution of biharmonic problems’, *Communications of the ACM* **15**(5), 347–350.
- Griffiths, I. M. and Howell, P. D. (2007), ‘The surface-tension-driven evolution of a two-dimensional annular viscous tube’, *Journal of Fluid Mechanics* **593**, 181–208.
- Griffiths, I. M. and Howell, P. D. (2008), ‘Mathematical modelling of non-axisymmetric capillary tube drawing’, *Journal of Fluid Mechanics* **605**, 181–206.
- Griffiths, I. M. and Howell, P. D. (2009), ‘The surface-tension-driven retraction of a viscida’, *SIAM Journal on Applied Mathematics* **70**(5), 1453–1487.
- Guiyao, Z., Zhiyun, H., Shuguang, L. and Lantian, H. (2006), ‘Fabrication of glass photonic crystal fibers with a die-cast process’, *Applied Optics* **45**(18), 4433–4436.

- Gupta, G. K., Schultz, W. W., Arruda, E. M. and Lu, X. (1996), 'Nonisothermal model of glass fiber drawing stability', *Rheologica Acta* **35**(6), 584–596.
- Heinrichs, W. (2004), 'Spectral collocation schemes on the unit disc', *Journal of Computational Physics* **199**(1), 66–86.
- Hellou, M. and Coutanceau, M. (1992), 'Cellular Stokes flow induced by rotation of a cylinder in a closed channel', *Journal of Fluid Mechanics* **236**, 557–577.
- Henrici, P. (1974), *Power Series - Integration - Conformal Mapping - Location of Zeros*, Vol. 1 of *Applied and Computational Complex Analysis*, John Wiley & Sons.
- Holloway, D. G. (1973), *The Physical Properties of Glass*, Wykeham Publications (London).
- Hopper, R. W. (1984), 'Coalescence of two equal cylinders: Exact results for creeping viscous plane flow driven by capillarity', *Journal of the American Ceramic Society* **67**(12), C-262–C-264.
- Hopper, R. W. (1990), 'Plane Stokes flow driven by capillarity on a free surface', *Journal of Fluid Mechanics* **213**, 349–375.
- Hopper, R. W. (1991), 'Plane Stokes flow driven by capillarity on a free surface. Part 2. Further developments', *Journal of Fluid Mechanics* **230**, 355–364.
- Hopper, R. W. (1992), 'Stokes flow of a cylinder and half-space driven by capillarity', *Journal of Fluid Mechanics* **243**, 171–181.
- Hopper, R. W. (1993), 'Capillarity-driven plane Stokes flow exterior to a parabola', *The Quarterly Journal of Mechanics and Applied Mathematics* **46**(2), 193–210.

- Horsfall, F. (1973), 'A theoretical treatment of die swell in a Newtonian liquid', *Polymer* **14**(6), 262–266.
- Howison, S. D. (1986*a*), 'Cusp development in Hele-Shaw flow with a free surface', *SIAM Journal on Applied Mathematics* **46**(1), 20–26.
- Howison, S. D. (1986*b*), 'Fingering in Hele-Shaw cells', *Journal of Fluid Mechanics* **167**, 439–453.
- Howison, S. D. and Richardson, S. (1995), 'Cusp development in free boundaries, and two-dimensional slow viscous flows', *European Journal of Applied Mathematics* **6**(5), 441–454.
- Huang, H., Miura, R. M., Ireland, W. P. and Puil, E. (2003), 'Heat-induced stretching of a glass tube under tension: Application to glass microelectrodes', *SIAM Journal on Applied Mathematics* **63**(5), 1499–1519.
- Huang, H., Miura, R. and Wylie, J. (2008), 'Optical fiber drawing and dopant transport', *SIAM Journal on Applied Mathematics* **69**(2), 330–347.
- Huang, H., Wylie, J. J., Miura, R. M. and Howell, P. D. (2007), 'On the formation of glass microelectrodes', *SIAM Journal on Applied Mathematics* **67**(3), 630–666.
- Huynh, B. P. (1998), 'A numerical investigation of non-isothermal extrusion through annular dies', *International Journal of Engineering Science* **36**(2), 171–188.
- Irgens, F. (2008), *Continuum Mechanics*, Springer.
- Ivanov, V. I. and Trubetskov, M. K. (1994), *Handbook of Conformal Mapping with Computer-Aided Visualization*, CRC press.

- Jeong, J.-T. and Moffatt, H. K. (1992), ‘Free-surface cusps associated with flow at low Reynolds number’, *Journal of Fluid Mechanics* **241**, 1–22.
- Karageorghis, A. and Fairweather, G. (1987), ‘The method of fundamental solutions for the numerical solution of the biharmonic equation’, *Journal of Computational Physics* **69**(2), 434–459.
- Karageorghis, A. and Fairweather, G. (1989), ‘The simple layer potential method of fundamental solutions for certain biharmonic problems’, *International Journal for Numerical Methods in Fluids* **9**(10), 1221–1234.
- Karageorghis, A. and Phillips, T. N. (1989), ‘Spectral collocation methods for Stokes flow in contraction geometries and unbounded domains’, *Journal of Computational Physics* **80**(2), 314–330.
- Karageorghis, A. and Smyrlis, Y.-S. (2008), ‘Conformal mapping for the efficient MFS solution of Dirichlet boundary value problems’, *Computing* **83**(1), 1–24.
- Kaye, A. (1991), ‘Convected coordinates and elongational flow’, *Journal of Non-Newtonian Fluid Mechanics* **40**(1), 55–77.
- King, J. (1989), ‘The isolation oxidation of silicon’, *SIAM Journal on Applied Mathematics* **49**(1), 264–280.
- Knight, J. C. (2003), ‘Photonic crystal fibres’, *Nature* **424**(6950), 847–851.
- Knight, J. C., Birks, T. A., Russell, P. S. J. and Atkin, D. M. (1996), ‘All-silica single-mode optical fiber with photonic crystal cladding’, *Optics Letters* **21**(19), 1547–1549.
- Kolosov, G. V. (1909), ‘On an application of complex function theory to a plane problem of the mathematical theory of elasticity’, *Yuriev, Russia* .

- Kostecki, R., Ebendorff-Heidepriem, H., Warren-Smith, S. C. and Monro, T. M. (2014), ‘Predicting the drawing conditions for microstructured optical fiber fabrication’, *Optical Materials Express* **4**(1), 29–40.
- Krakowski, M. and Charnes, A. (1953), *Stokes’ Paradox and Biharmonic Flows*, Technical report (Carnegie Institute of Technology. Department of Mathematics), Carnegie Institute of Technology, Department of Mathematics.
- Kreyszig, E. (2005), *Advanced Engineering Mathematics*, ninth edn, John Wiley & Sons.
- Kropf, E. (2009), A Fornberg-like method for the numerical conformal mapping of bounded multiply connected domains, Master’s thesis, Wichita State University.
- Kropinski, M. C. A. (1999), ‘Integral equation methods for particle simulations in creeping flows’, *Computers & Mathematics with Applications* **38**(5–6), 67–87.
- Kropinski, M. C. A. (2001), ‘An efficient numerical method for studying interfacial motion in two-dimensional creeping flows’, *Journal of Computational Physics* **171**(2), 479–508.
- Kropinski, M. C. A. (2002), ‘Numerical methods for multiple inviscid interfaces in creeping flows’, *Journal of Computational Physics* **180**(1), 1–24.
- Kropinski, M. C. A. and Lushi, E. (2011), ‘Efficient numerical methods for multiple surfactant-coated bubbles in a two-dimensional Stokes flow’, *Journal of Computational Physics* **230**(12), 4466–4487.

- Langlois, W. E. (1964), *Slow Viscous Flow*, first edn, The MacMillan Company, Collier–MacMillan Canada.
- Leal, L. G. (2007), *Advanced Transport Phenomena: Fluid Mechanics and Convective Transport Processes*, Cambridge Series in Chemical Engineering, Cambridge University Press.
- Lee, S. H. K. and Jaluria, Y. (1997), ‘Simulation of the transport processes in the neck-down region of a furnace drawn optical fiber’, *International Journal of Heat and Mass Transfer* **40**(4), 843–856.
- Lin, K. J. and Jou, R. Y. (1995), ‘Non-axisymmetric extrusion of viscous and viscoelastic liquids under gravity’, *International Journal of Non-Linear Mechanics* **30**(4), 449–463.
- Linkov, A. M. (2002), *Boundary integral equations in elasticity theory*, Vol. 99 of *Solid Mechanics and Its Applications*, Springer.
- Lyytikäinen, K., Zagari, J., Barton, G. and Canning, J. (2004), ‘Heat transfer within a microstructured polymer optical fibre preform’, *Modelling and Simulation in Materials Science and Engineering* **12**(3), S255–S265.
- Manning, S. (2011), A study of tellurite glasses for electro-optic optical fibre devices, PhD thesis, School of Chemistry and Physics.
- Mano, J. F. and Pereira, E. (2004), ‘Data analysis with the Vogel–Fulcher–Tammann–Hesse equation’, *The Journal of Physical Chemistry A* **108**(49), 10824–10833.
- Matovich, M. A. and Pearson, J. R. A. (1969), ‘Spinning a molten threadline.

- Steady-state isothermal viscous flows', *Industrial & Engineering Chemistry Fundamentals* **8**(3), 512–520.
- Middleman, S. and Gavis, J. (1961), 'Expansion and contraction of capillary jets of Newtonian liquids', *Physics of Fluids* **4**(3), 355–359.
- Mitsoulis, E. (1986), 'Extrudate swell of Newtonian fluids from annular dies', *AIChE Journal* **32**(3), 497–500.
- Modest, M. F. (2013), *Radiative Heat Transfer*, Elsevier Science.
- Monro, T. M. and Ebendorff-Heidepriem, H. (2006), 'Progress in microstructured optical fibres', *Annual Review of Materials Research* **36**(1), 467–495.
- Monro, T. M., Warren-Smith, S., Schartner, E. P., François, A., Heng, S., Ebendorff-Heidepriem, H. and V, S. A. (2010), 'Sensing with suspended-core optical fibers', *Optical Fiber Technology* **16**(6), 343–356. Special Fiber Structures and their Applications.
- Morey, G. W. (1938), *The Properties of Glass*, Reinhold Publishing Corporation.
- Munasinghe, H. T., Winterstein-Beckmann, A., Schiele, C., Manzani, D., Wondraczek, L., V., S. A., Monro, T. M. and Ebendorff-Heidepriem, H. (2013), 'Lead-germanate glasses and fibers: A practical alternative to tellurite for nonlinear fiber applications', *Optical Materials Express* **3**(9), 1488–1503.
- Muskhelishvili, N. I. (1975), *Some Basic Problems of the Mathematical Theory of Elasticity*, 4th edn, Noordhoff International Publishing. Translated by J. R. M. Radok, original publication 1954.
- Nehari, Z. (1975), *Conformal mapping*, Courier Dover Publications.

- Ogata, H. and Amano, K. (2010), ‘Fundamental solution method for two-dimensional Stokes flow problems with one-dimensional periodicity’, *Japan Journal of Industrial and Applied Mathematics* **27**(2), 191–215.
- Ogata, H., Amano, K., Sugihara, M. and Okano, D. (2003), ‘A fundamental solution method for viscous flow problems with obstacles in a periodic array’, *Journal of Computational and Applied Mathematics* **152**(1–2), 411–425. Proceedings of the International Conference on Recent Advances in Computational Mathematics.
- Orszag, S. A. (1980), ‘Spectral methods for problems in complex geometries’, *Journal of Computational Physics* **37**(1), 70–92.
- Owens, R. G. and Phillips, T. N. (1994), ‘Mass- and momentum-conserving spectral methods for Stokes flow’, *Journal of Computational and Applied Mathematics* **53**(2), 185–206.
- Paek, U. C. and Runk, R. B. (1978), ‘Physical behavior of the neckdown region during furnace drawing of silica fibers’, *Journal of Applied Physics* **49**(8), 4417–4422.
- Parikh, N. M. (1958), ‘Effect of atmosphere on surface tension of glass’, *Journal of the American Ceramic Society* **41**(1), 18–22.
- Petrie, C. (1995), ‘Extensional flow—a mathematical perspective’, *Rheologica Acta* **34**(1), 12–26.
- Poulikkas, A., Karageorghis, A., Georgiou, G. and Ascough, J. (1998), ‘The method of fundamental solutions for Stokes flows with a free surface’, *Numerical Methods for Partial Differential Equations* **14**(5), 667–678.

- Powell, M. J. D. (1970), A Fortran subroutine for solving systems of nonlinear algebraic equations, *in* P. Rabinowitz, ed., ‘Numerical Methods for Nonlinear Algebraic Equations’, Gordon & Breach Science Pub, chapter 7.
- Pozrikidis, C. (1992), *Boundary integral and singularity methods for linearized viscous flow*, Cambridge University Press.
- Pozrikidis, C. (2001), ‘Expansion of a compressible gas bubble in Stokes flow’, *Journal of Fluid Mechanics* **442**, 171–189.
- Price, T. J., Mullin, T. and Kobine, J. J. (2003), ‘Numerical and experimental characterization of a family of two-roll-mill flows’, *Proceedings of the Royal Society of London. Series A: Mathematical, Physical and Engineering Sciences* **459**(2029), 117–135.
- Reutskiy, S. Y. (2006), ‘The method of fundamental solutions for Helmholtz eigenvalue problems in simply and multiply connected domains’, *Engineering Analysis with Boundary Elements* **30**(3), 150–159.
- Richardson, K. (2012), Materials world network in advanced optical glasses for novel optical fibers. Private communication as part of NSF–DMR #0807016.
- Richardson, S. (1968), ‘Two-dimensional bubbles in slow viscous flows’, *Journal of Fluid Mechanics* **33**(03), 475–493.
- Richardson, S. (1970), ‘The die swell phenomenon’, *Rheologica Acta* **9**, 193–199.
- Richardson, S. (1972), ‘Hele Shaw flows with a free boundary produced by the injection of fluid into a narrow channel’, *Journal of Fluid Mechanics* **56**, 609–618.

- Richardson, S. (1973), ‘Two-dimensional bubbles in slow viscous flows. Part 2’, *Journal of Fluid Mechanics* **58**(01), 115–127.
- Richardson, S. (1982), ‘Hele-Shaw flows with time-dependent free boundaries in infinite and semi-infinite strips’, *The Quarterly Journal of Mechanics and Applied Mathematics* **35**(4), 531–548.
- Richardson, S. (1992), ‘Two-dimensional slow viscous flows with time-dependent free boundaries driven by surface tension’, *European Journal of Applied Mathematics* **3**, 193–207.
- Richardson, S. (1997*a*), ‘On the classification of solutions to the zero-surface-tension model for Hele-Shaw free boundary flows’, *Quarterly of Applied Mathematics* **55**(2), 313–319.
- Richardson, S. (1997*b*), ‘Two-dimensional Stokes flows with time-dependent free boundaries driven by surface tension’, *European Journal of Applied Mathematics* **8**(04), 311–329.
- Richardson, S. (2000), ‘Plane Stokes flows with time-dependent free boundaries in which the fluid occupies a doubly-connected region’, *European Journal of Applied Mathematics* **11**, 249–269.
- Russell, P. (2003), ‘Photonic crystal fibers’, *Science* **299**(5605), 358–362.
- Sauter, U. S. and Buggisch, H. W. (2005), ‘Stability of initially slow viscous jets driven by gravity’, *Journal of Fluid Mechanics* **533**, 237–257.
- Schott (2013), ‘Schott optical glass data sheets’.
- Schultz, W. W. and Davis, S. H. (1982), ‘One-dimensional liquid fibres’, *Journal of Rheology* **26**(4), 331–345.

- Shartsis, L. and Smock, A. W. (1947), ‘Surface tensions of some optical glasses’, *Journal of the American Ceramic Society* **30**(4), 130–136.
- Shelby, J. E. (2005), *Introduction to glass science and technology*, Royal Society of Chemistry.
- Sokolnikov, I. S. (1956), *Mathematical Theory of Elasticity*, 2nd edn, McGraw–Hill.
- Stokes, Y. M. (1999), ‘Flowing windowpanes: Fact or fiction?’, *Proceedings of the Royal Society of London Series A* **455**(1987), 2751–2756.
- Stokes, Y. M. (2000), ‘Flowing windowpanes: A comparison of Newtonian and Maxwell fluid models’, *Proceedings of the Royal Society of London Series A* **456**(2000), 1861–1864.
- Stokes, Y. M. (2010), Bending in extrusion of optical fibre preforms, *in* P. Howlett, M. Nelson and A. J. Roberts, eds, ‘Proceedings of the 9th Biennial Engineering Mathematics and Applications Conference, EMAC-2009’, Vol. 51 of *ANZIAM Journal*, pp. C124–C136.
- Stokes, Y. M., Bradshaw-Hajek, B. H. and Tuck, E. O. (2011), ‘Extensional flow at low Reynolds number with surface tension’, *Journal of Engineering Mathematics* **70**(1–3), 321–331.
- Stokes, Y. M., Buchak, P., Crowdy, D. G. and Ebdendorff-Heidepriem, H. (2014), ‘Drawing of micro-structured fibres: circular and non-circular tubes’, *Journal of Fluid Mechanics* **755**, 176–203.
- Stokes, Y. M. and Tuck, E. O. (2004), ‘The role of inertia in extensional fall of a viscous drop’, *Journal of Fluid Mechanics* **498**, 205–225.

- Szegö, G. (1950), ‘Conformal mapping of the interior of an ellipse onto a circle’, *American Mathematical Monthly* **57**(7), 474–478.
- Tammann, G. and Hesse, W. (1926), ‘Die abhängigkeit der viscosität von der temperatur bie unterkühlten flüssigkeiten’, *Zeitschrift für Anorganische und Allgemeine Chemie* **156**(1), 245–257.
- Tanveer, S. and Vasconcelos, G. L. (1995), ‘Time-evolving bubbles in two-dimensional Stokes flow’, *Journal of Fluid Mechanics* **301**, 325–344.
- Taroni, M., Breward, C. J. W., Cummings, L. J. and Griffiths, I. M. (2013), ‘Asymptotic solutions of glass temperature profiles during steady optical fibre drawing’, *Journal of Engineering Mathematics* **80**(1), 1–20.
- Thevenaz, L. (2011), *Advanced Fiber Optics*, Engineering sciences, EFPL Press.
- Trabelssi, M., Ebendorff-Heidepriem, H., Richardson, K. A., Monroe, T. M. and Joseph, P. F. (2015), ‘Computational modeling of hole distortion in extruded microstructured optical fiber glass preforms’, *Journal of Lightwave Technology* **33**(2), 424–431.
- Trabelssi, M., Ebendorff-Heidepriem, H., Richardson, K. C., Monroe, T. M. and Joseph, P. F. (2014), ‘Computational modeling of die swell of extruded glass preforms at high viscosity’, *Journal of the American Ceramic Society* **97**(5).
- Trefethen, L. N. (2000), *Spectral Methods in MATLAB*, Software, Environments, and Tools, Society for Industrial and Applied Mathematics.
- Tronolone, H., Stokes, Y. M., Foo, H. T. C. and Ebendorff-Heidepriem, H. (2016), ‘Gravitational extension of a fluid cylinder with internal structure’, *Journal of Fluid Mechanics* . Accepted for publication.

- Trouton, F. T. (1906), ‘On the coefficient of viscous traction and its relation to that of viscosity’, *Proceedings of the Royal Society of London Series A* **77**(519), 426–440.
- Urich, A., Maier, R. R. J., Yu, F., Knight, J. C., Hand, D. P. and Shephard, J. D. (2013), ‘Silica hollow core microstructured fibres for mid-infrared surgical applications’, *Journal of Non-Crystalline Solids* **377**, 236–239. {ISNOG} 2012 Proceedings of the 18th International Symposium on Non-Oxide and New Optical Glasses Rennes, France, July 1–5, 2012.
- van de Vorst, G. A. L. (1993), ‘Integral method for a two-dimensional Stokes flow with shrinking holes applied to viscous sintering’, *Journal of Fluid Mechanics* **257**, 667–689.
- van Eijkelenborg, M., Large, M., Argyros, A., Zagari, J., Manos, S., Issa, N., Bassett, I., Fleming, S., McPhedran, R., de Sterke, C. M. and Nicorovici, N. A. (2001), ‘Microstructured polymer optical fibre’, *Optics Express* **9**(7), 319–327.
- Vogel, H. (1921), ‘The temperature dependence law of the viscosity of fluids’, *Physikalische Zeitschrift* **22**, 645–646.
- Voyce, C. J., Fitt, A. D. and Monro, T. M. (2008), ‘The mathematical modelling of rotating capillary tubes for holey-fibre manufacture’, *Journal of Engineering Mathematics* **60**(1), 69–87.
- Wang, J. S., Vogel, E. M. and Snitzer, E. (1994), ‘Tellurite glass: A new candidate for fiber devices’, *Optical Materials* **3**(3), 187–203.
- Warren-Smith, S. C., Ebendorff-Heidepriem, H., Foo, T. C., Moore, R., Davis, C. and Monro, T. M. (2009), ‘Exposed-core microstructured optical fibers for real-time fluorescence sensing’, *Optics Express* **17**(21), 18533–18542.

- Wilmott, P. (1989), 'The stretching of a thin viscous inclusion and the drawing of glass sheets', *Physics of Fluids A: Fluid Dynamics* **1**(7), 1098–1103.
- Wilson, S. D. R. (1988), 'The slow dripping of a viscous fluid', *Journal of Fluid Mechanics* **190**, 561–570.
- Wirtinger, W. (1927), 'Zur formalen theorie der funktionen von mehr komplexen veränderlichen', *Mathematische Annalen* **97**(1), 357–375.
- Wylie, J. J. and Huang, H. (2007), 'Extensional flows with viscous heating', *Journal of Fluid Mechanics* **571**, 359–370.
- Wylie, J. J., Huang, H. and Miura, R. M. (2011), 'Stretching of viscous threads at low Reynolds numbers', *Journal of Fluid Mechanics* **683**, 212–234.
- Xue, S. C., Large, M. C. J., Barton, G. W., Tanner, R. I., Poladian, L. and Lwin, R. (2006), 'Role of material properties and drawing conditions in the fabrication of microstructured optical fibers', *Journal of Lightwave Technology* **24**(2), 853–860.
- Xue, S.-C., Poladian, L., Barton, G. W. and Large, M. C. J. (2007), 'Radiative heat transfer in preforms for microstructured optical fibres', *International Journal of Heat and Mass Transfer* **50**(7), 1569–1576.
- Xue, S. C., Tanner, R. I., Barton, G. W., Lwin, R., Large, M. C. J. and Poladian, L. (2005*a*), 'Fabrication of microstructured optical fibers—Part I: Problem formulation and numerical modeling of transient draw process', *Journal of Lightwave Technology* **23**(7), 2245–2254.
- Xue, S. C., Tanner, R. I., Barton, G. W., Lwin, R., Large, M. C. J. and Poladian, L. (2005*b*), 'Fabrication of microstructured optical fibers—Part

- II: Numerical modeling of steady-state draw process', *Journal of Lightwave Technology* **23**(7), 2255–2266.
- Yarin, A. L. (1995), 'Surface-tension-driven flows at low Reynolds number arising in optoelectronic technology', *Journal of Fluid Mechanics* **286**, 173–200.
- Yarin, A. L., Gospodinov, P. and Roussinov, V. I. (1994), 'Stability loss and sensitivity in hollow fiber drawing', *Physics of Fluids* **6**(4), 1454–1463.
- Yarin, A., Rusinov, V. I., Gospodinov, P. and Radev, S. (1989), 'Quasi one-dimensional model of drawing of glass microcapillaries and approximate solutions', *Journal of Theoretical and Applied Mechanics* **20**(3), 55–62.
- Young, D. L., Jane, S. J., Fan, C. M., Murugesan, K. and Tsai, C. C. (2006), 'The method of fundamental solutions for 2D and 3D Stokes problems', *Journal of Computational Physics* **211**(1), 1–8.
- Zhang, W. Q., Manning, S., Ebendorff-Heidepriem, H. and Monroe, T. M. (2013), 'Lead silicate microstructured optical fibres for electro-optical applications', *Optics Express* **21**(25), 31309–31317.
- Zhang, Y., Li, K., Wang, L., Ren, L., Zhao, W., Miao, R., C. J. Large, M. and Van Eijkelenborg, M. A. (2006), 'Casting preforms for microstructured polymer optical fibre fabrication', *Optics Express* **14**(12), 5541–5547.



# Index

- Airy stress function, 54, 57, 70, 83, 91
- annealing, 248
- argument principle, 137, 315
- bianalytic function, 70, 81
- biharmonic
- conjugate, 82
  - equation, 74, 75, 106
  - function, 70
  - operator, 75
- billet, 6, 234
- Biot number, 47, 173, 218–219
- Bond number, 173, 219
- boundary element method, 106
- cane, 8, 128, 146
- caning, 8, 121
- capillary number, 46
- capillary stacking, 6, 18, 255, 263
- Cartesian co-ordinate
- system, 34, 39, 217, 294
  - vectors, 102
- casting, 5
- Cauchy–Riemann equations, 79
- biharmonic, 82
  - complex, 81
  - vector form, 81
- circle domain, 110, 167, 257, 258, 271, 282, 295
- coefficient of thermal expansion, 24
- compatibility condition, 51, 66
- complete elliptic integral, 103, 145
- complex variables, 14, 70, 75, 107, 306
- conformal map, 71, 107, 109, 133, 135, 142, 167, 258, 267, 271, 282, 286, 315
- crisis time, 248
- Deborah number, 24
- die, 6, 33, 67, 127, 211, 213, 214, 227, 234, 256, 280, 293, 302, 307
- divergence theorem, 51, 57

- dot product, 93  
     complex, 94
- drawing, 6, 9, 10, 13, 18, 19, 22, 23, 29, 42, 49, 59, 65, 108, 178, 199, 231  
     tower, 6, 317
- drilling, 5, 203
- dynamic boundary condition, 41, 49, 57, 64, 71, 94, 95, 99, 109, 117, 136, 154  
     complex, 88, 90, 151  
     mapped, 112
- elastic material, 23, 70
- elliptical pore model, 72, 157, 306
- emissivity, 29, 48
- Eulerian co-ordinate, 11, 174
- exponential integral, 245
- extensional flow, 11, 34, 117, 174  
     uniaxial, 36
- extrudate, 6
- extrudate swell, 9, 214, 215, 252, 293, 309
- extrusion, 6, 9, 12, 18, 22, 33, 39, 67, 125, 128, 142, 157, 169, 181, 210, 213–255, 280, 307  
     tower, 6
- Fornberg methods, 110, 256
- Frenet–Serret formulae, 55, 92
- Froude number, 45
- glass, 1, 2, 5, 17–31, 39, 197, 202, 214, 234, 263, 277, 317  
     transition, 17  
     temperature, 18
- Goursat  
     exact annular solution, 101  
     functions, 70, 77, 86, 89, 106, 109–289  
     representation, 70, 77, 93  
     uniqueness, 95
- gradient, 86
- gravity, 9–15, 33–39, 41, 58–59, 67, 69, 117, 128, 171, 178–179, 183, 187, 194, 199, 207, 213, 248, 305, 317  
     dimensionless, 45, 218–219
- harmonic  
     conjugates, 79  
     function, 79  
     mean, 180, 224, 242, 245
- heat transfer coefficient, 29, 42
- Hele-Shaw flow, 72–73

- inertia, 11, 12, 38–39, 45, 58–59, 67, 172, 173, 178, 207–212, 223, 248
- jacket, 8, 121, 203
- Joukowski transformation, 144
- kinematic boundary condition, 41, 46, 49, 60, 63–66, 93–95, 99, 109, 117, 136, 153  
mapped, 114–116
- Kolosov–Muskhelishvili  
equations, 70  
functions, *see also* Goursat functions  
traction equation, 91
- Lagrangian co-ordinate, 11, 34, 58, 62–63, 66, 67, 174–177, 184, 196, 213, 220–224, 250, 252, 266, 305, 324
- Laplace  
equation, 48, 50, 79  
operator, 75
- Leibniz’s rule, 37, 38
- material derivative, 37, 175, 177, 222
- Maxwellian, 23
- Navier–Stokes equations, 41, 45, 218
- Newton cooling  
condition, 42, 48  
law, 29
- Newton’s method, 137, 314–315
- Newtonian fluid, 22, 34, 39, 217  
stress tensor, 36
- non-Newtonian, 23
- optical fibre, 1  
microstructured, 2–10, 31, 69, 108  
preform, 5–8, 19, 51, 121–130, 142, 146, 157, 160–166, 181, 203, 211, 213, 217, 219, 231, 233–248, 255, 277, 281, 307–309
- Péclet number, 46, 47, 173, 218–219
- pin, 127, 214–217, 281, 294, 296–300, 303
- pinch-off, 207, 248–252
- Poiseuille flow, 216, 294
- Poisson’s equation, 50, 66, 107, 295
- pressure, 10, 26, 36, 39, 41, 43, 64, 74, 78, 79, 87, 95, 99, 294
- pseudospectral method, 108
- reduced time, 11, 34, 64–66, 69, 78,

- 177–181, 185, 198, 209, 211,  
221–223, 225, 228, 233, 251,  
305, 319
- Reynolds number, 45, 173, 178, 207,  
211, 218–219, 223, 248
- Rosseland approximation, 42
- shear modulus, 23
- Sherman–Lauricella integral equations,  
106
- sieve plate, 214
- sintering, 72, 107, 281
- slenderness  
approximation, 10–12, 66, 69, 171,  
176, 187, 213, 219, 252, 305  
ratio, 43, 173, 219
- spectral method, 107–121, 130–146, 154,  
167–170, 203, 256, 266, 277,  
285, 286, 289, 306
- standard orientation, 51, 55, 90, 111
- Stefan–Boltzman constant, 29, 48
- Stokes equations, 61, 69–88, 105, 150,  
171, 294  
axisymmetric polar, 99
- stream function, 74, 78, 83, 85, 95, 102
- surface tension, 9–12, 25–28, 33, 37–39,  
41, 43, 58, 63–65, 67, 69, 73, 91,  
104, 105, 125, 128, 142, 148,  
157, 167, 170–172, 176, 187,  
189–196, 199, 202, 207, 209–  
211, 213, 222, 227–228, 252,  
254, 256, 280, 290, 305–307,  
319  
dimensionless, 46, 65, 173, 183, 218–  
219, 230–231  
weak, 181, 189, 209, 210, 224, 250  
zero, 181, 189, 209, 210, 224, 250
- susceptor, 8
- thermal diffusivity, 28, 41
- Trouton  
model, 34, 37  
ratio, 36
- velocity, 36, 39, 234  
axial, 33, 50, 61, 66, 213, 294–303,  
308  
complex, 86  
scale, 46, 172, 207, 217, 218  
transverse, 53, 64, 78, 93–95, 106,  
136, 153
- viscoelastic material, 23
- viscosity, 9, 17–22, 24, 39, 41, 44, 48,  
65, 66, 182, 184, 197, 198, 202,  
211, 217, 220, 225, 233, 234,

242, 245, 250, 252, 295, 305,  
309, 318–319

Trouton, 36, 58

vorticity, 78–79, 87, 106

welding chamber, 214, 281, 293, 296,  
300, 303

Wirtinger derivatives, 76, 81